DTU

SYNOPSYS®
Silicon to Software™

DTU Physics
Department of Physics

Atomic-scale modelling of interfaces in nanoscale electronics

Line Jelver

February 2021

Supervisors:

Prof. Karsten Wedel Jacobsen

CAMD, DTU Physics, Department of Physics

Technical University of Denmark

Fysikvej, Building 309, Room 207

2800 Kgs. Lyngby

kwj@fysik.dtu.dk

Prof. Kurt Stokbro

former CEO at Synopsys QuantumATK

Fruebjergvej 3

2100 København Ø

kurt.stokbro@gmail.com

Daniele Stradi

former Senior Applications Engineer at Synopsys QuantumATK

Fruebjergvej 3

2100 København Ø

danistradi@hotmail.com

Prof. Kristian Sommer Thygesen

CAMD, DTU Physics, Department of Physics

Technical University of Denmark

Fysikvej, Building 309, Room 202

2800 Kgs. Lyngby

thygesen@fysik.dtu.dk

Preface

This thesis is submitted in candidacy for a Ph.D. degree from the Technical University of Denmark (DTU). The work has been carried out between June 2016 and February 2021 at the Section of Computational Atomic-scale Materials Design at the Department of Physics and at the Copenhagen office of Synopsys Denmark (QuantumWise A/S at the beginning of the project). The studies have been supervised by Karsten Wedel Jacobsen, Kurt Stokbro, Daniele Stradi, and Kristian Sommer Thygesen. This project has been part of the Industrial PhD programme under the Innovation Fund Denmark (IFD) and has therefore been partly financed by Synopsys and by IFD under File No. 5189-00082B.

I have told my two daughters that I am writing a book. A book about the small spheres that I have inside my computer. I want too see, if I can build something which is good at controlling electrical current.
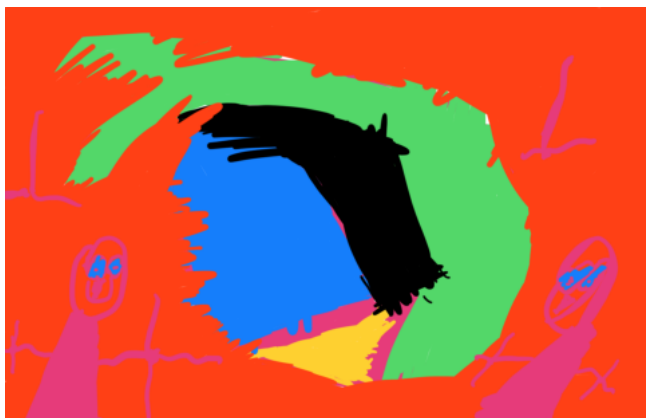
"Mor! Leger du nu med dine atomer igen?" - Lærke Jelver Mathiesen

Acknowledgements

Many people have contributed to this research project. First of all, I would like to thank Karsten. It has been a true honor and privilege to be supervised by Karsten. In my opinion, what marks a good scientist is a continuous curiosity to explore, stubbornness to understand, and courage to be honest. Karsten possesses all of these qualities combined with an impressive down-to-earth understanding of complicated physical concepts which I can only aspire to achieve. I will truly miss our marathon whiteboard discussions which I have gained so much from and which I have always enjoyed.

Secondly, I would like to thank Kurt Stokbro for shaping the original project and guiding the research efforts. I would like to extend a special thanks for allowing me to shape my PhD studies to fit my personal life. That I was allowed to go on part-time and later to work from home has allowed me to finish my PhD without sacrificing my family life. Thanks also goes to Daniele Stradi, who took great responsibility for the project during the transition period when QuantumWise was bought by Synopsys. I have been very happy for the guidance Daniele has provided.

The scientific communities both at the CAMD section and Synopsys have been a great privilege to be a part of. At both places, help is never far away. A special thanks goes to Peter Mahler Larsen whom I really enjoyed my collaboration with and to Thomas Olsen for contributing to the research on topological insulators. I would also like to thank Søren Smidstrup for helping me during the final part of the project.

Finally, I would like to thank my husband and two daughters. You bring meaning to my life in a way no PhD degree ever could. Special thanks to my husband for putting up with me while being completely out of reach in the final stage of writing the thesis, for proof reading, and for his unfaltering support. Without your belief in me, I wouldn't have achieved half of what I have today.

February 3, 2021
Line Jelver

Abstract

The evolution of field effect transistors (FETs) has enabled the digital revolution which shapes the everyday lives of people all over the world. Currently, new materials and designs are investigated in pursuit of continuing the improvement of device performance and efficiency.

This thesis investigates two-dimensional (2D) materials for future transistor designs. The research has mainly focused on the transition metal dichalcogenide (TMD) heterophase FET design which uses the metallic phase of the TMD as the source and drain electrodes and the semiconducting phase as the channel. Density functional theory and the non-equilibrium Green's function method are used to investigate the charge transfer at interfaces between these 2D materials and a method for predicting stable interfaces between two crystals has been developed.

The Schottky barrier between contact and channel in a transistor is perceived as an intrinsic property which predicts how well the device will perform. In this thesis, ab-initio calculations on phase-engineered $MoTe_2$ show that for these 2D Schottky contacts, this is not the case. Interface states and standing waves due to quantum confinement mediate tunneling current and renders the Schottky barrier height a poor descriptor of device performance. The results also demonstrate that the electrostatic response of the Schottky barrier can't be predicted by the conventional models which means the Schottky barrier found from the activation energy method isn't well-defined either.

The relevance of using a heterophase $MoTe_2$ design for next-generation transistors is assessed by reviewing the available literature and by comparing with the ab-initio calculations and the performance goals of a 2025 device as defined by the International Roadmap for Devices and Systems.[1] The comparison focuses on the ON-current, sub-threshold slope, and power supply voltage and concludes that the heterophase design has the potential to perform according to the goals of the roadmap if a high-κ dielectric is used as the gate oxide. The largest obstacle for this design to succeed is the lack of a scalable method for doping of 2D semiconductors. If such a method is developed, the heterophase TMD transistors seem to be a viable option for future transistor designs.

Resumé

Evolutionen af felteffekttransistorer (FET'er) har muliggjort den digitale revolution, som former hverdagen for mennesker over hele verden. I dag undersøges nye materialer og design muligheder, for at muliggøre den fortsatte optimeringen af transistorernes ydeevne of effektivitet.

Denne afhandling undersøger todimensionelle (2D) materialer til fremtidens transistordesign. Forskningen har hovedsageligt fokuseret på transitions-metal dichalkogen (TMD) heterofase transistordesignet, hvor den metalliske fase af TMD'en benyttes som elektroder, og den halvledende fase bruges som strømkanal. Tæthedsfunktionalteori og Greens funktion metoden benyttes, til at undersøge ladningsoverførslen ved disse 2D grænseflader, og en metode, der kan forudsige stabile grænseflader mellem to krystaller, er blevet udviklet.

Schottky barrieren mellem elektroden og strømkanalen i en transistor betragtes som en intrinsisk egenskab, der beskriver ydeevnen for enheden. I denne afhandling demonstrerer ab-initio beregninger på fasekontrolleret $MoTe_2$, at det ikke er tilfældet for disse 2D Schottky kontakter. Grænsefladetilstande og stående bølger grundet det begrænsende potentiale betyder, at Schottky barrieren bliver et dårligt mål for ydeevnen. Resultaterne demonstrer også, at det elektrostatiske respons af Schottky barrieren ikke kan forudsiges med de konventionelle modeller, hvilket betyder at en Schottky barriere fundet ved hjælp af aktiveringsenergimetoden, heller ikke er veldefineret.

Transistordesignet baseret på fasekontrolleret $MoTe_2$ vurderes ved at gennemgå den eksisterende litteratur og sammenligne den med ab-initio beregningerne og målsætningen for ydevenen af en 2025 transistor sat af 'International Roadmap for Devices and Systems'.[1] Sammenligningen fokuser på output strømmen, responset på gate spændingen og strømforsyningsspændingen og konkluderer, at det fasekontrollerede design viser potentiale til at kunne levere i overensstemmelse med målsætningen. Den største udfordring, for at få dette design til at blive en succes, er at der ikke findes en dopingmetode til 2D halvledere, som egner sig til opskalering. De fasekontrollerede transistorer kan blive en mulig løsning til fremtidens transistordesign, hvis sådan en metode bliver udviklet.

List of Publications

Method for determining optimal supercell representation of interfaces
Daniele Stradi, <u>Line Jelver</u>, Søren Smidstrup and Kurt Stokbro.
Journal of Physics: Condensed Matter, 29, 185901 (2017)

Determination of low-strain interfaces via geometric matching
<u>Line Jelver</u>, Peter Mahler Larsen, Daniele Stradi, Kurt Stokbro, and Karsten Wedel Jacobsen.
Physical Review B, 96, 085306 (2017)

Spontanous breaking of time-reversal symmetry at the edges of 1T' monolayer transition metal dichalcogenides
<u>Line Jelver</u>, Daniele Stradi, Kurt Stokbro, Thomas Olsen, and Karsten Wedel Jacobsen.
Physical Review B, 99, 155420 (2019)

Schottky barrier lowering due to interface states in 2D heterophase devices
<u>Line Jelver</u>, Daniele Stradi, Kurt Stokbro, and Karsten Wedel Jacobsen,
Nanoscale Adv., 573, 507 (2021).

Conference contributions

Spontaneous breaking of time-reversal symmetry at the edges of 1T' monolayer transition metal dichalcogenides.
Oral contribution
IVC-21, Sweden (2019)

Determination of Schottky barriers in 2D heterophase devices.
Oral contribution
Graphene 2020, Online (2020)

Contents

CHAPTER 1

Introduction

This thesis uses ab-initio methods to describe the charge transfer at atomic-scale interfaces specializing on interfaces between 2D materials. A general method for predicting interfaces between crystals is developed and the theory of the Schottky barrier is extended to 2D metal-semiconductor interfaces. Finally, the 2D transition metal dichalcogenide heterophase field effect transistor is modelled, analyzed, and evaluated as a future transistor design.

1.1 The Digital Revolution

When I put my children to bed at night, they sometimes ask me to tell a story from when I was a child. Then, I tell them something like 'when I was a child, the phone was connected to the wall by a wire and the only thing it could do was to phone other people' or 'when I was a child, the only cartoons I would watch, was the ones broadcasted on the television. If you missed the show, you had to wait at least a day before you got the chance again'. I am only 31 years old but the available computational power, data storage, and bandwidth has developed with unprecedented speed not only within my life span but ever since the beginning around the Second World War. Computer and information technology has been one of the fastest developing technologies in history. When I was a child, there was airplanes, cars, synthetic fertilizer, and nuclear power plants but there was no laptops, no smartphones, and absolutely no Netflix.

As a materials scientist, I will postulate that one of the main reasons that this development has been possible is simply that we have an abundance of silicon on Earth. 27.7% of the mass of Earths crust is made of silicon which makes it the second most abundant element of Earth, second only to oxygen. Silicon has been an almost supernatural material in terms of the applicability within electronics and optics. Due to the large impact

of silicon, the late 20th and beginning of the 21st century are being referred to as the 'Silicon Age' just as previous ages have been named from the utilization of a new material such as the Stone Age and Bronze Age.

The digital revolution which have resulted from the development of silicon technology shapes the everyday lives of people all around the world. 59% of the global population are active internet users and the majority of these users access the internet through a mobile device.[2] This global information sharing represents equal opportunities to self-educate and to contribute to the common pool of knowledge. The internet represents freedom of speech in the extreme limit, for better and worse. The massive amounts of information requires filtering to be of use and, in some cases, not to be harmful.

As in the case of most groundbreaking technologies throughout the history, also information technology can be used for ethically debatable purposes. The surveillance of citizens is one of the most pronounced examples of this. Considering the speed at which things have progressed, it is perhaps not surprising that humanity is struggling a bit to keep up. However, The benefits of the internet, hearing aids, pacemakers, autonomous vehicles, and, by the way, atomic-scale modelling are in in my opinion worth some struggling.

1.2   The Energy Crisis

The distribution of information and communication technology (ICT) has revolutionized our way of living but it has not come for free. In 2018, 1% of the annual global energy consumption was estimated to be related to ICT and by 2030, it is projected to be between 3 and 8%.[3] The large projected increase is primarily due to the energy demand of large data centers.

The world population is growing and so is the global energy demand. The energy hunger is still primarily being fed with energy from fossil fuels which are polluting the air and contributing to the global warming. According to the World Health Organization (WHO), 91% of the global population live in places where the air pollution exceeds the recommended values[4] and the global warming is steadily increasing. The temperature average had risen by 1 °C in 2017 compared to pre-industrial values and

is increasing at a pace of around 0.2 °C per decade.[5] The consequences of a continuous warming are predicted to cause both warmer and more extreme weather. Wild fires, drought, and tornadoes will make large areas, which are inhabited today, uninhabitable.

The greatest challenge of our time, will be to provide enough energy for the growing population on Earth. Even ignoring the fatal consequences of global warming, we will simply run out of fuels, if we continue to use the nonrenewable sources. It has been a great hope, that ICT will be part of the solution to the energy crisis. ICT is based on electricity which makes it easier to sustain by renewable energy sources. However, it is crucial that the development within this sector focuses on energy efficiency. ICT can only become part the solution if the production and utilization of ICT devices becomes sustainable. It is therefore imperative that the energy efficiency of these devices continues to increase.

1.3   The Transistor

The transistor is a key component in all modern technology and the improvement of the transistor is what has enabled the digital revolution
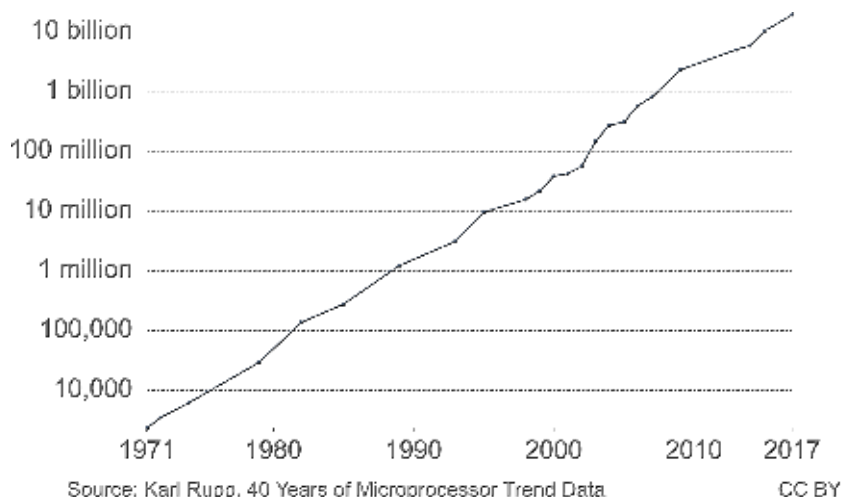
Figure 1.1: Moore's law. Number of transistors which fit into a microprocessor. Adapted from Ref. [6] and [7].

together with the development of hard drives and optical fibers. It is therefore also a key component in improving the sustainability of the ICT sector. There is approximately 8 billion transistors in a smartphone[8] and it is estimated that a total of 13 sextillion ($\times 10^{21}$) transistors where fabricated between 1960 and 2008.[9] Needless to say, any small improvement in the energy efficiency of the transistor will make a huge difference in the energy consumption of the ICT sector.

The first transistor was made in 1947 at Bell Laboratories and the first metal-oxide-silicon field effect transistors (MOSFETs) were developed in the 1960s. These types of transistors held the potential to be miniaturized and mass-produced and from that point, the technology really took off. In 1965, previous CEO and co-founder of Intel, Gordon E. Moore, noticed that the number of transistors per silicon chip had doubled every 18-24 months. He then postulated that this trend of a doubling every second year would continue the next decade.[10] It turned out that the trend would hold the next five decades and the statement has since been glorified as Moore's law. Some argue that it is still holding, see Figure 1.1.[7]

The transistor design has been improved tremendously over the decades. The commercial transistors have evolved from a planar transistor of a few different materials to devices using the finFET and Gate-All-Around (GAA) designs where each part and material of the device has been optimized. High-κ gate oxides, work function modulating gate metals, and channels doped with implanted ions are all examples of such optimizations. A simple sketch of a FET is shown on Figure 1.2. The main components
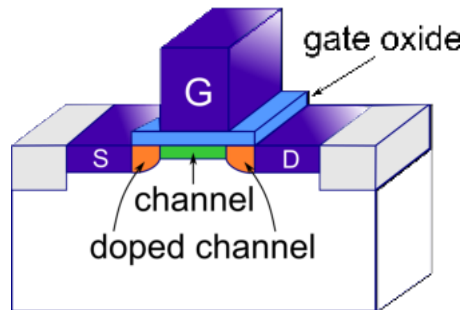

Figure 1.2: Sketch of a MOSFET showing the four main components, the source (S), drain (D), and gate (G) electrodes, and the semiconducting channel.

are the source and drain electrode, the semiconducting channel, and the gate electrode. An in-depths description of the transistor components and operation is presented in Chapter 9.

The evolution was originally aimed primarily at down-scaling the devices in order to improve the efficiency and computational power. The correlation between these quantities is known as Dennard scaling which predicts that each time the density of transistors double, the circuit becomes 40% faster while the power consumption stays the same, i.e. the power pr. transistor is reduced by 50%. Dennard scaling held up until around 2005-2010 when power began to be lost through tunneling processes in the nano-scale devices. Today, the semiconductor industry has entered the 'More than Moore' era where the efficiency and computational power of the transistors are attempted to be improved by tailoring the transistors to specific applications and investigate alternative materials.

The new era has fueled a massive amount of research in different materials and designs for the transistors of the future. A natural branch of these efforts has investigated semiconducting 2D transition metal dichalcogenides (TMDs) as a substitute for the silicon channels. The 2D materials do indeed offer the ultimate dimensional scaling by their layered structure and could enable an increased efficiency through further down-scaling. In contradiction to silicon, the TMDs retain good carrier mobilities down to the single layer limit (thickness around 0.7 nm's).

The greatest challenges related to utilizing the 2D TMDs in transistors are that a method for controlled doping of the 2D semiconductors isn't yet developed and that the deposition of metal contacts directly on the 2D material results in a large resistance. The heterophase TMD FET design is an attempt to solve the second of these challenges. The design utilizes that the TMDs can exhibit either metallic or semiconducting properties depending on the crystal phase and that phase transition techniques can be applied to control the phase. The semiconducting channel is contacted with the metallic phase which serves as source and drain electrodes. The conventional metal contacts is then deposited on the metallic 1T- or 1T'-phase of the TMD rather than the semiconducting 2H-phase which decrease the resistance.

The Schottky barrier is a quantity which can be used as an descriptor of the conductance between a metal and semiconductor. The charge transfer when the two materials, or in this case phases, are interfaced creates a potential barrier at the semiconductor-metal contact. The potential bar-

rier represents the minimal energy required for carriers to pass trough the contact. This minimal energy is called the Schottky barrier height and is, within this simple picture, directly correlated with the contact resistance. In order to evaluate the heterophase FET design, previous studies have investigated the Schottky barrier between the two TMD phases both by measurements and ab-initio calculations. The most investigated material was originally MoS_2 but $MoTe_2$ has been given great attention the last few years and seems to be the best candidate so far.

In this thesis, the general methods needed to do ab-initio modelling of atomic-scale interfaces are introduced and a method for predicting stable interfaces between two periodic crystals is developed. The electronic properties of the 2D TMDs are presented and the properties of these materials, which are of importance in the context of the heterophase FET design, are reviewed. The topological properties of T'-phase TMDs are also presented and it is shown that the topological protection of the edge states is broken at the edges which most commonly form the contacts to the semiconducting phase.

The theory of the Schottky barrier is reviewed and transferred to a 2D contact and heterophase contacts between T'- and H-phase $MoTe_2$ are investigated using ab-initio calculations. Finally, a heterophase FET is modelled and compared to the experiments in order to asses the performance. The heterophase FETs have shown impressive results in some of the newest experiments[11,12] but the technology is still in it's cradle. The objective of the ab-initio modelling of the devices is to illuminate some of the physical mechanisms behind the charge transfer in hope that this can help to speed up the development of this new technology.

1.4   Outline

The structure of the thesis has been chosen such that four parts each present a subject needed to understand the scientific results. The four subjects are,

Part I: Ab-initio Modelling of Interfaces which introduces a set of tools and methods that are necessary for doing ab-initio modelling of interfaces. Chapter 2 introduces density functional theory and the non-equilibrium Green's function, and Chapter 3 describes a

general method for finding the best orientation of two crystals when combining them to an interface.

Part II: 2D Transistion Metal Dichalcoginides which introduces the transition metal dichalcogenides (TMDs). Chapter 4 describes the structural phases and related electronic properties, Chapter 5 describes the fabrication and doping methods for the semiconducting TMDs, and Chapter 6 describes the phase transition between the semiconducting and semi-metallic phase and the topological properties of the latter.

Part III: 2D Schottky Barrier which describes how the dimensionality of the materials affects the electronic properties of a metal-semiconductor interface. Chapter 7 introduces the theory behind the Schottky barrier and charge transport across metal-semiconductor interfaces and Chapter 8 presents ab-initio calculations of the Schottky barrier and charge transport properties of T'-H $MoTe_2$ interfaces.

Part IV: Phase-engineered $MoTe_2$ as a Next-generation Transistor which describes field effect transistors (FETs) and how 2D materials can be utilized in future FET designs. Chapter 9 introduces modern field effect transistors, Chapter 10 outlines the possibilities of using 2D TMDs in FETs and reviews the progress of using phase-engineered MoS_2 or $MoTe_2$, and Chapter 11 presents ab-initio calculations on $MoTe_2$ heterophase field effect transistors.

Ab-initio Modelling of Interfaces

This part of the thesis will introduce tools and methods which are necessary for doing ab-initio modelling of interfaces. Ab-initio is a Latin term which translates to 'from the beginning'. In the natural sciences, ab-initio or 'first-principles' methods refers to methods where the results are based exclusively on the laws of nature and the only input is the fundamental physical constants. Within quantum chemistry, this means that the results must be based on the solution to the many-body Schrödinger equation.

Density functional theory (DFT) is an example of an ab-initio method for obtaining the ground-state electronic structure of materials. In this thesis, DFT is used to model interfaces and surfaces of crystalline 2D materials. The objective is to investigate the prospects of using the 2D transition metal dichalcogenides in field effect transistors and therefore to model the charge transport across interfaces consisting of these materials. DFT is an equilibrium method which cannot describe a system where a current is running, however, this can be achieved by combining DFT with the non-equilibrium Green's function method.

The interface between two crystalline materials should preferably preserve the periodicity of the two crystals. If this condition isn't fulfilled, the interface will be incommensurate and consequently unstable due to dislocations and strain. A tool for matching two crystals, while minimizing the strain and area of the coincidence interface cell, is therefore a basic requirement for modelling of interfaces. Besides evaluating the minimal strain between two crystals, this method also predicts which surfaces of the two crystals that are most likely to form a stable interface.

The following chapters are organized as follows,

Chapter 2 introduces density functional theory and the non-equilibrium Green's function method and explains how these have been applied.

Chapter 3 describes a general method for obtaining the possible matches between two periodic crystals such that they can be combined to form an interface.

Density Functional Theory

Density functional theory (DFT)[13,14] is perhaps the most successful method for describing the electronic structure of solid state materials. This chapter will introduce Kohn-Sham DFT and explain how the theory is implemented in the QuantumATK software[15] and how it can be combined with the non-equilibrium Green's function (NEGF) method in order to describe charge transport between two crystals.

DFT builds on the foundation that the electronic properties of a material can be uniquely determined if the ground state density is known. This is stated in the *Hohenberg-Kohn theorems*,

Hohenberg-Kohn Theorem 1 *The external potential, v_{ext}, is uniquely determined by the ground state density, n, besides a trivial additive constant.*

Hohenberg-Kohn Theorem 2 *The ground state density, n, uniquely determines the ground state electronic many-body wave function, $\Psi[n]$, and the ground state energy, E.*

$$E[n] = \langle \Psi[n] | \, \hat{T}_e + \hat{V}_{ee} \, | \Psi[n] \rangle + \int n(\mathbf{r}) v_{ext}(\mathbf{r}) \, \mathrm{d}\mathbf{r}$$

$$= F[n] + \int n(\mathbf{r}) v_{ext}(\mathbf{r}) \, \mathrm{d}\mathbf{r}.$$

$\hat{T}_e$ is the kinetic energy of the electrons and $\hat{V}_{ee}$ is the electron-electron interaction.

Two questions arise from these statements, *what* is the density? and *how* can the many-body wave function and ground state energy be determined from the density? These two questions can be answered trough a series of derivations and approximation which I will briefly outline in the following. For a more exhaustive review, I recommend the excellent textbook by Kohanoff.[16]

Adiabatic Approximation   The equilibrium state of a system consist-
ing of both nuclei and electrons which are interacting with each other is
described by the many-body Schrödinger equation. This equation is not
analytically nor feasible to solve numerically. In order to simplify mat-
ters, the adiabatic approximation, also known as the Born-Oppenheimer
approximation, is invoked. Since the nuclei are much heavier than the
electrons, it is assumed that the nuclei motion is slow enough, compared
to the electronic motion, such that the electrons will reach an equilibrium
state of the nuclei positions at every infinitesimal step of the nuclei motion.
In this picture, the nuclei can be seen as a background of positive charge
and the electronic Hamiltonian is,

$$\hat{H}_e = \hat{T}_e + \hat{V}_{ee} + \hat{V}_{e,ext}.$$

The electron-nuclei interaction has been included as an external poten-
tial, $\hat{V}_{e,ext}$, in this formulation since the ions are considered frozen and act
as a positive background. Note, that $\hat{V}_{e,ext}$ can include contributions from
external fields as well. The equation can be solved analytically in the case
of the hydrogen atom and yields the hydrogen electronic orbitals and lev-
els. However, larger atoms require a numerical solution and the memory
consumption when solving the equation makes it practically impossible to
do. The power behind DFT is the reformulation of the problem in terms
of the ground state density which reduces the dimensionality significantly.

Kohn-Sham Formalism   The second Hohenberg-Kohn theorem partly
answers how the ground state energy is dependent on the density, the
issue remains that $F[n]$ isn't known in terms the density. To circumvent
this, the Kohn-Sham (KS) formalism introduces a reference system of
non-interacting electrons. This allows to collect the contributions which
have an unknown dependence on the density in the exchange-correlation
energy,

$$F^{KS}[n] = T_R[n] + V_H[n] + E_{XC}[n] \tag{2.1}$$

where T_R is the kinetic energy of a reference system,

$$V_H[n] = \frac{1}{2} \int \int \frac{n(\mathbf{r}) - n(\mathbf{r}')}{|\mathbf{r} - \mathbf{r}'|} \, \mathrm{d}\mathbf{r} \, \mathrm{d}\mathbf{r}',$$

is the Hartree potential which is the classical electron-electron interaction, and E_{XC} is the exchange-correlation (xc) energy functional. The reference system is a system of non-interacting electrons which have the same ground state density as the real system of interacting electrons.

DFT Self-consistency Loop   The introduction of the reference system is useful for obtaining the relationship between the density and $F^{KS}[n]$. For non-interacting electrons, the many-body wave function can be written as a Slater determinant of single particle wave functions (KS orbitals). This decouples the many-body wave function and the problem is reduced to solving a system of single-particle equations. This means that an iterative procedure can be used to find the single particle states which reproduce the ground state density of the interacting system. The procedure is shown on Figure 2.1 and ensures that the density is determined self-consistently.

The starting point, is an initial guess of the density. Form this density, the effective KS potential, v_s, can be obtained. The third step defines the KS single-particle equations which can be solved to find the KS orbitals, ψ_i, and energy levels, ε_i. The final step calculates the density from the
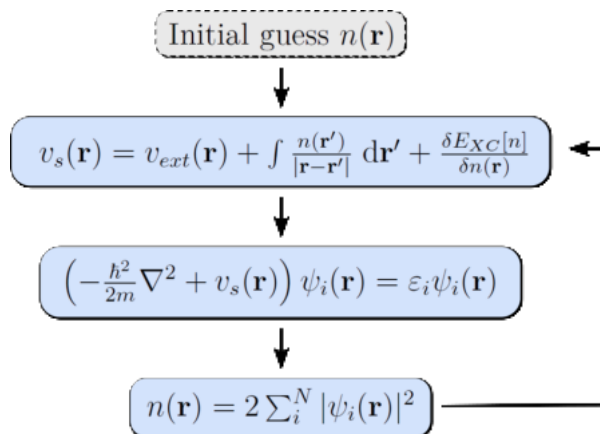

Figure 2.1: The DFT self-consistency loop.

KS orbitals. If the two densities match, the loop is closed, otherwise a new guess is constructed from a mixture of the computed density and the densities of the previous loops. This provides an answers to what the density of a many-body electronic system is. The ground state energy can be found from eq. (2.1) using the KS orbitals but the procedure does not provide the many-body wave function.

It is important to highlight, that the KS potential, states and eigenenergies are properties of the non-interacting system. The ground state energy and density, however, are properties of the interacting system. This means that all electronic properties which only depend on the energy or density can be directly obtained from these quantities. Examples are the relative heat of formation, inter-atomic forces, and magnetization of a material. However, if observables which depend directly on the energy levels or wave functions are calculated from the KS orbitals, it should be kept in mind that these does not represent the true wave functions and energy levels of the interacting system. Several methods which builds on top of DFT calculations can be used to address this issue but these methods are outside the scope of this thesis. Part of the reason why DFT has been so successful, is that for many systems, the KS wave functions and electronic levels actually represent the behavior of the interacting material rather well.

So far, the problem has only been reformulated and the theory is therefore, in principle, still exact (disregarding the adiabatic approximation). However, the exact exchange-correlation functional is not known.

Exchange Correlation Functionals Several degrees of approximations have defined a rich variety of exchange-correlation functionals which all have their advantages and limitations. The functionals are often grouped according to the accuracy, as illustrated on Figure 2.2. In this slightly simplified view, each group add a new component to the calculation of the exchange-correlation and thereby increase the accuracy but also the computational cost.

The local density approximation (LDA)[14] is the most simple approximation which is obtained assuming that the electrons locally act as a homogeneous electron gas. LDA only depends on the density and can be used to describe metals and other systems where the electrons are evenly distributed. The generalized gradient approximation (GGA) based func-
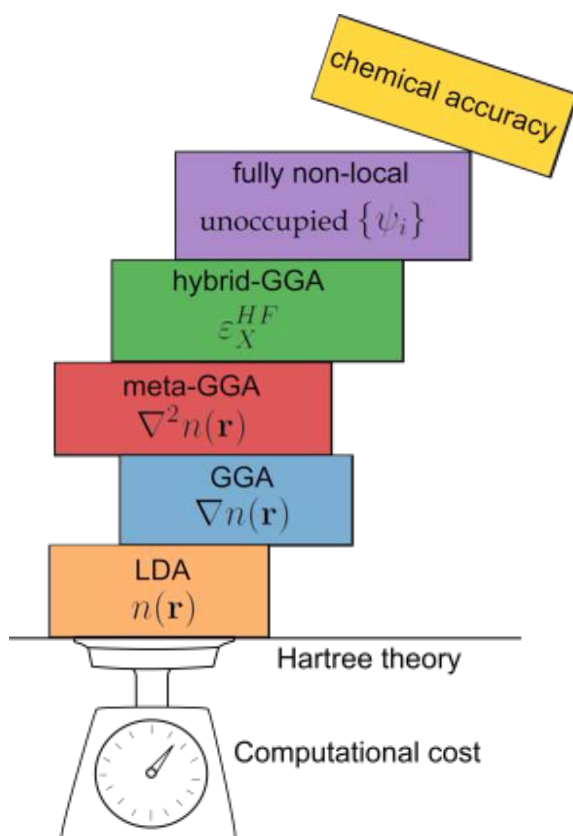
Figure 2.2: The groups of DFT functionals standing on the foundation of Hartree theory. Each group add a new component to the calculation of the exchange-correlation. As more components are added, the accuracy is increased and so is the computational cost.

tionals are a bit more advanced and depend on both the density and the gradient of the density and the meta-GGAs also take the Laplacian of the density into account. The next group are the hybrid functionals. These functionals use the exact exchange combined with a mixture of exchange and correlation from a GGA or meta-GGA level functional. Exact exchange can be obtained from Hartree-Fock theory and consists of a double summation over all occupied Kohn-Sham orbitals. Computing this quantity therefore increases the computational cost significantly. The last group consists of the fully non-local methods which describe the correlation through perturbation theory and require a double summation over both the occupied and unoccupied Kohn-Sham orbitals.

The Perdew, Burke and Ernzerhof functional (PBE)[17] is a GGA type of functional with the exchange correlation energy,

$$E_{XC}^{PBE} = \int n(\mathbf{r}) \varepsilon_{XC}^{PBE}(n(\mathbf{r}), \nabla n(\mathbf{r})) \, d\mathbf{r},$$

$$\varepsilon_{XC}(n, \nabla n) = \varepsilon_X^{LDA}[n] F_X \left[\frac{|\nabla n|}{n} \right] + \varepsilon_C^{LDA}[n] + H[n, \nabla n].$$

ε_X^{LDA} and ε_C^{LDA} are the LDA exchange and correlation functionals, and the functions F_x and H are used to fulfill a number of formal conditions which makes the system behave physically sound.

PBE is a local functional and performs best when calculating properties which have a small dependence on long-range interactions. In this thesis, the magnetic properties of the edges of semi-metallic 2D transition metal dichalcogenides (TMDs) and the transport properties between semi-metallic and semiconducting 2D $MoTe_2$ are described using PBE. The structural reconstruction at interfaces or edges and the local magnetization density at an edge are expected to be well-described within PBE. On the other hand, the non-local screening in 2D semiconductors results in a large bandgap which isn't reflected by the PBE KS energy levels. To include such effects, the long-range Coulomb interactions must be included which can be done within the framework of GW using the single particle Green's functions and many-body perturbation theory.[18] However, the charge transfer properties between a doped 2D semiconductor and a 2D metal depend on the qualitative features of the bands rather than the value of the gap.[19–22] In the case of $MoTe_2$, the band structure of the valence and conduction bands is relatively unchanged when going

from PBE to GW.[23] The main difference is that the conduction band is shifted 0.4-0.5 eV up in energy as the bandgap opens. The local charge transfer at the interface is therefore well described within PBE as well.

This more or less concludes the formal description of DFT and how it can be used to describe the electronic structure of a material. However, two rather important concepts are missing from this introduction, the Bloch states in a periodic crystal and the spin-dependence.

Bloch States and Spin-orbit Coupling   In a translational invariant crystal, the wave functions are described by Bloch states. This has the important consequence that for periodic crystals, a set of coupled KS equations has to be solved at each k-point in the Brillouin zone. Consequently, the KS orbitals have a k-index and the density has to by summed over the weighted contributions from each k-point.

To describe spin-polarized systems, the density can be described as a sum over the density of spin-up and spin-down electrons, $n = n_\uparrow + n_\downarrow$. The KS orbitals will get a spin-index and the density can be obtained from a sum over both particle, k-, and spin-index. The magnetization density becomes $m = n_\uparrow - n_\downarrow$. This is a fairly straight forward continuation of the existing framework but if non-collinear spin and the spin-orbit coupling is to be treated, the single particle wave functions must instead be described as spinors and the density becomes a matrix,

$$
n_{\alpha\beta}(\mathbf{r}) = \frac{1}{2} n(\mathbf{r}) \delta_{\alpha\beta} + \frac{1}{2} \sum_{i=0}^{3} m_i(\mathbf{r}) \sigma_{\alpha\beta}^i
$$
$$
= \frac{1}{2} \begin{bmatrix} n(\mathbf{r}) + m_z(\mathbf{r}) & m_x(\mathbf{r}) + im_y(\mathbf{r}) \\ m_x(\mathbf{r}) - im_y(\mathbf{r}) & n(\mathbf{r}) - m_z(\mathbf{r}) \end{bmatrix} .
$$

σ^i are the Pauli spin matrices. The Hohenberg-Kohn theorem still applies for the ground state density matrix and a KS potential and KS Hamilton can be defined in this matrix representation as well. To include the spin-orbit coupling, a term with an exchange-correlation field is added to the matrix KS equations. The field can be interpreted as an internal magnetic field which represents the variations in magnetization.

2.1   Technical Details

In this section, I will highlight some of the most important technical details on how DFT is implemented in the QuantumATK software.[15]

Basis Set and Pseudopotentials   A significant challenge, when applying DFT, is how to represent the wave functions. In QuantumATK, two methods are available, expansions in localized atomic orbitals (LCAO) or plane-waves (PW). The work presented in this thesis has exclusively used the pseudopotential method and LCAO basis sets.

The pseudopotential method freeze the core electrons to the nuclei creating a positive ionic background at each atom with the charge $Z_V = Z - Z_{core}$ where Z is the atomic number and Z_{core} is the charge of the core electrons. This saves a lot of computational resources since only the outer valence electrons have to be treated. The interaction between the electrons and the positive ions and frozen core electrons is replaced by a soft pseudopotential acting on pseudo wave functions which represent the valence electrons. The calculations on the magnetic edges use the SG15 pseudo potentials[24,25] whereas the charge transport properties of TMD interfaces are described using the PseudoDojo pseudopotentials.[26]

The basis set is constructed from the pseudo wave functions of the valence electrons. The pseudo wave functions are not orthogonal to the core states as the true valence wave functions but conserve the norm of these. They are products of spherical harmonics and radial functions which goes to zero outside a cutoff radius.

These pseudopotentials and wave functions are represented on a real space grid and the Brillouin zone is sampled by a k-space grid. Both of these grids should be converged with respect to the physical quantity which is being calculated. The real-space density cut-off value used in this thesis is consistently 100 Ha which corresponds to a grid spacing of 12 pm. The Brillouin zone samplings are summarized in Table 2.1.

Electronic Temperature   The discrete k-grid represents an issue when describing metals since the occupation of the electronic bands changes abruptly when crossing the Fermi level, ε_F. A very dense grid will therefore be required to ensure convergence of the calculation. To compensate for the discrete k-point sampling, a smearing of the occupations is included.

System	k-grid	electrode(s) k-grid
H-phase TMD Periodic Crystal	(7,7,1)	
T'-phase TMD Periodic Crystal	(6,11,1)	
H-phase TMD Triangular Nanoparticle	(1,1,1)	
T'-phase TMD Nanoribbon along x-axis	(6,1,1)	
T'-phase TMD Nanoribbon along y-axis	(1,11,1)	
T'-phase TMD Surface (x-edge)	(6,1)	(6,401,1)
T'-phase TMD Surface (y-edge)	(11,1)	(401,11,1)
Heterophase TMD Device	(6,1)	(401, 6, 1)

Table 2.1: The k-point samplings used in this thesis.

This smearing is achieved by including a Fermi-Dirac distribution, f, in the calculation of the density,

$$n(\mathbf{r}) = 2\sum_i^N f\left(\frac{\varepsilon_i - \varepsilon_F}{k_B T}\right)|\psi_i(\mathbf{r})|^2.$$

k_B is the Boltzmann constant and the degree of smearing is determined by the electronic temperature, T. This temperature is only included as a tool to help the convergence and the density and energy is always extrapolated back to zero Kelvin at the end of the calculation. All the self-consistent calculations presented in this thesis are performed at an electronic temperature of 300 K.

Doping To describe doped semiconductors, a continuous doping model is used. The electrons per atom are explicitly modified by scaling the atomic densities. This is possible since density is described in terms of the localized basis functions.[27]

2.2 Non-equilibrium Green's Function Method

Modelling of the current through an interface between two crystals has been one of main objectives of this thesis. In order for a current to run, the system must be brought out of equilibrium by applying a bias. Such a system can therefore not be described within standard DFT which is an equilibrium method. However, by combining DFT with the non-equilibrium Green's function (NEGF) method, self-consistent calculations on such system can be obtained.

An interface between two crystals can be modelled by combining two semi-infinite pieces of the crystals. This requires that the lattices of the two crystals can be matched such that the directions perpendicular to the interface share a periodicity. The next chapter will present a method for finding such a shared unit cell of two crystals. The system is illustrated on Figure 2.3a and consists of three regions, the left electrode, the central region, and the right electrode. Each electrode (also sometimes referred
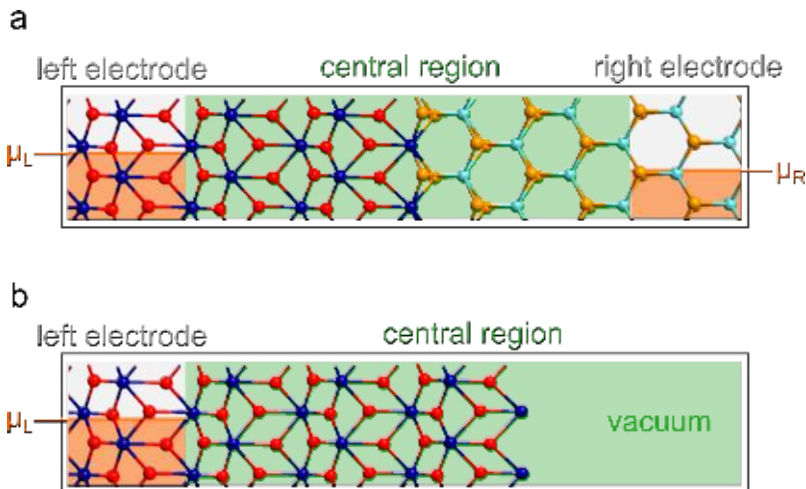

Figure 2.3: **a** Device for modelling an interface between two crystals. The difference between the two chemical potentials is determined by the bias, $eV_{bias} = \mu_L - \mu_R$. **b** Semi-infinite system for modelling the surface of a crystal. The central region is terminated by a vacuum region.

to as the lead or probe) should be considered as a semi-infinite system and acts as an electron reservoir. The number of occupied states in these reservoirs are determined by the chemical potentials which differ by the applied bias $eV_{bias} = \mu_L - \mu_R$.

A positive bias will make the electrons move from the left electrode through the scattering (central) region where they are either transmitted to the right electrode or scattered by the interface. The eigenstates, ψ_i^L and ψ_i^R of the two electrodes therefore represent the states available for transport across the scattering region.

The surface of a crystal can be modelled in a similar manner using a semi-infinite system. The setup allows for modelling of a single isolated surface. A single electrode is coupled to a central region which contains a surface as illustrated on Figure 2.3b. The NEGF method can be used to describe this system using the same procedures as those used for devices. The only differences are that only the left electrode yields contributions to the Green's function and that the electrostatic boundary condition at the right hand side is fixed by the vacuum potential rather than the potential of the right electrode.[28] In the following, I will explain the procedure for obtaining the non-equilibrium density of a device.

Since the central region has open boundary conditions, KS and Bloch states can not be defined. The energy-dependent retarded Green's function, on the other hand, is well-defined for open systems,

$$G(\varepsilon) = \frac{1}{(\varepsilon + i\eta)S - H - \Sigma^L(\varepsilon) - \Sigma^R(\varepsilon)}.$$

ε is the energy, H and S are the Hamiltonian and overlap matrix of the central region, and η is a positive infinitesimal. The self-energies of the two electrodes, Σ^L and Σ^R represent the coupling between the electrodes and the central region and can be obtained using a recursive method[29] from the left and right electrode Hamiltonians.

The retarded Green's function can be used to obtain the non-equilibrium density in the central region using a self-consistency loop for DFT+NEGF calculations which is illustrated on Figure 2.4. The starting point is to perform regular DFT calculations on each of the two electrode unit cells. The ground states of the electrodes are obtained using periodic boundary conditions which corresponds to finding the equilibrium state of the
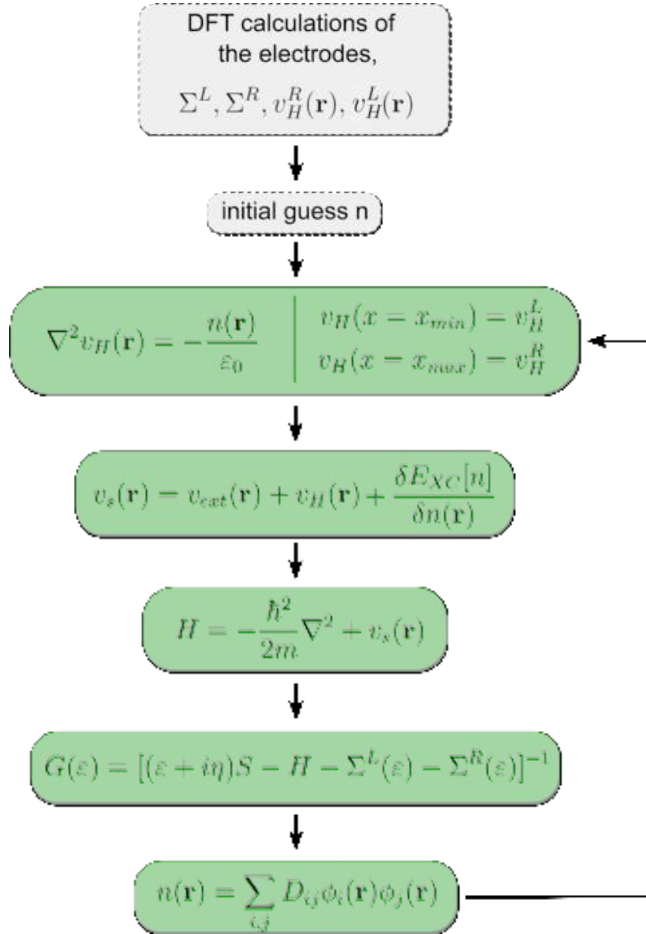
Figure 2.4: The self-consistency loop of DFT+NEGF calculations. The transport direction is along the x-axis.

isolated crystals. From this calculation, the self-energies and Hartree potentials are obtained. An initial guess is made on the density of the central region and the Hartree potential is found by solving the Poison equation using this density. The boundary conditions in the transport direction are determined by the Hartree potentials of the electrodes. When this is obtained, the KS potential and KS Hamiltonian are defined as in a regular DFT calculation.

The KS Hamiltonian and self-energies are used to obtain the retarded Green's function which in turn is used to obtain the density matrix,

$$D = \int \rho^L(\varepsilon) f\left(\frac{\varepsilon - \mu_L}{k_B T_L}\right) \, d\varepsilon + \int \rho^R(\varepsilon) f\left(\frac{\varepsilon - \mu_R}{k_B T_R}\right) \, d\varepsilon,$$

$$\rho^{L/R}(\varepsilon) = \frac{1}{2i\pi} G[\Sigma^{L/R} - (\Sigma^{L/R})^\dagger] G^\dagger.$$

T_L and T_R are the temperatures used to determine the occupation in each of the electrodes. Note, that this temperature is not the same as the electronic temperature used in a regular DFT calculation but describes how the charge transport across a device depends on the temperature. From the density matrix, the LCAO basis functions, $\phi(\mathbf{r})$, are used to find the density which concludes the self-consistency loop.

This procedure does not explicitly calculate the eigenstates of the central region. This means that not all the quantities which can be obtained from a regular DFT calculation are obtainable using the DFT+NEGF approach. In this thesis, such calculations are used to obtain the projected density of states (PDOS) along the transport direction, transmission, transmission eigenstates, and current across the device.

The projected density of states, assuming the x-axis is along the transport direction, can simply be obtained from the spectral density matrix, $\rho = \rho^L + \rho^R$,

$$n(\varepsilon, x) = \int \int \sum_{ij} \rho_{ij}(\varepsilon) \phi_i(\mathbf{r}) \phi_j(\mathbf{r}) \, dy \, dz.$$

The total transmission and transmission matrix can be found from the retarded Green's function and the imaginary part of the self-energies, $\Gamma^{L/R}$,

$$T(\varepsilon) = \text{Tr}[G(\varepsilon)\Gamma^L(\varepsilon)G^\dagger(\varepsilon)\Gamma^R(\varepsilon)],$$
$$T_{nm}(\varepsilon) = \sum_l t_{nl}(\varepsilon)t_{lm}^\dagger(\varepsilon).$$

t_{nl} is the transmission amplitude from Bloch state ψ_n^L in the left electrode to the Bloch state ψ_l^R in the right electrode. If the transmission matrix is diagonalized, the contributions to the transmission are divided in to transmission channels at each transmission eigenenergy. The sum over the eigenvalues yields the total transmission.

As mentioned previously, the wave functions of the system cannot be described by Bloch states. However, the Bloch states from the two electrodes can be used to describe the transmission eigenstates which provide the spatial distribution of the electrons using a specific transmission channel. The transmission eigenstates are found by propagating the states which diagonalize the transmission matrix as a linear combination of Bloch states from the left or right electrode.

The final quantity calculated using DFT+NEGF is the current across the device. This is obtained from the transmission using the Landuaer formula,

$$I = \frac{2q}{h} \int T(\varepsilon, \mu_L, \mu_R) \left[f\left(\frac{\varepsilon - \mu_L}{k_B T_L}\right) - f\left(\frac{\varepsilon - \mu_R}{k_B T_R}\right) \right] \mathrm{d}\varepsilon.$$

.

This concludes the theory behind DFT and the NEGF method and how these have been applied. The next chapter will present a general method for obtaining the possible matches between two periodic crystals in order to build an interface.

CHAPTER 3

Geometric Matching of Crystals

This chapter explains and demonstrates a general method for combining two crystals to an interface. The entire chapter is partly revised and reprinted from the paper published in Physical Review B in 2017.[30]

The development of modern technology has become increasingly dependent on knowledge of interfaces at the atomic scale. As the size of electronic devices decrease, interfaces become an increasingly dominant part of the system and thus become the limiting factor for device performance.[31–33] Many difficulties are related to obtaining a stable and defect free interface. When the materials are not commensurate, a large strain can build up at the interface, and result in defects and unstable interface geometries. The prediction of the stability of an interface is difficult and the commonly used approach is trial and error where many samples must be grown before it can be concluded whether a stable interface can be formed or not. This crystal matching method permits the combination of any two crystals and provides information on which crystal surfaces, if any, that allow for a low strain epitaxial interface. The method is solely based on geometrical considerations of the possible surface cells of the two crystals and it leads to an identification of interfaces where both the strain and the size of the coincidence interface cell are small. The input is therefore only the material lattices, not the atomic details. Having low stress and a small interface cell does not by itself guarantee a stable interface, as the atomic structure of the interface may also play an important role. However, the simple geometrical criteria provide a good starting point for further experimental or theoretical investigations.

3.1   Matching Method

The method for creating an interface between two crystals is completely general and based on 2D cells of the two crystal surfaces. The 3D vectors of the crystal, defining these surface cells, are projected from $\mathbb{R}^3$ to $\mathbb{R}^2$ as illustrated on Figure 3.1a. The surface cell of the first crystal is defined by two vectors $\mathbf{u_1}$ and $\mathbf{u_2}$, where $\mathbf{u_1} = [u_{1x}, u_{1y}]$. Similarly, $\mathbf{v_1}$ and $\mathbf{v_2}$ denote the two vectors which define the surface cell of the second crystal. The affine transformation $\mathbf{A}$ which maps $[\mathbf{u_1}, \mathbf{u_2}]$ onto $[\mathbf{v_1}, \mathbf{v_2}]$ is given by the following system of linear equations,

$$
\begin{bmatrix} A_{11} & A_{12} \\ A_{21} & A_{22} \end{bmatrix} \begin{bmatrix} u_{1x} & u_{2x} \\ u_{1y} & u_{2y} \end{bmatrix} = \begin{bmatrix} v_{1x} & v_{2x} \\ v_{1y} & v_{2y} \end{bmatrix}.
$$

Any square matrix can be decomposed into the product of an orthonormal matrix, $\mathbf{U}$ and a positive definite symmetric matrix, $\mathbf{P}$. This is known as a polar decomposition[34]. The symmetric matrix defines the 2D strain tensor, $\boldsymbol{\epsilon}$, for deforming one cell into the other,

$$
\mathbf{P} = \mathbf{I} + \boldsymbol{\epsilon} = \begin{bmatrix} 1 + \epsilon_{xx} & \epsilon_{xy} \\ \epsilon_{xy} & 1 + \epsilon_{yy} \end{bmatrix}. \tag{3.1}
$$

The first vectors are rotated along the x-axis such that $u_{1y} = v_{1y} = 0$. This can be done without loss of generality and leads to,

$$
\begin{aligned}
A_{11} &= \frac{v_{1x}}{u_{1x}}, \\
A_{12} &= \frac{v_{2x}}{u_{2y}} - \frac{v_{1x} u_{2x}}{u_{1x} u_{2y}}, \\
A_{21} &= 0, \\
A_{22} &= \frac{v_{2y}}{u_{2y}}.
\end{aligned}
$$

The polar decomposition of $\mathbf{A}$ is $\mathbf{A} = \mathbf{UP}$, where $\mathbf{U}$ is a rotation matrix because of the chosen projection to $\mathbb{R}^2$,
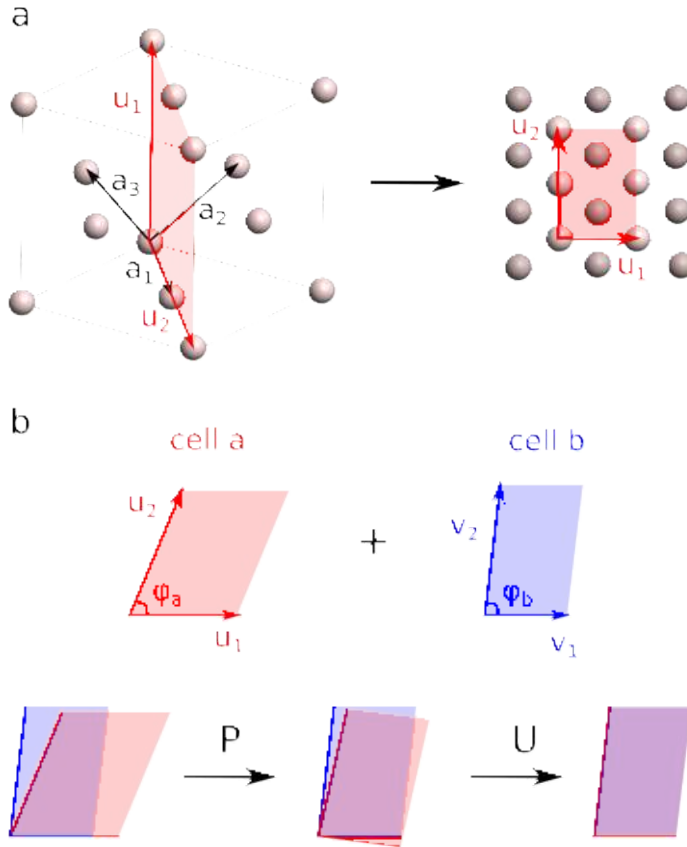
Figure 3.1: The method for finding and matching the 2D surface cells of two crystals. (a) The lattice vectors of the first crystal $(\mathbf{u_1}, \mathbf{u_2})$ are created from a linear combination of the Bravais vectors $(\mathbf{a_1}, \mathbf{a_2}, \mathbf{a_3})$. Here $\mathbf{u_1} = -\mathbf{a_1} + \mathbf{a_2} + \mathbf{a_3}$ and $\mathbf{u_2} = 2\mathbf{a_1}$. The two vectors are then projected from the 3D representation to a 2D representation on a crystal surface. (b) Two cells of two different crystals are matched by applying the affine transformation $\mathbf{A}[\mathbf{u_1}, \mathbf{u_2}] = [\mathbf{v1}, \mathbf{v2}]$, where $\mathbf{A} = \mathbf{UP}$ consists of a rotation, $\mathbf{U}$, and a strain matrix, $\mathbf{P}$. Reprinted with permission from Ref. [30].

$$\mathbf{U} = s \begin{bmatrix} A_{11} + A_{22} & A_{12} \\ -A_{12} & A_{11} + A_{22} \end{bmatrix}$$
$$= \begin{bmatrix} \cos(\phi) & -\sin(\phi) \\ \sin(\phi) & \cos(\phi) \end{bmatrix},$$
$$\mathbf{P} = \mathbf{U}^T \mathbf{A}.$$

s is a scaling constant which makes the columns of $\mathbf{U}$ unit vectors. The $\mathbf{U}$ matrix defines the counter-clockwise rotation of the $[\mathbf{u_1}, \mathbf{u_2}]$ cell onto the $[\mathbf{v_1}, \mathbf{v_2}]$ cell by the angle $\phi = |\phi_a - \phi_b|/2$ as shown on Figure 3.1b. Using this method, the above equations yield the strain matrix of any given cell combination. The algorithm behind the extraction of the strain matrix of all the possible matches between two crystals is illustrated on the flow chart on Figure 3.2. It consists of three main steps.

3.1.1 Create (i, j, k)-list from $\ell_{\max}$

The first step is to create all the possible lattice vectors of each crystal up to a specified maximum length, $\ell_{\max}$. The vectors are created as integer combinations of the Bravais vectors of the crystal, as illustrated on Figure 3.1a,

$$\mathbf{u} = i\mathbf{a_1} + j\mathbf{a_2} + k\mathbf{a_3}, \qquad |\mathbf{u}| < \ell_{\max}. \tag{3.2}$$

This will create a list of (i, j, k)-values for each crystal.

3.1.2 Create Vector Pair List

The next step is to combine the created vectors such that a list of unique surface cells is created for each crystal. This procedure uses two kinds of filters to remove equivalent surface cells from the list; the symmetry operations of the atom-free crystal and Niggli reductions of the cells.

The starting point is to create a list of symmetrically unique vectors of the crystal. This is done by applying the symmetry operations of the crystal on each vector in the generated (i, j, k)-list. This creates a symmetry group of vectors for each vector in the (i, j, k)-list. To avoid considering symmetrically equivalent vectors, only the canonical representation of
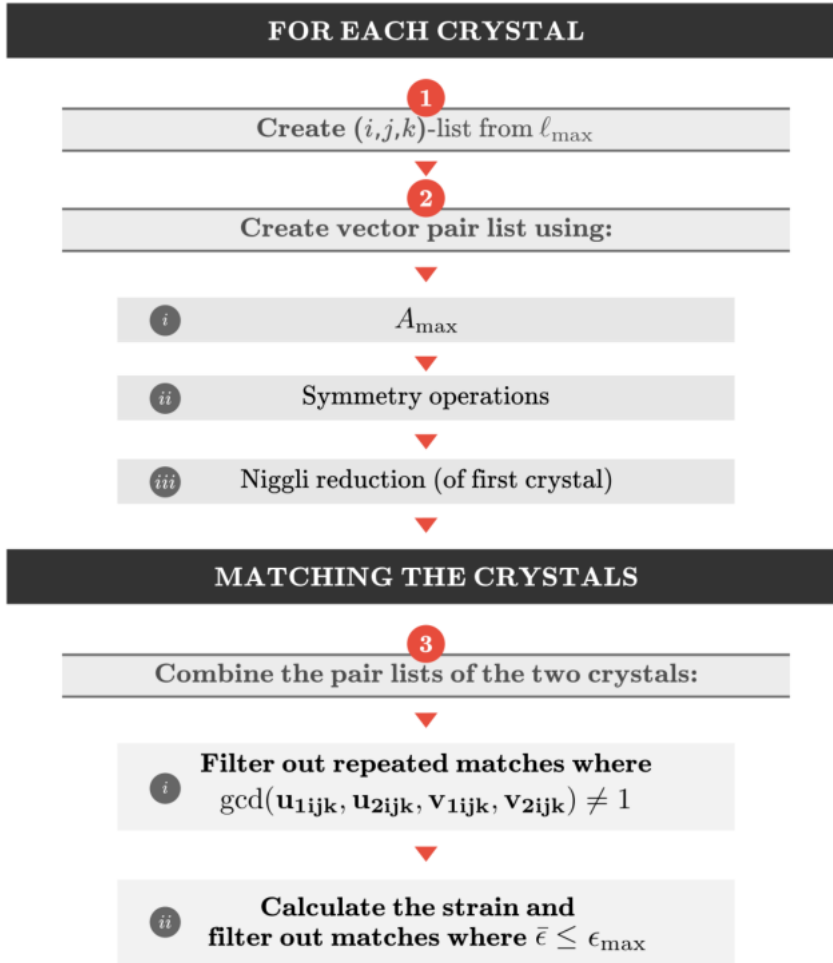
Figure 3.2: Flow chart behind the algorithm for matching two crystals. Reprinted with permission from Ref. [30].

each of these symmetry groups is kept. The canonical representation is, in this case, defined as the vector with the lowest value when comparing the vectors using lexicographic ordering. This results is a list of unique vectors which fulfill the requirement of eq. (3.2).

To create the unique surface cells, each vector from the original (i, j, k)-list is combined with the vectors in the symmetry reduced list. The combination is discarded, if one of the following conditions is fulfilled,

1. The area spanned by the two vectors exceeds the area threshold, A_{max}.

2. The two vectors are parallel.

3. The resulting surface cell is not a Niggli reduced cell.

4. The vector pair is not symmetrically unique.

The third condition checks whether the cell is a Niggli reduced cell. A Niggli reduced 2D cell, will fulfil,

$$\mathbf{u_1} \cdot \mathbf{u_1} \leq \mathbf{u_2} \cdot \mathbf{u_2}, \qquad \mathbf{u_1} \cdot \mathbf{u_2} \leq \frac{1}{2}\mathbf{u_1} \cdot \mathbf{u1}.$$

The cells that are not Niggli reduced, will be discarded. This is only done for the first crystal, since a Niggli reduced cell may be strained into a non Niggli reduced cell when the two crystals are combined. The final condition is investigated by applying the symmetry operations of the crystal on both vectors and thereby creating a symmetry group of surface cells. The cells which are not the canonical representation of the group, are discarded. After completing these steps, a list of unique surface cells of each crystal have been created. The next step is to combine these two lists.

3.1.3   Combine the Pair Lists of the Two Crystals

When the cells of the two crystals are matched, the first step is to filter out repeated matches. As an example, lets say that a $[\mathbf{u_1}, \mathbf{u_2}]$ cell of the first crystal is combined with a $[\mathbf{v_1}, \mathbf{v_2}]$ cell where $\mathbf{u_1}_{ijk} = (1, 0, 0)$, $\mathbf{u_2}_{ijk} = (2, 0, 1)$, $\mathbf{v_1}_{ijk} = (0, 0, 2)$ and $\mathbf{u_2}_{ijk} = (4, 4, 2)$. This combination

will be completely equivalent to the $((2, 0, 0), (4, 0, 2), (0, 0, 4), (8, 8, 4))$ combination. To avoid investigating both combinations, the greatest common divider (gcd) of all 4 vectors, $\gcd(\mathbf{u_1}_{ijk}, \mathbf{u_2}_{ijk}, \mathbf{v_1}_{ijk}, \mathbf{v_2}_{ijk})$, is calculated and the match is discarded if this differs from 1. After this preliminary check, the strain matrix of the match is calculated using the method explained above. The average strain of a match is defined as,

$$\bar{\epsilon} = \sqrt{\frac{\epsilon_{xx}^2 + \epsilon_{yy}^2 + \epsilon_{xx}\epsilon_{yy} + \epsilon_{xy}^2}{4}},$$

where the components are of the 2D strain tensor from eq. (3.1). This average strain is an invariant of the strain tensor, since $4\bar{\epsilon}^2 = \text{Tr}(\boldsymbol{\epsilon})^2 - \det(\boldsymbol{\epsilon})$. Matches with an average strain below a given strain threshold, ε_{max}, are kept.

This concludes the algorithm for finding all the matches between two crystals. The parameters determining which matches to include in the search are; ℓ_{max}, A_{max}, and ε_{max}. These parameters help to filter out the cells that wouldn't create a physically meaningful interface. The area and length threshold ensures that unreasonably large or narrow cells are discarded and the strain threshold filters out the most strained matches.

The algorithm is implemented using C++ with a Python interface. This makes the code quite efficient; finding all matches between a InAs fcc crystal and a Cobalt hcp crystal with the parameters, $\ell_{\text{max}} = 50$ Å, $A_{\text{max}} = 200$ Å^2, and $\epsilon_{\text{max}} = 2\%$, takes around twenty minutes on a normal laptop.

3.2   General Matches Between fcc and bcc Crystals

The algorithm can be used to find matches between any fcc crystal and any bcc crystal. To this end, an isotropic scaling parameter, k, is defined as the ratio between the lattice constants of the two crystals, $k = a_{\text{fcc}}/a_{\text{bcc}}$. The effect of k on the strain matrix will be linear,
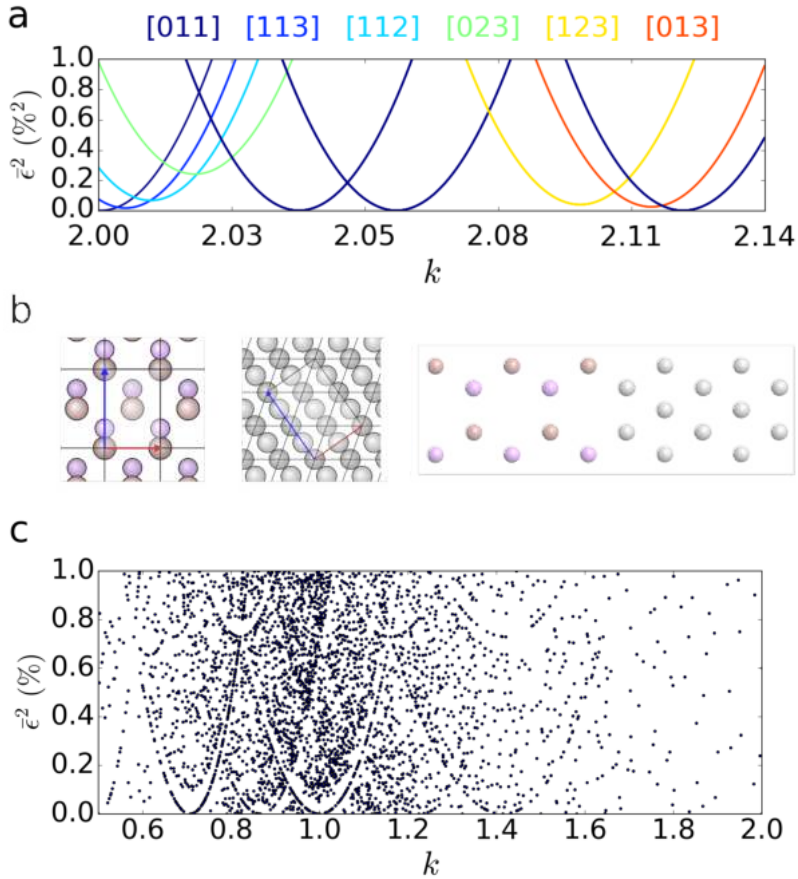
Figure 3.3:   The matches between a fcc and a bcc crystal. k represents the scaling between the two lattice constants, $k = a_{\mathrm{fcc}}/a_{\mathrm{bcc}}$. (a) The $\bar{\varepsilon}^2(k)$ relation of (3.3) for optimal matches involving the [110] surface of the fcc crystal. The color of the curves represents different surfaces of the bcc crystal. (b) The surface cells and corresponding interface of the perfect $k = 2$ match shown on (a). Illustrated here for InAs with Vanadium. (c) Scatter plot of matches where the minima of the strain parabola gets below 10%. The dots represent the minimal strain of the match and the k-value where this strain occurs. We have chosen ℓ_{max} and A_{max} as four times the lattice constant of the unstrained crystal. Reprinted with permission from Ref. [30].

$$\mathbf{A} = k\mathbf{U}\mathbf{P} = \mathbf{U} \begin{bmatrix} k\,(1 + \epsilon_{xx}) & k\epsilon_{xy} \\ k\epsilon_{xy} & k\,(1 + \epsilon_{yy}) \end{bmatrix}.$$

This means that the effect of the scaling parameter on the average strain can be described by the simple analytical relation,

$$\begin{aligned} 4\bar{\varepsilon}^2(k) = {} & k^2(\epsilon_{xx}^2 + \epsilon_{yy}^2 + \epsilon_{xx}\epsilon_{yy} + \epsilon_{xy}^2) \\ & + k^2(3\epsilon_{xx} + 3\epsilon_{yy} + 3) \\ & - k(3\epsilon_{xx} + 3\epsilon_{yy} + 6) + 3, \end{aligned} \tag{3.3}$$

where the strain tensor components are referring to the case of $k = 1$. This relation allows to calculate the average strain of a match at any k-value once the strain matrix has been calculated for any one specific value of k. Eq. (3.3) defines a strain parabola and the minimal strain of a match, along with the corresponding k-value, can be found from the minimum of this parabola. The strain parabolas for the optimal matches[i] between a fcc[110] surface and a bcc crystal with k-values between 2.0 and 2.14 is illustrated on Figure 3.3a. The two [110] surfaces has perfect matches at $k = 2.0, 2.04, 2.06$, and 2.12. The surface cells and corresponding interface of the perfect $k = 2.0$ match is illustrated on Figure 3.3b for InAs and Vanadium.

To find all the matches between a fcc and a bcc crystal, the algorithm on Figure 3.2 is used but where step **3.ii.** is altered. After calculating the strain matrix, eq. (3.3) is used to find the minimal strain of the match and only matches where this is lower than the strain threshold is kept. In this manner, the strain parabolas of all the relevant matches can be found by doing a single calculation at $k = 1$. ℓ_{max} and A_{max} is chosen as four times the lattice constant of the unstrained crystal and $\epsilon_{max} = 10\%$.

Figure 3.3c shows the results of this general investigation. For each match, the minimal strain and the corresponding k-value is plotted. Note, that the y-axis shows the squared strain, since this illustrates the general shape of the matches better. The structure shows parabola like shapes where zero strain minimas appear at the points $k = 1/\sqrt{2} \approx 0.71$, $k = \sqrt{3}/2 \approx 0.87$, $k = 1$, $k = \sqrt{3/2} \approx 1.22$, and $k = \sqrt{2} \approx 1.41$. Many low

---

[i]The matching parameters are $\ell_{\mathrm{max}} = 50$ Å, $A_{\mathrm{max}} = 200$ Å^2, and $\epsilon_{\mathrm{max}} = 2$ %.

strain solutions are found close to these points. The low strain solutions around $k = 1$ appear since this value corresponds to the [100] facets of the two cubic crystals fitting perfectly together. The other zero strain points also represent some symmetry of the two crystals. The matches around $k = 1/\sqrt{2}$ e.g. corresponds to matching the rotated bcc[100] surface with cell vectors $\mathbf{v_1} = [\sqrt{2}a_{\mathrm{bcc}}, 0]$ and $\mathbf{v_2} = [0, \sqrt{2}a_{\mathrm{bcc}}]$ to a [100] facet of the fcc crystal.

These results clearly show that the method represents a completely general tool for crystal matching. The strength of the method is that it only relies on the geometry of the crystals. This makes it possible to calculate results for two arbitrary crystals and apply these results to all interfaces between materials of these crystal structures. Furthermore, it is an ideal tool for investigating alloy crystals where the lattice parameter can be varied as the composition of the alloy is changed.

3.3 InAsSb and GaInAs Alloys Matched with Metals

Alloyes are e.g. used in the fabrication of core-shell nanowires. These nanowires have numerous applications e.g. for photodetectors[35], photo-electrodes[36], and thermoelectric devices[37]. In the following, matches between two different semiconductor alloys, InAs$_{1-x}$Sb$_x$ and Ga$_x$In$_{1-x}$As, with ten different metals (Al, Ni, Cu, Ag, Au, Pb, V, Fe, Nb, and Co) are found. The two alloys form a zincblende crystal and the relation between the lattice constant and mole fraction x can be approximated by the linear relation,[38]

$$a_{\mathrm{InAsSb}}(x) = 6.0583 + 0.4207x,$$
$$a_{\mathrm{GaInAs}}(x) = 6.0583 - 0.405x.$$

The experimentally determined lattice constants of the metals[39] are used and it is the metal surfaces which are strained to match the alloy surfaces. The chosen parameters are $\ell_{\max} = 50$ Å, $A_{\max} = 200$ Å^2, and
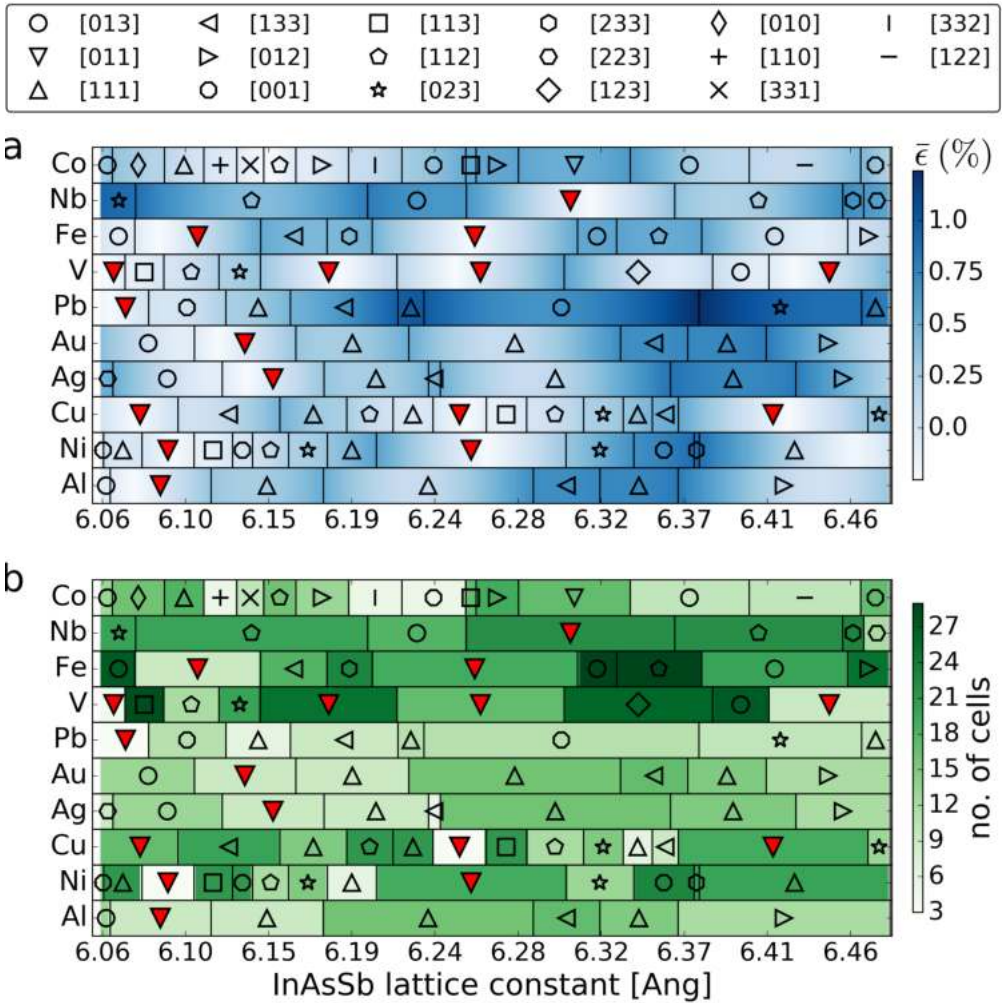
Figure 3.4: (a) The InAsSb[1$\bar{1}$0] surface matched with ten different metals. Each block represents the match which results in the lowest average strain between the two materials. The background color shows the strain in percent and the markers show the involved metal surface. Filled markers denote a match where zero strain can be obtained. (b) Same as (a) but where the background color shows the area given by the no. of alloy surface unit cells of the match. Reprinted with permission from Ref. [30].

$\epsilon_{\max} = 2$ %.[ii] Furthermore, a limit on the Miller index of the crystal surfaces is set. If the highest value in the Miller index is above the threshold, $m_{\max} = 3$, the match is discarded. The matches are calculated for a single value of the mole fraction and the scaling relation (3.3) is used to get the results for the rest of the x-values. This is possible, since each x-value directly corresponds to a k-value, $k = a_{\text{alloy}}(x)/a_{\text{metal}}$.

The matches involving the $[1\bar{1}0]$ surface of InAsSb is shown on Figure 3.4. Each block on the plot corresponds to a certain match and a certain strain parabola in a plot like Figure 3.3a. The background of Figure 3.4a therefore represents the strain value of the lowest lying strain parabola. Taking InAsSb$[1\bar{1}0]$ matched to Vanadium as an example, the variation of the lattice parameter results in different optimal matches. For instance, from a perfect [110] match to a low strain [113] match as the lattice constant is increased from 6.06 to 6.08. The area of the match, given as the number of alloy surface unit cells, is illustrated in Figure 3.4b. Several zero strain matches are possible between the InAsSb$[1\bar{1}0]$ surface and those of the metals. Nickel, Copper, Lead, and Vanadium even have perfect matches with very small unit cells, indicating that these interfaces will be stable.

Figure 3.5 shows all the perfect matches of the $[1\bar{1}0]$, [111], and $[11\bar{2}]$ surfaces of both InAsSb and GaInAs. The red triangles in Figure 3.5a therefore represents the same matches as those highlighted on Figure 3.4. The surfaces have been chosen since they typically terminate nanowires of the two investigated alloys. Many zero strain solutions are possible and especially the [111] surfaces show many results. The zero strain match between this surface of InAsSb and the Aluminum [111] surface close to $x = 0$ agrees with the geometry observed using HR-TEM imaging for InAs nanowires with a thick (> 30 nm) Al overlayer grown by Krogstrup et al..[40] The perfect matches are generally distributed well across the range of lattice constants which should make it easier to realize some of these interfaces experimentally. Details on all the matches of the remaining two surfaces of InAsSb and the three surfaces of GaInAs can be found in the Supplementary Material of Ref. [30].

[ii]The area constraint is set for the cell size when using the lowest lattice constant of each alloy.
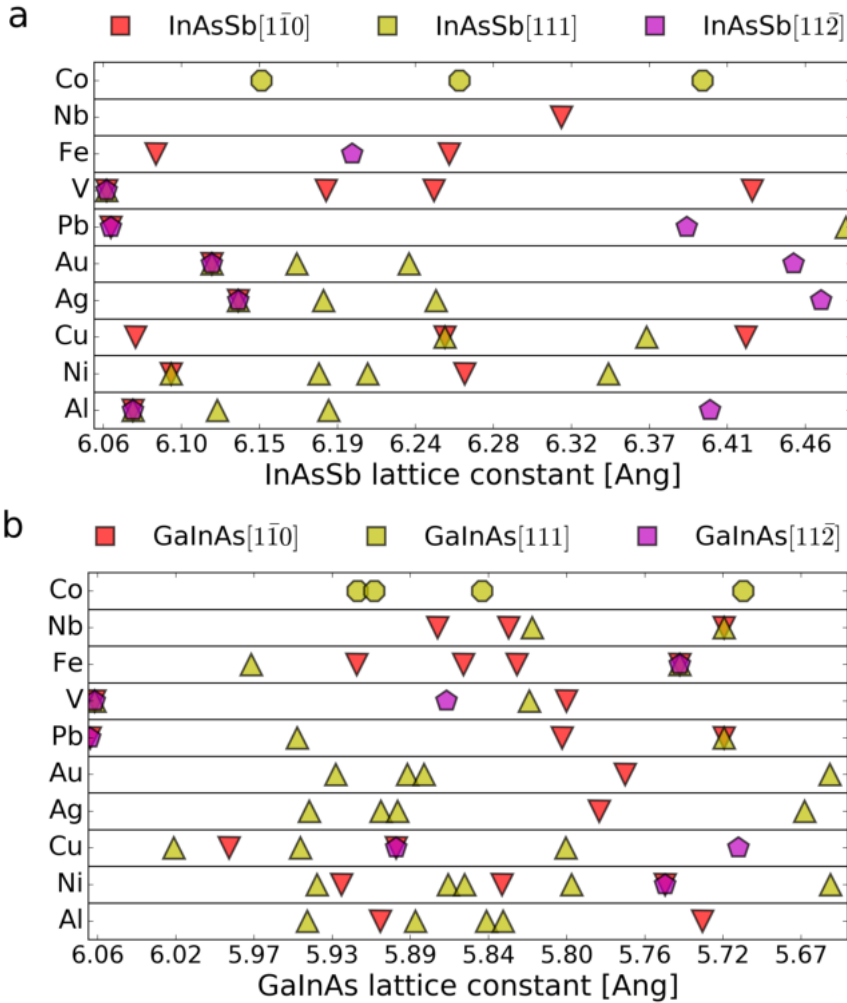
Figure 3.5: The perfect matches of the $[1\bar{1}0]$, $[111]$, and $[11\bar{2}]$ surfaces of (a) InAsSb and (b) GaInAs. The markers denote the metal surface (see Fig 3.4 for labels) and the color denotes the alloy surface. Each marker is placed at the alloy lattice constant which results in a zero strain match. Reprinted with permission from Ref. [30].

This concludes the part which introduces the general methods for performing ab-initio calculations on interfaces between crystallized solid state materials.

2D Transistion Metal Dichalcoginides

This part of the thesis is dedicated to introducing the transition metal dichalcogenides (TMDs) and reviewing their electronic properties in the context of their potential use in transistors. This group of materials have been the center of countless research activities in recent years. They represent a large variety of electronic and optical properties which make them suitable for applications within nano-electronics, catalysis, spintronics, light harvesting, and sensing. In the following, I will focus on the electronic properties, since the goal of the research has been to investigate TMDs as new materials for nanos-cale transistors.

The most famous TMD is MoS_2 which occur naturally in the form of the mineral molybdenite. Molybdenite is relatively abundant and easy to process and is used as a solid lubricant due to the layered structure of the crystal. It resembles graphite in appearance and single layers can be isolated like graphene from graphite. MoS_2 was the first TMD to be synthesized as a single layer in 1986.[42] Since then a large amount of layered TMDs have been synthesized and characterised. More than 40 TMDs had been identified in a layered structure already in the 1960s[43] and, in the Computational 2D Materials Database,[23] more than 110 thermodynamically stable TMDs have been identified in the single layer limit. The synthesized TMDs and their structural and electronic properties, as of
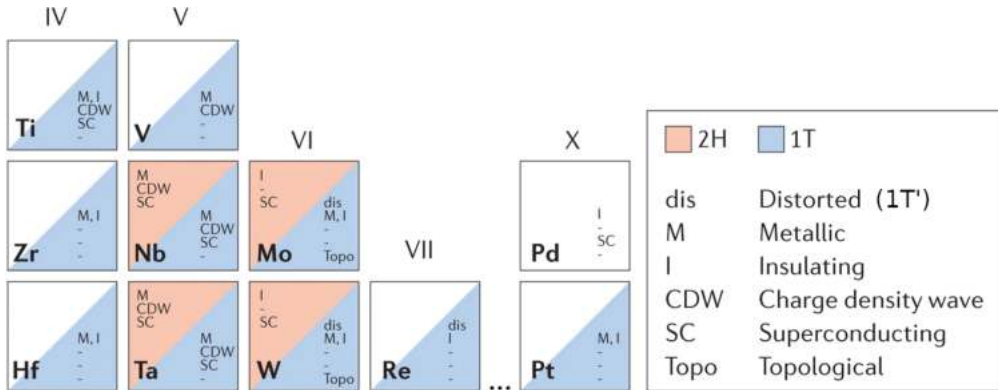
Figure 3.6: Periodic table of synthesized TMDs based on the transition metal element involved. The table show the existing structural phases (2H, 1T, 1T' or other) and the observed electronic phases as of 2017. Adapted with permission from Ref. [41]. Copyright 2017 Springer Nature.

2017, are illustrated on the periodic table on Figure 3.6. The variety of material properties within the group is quite astonishing. TMDs can be metallic (NbS_2), semi-metallic (WTe_2), semiconducting (MoS_2, $MoTe_2$), insulating (HfS_2), or superconducting (TaS_2).

The following chapters are organized as follows,

Chapter 4 describes the most common structural phases and the related electronic properties of the TMDs.

Chapter 5 elaborates on the properties and describe fabrication and doping methods used for the semiconducting 2H-phase of the group VI TMDs.

Chapter 6 describes the synthesis of the 1T- and 1T'-phase group VI TMDs, the phase transition between the 2H- and 1T- or 1T'-phase, and the topological properties of the T'-phase.

Structure and Electronic Properties

Transition metal dichalcogenides (TMDs) are layered materials where each layer consists of a transition metal atom sandwiched between two chalcogen atoms. The bonds within the layer are covalent whereas the interlayer bonds are van der Waals (vdW) type. The most common geometries of the single layers are triagonal prismatic with spacegroup P$\bar{6}$m2 (H-phase), octahedral with spacegroup P$\bar{3}$m1 (T-phase) or a distorted octahedral with spacegroup P12/m (T'-phase). These three different phases of the monolayer TMDs are shown on Figure 4.1. The layers can be stacked in different ways to form at least six different bulk phases of the TMDs. The H-phase layers stack to form 2Hc-, 2Ha-, or 3R-phase, the T-phase layers to form 1T-phase, and the T'-phase layers to form 1T'- or 2M-phase crystals.

Using a simple ionic picture, the covalent bonds in the TMDs result in an electron sharing where the metal atom gets the formal charge +4 and the two chalcogen atoms get formal charge -2 each. This will result in a filled outer p-shell of the chalcogens and an electron configuration xd^n of the metal, where x is the row in the periodic table, and $n = 0$ for group-IV transition metals, $n = 1$ for group-V, and so on. In this simple picture, the filling of the d-orbitals therefore dominates the electronic properties.

Some of the trends in the electronic properties can be explained by ligand field theory arguments. The d-orbitals of the transition metals are split by the hybridization and electrostatic interaction with the chalcogen orbitals. According to the ligand field theory, a triagonal prismatic coordination will split the orbitals of the metal in to a singlet, a_1', and two doublets, e' and e''. There is a relatively large gap between the singlet and the two doublet states. If the metal atom is in the octahedral coordination, the orbitals are split into two levels, a triplet, t_{2g}, and a doublet,
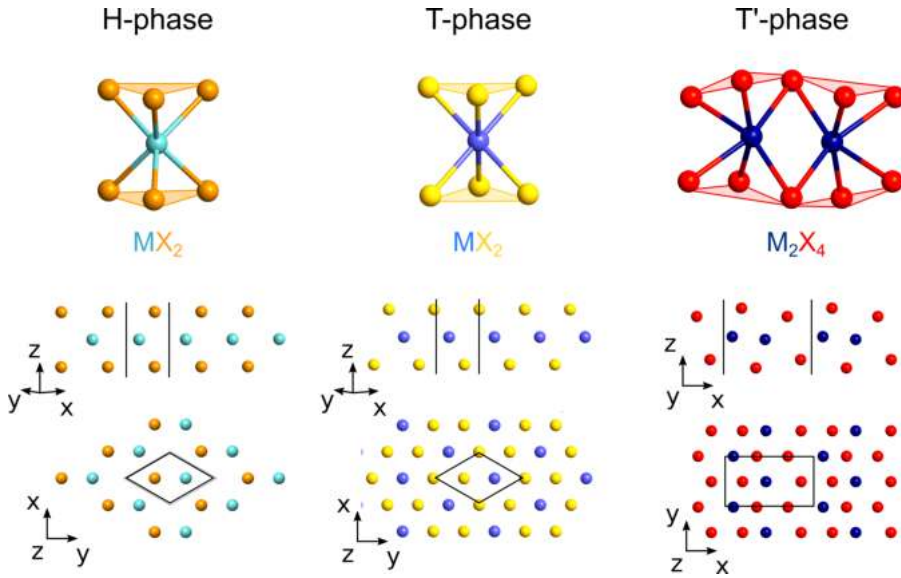
Figure 4.1: Three phases of a single layer TMD. Transistion metals atoms (M) are shown in the blue nuances and chalcogen atoms (X) are shown in orange, yellow and red. The top part shows the metal atom(s) of a single unit cell with the nearest neighbour chalcogen atoms. The bottom part shows a side and top view of the layer. The unit cells are marked by the black lines.

e_g. The splitting is illustrated on Figure 4.2a and 4.2b, respectively. In a crystal, the ligand field splitting results in d-bands which are placed inside a gap between the σ bonding and antibonding bands of the metal-chalcogen bonds. This is illustrated on the right hand side of Figure 4.2a and 4.2b.

The filling of the ligand field levels can be used to predict both the electronic state and the most stable structural phase. As an example, the Group-VI TMDs have a formal d occupation of $n = 2$, filling two electrons into the ligand field levels, as shown on Figure 4.2a and 4.2b. Because the a_1' level is lower in energy compared to the t_{2g} level, the triagonal prismatic phase becomes the most stable phase and is semiconducting with a filled a_1' level as the valence band and unoccupied e' and e'' levels. If more electrons are filled into the ligand field levels, the large energy gap between the singlet and the two doublets, makes the H-phase less stable
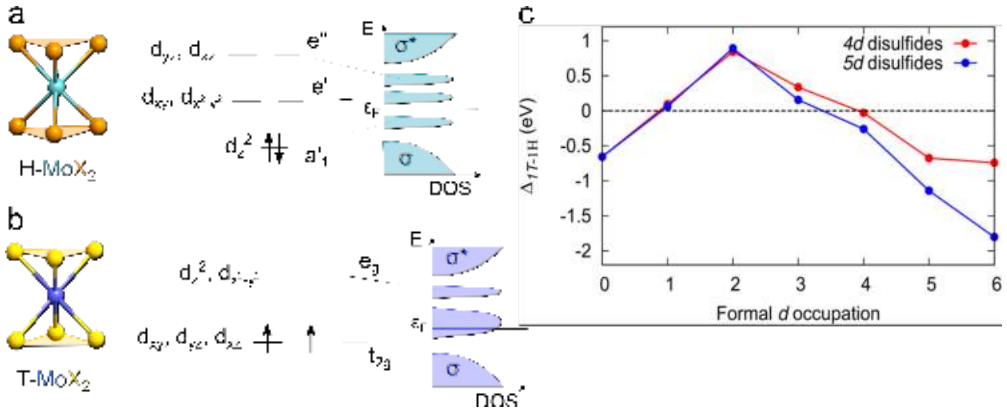
Figure 4.2: Ligand field splitting in TMDs. **a** shows the ligand field split-
ting of a molybdenum based TMD in the triagonal prismatic coordination
of the H-phase, **b** shows the splitting in the octahedral coordination of the
T-phase, and **c** shows the relative stability of T- and H-phase disulfides in
the 4d and 5d transition metals from Ref. [44]. Copyright IOP Publishing.
Reproduced with permission. All rights reserved.

compared to the octahedral structures. This becomes the most stable
phase and is metallic up to a filling of 6 electrons. Using these arguments,
the stability of the H-phase TMDs should decrease when moving to the
right in the periodic table.

The trends in relative stability between the H- and T-phase of tran-
sition disulfides have been investigated using DFT and a tight-binding
Hamiltonian constructed from Wannier functions by Pasquier *et al.*[44] The
trends are shown on Figure 4.2c and agree with the trends in a high-
throughput DFT study by Rasmussen *et al.*[45] and partly with the simple
picture presented by the ligand field theory. If $n > 2$, the relative stabil-
ity of the H-phase is maximized, and when moving to the higher group
transition metals, the stability decreases. However, the trend of desta-
bilization when going to the left from $n = 2$ can not be explained from
this simple theory. In fact, the study by Pasquier *et al.*,[44] concluded that
the ligand field splitting between the a'_1 and e' levels where almost negli-
gible and that the stability trends should be explained by hybridization
between the different d-orbitals instead. The result of this hybridization
is a maximum stabilization of the H-phase when the low-energy d-band is

filled, i.e. n is close to 2. Both theories therefore agree that the H-phase is most stable at $n = 2$ and decreases compared to the T-phase when more electrons are filled in.

The trends in Figure 4.2c are useful for identifying the most stable phase between the H- and T-types but doesn't contain any information on the stability of the T'-phase. This phase is more stable than the T-phase for the group-VI and -VII transition metals.[44,46] Group-VII TMDs therefore become more stable in the 1T'-phase than in the 2H-phase. The group-VI TMDs are most stable in the 2H-phase, except for WTe_2 which is more stable in the 1T'-phase and is a quantum spin Hall insulator.[47–49] Group-VIII to X are generally most stable in the 1T-phase as predicted by Pasquier *et al.* but some of them (e.g. PdS_2) are more stable in completely different phases[50] and Group-XI to XII are unstable in both the H- and T-phase.[45] These trends are also summarized in the periodic table on Figure 3.6. In the remaining part of the thesis, I will focus on the group-VI TMDs (VI-TMDs). The heat of formation of the H- and T'-phase are close in this group which makes them suitable for phase engineering.

The spin-orbit coupling (SOC) plays an important role in the electronic properties of these TMDs. The H-phase lacks inversion symmetry
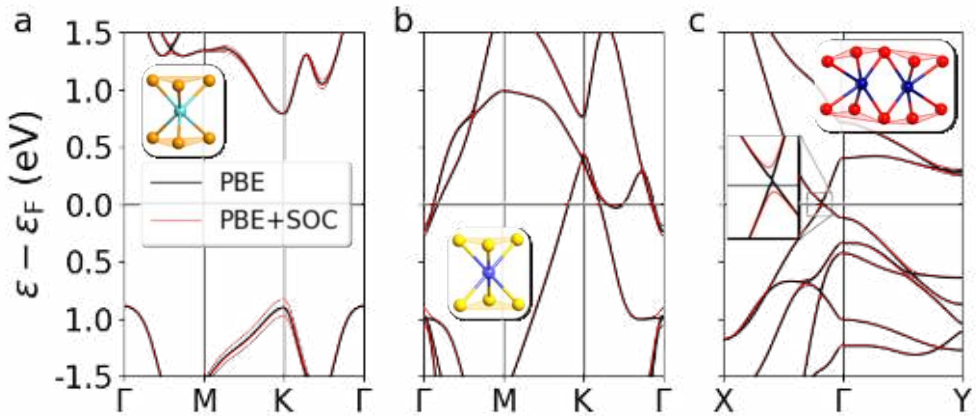

Figure 4.3: The band structure of monolayer MoS_2 in the **a** H-phase, **b** T-phase, and **c** T'-phase calculated using the PBE functional w. and w.o. spin-orbit coupling (SOC).

which lead to a spin splitting of both the valence and conduction band. The spin splitting results in opposite spins residing in the K and K' valley and provides a platform for novel spintronic devices. Due to the relativistic nature of the spin-orbit interaction, heavier elements have larger spin splittings. The spin splitting of H-phase MoS_2 is shown on Figure 4.3a. The T-phase and T'-phase bandstructures are shown on Figure 4.3b and Figure 4.3c, respectively. The T-phase is clearly metallic with several bands crossing the Fermi level, the T'-phase is semi-metallic with a small gap which is opened by the SOC. The lattice distortion of the T'-phase results in a band inversion and a Dirac-cone between the X- and Γ-point. The part of the cone which is above the Fermi level is dominated by p-orbitals of sulfur whereas the part below the Fermi level is dominated by the d-orbitals of molybdenum.[51] The spin-orbit coupling opens a gap between the d- and p-bands which leads to a topological non-trivial phase of the material; the Quantum Spin Hall insulator state. The topological properties of the T'-phase VI-TMDs will revisited in Chapter 6.

Note, that the band structures on Figure 4.3 have been calculated using the PBE functional which does not correctly capture the non-local screening in the TMDs. This means that the bandgaps of the H- and T'-phase are underestimated but otherwise, the qualitative behavior of the bands of all three phases is in agreements with the behavior predicted by GW calculations.[23,51] This concludes the description of the general structural and electronic properties of the TMDs, the following chapters will elaborate on the synthesis methods and electronic properties of the H-, T- and T'-phase of the VI-TMDs.

CHAPTER 5

Semiconducting H-phase

In this chapter, I will present the general fabrication and doping methods of the semiconducting phase of the group-VI TMDs (VI-TMDs) which is the most stable phase of these TMDs. The fabrication methods are important to understand since the electronic properties depend on the quality of the grown crystals and doping methods are important in the context of using doped TMDs as transistor channels. In the following, whenever the TMDs are mentioned as a group, I am referring to the semiconducting VI-TMDs. I will focus on the electronic properties of the materials and on how these are altered by the fabrication method and the presence of defects.

The semiconducting TMDs have indirect band gaps around 1 eV in the multilayer limit[52] but change to a direct band gap semiconductor with band gaps around 1.5-3 eV[45] in the monolayer limit. The size of the monolayer gap is typically about 50 % larger than the bulk gap and the gap size decreases with the atomic number of the chalcogen atom.[52] The direct bandgap of ML MoS_2 was illustrated on Figure 4.3a. The geometric confinement and weak screening results in a large exciton binding energy which can decrease the optical bandgap compared to the electronic by up to 30%.[53] Since the scope of this thesis is to investigate the electronic properties of these materials rather than the optical properties, I will not go into further details with the properties of the excitons.

5.1 Synthesis

MoS_2 and WS_2 are the only TMDs which are known to exist in nature as layered crystals. MoS_2 was therefore naturally the first TMD to be investigated in the few layer limit back in the 1960s[54] using the 'Scotch tape' method where the crystal is thinned by continues folding and unfolding of a piece of Scotch tape with a multilayer crystal on it. In the pursuit
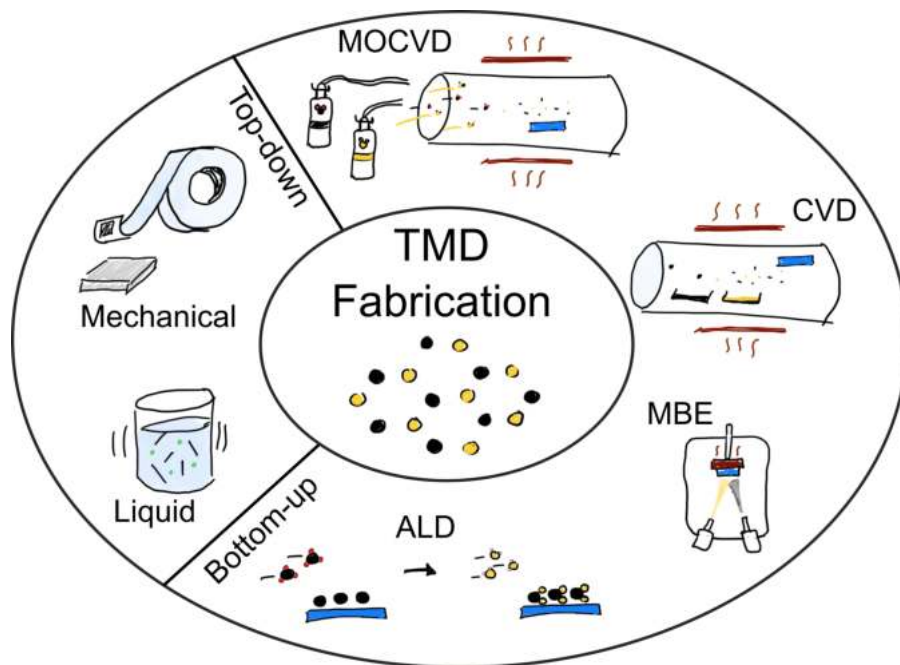
Figure 5.1: The most common fabrication methods for synthesis of TMDs divided into the top-down and bottom-up methods.

of a more scalable fabrication process and in order to investigate a larger range of TMDs, molecular beam epitaxy (MBE) was extensively used in the 1980s and 1990s to fabricate and investigate a range of layered materials. However, it was not until 2013, that single layer MoS_2 was successfully grown on a substrate using chemical vapor deposition (CVD).[55,56] In the last decade, a number of studies have shown that also the metal-organic CVD (MOCVD) method can produce large area single layers with a high electron mobility.[57,58]

The most common fabrication methods for synthesis of TMDs are illustrated on Figure 5.1. They can be divided into the top-down and bottom-up methods. The most common top-down approaches are either mechanical exfoliation, i.e. the Scotch tape method, or liquid exfoliation. Liquid exfoliation can be performed using a solution containing the layered crystal and Li-ions. The Li-ions become intercalated in the interlayer spacing of the crystal and a sonication process can be used to 'shake' the layers apart. The first reported monolayer of MoS_2 was exfoliated

using this method in 1986.[42] Both of these top-down approaches have the disadvantages that only relatively small flakes can be produced and that they result in large variations in thickness of the samples. In the case of the Scotch tape method, it is also rather destructive and not scalable for practical applications.

The most common bottom-up methods are MBE, CVD, MOCVD and atomic layer deposition (ALD). As mentioned above, MBE was extensively used in some of the early studies. MBE works by heating elementary sources which sublime and then combine at a wafer target to grow the desired crystal. The method requires a growth chamber which is held at ultrahigh vacuum and a wafer material which is commensurate with the growing crystal to avoid defects and grain boundaries. A cheaper alternative is the CVD method which does not require ultrahigh vacuum. In the CVD process, powders of the chalcogen and metal or metal oxide are heated and moved by a carrier gas to the wafer where it combines to form the crystal. Using an atomically smooth sapphire wafer, large area monolayer MoS_2 with high electron mobility has been grown using this method.[59] The high electron mobility suggests that the sample consists of large domains with few defects. The MOCVD method has also produced large area samples with high mobilities. The method uses gas phase precursors rather than heated powders for the crystal growth. The gases can e.g. be $Mo(CO)_6$ or $W(CO)_6$ and $(C_2H_5)_2S$ to grow MoS_2 or WS_2.[57] ALD is a layer-by-layer growth method which therefore naturally has some advantages when growing layered materials and single layers. In CVD and MBE methods, the crystal is grown from several seeds point on the wafer which results in grain boundaries between the different seeds whereas, in ALD, the crystal grows as one single layer at a time and grain boundaries are therefore avoided. In the ALD method, one species is allowed to bond to a wafer at a time. In the case of TMD growth, the metal atom is first introduced, e.g. as the metal oxide gas, and allowed to fully cover the surface of the sample. Afterwards, the chalcogen is introduced, also in a gas form, and reacts with the metal atoms to form a single layer. The process can be repeated to grow multiple layers. Recently, high quality monolayer WS_2 crystals were selectively grown over a length scale of more than 200 μm using ALD.[60]

Other less common methods for TMD synthesis are magnetron sputtering, pulsed laser depostion, electric chemical exfoliation, and the thermolysis method. Even though tremendous progress has been made in the

synthesis of TMDs, there is still no method which, in a scalable and reproducible manner, can produce large area samples of good quality and with a controlled thickness down to the monolayer limit.

5.2   Defects and Intrinsic Doping

Due to the many different fabrication methods, the quality of the produced samples varies a lot. In this section, I will describe the most common defects occurring in TMDs and how they affect the electronic properties. The defects are often divided into groups with the same dimensionality. Examples of 0D or point defects are vacancies, substitutions and adatoms. 1D defects are also known as line defects and examples are lines of vacancies or a grain boundaries. Examples of 2D defects are wrinkling and scrolling of the layers. The 0D and 1D defects can typically act as scattering centers of electrons which decreases the carrier mobility in the sample. As mentioned above, grain boundaries are a common source of low mobility in various TMD samples.

Until recently, there has been agreement that the most commonly observed type of point defect in monolayer TMDs was a chalcogen vacancy. In a DFT study by Haldar *et al.*[61], the formation energies of a long range of point defects were investigated in single layer TMDs. This study concluded that the chalcogen vacancy was the most stable defect at metal rich conditions except in $MoTe_2$ where a Te-interstitial is the most stable defect. In chalcogen rich environment, this chalcogen interstitial was found to be the most stable stable in all the materials. However, a recent study by Barja *et al.*[62] has showed that chalcogen vacancies and oxygen substitutions at a chalcogen site cannot be distinguished on a tunneling electron microscope (TEM) image. A combination of GW calculations, scanning tunneling microscopy (STM) and spectroscopy (STS), and non-contact atomic force microscopy (nc-AFM) imaging concluded that the most commonly observed defect in their MBE grown $MoSe_2$ and CVD grown WS_2 samples was of the oxygen substitution type rather than the chalcogen vacancy. One of the main arguments of this work is that the chalcogen vacancies result in in-gap states which are not observed in their samples.

Regardless of the nature of the most common defect, the literature

seems to agree that the defects lead to an intrinsic n-type doping. Using the simple ionic picture from the previous chapter, a chalcogen vacancy corresponds to an n-doping of the TMDs since the metal atom is unable to donate electrons to the missing chalcogen and two electrons remain in the metal d-orbital. A recent study by Jeong et $al.$[63] has investigated these vacancies in mechanically exfoliated ML MoS_2, $MoSe_2$, WS_2, and WSe_2 using electrical and optical measurements and found that the occupation of the related in-gap states pushes the Fermi level closer to the conduction band in the S-based materials. The vacancies therefore act as n-type dopants of the material in agreement with the simple picture. In the Se-based materials the effect is less pronounced leading to only a weak n-doping in $MoSe_2$ and no significant doping in WSe_2. The samples with oxygen substitutions observed by Barja et $al.$[62] have Fermi levels about three quarters of the band gap above the valence band edge corresponding to a small n-doping even though the substitution, using the simple ionic picture, does not donate any further electrons to the crystal.

Adsorbates from exposure to air can also play a large role in the electronic properties and intrinsic doping. Liu et $al.$[64] have demonstrated that a multilayer $MoTe_2$ transistor, fabricated using mechanical exfoliation of a CVD grown $MoTe_2$ crystal, can be converted from p- to n-type by annealing in vacuum. The p-type behavior is believed to be due to electron transfer to a oxygen/water redox couple which can be removed from the surface in the annealing process. The n-type behavior after annealing is attributed to Te-vacancies.

In conclusion, the research in TMD defects and their effect on the electronic properties is ongoing and even though some trends are understood, many things remain uncertain. Investigating the effects of defects in the monolayers is very challenging since TEM exposure, which is the common technique for investigating defects, introduces defects in itself and since AFM and STM methods cannot unambiguously identify the defects on their own. The synergy between combined experimental methods and theoretical predictions using GW calculations therefore seems to be necessary to gain insight on the nature and consequences of these defects. The two main materials investigated in this thesis are MoS_2 and $MoTe_2$. The conclusions regarding these materials are that intrinsic n-type doping is most common when the monolayer is encapsulated or in vacuum and might be due to S and Te vacancies and that p-doping is most common in air-exposed $MoTe_2$ which may be due to adsorbed oxygen/water redox

couples.

5.3   Doping Techniques

Since the intrinsic doping of the monolayer TMDs is barely understood, controlling the doping density in these 2D semiconductors presents a great challenge. The common method for 3D semiconductor doping where ion implantation is achieved by ion bombardment of the sample is much too destructive for these atomically thin layers and other solutions are therefore being investigated. The doping techniques are illustrated on Figure 5.2 and can be divided into four categories; substitutional doping, charge transfer doping, intercalation doping, and electrostatic doping. Both metal and chalcogen atoms can be substituted by foreign atoms of comparable radii resulting in a n- or p-type doping depending on the number of valence electrons in the dopant atom. For non-metal atoms, the chalcogen sites are occupied whereas metal dopants will occupy the metal sites for heavy atoms or the interlayer spacing for light atoms.[66] Depending on the type of dopant atom, large structural distortions may occur which can alter the material significantly. Suh *et al.*[67] have reported that substitution of Nb with sulfur in MoS_2 crystals drive a transformation of the stacking sequence from 2H to 3R, and the intercalation of Li-atoms in the interlayer spacing drives a phase transition in MoS_2 from the 2H-phase to the 1T or 1T'-phase.[11,68–72]

Charge transfer doping through the adsorption of gaseous molecules on the basal plane of the TMDs is less volatile since lattice distortions are avoided. Recently, Chamlagain *et al.*[73] have demonstrated that adsorption of benzyl viologen (BV) molecules on MoS_2 and $MoSe_2$ can be used for area selective doping. A polymethylmethacrylat (PMMA) mask is used to cover part of the MoS_2 flake and the sample is then immersed in a BV solution. Using this approach, the doping degree can be controlled by the immersion time. 2D semiconductors are very susceptible to electrical fields in the atomically thin dimension. Charge can therefore be electrostatically transferred by gate-control as a non-volatile and high-control doping mechanism. This can be achieved e.g. through a floating gate set-up[74,75] or by charge transfer from an ionic liquid.[76–78]

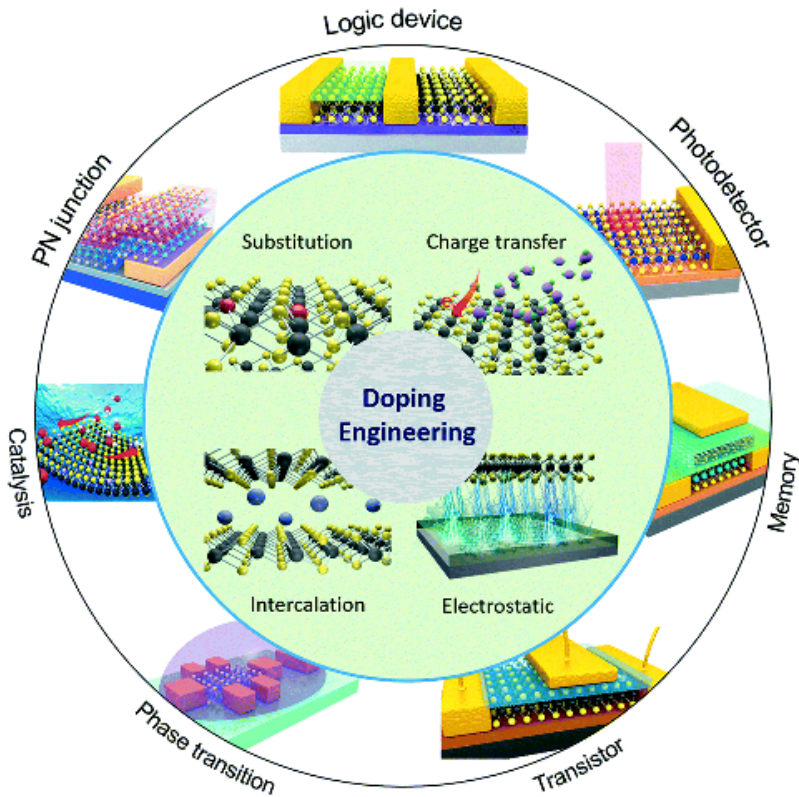This concludes the chapter concerning the properties of the semicon-

Figure 5.2: Doping strategies of 2D TMDs and their potential applications. Reprinted from Ref. [65] with permission from The Royal Society of Chemistry. Copyright 2019.

ducting group-VI TMDs. The next chapter will concern the metallic and semi-metallic phase of these materials.

Semi-metallic T'-phase

This chapter describes the synthesis and electronic properties of the 1T'- and T'-phase VI-TMDs. The section on synthesis also describes the synthesis of the 1T-phase since the methods for obtaining both of these phases are the same. Even though the 1T'-phase is more stable than the 1T-phase, many of the early attempts on inducing a phase transition of 2H-MoS$_2$ samples have been reported to result in the 1T-phase.

6.1   Synthesis and Phase Transition

The 1T- or 1T'-phase TMDs can be synthesized either by growing or exfoliating a 2H-phase sample using the methods described in the previous chapter and afterwards induce the other phase or by varying the growth conditions in a CVD process to directly obtain the meta-stable phase. This section will present both types of approaches and therefore serves to describe both how the 1T- and 1T'-phase TMDs can be synthesized but also how heterophase devices with phase boundaries can be fabricated.

The 1T'-phase can be induced from a 2H-sample by creating chalcogen vacancies resulting in an excess of electrons in the metal d-orbitals which drives the phase transition. The vacancies can e.g. be created from e-beam[69,79] or laser irradiation[80] or by Ar-plasma treatment.[81] In the case of e-beam or laser irradiation, the beam can be used to selectively target an area of the sample whereas the plasma treatment method requires a protective mask if some areas are indented to remain in the 2H-phase. Another method, which was extensively used in the early studies, also uses excess charge to drive the phase transition by intercalating electron-donating alkali metals such as Li, Na or K into the 2H-phase TMD.[11,68–72] An excess charge can be added from the decay of a plasmon into hot electron-hole pairs. That can e.g. be realised by placing gold nanospheres on a 2H-MoS$_2$ sheet and illuminating the sample with laser light.[82] The

plasmonic generated hot electrons can transfer into the conduction band of the 2H-phase and drive the phase transition.

Another method for phase transition is to induce strain on the 2H-phase. Since the lattice constant of the 1T'-phase is slightly larger than the lattice constant of the 2H-phase, a tensile stress lowers the barrier for phase transition. The method was proposed by Duerloo *et al.*[46] in 2014 and has later been experimentally verified.[83,84] As an example, Song *et al.*[83] used an AFM tip to apply tensile stress to the 2H-phase of $MoTe_2$ and were thereby able to lower the temperature of phase transition to 1T'-$MoTe_2$ from 900 °C to room temperature. Besides the phase transition methods mentioned here, several other have been demonstrated, such as phase transition via electrostatic gating[85], a photochemical method[86], or exposure to chemical vapor analytes.[87]

The meta-stable phases can also be directly synthesised by changing the growth conditions in a CVD process. This method has mainly been achieved for $MoTe_2$,[46] where the energy difference between the 2H- and 1T'-phase is very low (11 meV/atom).[i] By varying the temperature, the flux of Te atoms can be controlled. A high flux of Te will form the 2H-phase whereas a lower flux will result in the 1T'-phase presumably due to Te vacancies. At intermediate temperatures, a mixture of the two phases can be achieved.[88–90] Sung *et al.*[91] have used this approach together with an excess of NaCl vapor to grow polymorphic structures of the 2H and 1T'-phase of $MoTe_2$. The 1T'-phase grows as needles from a larger pad of the 2H-phase and crystalline interfaces are formed. The NaCl vapor is believed to help preserve enough Te vapour pressure to ensure crystalline growth. Similarly, the growth time of the CVD can be varied which either allows the sample to be fully tellurized, resulting in the 2H-phase, or ends before full tellurization, resulting in the 1T'-phase.[92] Patterned structures, e.g. for transistor applications, can be achieved by masking a 2H-region followed by an etch and growth of pure 1T'-phase by flux-control. This method can also be applied to stitch different TMDs together which was achieved by Sung *et al.*[91], creating 2H-WSe_2 - 1T'-WTe_2 devices. Zhang *et al.*[12] have used two different Mo-precursors which results in different defect densities of the CVD-grown $MoTe_2$, selectively stabilizing either the 1T'- or 2H-phase. A MoO_3 precursor results in 1T'-growth in a temperature range between 500 and 800 °C whereas a $MoO_{2-2.5}$ precursor can result

---

[i]Using calculations from this work.

in either pure 2H-phase, mixed 2H and 1T' or pure 1T' depending on the tellurization. This method allows for a single-step CVD growth of heterophase MoTe$_2$ with high crystallinity and atomically sharp interfaces. To summarize, many different methods have been applied to successfully synthesize the less stable phases of the TMDs. Heterophase devices with atomically sharp interfaces have primarily been achieved for MoS$_2$ based devices using Li-intercalation and for MoTe$_2$ based devices using various CVD approaches.

6.1.1   Phase Boundaries

Substantial work has been put into investigating the properties of the phase boundaries which result from a phase transition. Here, I will briefly review the work concerning phase boundaries in MoS$_2$ and MoTe$_2$. Lin *et al.*[69] have investigated the 2H to 1T-phase transformation of MoS$_2$ using an aberration-corrected scanning transmission electron microscope (STEM). Their investigations have revealed both how the atoms move doing the phase transition but also the atomic configuration of the phase boundaries when phase transition is induced by Li-intercalation. On Figure 6.1a-c, the three phase boundaries discovered in this study, the α, β, and γ boundaries, are shown. The atomic configurations of these three boundaries are illustrated on figure 6.1d illustrating that they form along the zigzag direction. Li-intercalation driven phase transitions by Eda *et al.*[68] and Kappera *et al.*[70] (Figure 6.1e) have revealed boundaries similar to the γ-boundaries found by Lin *et al.*[69]. Sun *et al.*[72] have investigated interfaces between monolayer H-phase and multilayer 1T'-phase MoS$_2$ and find that the phase boundaries form along the zigzag directions of the two phases as illustrated on Figure 6.1f.

Sung *et al.*[91] reported that two types of boundaries form between 2H- and 1T'-phase MoTe$_2$ when flux-controlled growth is used to induce the phase transition. One type forms along the zigzag direction of the two phase, as illustrated on Figure 6.2a, and the other forms between the zigzag edge of 2H and the zigzag direction of 1T' turned by 60 degrees, as illustrated on Figure 6.2b. These two types have also been reported by Xu *et al.*[93] (Figure 6.2c) where variation of the growth time is used to grow the 1T'-phase beside the 2H-phase.

Han *et al.*[94] have conducted a comprehensive study of the variation of
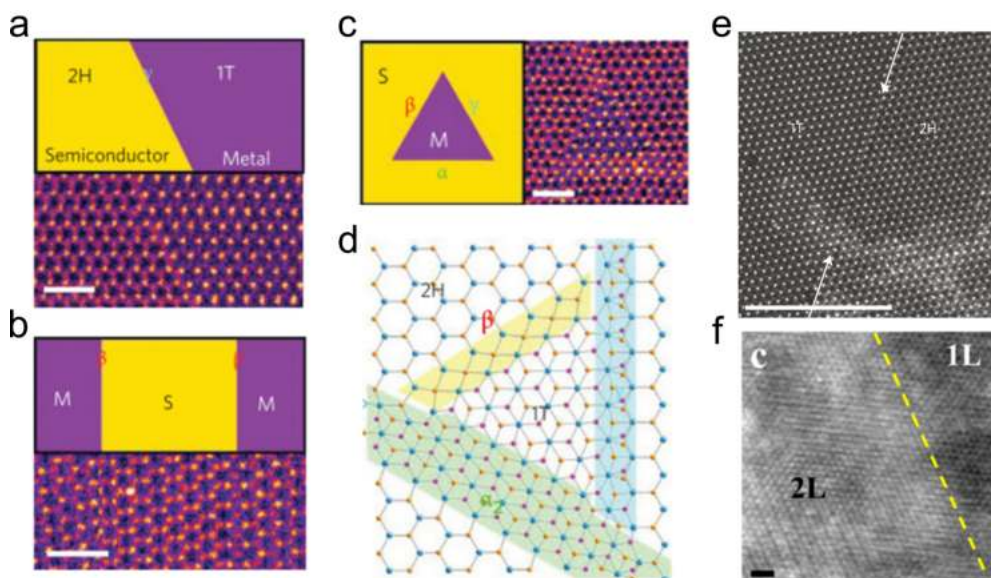
Figure 6.1: MoS$_2$ phase boundaries. **a-c** show STEM images of 1T-2H structures obtained by Lin *et al.* using Li-intercalation to drive the phase transition, and **d** shows the atomic configurations of the three types of boundaries. Reprinted with permission from [69]. Copyright 2014 Springer Nature. **e** shows a HRTEM image of the 2H-1T phase boundary found by Kappera *et al.*. Reprinted with permission from [70]. Copyright 2014 Springer Nature. **f** shows STEM image of the boundary between double-layered 1T'-phase and monolayer H-phase observed by Sun *et al.*. Reprinted with permission from [72]. Copyright 2018 American Chemical Society.
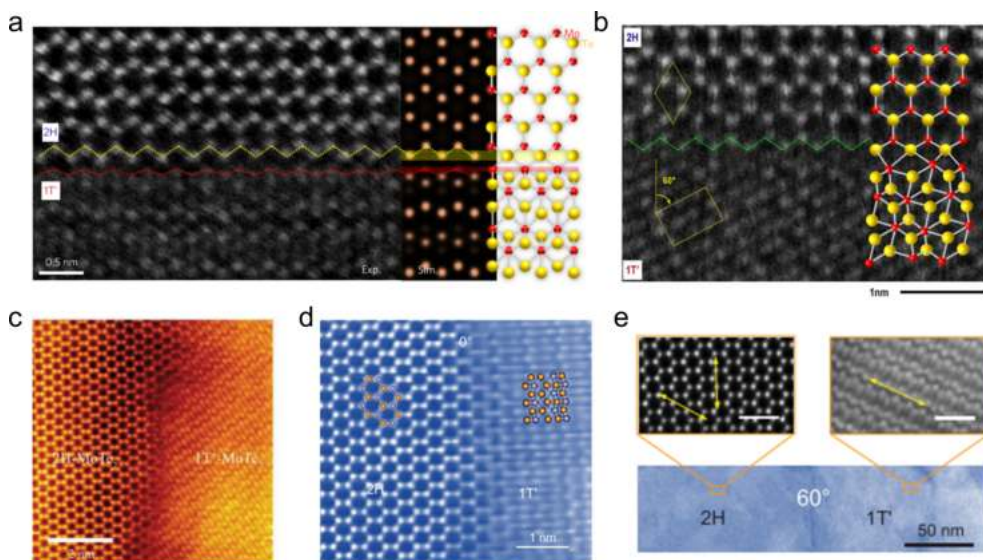
Figure 6.2: MoTe$_2$ phase boundaries. **a** and **b** show the HAADF-STEM images and interpreted atomic configurations of the two types of 2H-1T' phase boundaries observed by Sung *et al.* Reprinted with permission from [91]. Copyright 2017 Springer Nature. **c** shows a HAADF-STEM image of a representative 2H-1T' boundary observed by Xu *et al.*[93] where both of the types reported by Sung *et al.*[91] are present. Reprinted with permission from [93]. Copyright 2020 John Wiley and Sons. **d-e** show the HAADF-STEM images of the 0 and 60 degree rotation 2H-1T' boundaries investigated by Han *et al.*[94] corresponding to the boundaries seen on **a** and **b**. Reprinted from [94] under a CC license.

the deep ultraviolet plasmon oscillation $(\pi + \sigma)$ peak as a function of the rotation angle between the zigzag directions of 2H- and 1T'-phase $MoTe_2$. The study looks at angles between 0 and 60 degrees and concludes that the red shift of the plasmon is minimized at 0 and 60 degrees (Figure 6.2d-e). This is interpreted as a sign of a good overlap between the σ electron clouds of Mo and Te atoms which should result in a low barrier for carrier injection.

To summarize, phase boundaries of 1T-2H (or 1T'-H) MoS_2 tend to form along the zigzag direction of both crystals and 1T'-1H $MoTe_2$ boundaries have primarily been observed to form either along the zigzag direction of both phases or at a 60 degrees angle from this directions.

6.2   Topological Properties

As mentioned previously, the T'-phase of the VI-TMDs are Quantum Spin Hall Insulators (QSHIs).[51] This section is a partly revised and partly reprinted from the paper published in Physical Review B in 2019[95] and will introduce the topological properties of T'-phase MoS_2, $MoTe_2$, WSe_2, and WTe_2. It turns out, that some zigzag edge terminations host magnetic states which breaks the time-reversal symmetry. This first of all breaks the topological protection of the edge states and furthermore results in conducting channels at the edge which no longer can be removed by changing the topological phase of the bulk.

2D insulators with an electronic structure which is invariant under time-reversal symmetry can be characterized as being either trivial insulators or quantum spin Hall insulators.[96] It is only possible for a material to change from one of these topological states to the other if either the gap closes or time-reversal symmetry is broken. For bulk materials, the topological state does not have any direct observational consequences. However, any interface between a trivial insulator and a QSHI e.i. between the two different topological states, is guaranteed to host gapless (conducting) boundary states. Since vacuum can be regarded as a trivial insulator it follows that also any edge of a quantum spin Hall insulator hosts gapless states.

These boundary or edge states are protected from back scattering by time-reversal symmetry and the states are always pairs of opposite spin

such that a spin-up and spin-down channel is present at each edge. The non-trivial topology simply implies that there is no available scattering channel and the edge conductance is predicted to be exactly $\pm e^2/h$ for spin-up and spin-down electrons, respectively. If time-reversal symmetry is broken, it is no longer guaranteed that gapless edge states persist at the edge. Even if they do, the conductance may deviate from the quantized value due to impurity scattering. This has been observed in WTe_2 where the presence of an external magnetic field significantly reduces the edge conductance.[49] Likewise, the presence of magnetic impurities at edges which may lead to broken time-reversal symmetry[97–99] and destroy the topological edge states. Finally, time-reversal symmetry may be broken *spontaneously* by the presence of magnetism without introducing any impurities. This possibility seems to be largely overlooked in the literature although it by no means is an unlikely scenario. For example, first principles calculations have shown that edges of a monolayer MoS_2 in the 2H-phase acquires magnetic edge states although the bulk 2D material is non-magnetic.[100] If time-reversal symmetry is spontaneously broken at an edge of a quantum spin Hall insulator, the presence of gapless edge states is no longer guaranteed. Even if they persist, the observable consequences of the quantum Hall state could in principle be removed by a suitable edge modification.

As a starting point, let us consider the T'-phase of ML MoS_2. This phase possesses a small band gap of 80 meV[101] due to spin-orbit splitting of the bands occurring between the Γ- and Y-point in the Brillouin zone
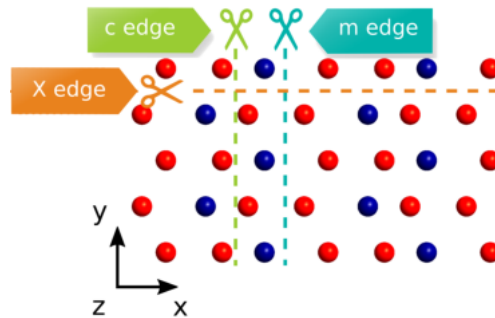

Figure 6.3: Top view of a T'-phase TMD showing the (X), (m), and (c) edge.

(BZ). The band structure was shown on Figure 4.3c. Note, that using this method, the gap is 48 meV which is only slightly lower than the experimental value obtained using STS.[101] Three different edges will be considered, as indicated on Figure 6.3. The (X) edge is a cut along the x direction and the (m) and (c) edges are cuts along the y direction. The y-cut can be made in several different ways, but these two edges represent the must stable ones for the Mo and single-S terminated kinds respectively, see Appendix B.1 for a stability analysis.

In order to study the electronic bands of the three different edges, DFT+NEGT calculations on a surface configuration can be used. This type of configuration consists of two regions; the electrode and the central region and was described in Chapter 2.2. Green's functions to couple the central region to the electron reservoir of a monolayer which is periodic in the x and y direction (2D crystal). Details on how the systems are set up can be found in Appendix A.1.

The band structures can be seen on Figure 6.4 showing the density of states for the k-points along the $Y \rightarrow \Gamma \rightarrow Y$ path of the BZ. The total number of states is seen on the left hand side and the spin-polarized states on the right hand side. The solid areas represents the bulk states and the edge states can be identified as the isolated and spin-polarized bands. All three edges host gapless edge states. The (X) edge has 4 edge states which are degenerate two-by-two in the high symmetry points of the Brillouin zone. Two states can be seen at the region around the Fermi level and Γ-point and two more states can be distinguished from these around X and $-X$ at low energies. The pair which is degenerate at the Γ-point both crosses the Fermi level corresponding to one spin-up (spin in the $+y$ direction in this case) channel and one spin-down (spin in the $-y$ direction) channel at the edge. This is exactly what is expected for the topologically protected edge states of a topological insulator. However, the behavior is different at the two other edges where time-reversal symmetry is broken. The effect is most pronounced for the (m) edge and as seen on Figure 6.4b where the spin polarization is equal instead of opposite for any k and $-k$ pair of the edge state. Furthermore, the degeneracy at the high symmetry points is lifted and the bands are separated by approximately 0.25 eV at the Y and $-Y$ points. For the (c) edge, the effect is more subtle and can only be seen for the edge states close to the Gamma point between the two dips of the conduction band. Here, the spin polarization changes, not at the Γ point, but at a small positive value of k going in the Y direction.
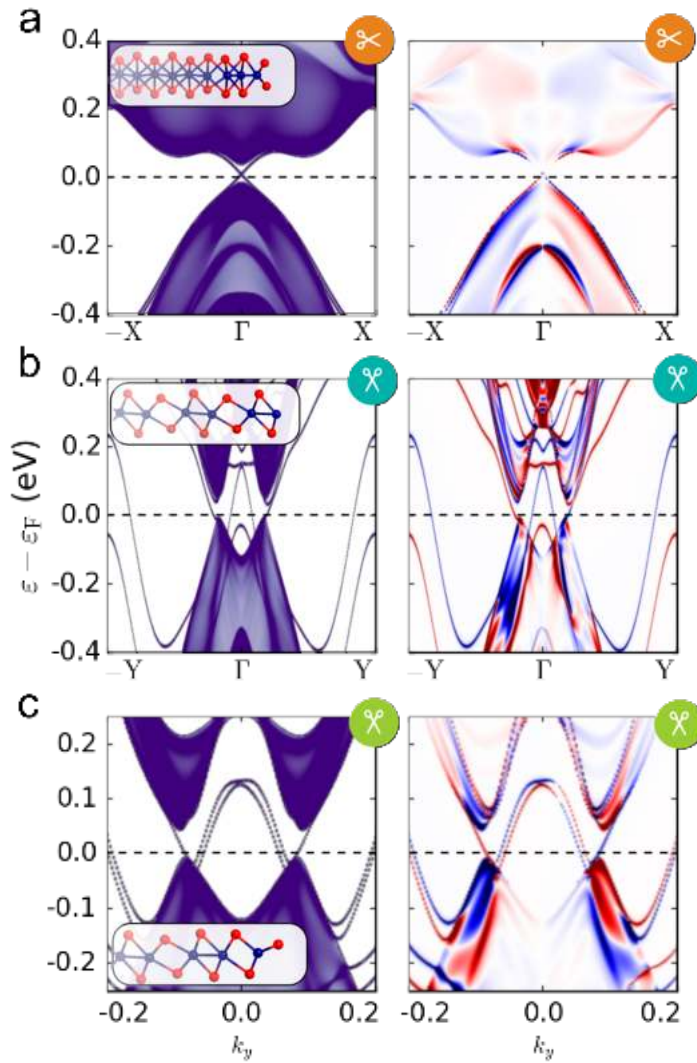
Figure 6.4: The electronic bands for **a** the (X) edge, **b** the (m) edge, and **c** the (c) edge of monolayer 1T' MoS_2. **left** side shows the sum of all spin components and **right** side shows the spin-polarized density of states wrt. the y and x direction, respectively. Adapted with permission from Ref. [95].

The origin of this effect is, that the time-reversal symmetry is spontaneously broken as a magnetic state is formed at the edge. This can be illustrated by a plot of the magnetization density as shown on Figure 6.5. Note, that the spin configuration is non-collinear and we therefore have a magnetization density wrt. each spatial direction. The figure only shows the x and z components, since the y component is zero. The magnetic moments point to the right and downwards (upwards) for the m (c) edge and have most weight on the last Mo-atom of the surface. The edge states primarily stems from the Mo d-orbitals and S p-orbitals with the approximate relative weight of 3:1 for the (m) edge and 5:2 for the (c) edge.

The surface configuration allows for observing only a single edge or surface of a material. This is advantageous in showing phenomenons such as the ones described above, but some more insights can be gained from comparing with a nanoribbon configuration as well. Calculations on such a configuration with two (m) type edges show that the magnetic state points in the same spatial direction on both edges.[95] This is also in contrast to the QSHI where two spin channels going in opposite directions resides on each edge. In conclusion, these investigations show that the time-reversal symmetry can be spontaneously broken on the edges of T'-MoS_2 and that it leads to magnetic states which behaves very differently from the expected topological states. This means that the gapless states on these edges are not topologically protected.

The magnetization vector, $\vec{m}$, and the total magnetization, m, can be used to quantify the magnetization.

$$\vec{m} = \frac{1}{N_M} \int \vec{m}(\vec{r}) \, \mathrm{dV},$$
$$m = \frac{1}{N_M} \int \sqrt{\vec{m}^2(\vec{r})} \, \mathrm{dV}.$$

The magnetization is defined per transition metal atom on the edge, N_M. Note, that for all three edges, $N_M = 1$. Studies of the T'-TMD phase have primarily been based on $MoTe_2$,[91,93,94] WSe_2,[102,103] and WTe_2[47–49] where the T'-phase is relatively more stable compared to the H-phase than it is for MoS_2. The magnetization vector and total magnetization of the MoS_2 (m) and (c) edges are compared to the edges of these materials in Table 6.1. Note, that $MoTe_2$ and WTe_2 are metallic since the valence and conduction bands overlap in energy. However, the bands are separated in
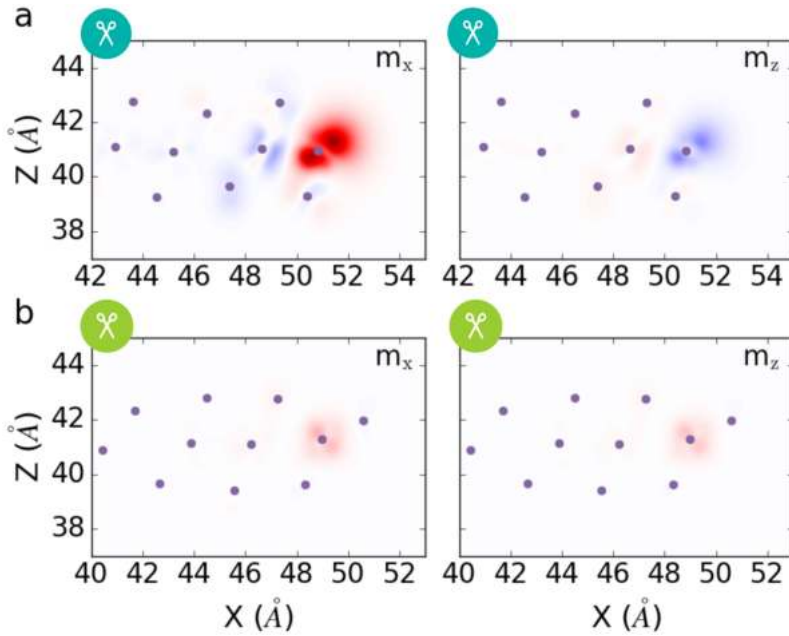
Figure 6.5:   The magnetization density wrt. the x and z axis of **a** the (m) edge and **b** the (c) edge of MoS_2. Adapted with permission from Ref. [95].

k-space which means that the character of the electronic structure is similar to the other materials and that a topological index can be defined. The magnetic edge state is present for MoS_2, $MoTe_2$, and WTe_2 but missing for WSe_2.

The magnetic (m) edges show a higher magnetism than the magnetic (c) edges for the same material. This can be understood through the different stoichiometry of the two termination. At the (m) type edge, the outermost metal atoms are completely exposed and missing 3 of the nearest chalcogenide atoms. This means that the metal atoms end up with a small excess of electrons compared to a metal atom in the 2D crystal. These excess electrons will be filled into the d-band resulting in a higher DOS at the Fermi level. This higher DOS results in magnetism in accordance with the Stoner criterion. At the (c) type edges, the outermost metal atoms only lacks a single chalcogenide neighbor. The bonds are therefore more saturated, the d-band less filled, and the magnetism smaller. The edges which become magnetic have edge states where the d-orbitals have

a weight which is larger than twice the weight on the p-orbitals. This agrees with the explanation above and shows that the magnetism arise when d-type states dominate at the Fermi level.

It is highly desirable to be able to change the topological index of insulators by external means. This would imply that gapless surface states can be removed or introduced at a given edge which may form the basis of one-dimensional transistors. In the case of the T'-phase TMDs, an external electric field perpendicular to the layer can induce a transition from the quantum spin Hall state to a trivial state.[51,95] External electric fields can therefore be used to switch between conductive and insulating edges. The topological state of the material can be changed since the electric field at closes the band gap. At a higher field strength, the gap opens again and the system has become topologically trivial. This is illustrated on the top part of Figure 6.6 where the distance between the valence and conduction band is plotted against the field strength. The vacuum and ML field strength is defined as the slope of the effective potential in the vacuum an ML region, respectively.

The critical fields, where the gap is closed, are $E_c^{vac} = 1.7$ V/Å in the vacuum and $E_c^{ML} = 6.4 \times 10^{-2}$ V/Å in the ML. The large difference between the vacuum field and and field inside the material shows that the monolayer strongly screens the field. In particular, the longitudindal part of the dielectric constant in the z direction can be estimated as the ratio between the vacuum field and the ML field, $\varepsilon_{ML} = E^{vac}/E^{ML} = 27$.

The electronic bands of the MoS_2 edges is seen on Figure 6.6 at zero field, the critical field strength, and twice the critical field strength. The

	E_g	(m) edge		(c) edge	
		m	$\vec{m}$	m	$\vec{m}$
MoS_2	48 meV	6.7	(0.26,0,-0.069)	0.82	(0.035, 0, 0.028)
$MoTe_2$	0 meV	17	(0.75, 0, 0.26)	-	
WSe_2	10 meV	-		-	
WTe_2	0 meV	5.7	(0.23, 0, 0.10)	1.0	(0.035, 0, -0.030)

Table 6.1: Calculated band gaps, total magnetization in $\mu_B \times 10^{-2}$ and magnetization vector in μ_B pr. transition metal atom on the edge for 4 different T'-TMDs.

Figure 6.6: **Top:** Gap between valence and conduction band of T'-MoS$_2$ as function of the effective potential in the vacuum region and the ML. **Bottom:** Response from of the electronic bands when applying a perpendicular field. **a** the (X) edge, **b** the (m) edge, and **c** the (c) edge. Adapted with permission from Ref. [95].
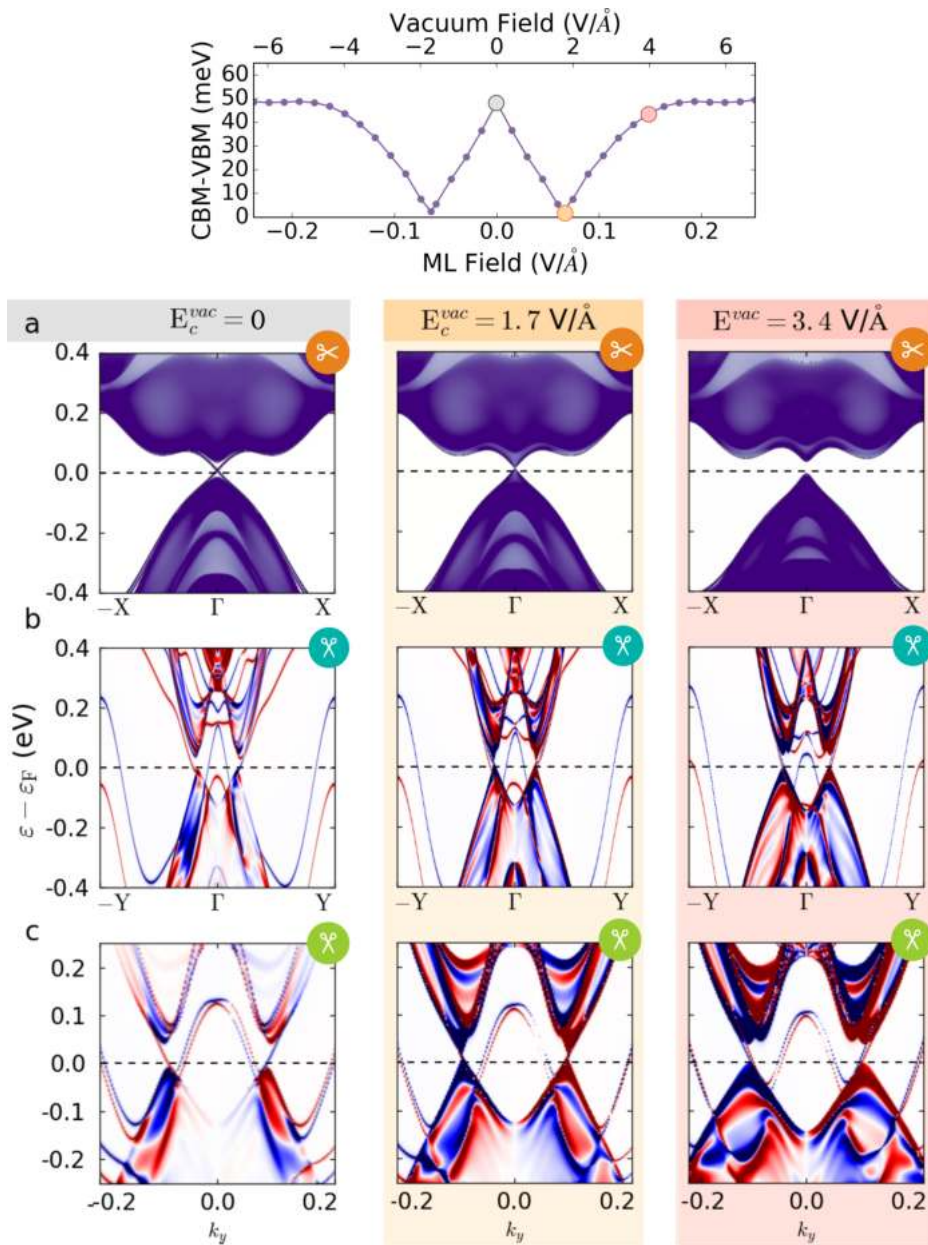
non-magnetic (X) edge show the expected behavior. Above the critical field, the gapless states have disappeared and no conducting channels are available. For the two magnetic edges, on the other hand, the metallic edge states persist relatively unaltered above the critical field. In the case of the magnetic edges, it is therefore not possible to remove the conducting states by applying a field. Due to the weak coupling between the magnetic and electronic degrees of freedom, the total magnetization also remains relatively unaltered with respect to the field strength.

A study by Gibertini *et al.*[104] has shown that H-phase TMDs generally have metallic edge states on the edges along the zigzag direction since these edges have a polar discontinuity. The polarization of the H-phase is along the armchair direction which means that an edge termination along the zigzag edges represents a discontinuity in the polarization and polarization charges appear at the edge creating a field between the two edges. This field drives a charge reconstruction where electrons from the valence bands on one edge is transferred to the conduction band on the other edge. Put in another way, free electrons and holes are driven to the edges to screen the polarization charge. These free charges are associated with the gapless states localized at the edges. The T'-phase also has a polarization along the armchair direction (x direction) due to the zigzag chains of metal atoms. One might therefore speculate that the edge states appearing on the edges which are terminated along the y direction are related to a discontinuity in the polarization rather than the topological state of the crystal.

In conclusion, even though the T'-phase TMDs are QSHIs, several of the edges show breaking of the time-reversal symmetry and exhibits magnetic edge states. This means that the gapless edge states of these edges are no longer protected against impurity scattering. The total magnetization varies between different TMDs and is strongest for the Mo-terminated $MoTe_2$ edge with a value of 0.17 μ_B pr. unit cell. The topologically protected edge states can be removed above a critical field while the gapless magnetic edge states remain relatively unaltered.

The topological properties of the T'-phase zigzag edges is important for the charge transport along the edge but do not play a significant role in the charge transfer across the edge.[105] Calculations on the charge transfer between the T'- and H-phase TMDs will therefore not take these effects in to consideration.

2D Schottky Barrier

The two previous parts have introduced the tools and materials which are the foundation of the research presented in this thesis. In this part, I will explain the physics behind the Schottky barrier which forms when a metal and semiconductor are interfaced. The theory is introduced both in the case of 3D and 2D materials and ab-initio calculations are used to illustrate how the atomic-scale properties of the interface dominate the behavior of interfaces between 2D materials.

Metal-semiconductor contacts are some of the main components in countless electronic devices. The theory behind the Schottky barrier was formulated by Schottky in 1938[106] and in 1942, Bethe refined the theory by formulating the thermionic emission model.[107] The theory has therefore been around for more than half a century and has been very successful in describing properties of 3D contacts. However, since modern technological applications of metal-semiconductor contacts operate on the nano-scale, it seems reasonable to revisit the subject.

The objective of this part is to gain a basic understanding of how the dimensionality of the materials affects the electronic properties of a metal-semiconductor interface. More specifically, the charge transport properties of interfaces between T'- and H-phase $MoTe_2$ are investigated using ab-initio modelling. This will build the foundation needed to evaluate these contacts for usage in a field effect transistor which is the subject of the final part.

The following chapters are organized as follows,

Chapter 7 describes the basic theory behind the Schottky barrier and charge transport across metal-semiconductor interfaces and summarizes the most common methods used for determining the barrier.

Chapter 8 presents ab-initio calculations of the Schottky barrier and charge transport properties of T'-H $MoTe_2$ interfaces.

2D Schottky Contact

In this Chapter, I will describe the theory behind the Schottky barrier and how the charge transport across metal-semiconductor contacts are changed by the dimensionality of the materials going from 3D to 2D. The theory behind the 3D Schottky contact follows Chapter 3 of Ref. [108] and the 2D expressions are derived using corresponding methods.

The emergence of a Schottky barrier at a metal-semiconductor contact can be explained by imagining that the two materials are contacted step-by-step as illustrated on Figure 7.1 and 7.2. Figure 7.1a shows a metal with work function, $q\phi_m$, and an n-doped semiconductor with electron affinity, $q\chi$, and with a distance between the Fermi level and conduction
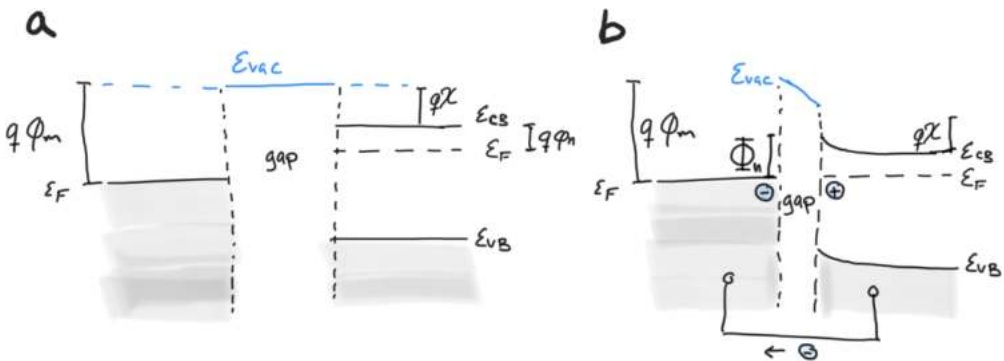
Figure 7.1: Schottky barrier, Φ_n, at metal-semiconductor interface. **a** shows the isolated metal and n-doped semiconductor with the metal work function, $q\phi_m$, and semiconductor electron affinity, $q\chi$. The valence band maximum, ε_{VB}, conduction band minimum, ε_{CB}, Fermi level, ε_F, distance between conduction band and Fermi level in the semiconductor, $q\phi_n$, and vacuum potential, ε_{vac}, are marked. **b** shows the metal and semiconductor in electrical contact but separated by a small spatial gap.

band of qϕ_n. q is the elementary charge. On Figure 7.1b, these two materials have been electrically connected but are still separated in space. When the contact is formed, electrons flow from the semiconductor to the metal to reach equilibrium. The electric field in the gap creates negative charge on the metal side and positive charge on the semiconductor side. The conduction band starts to bend and electrons are depleted from the area close to the interface.

As the distance between the two materials decreases, the field in the gap increases until the two materials are combined to an interface and the electrons have been completely depleted from the part of the semiconductor closest to the interface. This depletion region corresponds to a band bending of $\Delta V = q(\phi_m - \chi - \phi_n)$ (often called the built-in potential). A Schottky barrier has formed with a barrier height of

$$\Phi_n^{SM} = q(\phi_m - \chi). \tag{7.1}$$

This is known as the Schottky-Mott limit and represents the simplest way of predicting the Schottky barrier height of a metal-semiconductor contact. The final interface is illustrated on Figure 7.2 for 3D and 2D interfaces, respectively. If the semiconductor had been p-doped, the barrier would be

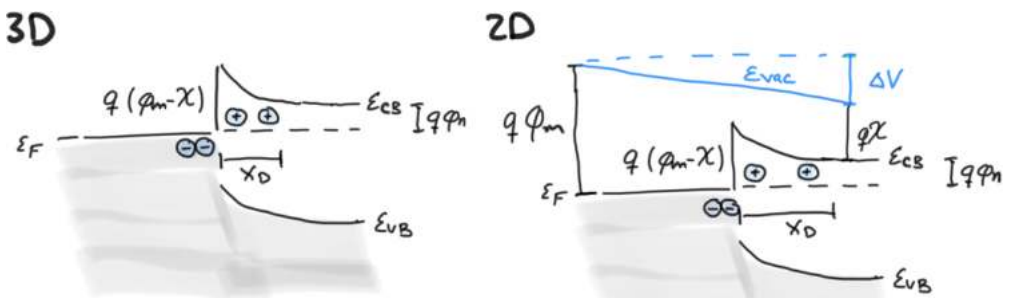$$\Phi_p^{SM} = E_g - q(\phi_m - \chi), \tag{7.2}$$

Figure 7.2: Schottky-Mott Schottky barrier in 3D (left) and 2D (right). The 2D case differs from the 3D case by the created vacuum field, ε_{vac}, and the longer depletion width, x_D.

where E_g is the band gap of the semiconductor. This shows that the size of the n- and p-type barrier will be anti-correlated since the sum must equal the semiconductor gap.

In 3D, the charge build-up at each side forms two sheets of opposite charge. This is the interface dipole. At the metal side, the surface charge completely screens the build-up charge on the semiconductor side. The length of the depletion width can be estimated by the assumption that the charge density equals the doping level, N_{3D}, inside the depletion region, $\rho(x < x_D) = qN_{3D}$ and vanishes outside and that the field created by the depleted charge vanishes outside the depletion region as well. This is known as the depletion approximation and separates the Schottky contact into three areas, the metal side ($x < x_{int}$), the depletion region ($x_{int} < x < x_D$), and the quasi-neutral region ($x > x_D$), where x_{int} is the position of the interface. The term 'quasi-neutral' refers to the fact that in a real Schottky contact the field does not vanish completely in this region. The field created by the charge in the depletion region can be found from the Poison equation,

$$\frac{\mathrm{d}^2\phi}{\mathrm{d}x^2} = -\frac{\mathrm{d}E^{3D}}{\mathrm{d}x} = \frac{qN_{3D}}{\varepsilon_s} \Rightarrow$$
$$E^{3D}(x) = -\frac{qN_{3D}}{\varepsilon_s}(x_D - x).$$

where ε_s is the dielectric constant of the semiconductor. The corresponding electrostatic potential is parabolic and shown in Table 7.1. The depletion width is found from the condition that the potential difference between the two sides equals the built-in potential. This leads to the square root dependence seen in Table 7.1.

In 2D, charge flows towards the edges of the two materials but this does not create a uniform field in the depletion region as it does at the 3D contact. The electrostatics at the interface differs from the 3D case in two important ways.

1. A macroscopic field is created in the vacuum region.

2. The field from the interface dipole is long-ranging which results in a longer depletion width.

3D	**2D**
$E(x) = -\frac{qN_{3D}}{\varepsilon_s}(x_D - x)$	$E(x) \approx -\frac{qN_{2D}}{\pi\varepsilon_{eff}}(\ln(2x_D - x) - \ln(x))$
$\phi(x) = -\frac{qN_{3D}}{\varepsilon_s}(\frac{x^2}{2} - x_D x)$	$\phi(x) \approx -\frac{qN_{2D}}{\pi\varepsilon_{eff}}[(2x_D - x)\ln(2x_D - x)$
	$+ x\ln(x) - 2x_D \ln(2x_D)]$
$x_D = \sqrt{\frac{2\varepsilon_s \Delta V}{q^2 N_{3D}}}$	$x_D = \frac{\pi\varepsilon_{eff}\Delta V}{q^2 N_{2D}\ln 4}$

Table 7.1: Field and potential inside the depletion region of a metal-semiconductor interface and the depletion width in 2D and 3D. The interface is positioned at $x = 0$. The expressions for a 2D interface follows the derivations by Ilatikhameneh et al.[109]
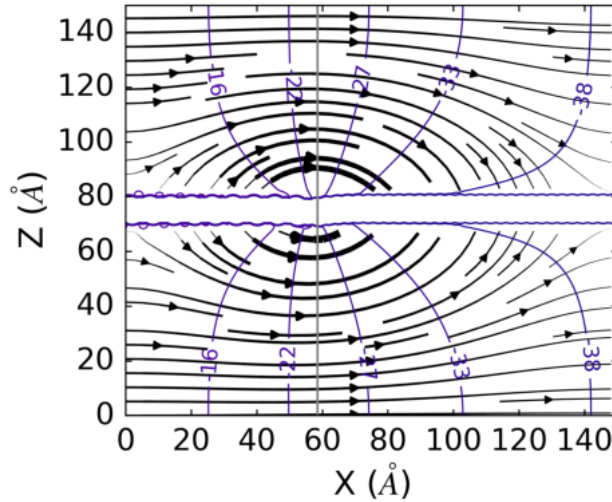

Figure 7.3: Equipotential lines (purple) and field lines (black) of the field created in the vacuum region outside a 2D metal-semiconductor interface. The interface position is marked by the grey line and the atomic positions are at the center of the z-axis. The values of the equipotential lines are in meV.

The first property arises since the 2D system continues to be referenced to the vacuum level after the interface has been formed. This is to be understood the following way; If an electron is taken from the metal side far away from the interface, transported through the vacuum, and returned to the system through the semiconductor, the work done on the electron must be zero since the system in equilibrium. This implies,

$$q\phi_m - \Delta\varepsilon_{vac} - q(\phi_n + \chi) = 0 \Rightarrow \Delta\varepsilon_{vac} = -q(\phi_m - \phi_n - \chi) = -\Delta V.$$

A macroscopic field is therefore generated in the vacuum region corresponding to the potential shift, $\Delta\varepsilon_{vac}$. This is equivalent to the field generated when two metal surfaces with different work functions are interfaced (see e.g. Landau and Lipshift[110], Chapter 3, §23). The vacuum potential can be found by solving the Laplace equation in the vacuum region above the interface,

$$\nabla^2\phi_{vac}(x, z) = 0 \qquad\qquad \text{for } z > 0$$
$$\phi_{vac}(x) = 0 \qquad\qquad \text{for } x \to -\infty$$
$$\phi_{vac}(x) = \Delta V \qquad\qquad \text{for } x \to +\infty$$

The x-direction is perpendicular to the interface which is positioned at $x = 0$ with the metal to the left and the semiconductor to the right and the z-direction is perpendicular to the nanoribbon which is placed at $z = 0$. The energy scale has been chosen such that the work function of the metal is set to zero. The solution is most easily expressed using spherical coordinates,

$$\phi_{vac}(r, \theta) = \frac{\Delta V}{\pi}\theta.$$

The equipotential lines extends from the interface as rays placed at every value of θ and the corresponding electrical field is,

$$\vec{E}_{vac} = -\nabla\phi_{vac}(r, \theta) = -\frac{\Delta V}{\pi r}\hat{\theta}$$

The field lines are completely circular and the strength is determined by the difference between the two work functions. The vacuum potential

and field are illustrated on Figure 7.3 for an interface between H- and T'-phase MoTe$_2$. Note, that these field lines are elliptical rather then circular due to the boundary conditions in the calculation.

In order to obtain the potential and field from the interface dipole and the depletion width, the 2D Poisson equation must be solved. In 3D, the depletion approximation was used to define the boundary conditions when solving this equation. Unfortunately, these boundary conditions leads to unphysical behavior at a 2D contact.

I will attempt to explain this behavior by considering a charged metallic nanoribbon. This example illustrates that when a 2D material is charged, a divergence in the surface charge density arises. Let us consider the charge density of a charged 2D metal nanoribbon at a constant potential, $-\phi_0$,

$$\sigma(x) = \frac{2\varepsilon_{eff}\phi_0}{\sqrt{1 - \left(\frac{x}{x_{edge}}\right)^2}}.$$

ε_{eff} is the dielectric constant of the surroundings and the edges of the ribbon are placed at $x = \pm x_{edge}$. The derivation is carried out in Appendix C.1. From this expression it is seen that a charged 2D material in a constant potential will have a surface charge accumulation which diverges at the edges.

Returning to the 2D interface, the boundary conditions from the depletion approximation are $\sigma(x < x_D) = qN_{2D}$, $\sigma(x \geq x_D) = 0$ and $E(x \geq x_D) = 0$. The depletion region is charged due to the depleted electrons and the boundary conditions demand that the potential is constant in the quasi-neutral region. A divergence in the surface charge density between depletion and quasi-neutral region therefore appears in correspondence with the example above. This makes the second of the boundary conditions impossible to fulfill. A derivation showing this in detail can be found in Appendix C.1.

The charge density divergence at the interface between the depletion and quasi-neutral region in unphysical since the transition from depletion region to quasi-neutral region should be smooth. Possible solutions to this issue, have been presented both by Ilatikhameneh *et al.*[109] and Nipane *et al.*[111]. Both of these derivations use an infinite repetition of image charges in the quasi-neutral region. The charge density is the first part of the

quasi-neutral region is constant and equal to the charge density in the depletion region but the infinite repetition of image charges ensures an overall neutrality. The resulting potential, electrostatic field, and depletion width obtained by Ilatikhameneh *et al.*[109] are included in Table 7.1.

Both of the derivations result in a depletion width which scales linearly with $\Delta V / N_{2D}$. This linear dependence is confirmed using ab-initio methods in Chapter 8. A corresponding 3D interface has a square root dependence on this term which means that the 2D depletion width is longer. The potential and field from a 2D interface dipole are therefore longer ranging than the 3D counterparts. It is important to note that it is the dimensionality of the contact which results in the longer depletion width. Screening in 2D materials is generally weaker than in 3D which also leads to a longer depletion width but this is an effect which is on top of the dimensionality effect.

This concludes the most simple approximations for obtaining the barrier height and the main differences between a 3D and 2D Schottky contact.

7.1   Fermi Level Pinning

The Schottky-Mott rule assumes an ideal contact. Many physical phenomena can be responsible for breaking the behavior predicted by this rule. One of the most simple examples is to consider how the image-force can decrease the Schottky barrier. When an electron moves in the semiconductor towards the metal, it will be affected by an attractive force from the induced charge on the metal side. This attractive force lowers the effective Schottky barrier which the electron must overcome to move from the semiconductor to the metal.

The Schottky barrier height can also be altered by the presence of interface states. If the interface states are a property of the semiconductor surface, the neutrality level of the semiconductor can pin the Fermi level at the interface. At a 2D contact, the interface states can also originate from the metallic edge. Chapter 8 will elaborate on this using ab-initio calculations. In this section, I will consider the effect of interface states originating from the semiconductor surface.

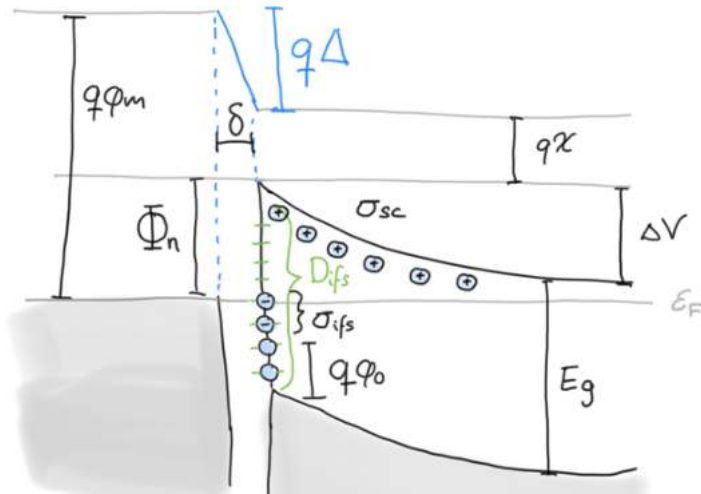Consider a semiconductor surface with a density of interface states,

Figure 7.4: Fermi level pinning due to interface states (green) originating from the semiconductor surface. The Schottky barrier height, Φ_n depends on both the difference between the metal work function, $q\phi_m$, and semiconductor electron affinity, $q\chi$, and on the total charge accumulation at the interface due to the carrier depletion in the semiconductor, σ_{sc}, and the interface charge traps, σ_{ifs}. $q\phi_0$ is the charge neutrality level of the semiconductor and δ is the small gap between the metal and semiconductor which is of atomic dimensions and supports a potential drop, Δ. Inspired by Ref. [108].

D_{ifs}, inside the gap. Some of these states will be donor type which is neutral when occupied and positively charged when empty. Others will be acceptor type which are neutral when empty and negatively charged when occupied. The energy level separating these two types is called the neutrality level, $q\phi_0$. The Fermi level of the surface will therefore coincide with this level at a neutral surface. This semiconductor surface is interfaced with a metal surface such that they are separated by a gap of atomic dimensions. The gap will be transparent to electrons but large enough to contain a small potential drop.

Let us consider a case where negative charge is trapped at the interface due to acceptor states of the semiconductor which became occupied when the semiconductor was interfaced with the metal. This means that the Fermi level is above the charge neutrality level as seen on Figure 7.4. The

charge density of these interface charge traps is,

$$\sigma_{ifs} = -qD_{ifs}(\varepsilon_F - q\phi_0) = -qD_{ifs}(E_g - q\phi_0 - \Phi_n).$$

The space charge inside the depletion region of the semiconductor is given by,

$$\sigma_{sc} = qN_{3D}x_D = \sqrt{2\varepsilon_s N_{3D}\Delta V}.$$

The sum of the charge density on the semiconductor side of the interface is therefore the sum of the trapped charge and the charge in the depletion region. In the metal, an equal and opposite charge is induced, $\sigma_m = -(\sigma_{ifs} + \sigma_{sc})$. The potential inside the small gap at the interface, δ, is

$$\Delta = -\frac{\delta\sigma_m}{\varepsilon_i} = \phi_m - (\chi + \Phi_n/q) \Rightarrow$$
$$\Phi^{SM} - \Phi_n = q\sqrt{\frac{2\varepsilon_s N_{3D}\Delta V\delta^2}{\varepsilon_i^2}} - \frac{q^2 D_{ifs}\delta}{\varepsilon_i}(E_g - q\phi_0 - \Phi_n).$$

It has been used that $\Phi^{SM} = q(\phi_m - \chi)$ and the dielectric constant of the interface region is defined as ε_i. The barrier height becomes,

$$\Phi_n = \frac{\varepsilon_i}{\varepsilon_i + q^2 D_{ifs}\delta}\Phi^{SM} + \frac{q^2 D_{ifs}\delta}{\varepsilon_i + q^2 D_{ifs}\delta}(E_g - q\phi_0)$$
$$= S\Phi^{SM} + (1 - S)(E_g - q\phi_0)$$

The term related to the charge in the depletion region, $q\sqrt{\frac{2\varepsilon_s N_{3D}\Delta V\delta^2}{\varepsilon_i^2}}$, is small unless the doping is very high and has been neglected. S is known as the pinning factor. For $S = 1$, there is no Fermi level pinning and the barrier is determined by the Schottky-Mott rule. This limit corresponds to $D_{ifs} \to 0$. If $S = 0$ the Fermi level is completely pinned, and the barrier height equals the difference between the band gap and the charge neutrality level. This limit corresponds to $D_{ifs} \to \infty$. The same expressions can be derived for a 2D Schottky contact since the charge density in the

> **Box 7.1.1: 2D interface**
>
> $$\lambda_{ifs} = -qD_{ifs}(\varepsilon_F - q\phi_0) = -qD_{ifs}(E_g - q\phi_0 - \Phi_n).$$
>
> $$\lambda_{sc} = qN_{2D}x_D = \frac{\pi\varepsilon_{eff}\Delta V}{q\ln 4}.$$
>
> $$\Delta = -\frac{\delta\sigma_m}{\varepsilon_i} = \phi_m - (\chi + \Phi_n/q) \Rightarrow$$
>
> $$\Phi^{SM} - \Phi_n = \frac{\pi\varepsilon_{eff}\Delta V\delta}{\ln 4\varepsilon_i} - \frac{q^2 D_{ifs}\delta}{\varepsilon_i}(E_g - q\phi_0 - \Phi_n).$$
>
> The term $\frac{\pi\varepsilon_{eff}\Delta V\delta}{\ln 4\varepsilon_i}$ is neglected,
>
> $$\Phi_n = \frac{\varepsilon_i}{\varepsilon_i + q^2 D_{ifs}\delta}\Phi^{SM} + \frac{q^2 D_{ifs}\delta}{\varepsilon_i + q^2 D_{ifs}\delta}(E_g - q\phi_0)$$
> $$= \Phi_n = S\Phi^{SM} + (1 - S)(E_g - q\phi_0).$$

depletion region, which is the term with all the dimensionality dependent parameters, is even smaller in the 2D case. The derivation is shown in Box 7.1.1.

Since Φ^{SM} is proportional to the metal work function, the pinning factor can be determined by measuring the barrier height between the same semiconductor interfaced with different metals. The Schottky contact between few or single layered TMDs and different 3D metals are systems which have turned out to be highly dominated by Fermi level pinning. MoS_2 has a pinning factor of ≈ 0.3 and a pinning factor of only 0.07 has been measured for monolayer $MoTe_2$.[19,21]

The image force effect and Fermi level pinning are two well-known effects which may alter the barrier size in a reasonably predictable manner. However, many other effects can alter the barrier as well. Most noteworthy, is perhaps the possibility of charged defects or impurities at the interface which will change the field and thereby the barrier height. When combining two materials to an interface, contamination of the interface region is difficult and expensive to avoid. 3D interfaces are not that vulnerable to such defects since the interface spans a large region of space and a low concentration of defect will not change the overall behavior.

In 2D, where the interface is atomically thin, much lower concentrations of defects will alter the interface properties. Local stress and strain may also result in small fields which can alter the barrier height and, finally, a non-uniform doping will also affect the barrier.

This concludes the part concerning Schottky contacts in equilibrium. The next section will explain the theory behind charge transfer across a Schottky contact which is the basis for understanding how field effects transistors operate.

7.2   Charge Transfer Mechanisms

If a bias is applied across a Schottky contact, an electron current can be driven from the semiconductor to the metal (forward bias). The charge transport at a Schottky contact primarily occurs through the 4 mechanisms illustrated on Figure 7.5.

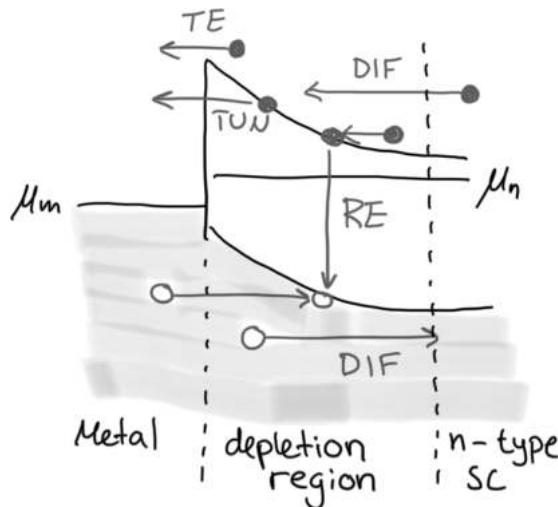1. Thermionic emission (TE)

2. Tunneling (TUN)

Figure 7.5: The 4 charge transport mechanisms at a Schottky barrier; Thermionic emission (TE), tunneling (TUN), recombination in the depletion region (RE), and diffusion (DIF). Inspired by Ref. [108].

3. Recombination in the depletion region (RE)

4. Diffusion (DIF)

Thermionic emission occurs when thermal excitation of the carriers allows them to be transported over the barrier. This is the dominating transport mechanism for 3D semiconductors with a high mobility such as Si and GaAs as long as the Schottky barrier is significantly larger than $k_B T$. Quantum mechanical tunneling of electrons through the barrier is the second transport mechanism. This dominates in the 2D Schottky contacts of heterophase MoTe$_2$ which will be the subject of the next chapter. Recombination of an electron in the conduction band with a hole from the metal side also leads to a current. Recombination processes are not treated directly here but can be inferred trough an ideally constant which is briefly discussed in the section on thermionic emission. Diffusion of carriers in and out of the depletion region is the final transport mechanism. Transport by diffusion of carriers is mostly relevant for low mobility semiconductors and is out of the scope of this thesis. See e.g. Ref. [108] Section 3.3 on this subject.

7.2.1 Thermionic Emission

An n-type Schottky barrier at forward and backwards bias is illustrated on Figure 7.6. The forward bias, V, raises the electronic levels of the semiconductor by qV compared to the metal Fermi level whereas a backwards bias lowers the levels. The built-in potential in both cases becomes $\Delta V = \Phi_n - q\phi_n - qV$. Let us assume that for a given system, thermionic emission is the dominating current transport mechanisms and that the system is in thermal equilibrium even though a net current is running. The total current can be found as a sum of the current running from the semiconductor to the metal and the current running in the opposite direction. The current density towards the metal is determined by the availability of electrons which have sufficient energy to overcome the barrier height, $\mu_n + \Phi_n - qV$,

$$J_{s \to m}^{TE} = \int_{\mu_n + \Phi_n - qV}^{\infty} q v_x \, \mathrm{d}n.$$
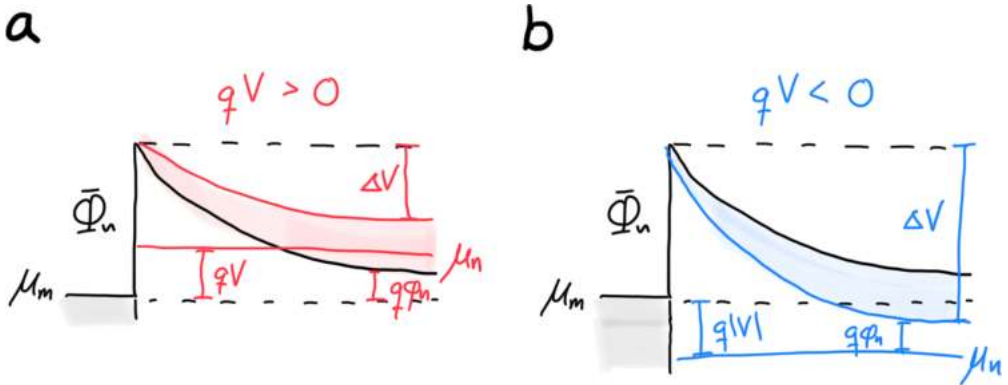
Figure 7.6: A n-type Schottky contact at **a** forward and **b** backwards bias. μ_m and μ_n are the chemical potentials of the metal and semiconductor respectively, Φ_n is the barrier height from the metal to the semiconductor and $\Phi_n - qV$ is the barrier height from the semiconductor to the metal.

v_x is the electron velocity in the x-direction and n is the electron density. The change in electron density with energy is,

$$\frac{\mathrm{d}n}{\mathrm{d}E} = D(E)f(E + q\phi_n) = \frac{1}{2\pi^2}\left(\frac{2m_e^*}{\hbar^2}\right)^{3/2}\sqrt{E}f(E + q\phi_n)$$

$$\approx \frac{1}{2\pi^2}\left(\frac{2m_e^*}{\hbar^2}\right)^{3/2}\sqrt{E - \varepsilon_{CB}}\exp\left(-\frac{E - \varepsilon_{CB} + q\phi_n}{k_BT}\right).$$

Box 7.2.1: 2D interface

$$\frac{\mathrm{d}n_{2D}}{\mathrm{d}E} = D_{2D}(E)f(E + q\phi_n)$$

$$\approx \frac{m_e^*}{\pi\hbar^2}\exp\left(-\frac{E - \varepsilon_{CB} + q\phi_n}{k_BT}\right).$$

$$\frac{\mathrm{d}n_{2D}}{\mathrm{d}v} = \frac{(m_e^*)^2}{\pi\hbar^2}\exp\left(-\frac{q\phi_n}{k_BT}\right)\exp\left(-\frac{m_e^*v^2}{2k_BT}\right)v.$$

The Fermi distribution function has been approximated by $f(E) = 1/(1 + \exp(E/k_B T)) \approx \exp(-E/k_B T)$ assuming that $E >> k_B T$. $D(E)$ is the density of states of a 3D electron gas, m_e^* is the effective electron mass in the semiconductor, $\hbar$ is the reduced Planck's constant, and ε_{CB} is the conduction band minima. Assuming that the energy of the electron in the conduction band is kinetic, the following can be used to rewrite the expression for $\mathrm{d}n$,

$$E - \varepsilon_{CB} = \frac{1}{2} m_e^* v^2 \Rightarrow \frac{\mathrm{d}E}{\mathrm{d}v} = m_e^* v \Rightarrow$$

$$\frac{\mathrm{d}n}{\mathrm{d}v} = \frac{1}{\pi^2} \left(\frac{m_e^*}{\hbar} \right)^3 \exp\left(-\frac{q\phi_n}{k_B T} \right) \exp\left(-\frac{m_e^* v^2}{2k_B T} \right) v^2.$$

using that $v^2 = v_x^2 + v_y^2 + v_z^2$ and $4\pi v^2 \, \mathrm{d}v = \mathrm{d}v_x \mathrm{d}v_y \mathrm{d}v_z$,

$$J_{s \to m}^{TE} = \frac{q}{4\pi^3} \left(\frac{m_e^*}{\hbar} \right)^3 \exp\left(-\frac{q\phi_n}{k_B T} \right) \int_{v_{0x}}^{\infty} v_x \exp\left(-\frac{m_e^* v_x^2}{2k_B T} \right) \, \mathrm{d}v_x \times$$

$$\int_{-\infty}^{\infty} \exp\left(-\frac{m_e^* v_y^2}{2k_B T} \right) \, \mathrm{d}v_y \int_{-\infty}^{\infty} \exp\left(-\frac{m_e^* v_z^2}{2k_B T} \right) \, \mathrm{d}v_z$$

$$= \frac{q m_e^* k_B^2}{2\pi^2 \hbar^3} \, T^2 \, \exp\left(-\frac{\Phi_n}{k_B T} \right) \exp\left(\frac{qV}{k_B T} \right).$$

Box 7.2.2: 2D interface

$$\text{Using } v^2 = v_x^2 + v_y^2 \text{ and } 2\pi v \, \mathrm{d}v = \mathrm{d}v_x \mathrm{d}v_y,$$

$$J_{s \to m}^{TE} = A_{2D}^* \, T^{3/2} \, \exp\left(-\frac{\Phi_n}{k_B T} \right) \exp\left(\frac{qV}{k_B T} \right).$$

$$A_{2D}^* = \sqrt{\frac{m_e^*}{2}} \frac{q k_B^{3/2}}{\pi^{3/2} \hbar^2}.$$

---

where v_{0x} is the velocity required to overcome the barrier, $\Phi_n - qV = \frac{1}{2} m_e^* v_{0x}^2$. The pre-factor $A^* = \frac{q m_e^* k_B^2}{2\pi^2 \hbar^3}$ is called the effective Richardson constant. If the electrons are free, the value is $A^*(m_0) = A = 120$ A cm^{-2} K^{-2}. The corresponding derivations for a 2D Schottky contact are shown

in Box 7.2.1 and 7.2.2 and agree with the derivations by Ang et al.[112] using a different approach. The 2D effective Richardson constant of free electrons is $A_{2D}^*(m_0) = A_{2D} = 0.895$ mA cm^{-1} K$^{-3/2}$.

Assuming that the barrier from the metal to the semiconductor is unaffected by the bias, the current running in that direction must be independent on the bias as well. Without any applied bias, the system is in equilibrium and no net current is running,

$$J_{eq}^{TE} = J_{s \to m}(V = 0) + J_{m \to s} = 0 \Rightarrow$$

$$J_{m \to s}^{TE} = -A^* \, T^2 \, \exp\left(-\frac{\Phi_n}{k_B T}\right).$$

The total current out of equilibrium is then,

$$I_{3D}^{TE} = A_\perp A^* \, T^2 \, \exp\left(-\frac{\Phi_n}{k_B T}\right) \left(\exp\left(\frac{qV}{k_B T}\right) - 1\right). \tag{7.3}$$

$$I_{2D}^{TE} = W_\perp A_{2D}^* \, T^{3/2} \, \exp\left(-\frac{\Phi_n}{k_B T}\right) \left(\exp\left(\frac{qV}{k_B T}\right) - 1\right). \tag{7.4}$$

$A_\perp$ and $W_\perp$ are the area and width of the contact perpendicular to the transport direction. At negative biases, a small current will run from the metal to the semiconductor and at positive biases, the current will run from the semiconductor to the metal and rise exponentially with the bias. These expressions are derived for n-type semiconductors, for p-type semiconductors, holes are the majority carriers. The main electron current will run in the opposite direction (metal to semiconductor) when a negative bias is applied. This corresponds to a negative sign in front of the total current and the bias in the expressions in eq. (7.3) and (7.4).

Charge transfer due to recombination in the depletion region is sometimes included in these expressions as an ideality factor. The ideality factor, η, is unity if no recombination occur in the depletion region and increases as this effect becomes more dominant. The factor is included in the exponential dependence of the bias as $\exp(qV/\eta k_B T)$. The ideality factor is sometimes also used to include the effect of tunneling. As we shall see in the following, this might not be completely justified.

The difference between the 2D and 3D expression is most pronounced in the different temperature dependency. For free electrons at 300 K,

the prefactor of the 2D thermionic current is 4.65 A cm^{-1} and the 3D prefactor, using a thickness of 1 nm, is 1.08 A cm^{-1}. This illustrates that the total amount of thermionic current does not differ that much between comparable 2D and 3D contacts.

7.2.2 Tunneling

Besides transport of thermally excited electrons, a large contribution to the current can arise from the quantum mechanical tunneling of electrons through the Schottky barrier. In this section, I will derive expressions for the current due to tunneling using the Landuer formula. The electron current is the tunneling probability times the difference in occupation functions of the metal and semiconductor,

$$
\begin{aligned}
I^{TUN} &= \frac{2q}{h} \int_{\mu_n}^{\Phi_n - \mu_m} T(E, \mu_n, \mu_m) \left[f\left(\frac{E - \mu_n}{k_B T} \right) - f\left(\frac{E - \mu_m}{k_B T} \right) \right] \mathrm{d}E \\
&\approx \frac{2q^2 V}{h k_B T} \int_0^{\Phi_n - qV} T(E, 0, -qV) \exp\left(-\frac{E}{k_B T} \right) \mathrm{d}E.
\end{aligned}
$$

μ_n and μ_m are the Fermi levels of the semiconductor and the metal, $\mu_m - \mu_n = qV$. In the second line, the energy zero point has been set at the Fermi level of the semiconductor and the difference in the Fermi functions has been approximated assuming that $qV >> k_B T$ and $E >> k_B T$ which is valid at forward bias and barriers significantly larger than $k_B T$. The tunneling probability can be found using the Wentzel–Kramers–Brillouin (WKB) method[113] and by approximating the potential as a triangular barrier,

$$
T(E) = \exp\left(-2\sqrt{\frac{2m_e^*}{\hbar^2}} \int_{x_{cl}}^{x_D} \sqrt{\phi(x) - E}\, \mathrm{d}x \right),
$$
$$
\phi(x) = q\phi_n - qV + \frac{\Phi_n - qV - q\phi_n}{x_D} x.
$$

x_{cl} is the classical turning point of the barrier and $\phi(x)$ is the potential in units of energy. This results in,

$$T(E) = \exp\left(-\frac{4}{3}\sqrt{\frac{2m_e^*}{\hbar^2}}\frac{x_D}{\Phi_n - qV - q\phi_n}(\Phi_n - qV - E)^{3/2}\right).$$

Reintroducing the built-in potential, $\Delta V = \Phi_n - qV - q\phi_n$, and using the expression for x_D in Table 7.1, the tunneling current becomes

$$I^{TUN} \approx \frac{2q^2V}{hk_BT}\int_0^{\Phi_n - qV}\exp\left(-\frac{2}{3}\frac{(\Phi_n - qV - E)^{3/2}}{E_{00}\sqrt{\Delta V}} - \frac{E}{k_BT}\right)dE. \quad (7.5)$$

$$E_{00} = \frac{q\hbar}{4}\sqrt{\frac{N_{3D}}{m_e^*\varepsilon_s}}.$$

To get some insights, we can look at the energy where the tunneling current has the maximum contribution, i.e. where the term inside the integral is maximized,

$$E_{max} = \Phi_n - qV - \left(\frac{E_{00}}{k_BT}\right)^2\Delta V$$

$$= (\Phi_n - qV)\left(1 - \left(\frac{E_{00}}{k_BT}\right)^2\right) + q\phi_n\left(\frac{E_{00}}{k_BT}\right)^2.$$

Box 7.2.3: 2D interface

$$T_{2D}(E) = \exp\left(-\frac{4}{3}\sqrt{\frac{2m_e^*}{\hbar^2}}\frac{\pi\varepsilon_{eff}}{q^2N_{2D}\ln 4}(\Phi_n - qV - E)^{3/2}\right).$$

$$E_{max} = \Phi_n - qV - \left(\frac{E_{00}^{2D}}{k_BT}\right)^2.$$

$$E_{00}^{2D} = \frac{q^2N_{2D}\ln 4}{2\pi\varepsilon_{eff}}\sqrt{\frac{\hbar^2}{2m_e^*}}.$$

If $E_{00} << k_BT$, the system is dominated by thermionic emission and tunneling contributions are primarily from tunneling near the top of the

barrier. On the other hand, if $E_{00} \approx k_B T$, the tunneling contributions are primarily at the conduction band of the semiconductor. If $N_{3D} = 10^{18}$ cm $^{-3}$, $\varepsilon_s = 10\varepsilon_0$ and $m_e^* = m_0$, then $E_{00} = 2.9$ meV and a doping level of $N_{3D} = 10^{19}$ cm $^{-3}$ will correspond to $E_{00} = 9.3$ meV.

A corresponding derivation using the 2D depletion width from Table 7.1 is shown in Box 7.2.3. The result is the same but with the difference that $E_{00}^{3D}\sqrt{\Delta V} \rightarrow E_{00}^{2D}$ which means that the current becomes independent on the built-in potential. The tunneling though a 2D Schottky contact is therefore primarily dominated by the doping level and the dielectric constant of the surroundings. The energy of maximum transmission is lowered from the top of the barrier by $(E_{00}^{2D}/k_B T)^2$. The unit of E_{00}^{2D} is eV$^{3/2}$ and if $N_{2D} = 10^{12}$ cm $^{-2}$, $\varepsilon_{eff} = 3.9\varepsilon_0$, $m_e^* = m_0$, and $T = 300$ K, then $(E_{00}^{2D}/k_B T)^2 = 6.0$ meV whereas a doping level of $N_{2D} = 10^{13}$ cm $^{-2}$ results in a value of 0.60 eV.

E_{max} decreases from the top of the barrier linearly with the doping level in 3D but quadratically in 2D. Tunneling therefore becomes relatively more probable in 2D contacts compared to 3D for medium and high doping levels. Since E_{max} also depends on the built-in potential in 3D, the difference between 2D and 3D will be increased even further.

The integral in eq. (7.5) can be approximated using the method of steepest descent. This is carried out in Appendix C Section C.2 and results in

$$I_{3D}^{TUN} \approx A_{3D}^{TUN} \frac{qV\sqrt{\Delta V}}{T^{3/2}} \exp\left(\frac{E_{00}^2}{3(k_B T)^3}\Delta V\right) \exp\left(-\frac{\Phi_n}{k_B T}\right) \exp\left(\frac{qV}{k_B T}\right).$$

$$A_{3D}^{TUN} = \frac{2q}{h}\frac{E_{00}}{k_B^{3/2}}\sqrt{4\pi} = \frac{q^2}{k_B^{3/2}}\sqrt{\frac{N_{3D}}{4\pi m_e^* \varepsilon_s}}.$$

The 2D expression is shown in Box 7.2.4. A^{TUN} is an effective tunneling constant which is $A_{3D}^{TUN}(m_0) = 1.0$ A K$^{3/2}$ eV$^{-3/2}$ and $A_{2D}^{TUN}(m_0) = 0.69$ A K$^{3/2}$ eV^{-1} using the same parameters as the estimation of E_{00}. Compared to the thermionic current, the tunneling current has a very different dependence on the temperature. This can have some importance when attempting to measure a Schottky barrier which I will return to in the following section. The dependence on the applied bias is similar to the expressions for the thermionic current which makes this model con-

> **Box 7.2.4: 2D interface**
>
> $$I_{2D}^{TUN} \approx A_{2D}^{TUN} \frac{qV}{T^{3/2}} \exp\left(\frac{(E_{00}^{2D})^2}{3(k_B T)^3} \right) \exp\left(-\frac{\Phi_n}{k_B T} \right) \exp\left(\frac{qV}{k_B T} \right).$$
>
> $$A_{2D}^{TUN} = \frac{2q}{h} \frac{E_{00}^{2D}}{k_B^{3/2}} \sqrt{4\pi} = \frac{q^3}{k_B^{3/2}} \frac{N_{2D} \ln 4}{\pi \varepsilon_{eff}} \sqrt{\frac{1}{2\pi m_e^*}}.$$

tradicts the idea of defining an ideally factor to include the tunneling contributions.

This concludes the part describing the charge transfer methods. The investigations have concluded that thermionic emission follows a different temperature dependence in 2D compared to 3D but comparable values are expected around room temperature and that tunneling is more probable in 2D than in 3D at high or intermediate doping levels.

7.3   Barrier Extraction Methods

The Schottky barrier height may be determined using a range of different approaches. Current-voltage (IV) measurements can be used to obtain the barrier directly from eq. (7.3), assuming that thermionic emission is the dominating transport mechanism,

$$\Phi_n = \frac{q}{k_B T} \ln\left(\frac{A_\perp A^* T^2}{J_0} \right),$$

where J_0 is the saturation current density which can be found by extrapolating the current value corresponding to zero bias. This method requires that the contact area and effective Richardson constant are known. If these quantities are difficult to estimate, the activation energy method can be applied. This method still assumes that thermionic emission is the dominating transport mechanism and relies on eq. (7.3) and (7.4) which can be rewritten as,

$$\ln(I_{3D}/T^2) = \ln(A_\perp A^*) - \frac{\Phi_n - qV}{k_B T}. \tag{7.6}$$

$$\ln(I_{2D}/T^{3/2}) = \ln(W_\perp A_{2D}^*) - \frac{\Phi_n - qV}{k_B T}. \tag{7.7}$$

The barrier height is extracted by measuring the current in a range of different temperatures and extracting the slope in an Arrhenius plot of eq. (7.6) or (7.7) vs. 1/T. The barrier height becomes $\Phi_{n/p}^{\text{TE}} = \pm qV - \alpha k_B$ for n- or p-type devices respectively where α is the slope. As mentioned above, this model assumes a purely thermionic current. However, many metal-semiconductor junctions form barriers where the current will have contributions from both thermal excitation of electrons and tunneling. Suppose that the Schottky diode is dominated by tunneling rather than thermionic emission, then

$$\ln(I_{3D}/T^2) = \ln(A_{3D}^{TUN} qV \sqrt{\Delta V})$$
$$+ \frac{7}{2}\ln(1/T) - \frac{\Phi_n - qV}{k_B T} + \frac{E_{00}^2}{3(k_B T)^3}\Delta V.$$
$$\ln(I_{2D}/T^{3/2}) = \ln(A_{2D}^{TUN} qV) + 3\ln(1/T) - \frac{\Phi_n - qV}{k_B T} + \frac{(E_{00}^{2D})^2}{3(k_B T)^3}.$$

The barrier height will therefore be underestimated by,

$$\Delta\Phi_{3D}^{TE} = \frac{7}{2}k_B T + \frac{(E_{00}^{3D})^2}{3(k_B T)^2}\Delta V \approx 98 \text{ meV} + 1.4 \times 10^{-3}\Delta V. \tag{7.8}$$

$$\Delta\Phi_{2D}^{TE} = 3k_B T + \frac{(E_{00}^{2D})^2}{3(k_B T)^2} \approx 78 \text{ meV}. \tag{7.9}$$

These estimates are made at 300 K and using the same values for the doping and dielectric constants as in the previous section. The numbers represent an upper bound for the underestimation of the barrier since most Schottky contact will have contributions from both tuneling and thermionic emission and the estimated barrier height using the activation energy method will lie between Φ and $\Phi - \Delta\Phi^{TE}$.

The most commonly applied experimental method for measuring the Schottky barrier in 2D devices is the activation energy method.[79,80,89,91,114–116]

Other methods worth mentioning are: measuring the capacitance-voltage relationship or generating a photocurrent by illumination of the sample. The relationship between the photocurrent and the energy of the adsorbed photons can be used to obtain the barrier height. Finally, the barrier can be measured using Kelvin Probe Force Microscopy (KPFM) which has been used to measure the barrier height of 2D Schottky contacts as well.[92]

KPFM is a method using the same principles as atomic force microscopy. A probe is electrically contacted to a sample and scanned across the surface. The electrical contact align the Fermi levels of the probe and sample giving rise to charge accumulation and creating a potential drop in the vacuum region between the probe and sample. The potential drop equals the difference in workfunction. Both a direct-current voltage, V_{bias}, and an alternating-current voltage $V_{AC}\sin(\omega t)$, is then applied between the probe and sample. The total potential difference becomes,

$$V = V_{bias} - (\phi_{probe} - \phi_{sample}) + V_{AC}\sin(\omega t),$$

where $q(\phi_{probe} - \phi_{sample})$ is the difference in workfunction between the probe and sample. The accumulated charge creates an electrostatic force between the probe and sample,

$$F = \frac{1}{2}\frac{\mathrm{d}C}{\mathrm{d}z}V^2,$$

where C is the capacitance and z is the distance between the probe and sample. Due to this force, the probe will oscillate above the surface. The oscillation will have a component with frequency ω and a component with frequency 2ω. The bias is adjusted to counteract the oscillation with frequency ω, which corresponds to $V_{bias} = \phi_{probe} - \phi_{sample}$ and reveals the difference in workfunction between the sample and probe. If the probe is scanned across a Schottky contact, a plot of the counteracting bias vs. the probe position will show the change in workfunction across the barrier. The difference between the value at the metal side and the semiconductor side will equal the built-in potential of the Schottky contact. This method therefore probes the barrier within the Schottky-Mott limit.

7.3.1 Barrier Calculation Methods

In this thesis, density functional theory (DFT) and the non-equilibrium Green's function (NEGF) method are used to calculate Schottky barrier heights of different 2D metal-semiconductor contacts. The barrier height can be extracted from the work difference, from the projected density of states (DOS) along the transport direction, from the transmission spectrum (TS), or using the activation energy method and the calculated current. The two three methods can be performed using equilibrium DFT calculations whereas the last one requires a NEGF calculation. When calculated Schottky barriers are reported in the remainder of this thesis, the barriers are defined as in Ref. [22]:

The SM barrier, Φ^{SM}, is extracted from the work difference between the two isolated crystals and represents the barrier height within the Schottky-Mott limit.

The DOS barrier, Φ^{DOS}, is extracted from the projected DOS as the distance between the Fermi level and the maximum (minimum) of the conduction (valence) band for the n-type (p-type) devices. Φ^{DOS} therefore includes the band bending due to the electric field created by the interface dipole. This is a macroscopic electrostatic effect ranging over many atomic layers.

The TS barrier, Φ^{TS}, is defined as the distance between the Fermi level and the energy at which the device experience full transmission, defined as 1% of maximum transmission.[i] Φ^{TS} represents a microscopic quantity that depends directly on the electronic states available for transport.

The TE barrier, Φ^{TE}, is found by applying the activation energy method to find the barrier from the temperature dependence of the current using eq. (7.6) and (7.7). This method therefore assumes that the current is dominated by coherent transport of thermally excited electrons above the Schottky barrier.

---

[i]The threshold of full transmission is discussed in Ref. [22].

Ab-initio Modelling of Heterophase MoTe$_2$ Contacts

This chapter illustrates some of the rich physics which takes place at the interface between T'- and H-phase MoTe$_2$. The Schottky barrier which is formed between the two phases is highly dominated by the local atomic configuration at the phase boundary and by the density of states at the interface. States in the interface are present at all of the investigated phase boundaries and originates from the T'-phase. The states are either metal induced gap states or resonances originating from T' edge states. Both types of interface states greatly affect the charge transport leading to lower Schottky barriers. The first section will illustrate how the atomic positions at the boundary can change the barrier height by more than 0.6 eV and the depletion width by more than 3 nm's. The next section dives into the role and origin of the interface resonances and the last part demonstrates how the electrostatic response is affected by the interface states as well. The objective of these investigations is to gain a better understanding of the charge transport mechanisms across these heterophase contacts and the main conclusion is that they are dominated by quantum mechanical effects.

8.1   Variation with Phase Boundaries

This section will illustrate how the atomic rearrangements, potential profile, and charge transport properties show large variations across different phase-boundaries between the T'- and H-phase. As discussed in Section
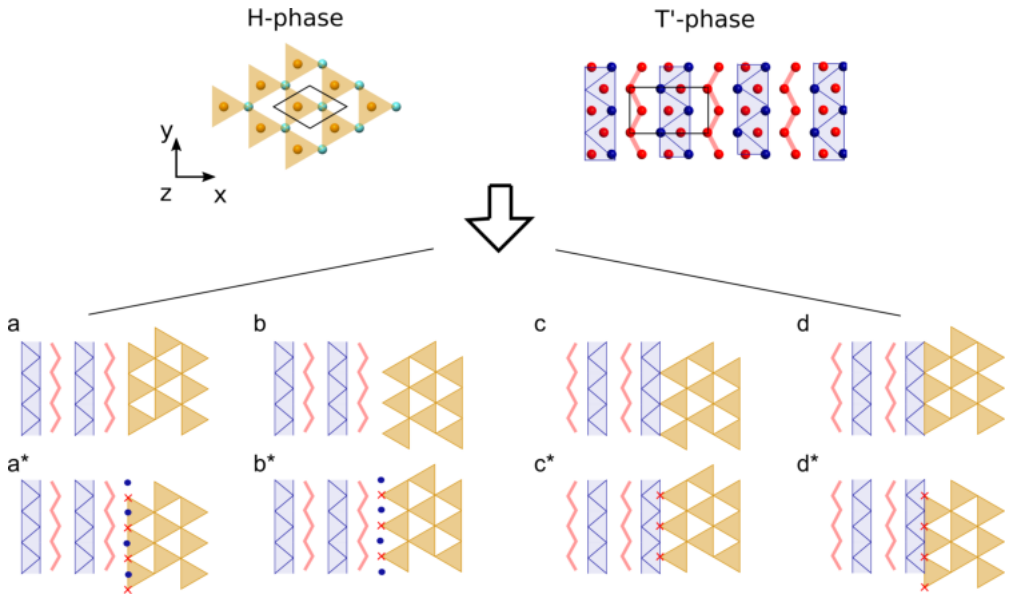
Figure 8.1: The eight possible phase boundaries along the zigzag direction between H- and T'-phase TMDs. Yellow triangles represent the H-phase geometry and red and blue zigzag chains represent the T' geometry. The metal atoms are placed at the corners of the blue and yellow triangles. In the lower panel, red crosses mark a triangle corner without a metal atom and blue circles mark metal atoms placed away from a triangle corner.

6.1.1, phase boundaries of T'-H MoTe$_2$ have primarily been observed to form either along the zigzag direction of both phases or at a 60 degrees angle between these directions. DFT calculations by Li *et al.*[117] on 12 different interface geometries along the zigzag direction have shown that the interfaces which conserve the local atomic structure of the two phases close to the interface result in the most stable configurations. Phase-boundaries along the zigzag direction which conserve the stoichiometry of the two phases are therefore of interest. Eight such unique boundaries can be made, as illustrated on Figure 8.1.

The properties presented in this section are all calculated without including the spin-orbit coupling since neither the atomic rearrangements nor the charge transport are expected to depend significantly on this. The T'-phase is therefore a semi-metallic phase with a Dirac cone between the

X- and Γ-point as illustrated on Figure 4.3c.

As a starting point, let us consider the stability of these phase boundaries. The stability can be calculated using nanoribbon configurations of the eight boundaries consisting of an H-phase edge, an H-phase region, the phase boundary, a T'-phase region, and a T'-phase edge. The unit cell is doubled in the y-direction which allows for a small stabilizing distortion at some of the boundaries. In order to match the unit cells, the T'-phase is strained by 2.12 % along the y direction to make a match between the (200)-edge of T' and the (02-20)-edge of H. The details on how the interfaces are build are outlined in Appendix A.2.

The total energy of such a nanoribbon can be divided into the following contributions,

$$E^{ribbon} = n_{T'}E^{T'} + n_H E^H + W(E_F^{edge(T')} + E_F^{edge(H)} + E_F^{boundary}).$$

W is the width of the ribbon in the x-direction, E^{ribbon} is the total energy of the ribbon, and $n_{T'}E^{T'}$ and $n_H E^H$ are the energies of $n_{T'}$ and n_H unit cells of the T'- and H-phase, respectively. $E_F^{edge(T')}$, $E_F^{edge(H)}$, and $E_F^{boundary}$ are the heat of formations of the edges terminating the nanoribbons and the phase boundary pr. unit length of the edge or boundary.

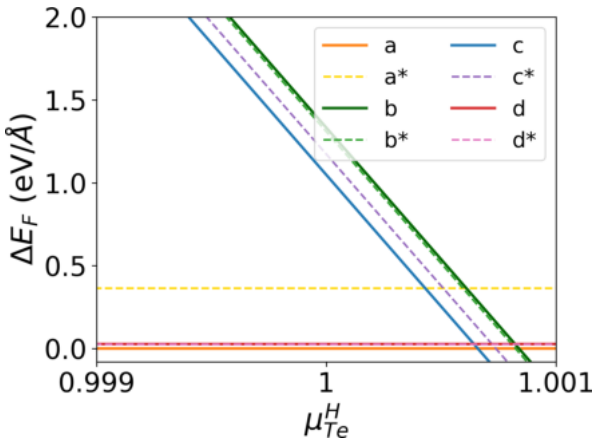|			
ΔE_{int}^a	Ref	ΔE_{int}^{a*}	0.364
ΔE_{int}^b	1.33	ΔE_{int}^{b*}	1.31
ΔE_{int}^c	1.05	ΔE_{int}^{c*}	1.17
ΔE_{int}^d	0.0273	ΔE_{int}^{d*}	0.0263

Figure 8.2: The relative stability of the eight phase boundaries between H- and T'-phase MoTe$_2$ as a function of the chemical potential of tellurium in the H-phase.

Table 8.1: Relative stability in eV/Å of the eight phase boundaries at $\mu_{Te}^H = 1$.

Note, that the edges are fixed in the crystal structure of the 2D crystal. The energy of the free edges of each phase must be subtracted in order to isolate the formation energy of the phase boundaries. The energy of the free edges can be found from T'-phase nanoribbons and H-phase triangular nanoparticles and are dependent on the chemical potential of tellurium. The expressions for the stabilities are derived in Appendix B.2 and the results are illustrated on Figure 8.2 relative to the most stable interface at $\mu_{Te}^H = 1$. This corresponds to Te atoms at the same chemical potential as in a tellurium alpha crystal. At Mo-rich or intermediate conditions, $\mu_{Te}^H \leq 1$, the a- d- and d* boundaries are most stable whereas in Te-rich conditions, $\mu_{Te}^H > 1$, the c and c* boundaries become the most stable. The stabilities at $\mu_{Te}^H = 1$ are summarized in Table 8.1.

These stabilities assume a that the position of the interface is exactly between the atoms which originally belonged to the H-phase on one side and the T'-phase on the other. This is justified since the energy of the T'- and H-phase unit cells only differs by 11 meV/atom such that shifting the interface position a few atomic layers will have limited impact on the formation energy.
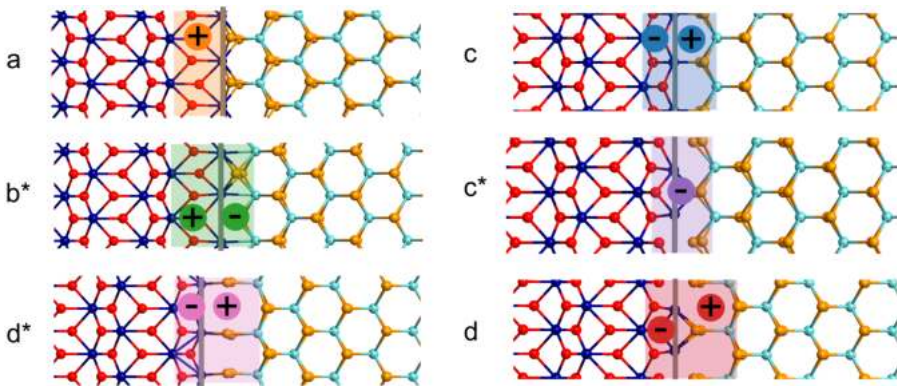
Figure 8.3: Charge redistribution due to the rearrangement of atoms at the six phase boundaries. The colored charges represent the trend due to atomic rearrangements at the boundaries. '-' signs represent a region where the atoms have been pushed closer together and '+' signs represent a region where the atoms are further apart compared to the original crystal structure. The grey vertical line marks the boundary and is placed at the rightmost atom of the T'-phase.

In the following, I will describe the trends in the charge transfer prop-
erties of the six types of boundaries, a, b*, c, c*, d and d*. The effective
potential perpendicular to the transport direction contains information on
the charge transfer since this is the potential that the charge carriers must
overcome in order to be transmitted across the phase boundary. However,
the potential is difficult to interpret since two contributions are coupled;
the change in potential due to atomic rearrangements at the boundary and
the potential from the interface dipole. To interpret the potential profile,
it can therefore be instructive to inspect the atomic rearrangements at
the relaxed boundary first. The relaxed boundaries are shown on Figure
8.3. Areas where atoms have been pushed further apart compared to the
position in the 2D crystal are marked by a '+' charge. The electron gas is
thin in these areas compared to the electron gas in the undistorted crystal.
Likewise, areas where the atoms have been pushed closer are marked by
a '-' charge.

The transport properties across the phase boundaries can be investi-
gated by using DFT+NEGF calculations and converting the nanoribbons
into device configurations which have an H and T' electrode and a cen-
tral region with the phase boundary. Details on this procedure and the
calculations are explained in Appendix A.2. Figure 8.4 shows effective
potentials both for p- and n-doping with $N_{D/A} = 4.6 \times 10^{12}$ cm^{-2}. The
doping has been added to atoms which originally belonged to the H-phase.

The effective potential is the sum of the Hartree potential, the exchange-
correlation potential, and the electrostatic potential of the ions. To avoid
including the effects of the potential drop in the vacuum region, the poten-
tials have been averaged over a strip placed 4 Bohr radii above the highest
positioned atom, z_{max}, and 4 Bohr radii below the lowest positioned atom,
z_{min},

$$V_{eff}(x) = \frac{1}{W(z_{max} - z_{min})} \int_{z_{min}}^{z_{max}} \int V_{eff}(x, y, z) \, \mathrm{d}y \, \mathrm{d}z. \qquad (8.1)$$

Gaussian functions have been used to remove the fluctuations at the
atomic positions. Note, that the value of the potentials at the left bound-
ary should be equal, but isn't, due to the difference in how much the
nanoribbon buckle at the phase boundary. The buckling creates different
z off-sets between the two phases and gives a slightly different average.
Since the plots are used to investigate the change in potential at the
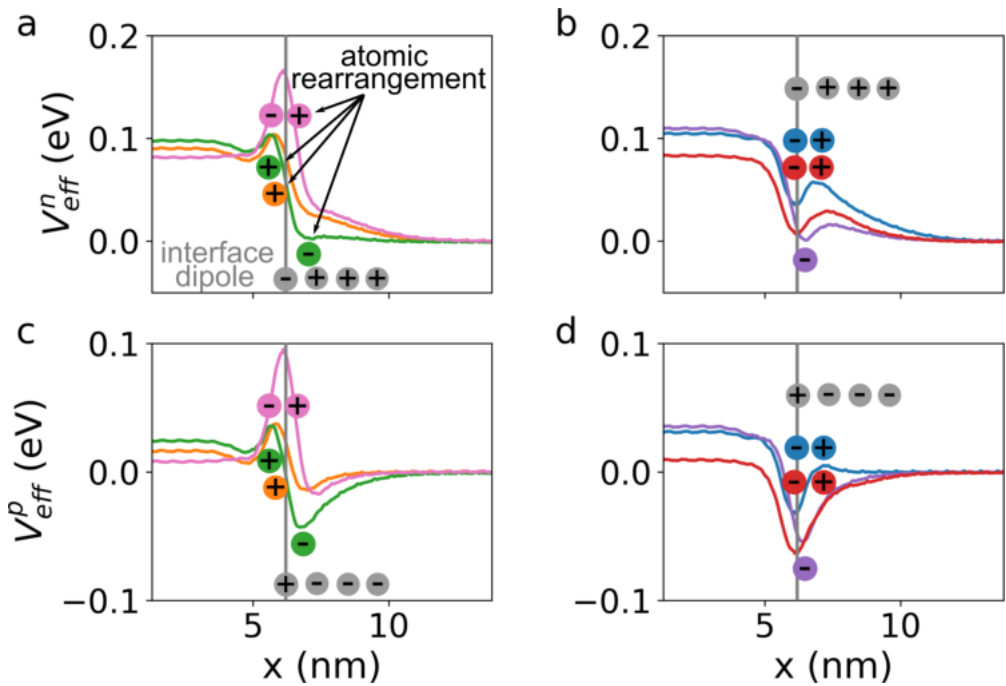
Figure 8.4: Effective potential of the 6 interfaces for both n- and p-doping. **a** and **c** shows the n-type and p-type d*-, a-, and b*-interfaces respectively. **b** and **d** shows the potential of the c-, c*-, and d-interfaces. The colors denote the different boundaries and follow the legend on Figure 8.2 and grey charges represent the interface dipoles created by charge transfer between the two phases. The grey vertical line marks the boundary and is placed at the rightmost atom of the T'-phase.

boundary, these slight differences should not affect the conclusions. The charge accumulation in the semiconductor and on the metal edge creating the interface dipole is illustrated by grey charges. The rearrangements which were highlighted on Figure 8.3 are also marked by colored '+' and '-' signs. The trends in the rearrangements are generally reflected by the potentials such that regions with an thin electron gas are accompanied by a rise in the effective potential whereas the regions with a dense gas correspond to a dip in the potential.

The 6 interfaces have been paired up 3-by-3 depending on what type of behavior the potential shows. The first group is the d*-, a- and b*-interfaces which all show a rise in the potential at the phase boundary independent on the type of doping. The sign of the interface dipole is inverted between n- and p-doping and this rise is therefore concluded to be due to the atomic rearrangements. The b*-type furthermore shows a dip in the potential to the right of the interface for both types of doping. This is interpreted as a strong dipole due to the rearrangements. At the d*-boundary, a dip in the potential is expected to the left of the interface from the observed rearrangements. The reason that this doesn't show up in the potential may be that the rise in potential due to the rearrangement to the right of the interface is much larger.

The second group is the c-, c*-, and d-interfaces. These all have a dip in the potential at the phase boundary. The c-type also has a rise in the potential at the semiconductor side of the interface for both types of doping. The dipole of the c-boundary point opposite to the interface dipole of the p-type devices creating a very flat potential. In conclusion, the atomic rearrangements have a large influence on the potential profile. At several of the boundaries, this is the only visible contribution at the phase boundary whereas the potential from the interface dipole only shows up as a tail in the depletion region.

Figure 8.5 shows the projected density of states (DOS) across the boundaries. The projected DOS directly shows the band bending of the semiconductor and the height of the Schottky barrier. According to the Schottky-Mott rule, all of these boundaries should result in the same barrier height and depletion width. The work function of T' MoTe$_2$ lies within the gap of the H-phase which leads to a work function difference of $\Phi_n^{SM} = 0.76$ eV and $\Phi_p^{SM} = 0.20$ eV for n- and p-doping respectively. However, the large variation in barrier heights between these 6 different phase boundaries demonstrates that a quantum mechanical description is
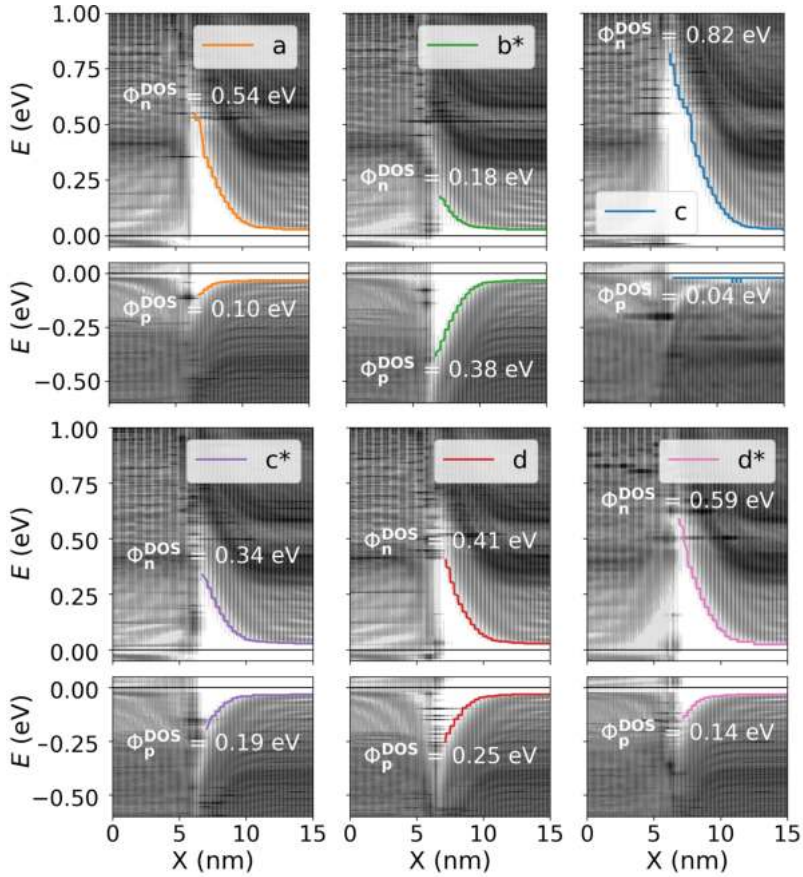
Figure 8.5: Projected density of states and Schottky barrier heights of the six interfaces between T' and H-phase MoTe$_2$. The corresponding atomic arrangements are illustrated on Figure 8.1. Top and bottom panels show interfaces where the H-phase has been n- or p-doped with a doping level of $N_{D/A} = 4.6 \times 10^{12}$ cm^{-2}.

absolutely necessary. It is worth noticing, that the p-type c-interface has a vanishing Schottky barrier which makes this kind of phase boundary promising for device applications.

Interface states, where the DOS is increased locally at the boundary but decreases both towards the metal and semiconductor side, can be observed in all of the 6 boundaries. Examples, which can be observed easily from Figure 8.5, are at 0.35 above the Fermi level for the n-type a-interface, at 0.6 eV above the Fermi level for the n-type c-interface, at 0.11 eV below the Fermi level for the p-type a-interface, and at 0.15 eV below the Fermi level in the p-type c*-interface. The origin of some of these interface states is discussed in the next section.

The barrier heights and depletion widths are summarized on Figure 8.6 where the p-type barriers have been defined as a negative barrier, in order to illustrate the trends. The n- and p-type DOS barriers mostly show opposite trends which is in agreement with the Schottky-Mott rule. The p-type a- and c*-interfaces have a lower barrier than what the corresponding n-type barrier would predict. This seems to be due to the large interface DOS near the top of the barrier in these two devices. The large interface DOS bridges the gap between the valence band and metal and results in an effectively lower barrier than what the potential would dictate. The difference between the p- and n-type barrier also varies between the 6 interfaces. The largest difference is for the c-type interface and the lowest is for the c*- and b*-interfaces. These differences seems to be due to the amount of interface DOS at either the n- or p-type barrier or both.

Comparing with the trends seen in the effective potentials, the boundaries, where the atomic rearrangements result in a charge distribution which is opposite of the interface dipole, generally show flatter potentials and lower barriers. The charge distribution from the rearrangements therefore seems to be able to screen the interface dipole resulting in a smaller barrier for transport. This is e.g. the case at the n-type b*-boundary which can explain why the b*-interface has a smaller n-type barrier than p-type barrier in contrast to the other five interfaces. Likewise, the p-type c-boundary has a very small barrier reflected in the flat potential on Figure 8.4.

The transport properties can also be described by the size of the TE barriers which are shown on Figure 8.6a as well. They have been extracted from the temperature dependence of the current at a small bias of ± 0.01 V for n- and p-doping and using the method explained in Section 7.3. These
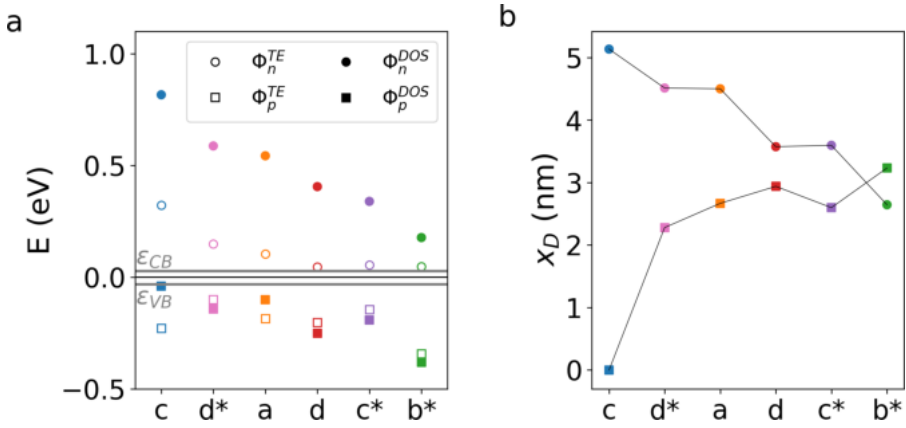
Figure 8.6: Schottky barrier heights and depletion widths of six interfaces between H- and T'-phase MoTe$_2$ where the H-phase has been n- or p-doped with $N_{D/A} = 4.6 \times 10^{12}$ cm^{-2}. **a** Schottky barrier heights from the projected density of states, Φ^{DOS}, and the thermionic emission model, Φ^{TE}. **b** Depletion widths. The colors denote the different boundaries and follow the legend on Figure 8.5 and the boundaries have been placed in the order of decreasing n-type DOS barriers.

barriers follow the trends seen in the DOS barriers. However, the p-type c- and a-boundary have TE barriers that are larger than the DOS barrier. This can be explained by the current transport being limited by momentum conservation when the barrier in the DOS is very low. On the other hand, the n-type TE barriers are very low and become comparable to the value of the conduction band for both the d-, c*-, and b*-interface. The reason for these very low TE barriers is that the transport is dominated by tunneling which can be enhanced by the presence of the interface states. Both of these phenomena are described in more detail in the next section which deals with the effect of these interface states. Figure 8.6b shows the depletion widths which are defined from the band bending seen on Figure 8.5. The depletion width is the distance from the top of the barrier to the point where the band becomes flat. The trend in barrier heights are generally followed by the depletion width.

In conclusion, these results underline that the charge transfer at these heterophase interfaces is dominated by atomic-scale effects and that both DOS barrier heights and potentials show very large variations with the

type of phase boundary.

8.2   Role and Origin of Charge Carrying Interface States

As demonstrated in the previous section, interface states appear at many types of phase boundaries between T' and H $MoTe_2$. The effects of these states on the charge transport are nicely illustrated at an n-doped c*-type interface. However, before starting the analysis of this device, let me distinguish between the different types of quantum states which can be present at a 2D metal-semiconductor interface.

- *Semiconductor edge states* are a property of the isolated semiconductor edge and can act as charge traps at the interface. The presence of such states tend to lead to Fermi level pinning (FLP), see Section 7.1.

- *Metal edge states* are a property of the isolated metal edge. They will not pin the Fermi level as charge cannot be trapped at the edge.

- *Metal-induced gap states (MIGS)* stems from the extended bulk metal states protruding into the gap region of the semiconductor with their exponential tail.

- *Topological interface states* are worth mentioning since the interface between the T'-phase and H-phase TMDs represent a boundary between a topological and a trivial material which will lead to topologically protected interface states. However, since these states travel along the interface, they will not participate in the transport.

Both the semiconductor and metal edge states can be the result of a hybridization between bulk states and discrete states related to defects or atomic rearrangements at the boundary. The states may also appear due to a discontinuity in the polarization[104], or a finite magnetization[95] at the edge which can prevail even after the edge is interfaced with another material. The types of interface states which aren't localized can contribute to the charge transport between the metal and semiconductor. This is

e.g. the case, when edge states become resonances. The MIGS will also contribute to transport if they have overlap with semiconductor states at the other side of the boundary.

The effect of a hybridization between a discrete state and a continuum of states can be illustrated through the Newns-Anderson model. This is a tight-binding model consisting of an semi-infinite chain, often representing the sp- or d-band of a metal, and an end-site which represents a discrete state with a specified coupling to the chain. The DOS inside the chain (grey) and at the last site (blue and red) are illustrated on Figure 8.7a. In the case where the discrete state couples strongly with the bulk states, corresponding to a defect at the metal edge, the discrete state will be broadened and lowered in energy. The projected DOS along the chain is illustrated on Figure 8.7b for this case. In the case of weak coupling, corresponding to a defect state which couples to a bend semiconductor band, the discrete state experiences only a small broadening and energy shift and may become a resonance. The resonance only has finite lifetime at the edge and then decays into the bulk, as illustrated on Figure 8.7c.

Let us continue with a concrete example of the effects of these interface resonances. The following analysis is partly revised and reprinted from the paper published in Nanoscale Advances in 2021[22]. The projected DOS
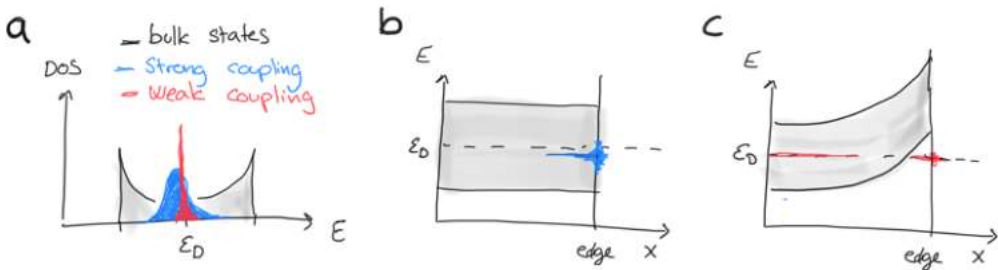
Figure 8.7: The DOS resulting from the Newns-Anderson model, when a discrete state coupled to a continuum of states. **a** shows the DOS at the end of the chain in grey and at the last site in blue and red for strong and weak coupling respective. **b** illustrates the projected density of states along the chain for the bulk and edge states in the case of a metal whereas **c** shows the case of a semiconductor with bend bands and a resonance at the edge.
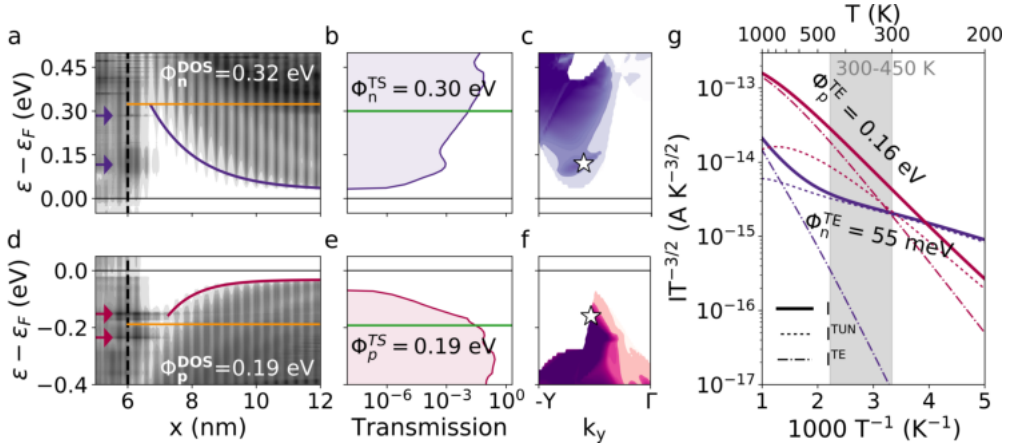
Figure 8.8: Projected DOS, transmission spectrum, and Arrhenius plot of the devices with a doping of $N_{D/A} = 4.6 \times 10^{12}$ cm^{-2}. **a** and **d** show the band bending, interface states (indicated by the arrows), and DOS barrier (orange) of the n- and p-doped device respectively. **b** and **e** show the transmission spectrum and the TS barrier (green) of the two devices. **c** and **f** show the k_y-dependence of the transmission spectra of the devices. The white star on **c** marks the position at which the transmission eigenstates on Figure 8.9 have been calculated. **g** shows the Arrhenius plot and TE barriers at ± 0.01 V bias. 201 k_y-points have been used for the non-selfconsistent calculations of the transmission spectra and current. Revised with permission from [22].

of two c*-boundary devices, where a doping of $N_{D/A} = 4.6 \times 10^{12}$ cm^{-2} has been added to the atoms which belonged to the H-phase before relaxation, are seen on Figure 8.8a and 8.8d. The DOS barriers are 0.32 eV[i] and 0.19 eV for the n- and p-doped devices respectively. One or more interface states are present in the band bending region between the Fermi level and the barrier height. The positions of the interface states are indicated with arrows. In the n-doped device, interface states or resonances are seen around 0.12 eV and 0.28 eV above the Fermi level. The states are predominantly localized in the interface region with a high DOS which

---

[i]The energy resolution of this DOS is slightly lower than on Figure 8.5 resulting in a n-type barrier of 0.32 eV in stead of 0.34 eV.

decays both towards the metal and the semiconductor. In the p-doped device, interface states are seen 0.15 eV and 0.24 eV below the Fermi level.

The transmission spectra are illustrated on Figure 8.8b and 8.8e. The TS barrier of the n-doped device is 0.30 eV and the p-doped device has a TS barrier of 0.19 eV which agrees with the DOS barrier heights. A peak is seen in both transmission spectra around the energy of the interface states closest to the Fermi level which illustrates that these states contribute significantly to the charge transport. The peak is most visible in the n-doped device where the position of the interface state is well below the barrier height whereas it is more difficult to see in the p-doped device, where the interface state is positioned very close to the barrier.

To investigate the origin of these interface states, the transmission eigenstates of the n-doped device at 0.12 eV above the Fermi level and at the k_y-value of -0.3 (as indicated by the white star on Figure 8.8c) are plotted on Figure 8.9a and 8.9b. The green and yellow isosurface illustrate the eigenstate originating from the T' electrode, Ψ^L, and the pink and cyan isosurface illustrate the eigenstate originating in the H electrode, Ψ^R. It is seen that the transport primarily occurs between d_{yz} like orbitals on the molybdenum atoms in the interface and d_{z^2} like orbitals in the H-phase.

The DOS close to the interface at the position of the last Mo-atom belonging to the 1T'-phase is seen on Figure 8.9c for the two devices along with corresponding devices with a lower doping density. The peak of the interface states just above and below the Fermi level only moves about 60 meV between the 4 devices. An isosurface plot of the left trans-mission eigenstate of the low n-doped device at 0.14 eV above the Fermi level results in the same isosurface as seen on Figure 8.9, identifying it as the same state. Based on these observations, the conclusion is that the interface states are mainly determined by the 1T'-phase rather than H-phase. These heterophase junctions are therefore free of FLP despite hosting interface states. This agrees with a recent study by Urquiza et al.[118] who have investigated doped T'-H MoS_2 junctions. The FLP of interfaces between 3D metals and H-phase TMDs has in previous stud-ies been attributed to defects[119] or negative ionization of the outmost S atom complex.[20] The reason why such behavior isn't present in these sys-tems might therefore be that they represent perfect crystalline interfaces without any defects with dangling bonds.

To summarize, these interface states are most likely resonances which stems from a metal edge state broadened by a strong coupling to the
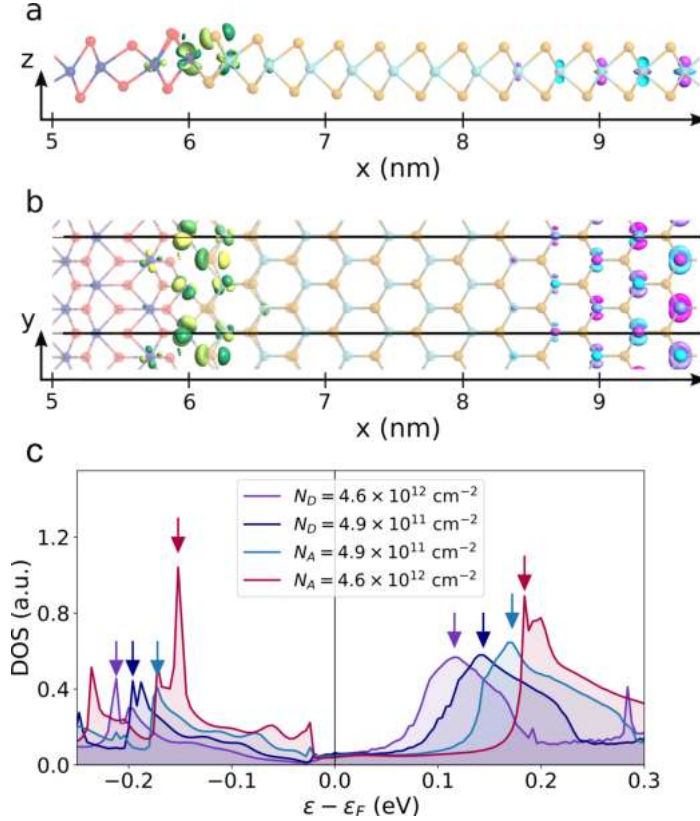
Figure 8.9: Transmission eigenstates of the c*-boundary with n-doping $N_D = 4.6 \times 10^{12}$ cm^{-2} at $\varepsilon = 0.12$ eV and $k_y = -0.3$. **a** and **b** show the isosurfaces of the eigenstate from the T' electrode, Ψ^L, (green and yellow isosurface) and the eigenstate from the H electrode, Ψ^R, (cyan and pink isosurface) seen from the side and top of the ML respectively. **c** the DOS around the Fermi level projected on the final Mo atom of the T'-phase at x = 6.0 nm. The arrows indicate the energy of maximum DOS of the two interface states placed closest to the Fermi level. Revised with permission from [22].

bulk metallic states and with a weak coupling with the semiconductor states at the conduction or valence band. This conclusion agrees with the decaying DOS both towards the metal and semiconductor. As already mentioned, these resonances play a large role in the charge transport which can be seen in the transmission spectrum but becomes even more evident considering the effective Schottky barriers found from thermionic emission (TE) theory. The temperature dependence of the current through the devices is seen on Figure 8.8g and shows an TE barrier of 55 meV for the n-doped device and 0.16 eV for the p-doped device between 300 and 450 K. The n-doped device shows tunneling dominated current up to around 740 K whereas the p-doped device becomes dominated by thermal excitation already around 320 K. The very low TE barrier in the n-doped device reflects the steep increase in the transmission spectrum. The temperature dependence of the current is evaluated as,

$$I = \frac{2q}{h} \int T(E, \mu_L, \mu_R) \times$$
$$\left[f\left(\frac{E - \mu_L}{k_B T} \right) - f\left(\frac{E - \mu_R}{k_B T} \right) \right] \mathrm{d}E, \qquad (8.2)$$

where the transmission is integrated with the two Fermi distributions of the electrodes. A steep transmission onset therefore results in a significant amount of current running already at low temperatures and the current will only have a weak dependence on the temperature. In the p-doped device, the interface states only has a small effect. This is partly because these interface states are positioned close to the DOS barrier and partly because only few states are available for transport due to the symmetry of the system.

This symmetry is illustrated on Figure 8.8c and 8.8f which shows the k_y-resolved transmission spectrum for both devices. For the n-doped device, a reasonably range of k_y points contribute to the transmission already at the conduction band edge. For the p-doped device, the transmission is much more narrow in k-space. This is reflected in the rapid decay of the transmission from the energy of the interface states towards the transmission onset on Figure 8.8e where the transmission is summed over all k_y-points. The k-dependence of the transmission arises due to the different dispersion relations of the T'- and H-phase. In order to have momentum conservation perpendicular to the transport direction, a state

must be available at the same k_y-value in both phases. This is possible for a larger range of k_y-points for the n-doped device than for the p-doped device. This is also the reason why the transmission onset of the p-doped device occurs below the valence band edge. There are no states available in the T'-phase for transport at the valence band edge of the H-phase.

The lowering of an TE barrier due to tunneling is described in Section 7.3. The maximum barrier underestimation due to tunneling, using eq. (7.9), is between 97 meV and 0.12 eV at 300 K and 450 K, respectively.[ii] This can not account for the entire difference between the TE and DOS barrier of the n-doped device. Using the Wentzel–Kramers–Brillouin (WKB) method, the transmission probability across a potential barrier with the shape of the conduction band can be calculated. From this transmission and eq. (8.2), the TE barrier can be estimated when the effects of the resonances are omitted. This results in an TE barrier of 0.18 eV in reasonable agreement with the underestimation predicted by the simple model. This supports that it is the presence of the resonances, and not the well-known barrier tunneling, which is responsible for the very low TE barrier of this junction.

In conclusion, the charge transport and effective Schottky barrier can be decreased dramatically due to the presence of interface states. In contrast to the effect of Fermi level pinning where the charge neutrality level of the semiconductor edge dominates the band bending and DOS barrier, in these cases, interface resonances originating from the metallic phase dominates the size of the effective barrier by enhancing the tunneling current. Since TMDs with group six metals have very similar dispersion relations and chemical bonds it seems likely that the effect will be present in other heterophase devices as well.

8.3   Electrostatic Response

In the following section, I will highlight some of the differences between the electrostatic response of the interfaces calculated with ab-initio methods and the response predicted by classical electrostatics. The electrostatic response of the Schottky barrier is one of the main mechanisms in a field

---

[ii]With the doping level of $N_{D/A} = 4.6 \times 10^{12}$ cm^{-2} and using the effective mass of carriers in ML MoTe$_2$ at the Γ-point of the valence band, $m^* = 10.93 m_0$.[120]
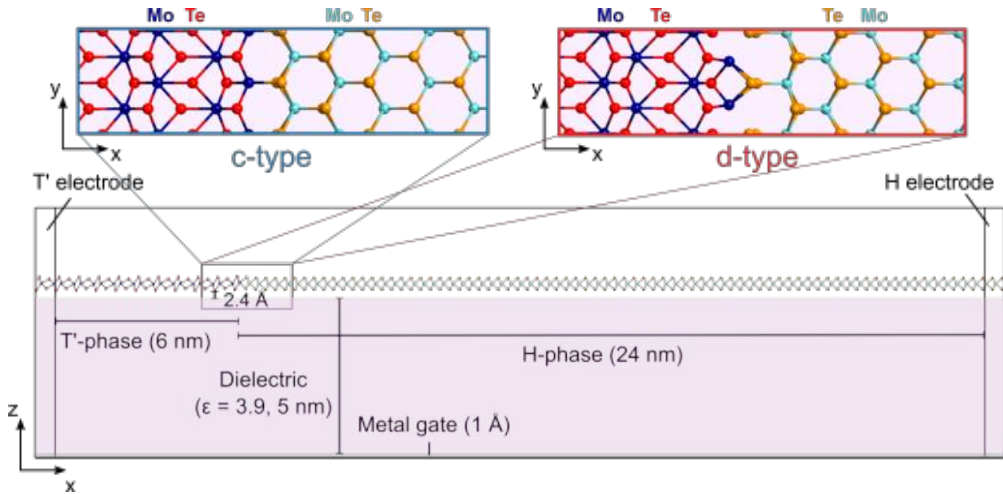
Figure 8.10: The T'-H device of ML MoTe$_2$ on a substrate and back-gate. The top part shows the atomic configurations of the two investigated boundaries seen from the top. The bottom part shows the device seen from the side and consisting of a central region and two electrodes. The total cell size is (30.0, 0.718, 15.0) nm.

effect transistor (FET). In the FET, a gate potential is used to draw in or push out carriers from the semiconducting channel and thereby turn the device on or off. Here, the doping level in the H-phase is tuned in order to mimic this electrostatic effect and investigate the response of the Schottky barrier.

In the calculations, the interfaces are placed on a 5 nm substrate which is represented as a continuum dielectric with a dielectric constant of $\varepsilon = 3.9$, in agreement with the dielectric constant of SiO$_2$, and a thin back-gate of 1 Å as shown on Figure 8.10. The distance between SiO$_2$ and 2H-MoS$_2$ has been estimated to be 2.96 Å[121] and the smallest distance between SiO$_2$ and T'-MoTe$_2$ has been calculated[iii] to be 2.32 Å. The 2D interface is placed such that the lowest atom is 2.4 Å above the substrate

---

[iii]Using the PBE-D2 functional and the counterpoise correction, small k-point density as the MoTe$_2$ calculations, 125 Ha cut-off, PseudoDojo pseudo potentials and a match between 4 unit cells of SiO$_2$ to 9 unit cells of T'-MoTe$_2$ resulting in 0.6 % strain. The relaxation was performed with a fixed SiO$_2$ crystal and a rigid MoTe$_2$ crystal to get the spacing.

since varying this distance between 2.2 and 4 Å did not change the barrier height or depletion width.

The screening by the substrate is an important part of the electrostatics involved when the Schottky barrier is formed. The substrate will enhance the screening of the interface dipole field at the interface and result in a larger charge transfer since the overall potential difference between the two phases is independent on the substrate. The substrate will therefore increase the depletion width but not alter the barrier height. In an experiment, a substrate below a 2D TMD may have several effects: a small change of the band gap[122], longer depletion widths[123], and a modulation of the work function or doping level[109].

To illustrate the electrostatic response, the valence band bending of a c- and d-type interface with p-doping between 10^{12} and 1.5×10^{13} cm^{-2} is shown on Figure 8.11a and 8.11c. The doping is added to all of the atoms to avoid any dependence on the choice of which atoms belongs to which phase. As the doping density is increased, the barrier is decreased and the depletion width becomes shorter. The c-type device has flat bands already at a doping level of 4×10^{12} cm^{-2} where the barrier height starts to follow the valence band edge. The d-type, on the other hand, shows band bending for all these doping densities.

Figure 8.11b and 8.11d show the p-type barrier height as a function of the doping density together with a grey scale contourplot of the density of states projected on the boundary. The position of the boundary is illustrated by the grey vertical line on Figure 8.11a and 8.11c and is defined as the x-coordinate of the leftmost Mo-atom which belonged to the H-phase before relaxation. The movement of the valence band edge as a function of doping is indicated by the black line. In the case of a c-type interface, the barrier height follows the movement of the valence band maximum, ε_{VB}, for the first 3 doping levels and then jumps to the value of ε_{VB} after which the bands become flat. A high density of interface states is present between the barrier height where the jump occurs and the valence band edge. When the doping is increased, the barrier is lowered, i.e. moved upwards on the figure, but enters a region with a large density of interface states (DOIS). These states bridge the narrow part of the barrier and allows for charge to be transported resulting in the top of the barrier being pushed up in energy to a point where the DOIS becomes negligible or the valence band becomes flat. The behavior is perhaps even more pronounced in the d-type case, where a large DOIS is seen in the
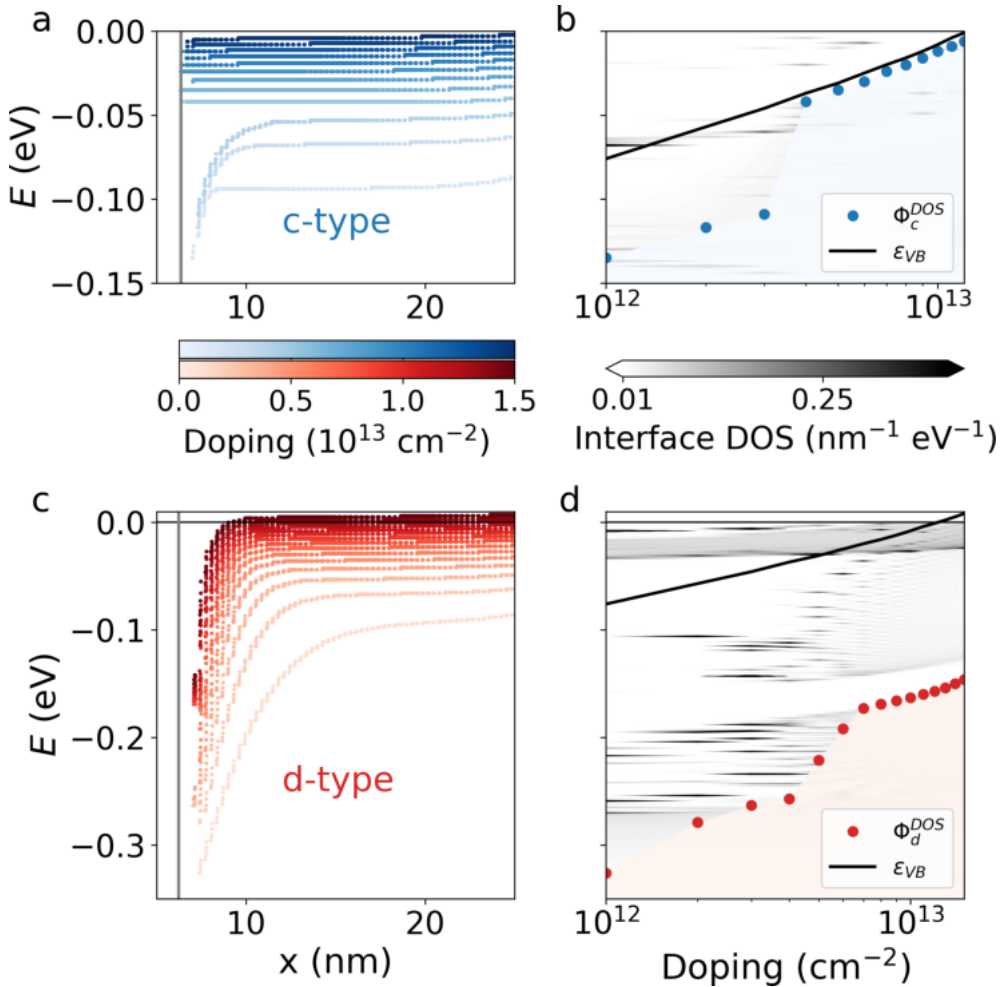
Figure 8.11: The Schottky barriers of c- and d-type interfaces with varying levels of p-doping. **a** and **c** show the valence band edge of the H-phase found from the projected density of states for the c- and d-type respectively. The grey line indicates the first Mo-atom belonging to the H-phase. **b** and **d** show the barrier heights as a function of the doping level (circles) along with the valence band edge of the H-phase electrode (black line). The density of states at the position of the grey line on **a** and **c** at each doping level are included as a grey-scale contour to illustrate the density of interface states between the band edge and Fermi level. The red and blue shaded regions mark the valence band states.

entire region between -0.3 and -0.2 eV and between -0.15 and 0 eV. The barrier height follows the band movement when the DOIS is low around $E = -0.26 eV$ and above $E = -0.19$ eV. Between these plateaus it jumps between the small energy windows where the DOIS is low. From a classical point of view, we would expect that the barrier height would follow the band movement but, as we have seen here, the interface states result in a very different behavior and once more underlines the quantum mechanical nature of the barrier forming in these interfaces.

The DOIS of both types of interfaces show that the interface states all move with a smaller slope than the valence band wrt. the change in doping level. The interface states are not moving together with the semiconductor states but, as was the case for the c*-type boundary, have origin in the metallic phase. The states are therefore expected to be either MIGS or resonances originating from metal edge states.

Figure 8.12a shows the change in electron density at the d-type interface as the doping level is increased. The plot shows the difference in the 2D electron density between the doping level, N_{2D}^{dop}, and the density of a reference device with doping level $N_{2D}^{ref} = 1 \times 10^{11}$ cm^{-2} where almost no charge transfer is possible since less than 0.02 holes are available in the entire semiconductor region. This reference removes the contributions from the atomic rearrangements at the boundary. After the subtraction of the reference density, the doping difference between the reference device and this device is subtracted in order to remove the background doping density,

$$\Delta n_e(x) = \frac{1}{W} \int n_e(x, y, z) - n_e^{ref}(x, y, z) \, \mathrm{d}y \, \mathrm{d}z - (N_{2D}^{dop} - N_{2D}^{ref}).$$

W is the width of the device in the y-direction. Finally, the density has been smoothed using Gaussian curves to remove the fluctuations at the atomic positions. The result clearly illustrates how the interface dipole changes with an increasing doping level. The device with the lowest doping shows an increase in electron density at the H side which extends far to the right and is almost flat at the top showing that the semiconductor becomes completely depleted of holes. When the doping level increases, the dipole becomes more narrow since more charge carriers are available close to the boundary. The charge build-up in the T'-phase also has some spatial extend which is somewhat unexpected in a metal where a large
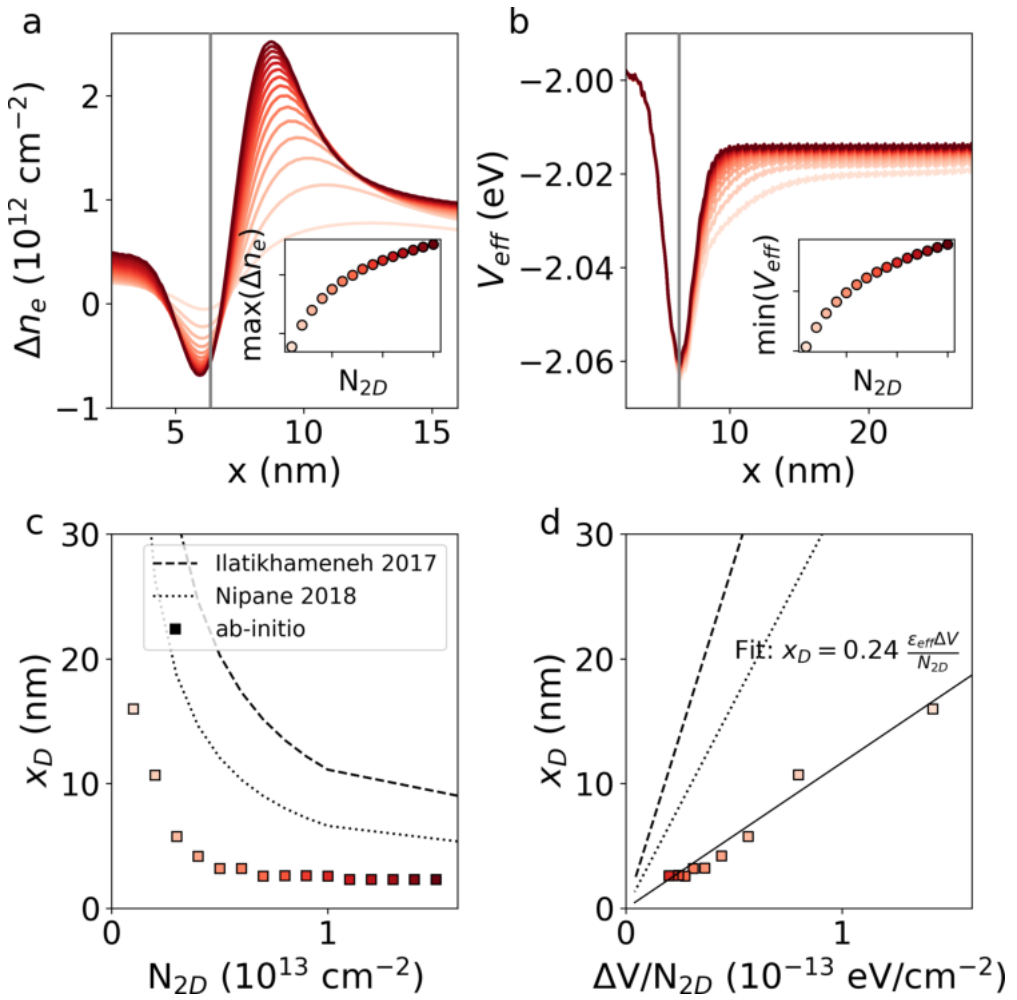
Figure 8.12: The electron density (**a**), effective potential (**b**), and depletion width (**c** and **d**) of the d-type interface with varying p-doping following the color-scale on Figure 8.11c. The depletion width is compared to the model predictions by Ilatikhameneh *et al.*[109] (dashed line) and Nipane *et al.*[111] (dotted line). **d** shows the depletion width as a function of the work-function difference divided by the doping density and a linear fit to the calculated depletion widths (solid line).

density of charges is available. This is due to the 2D nature of the metal. Even though it is a metal, charge can not build up as line charge along the interface and the charge density instead decreases as $1/x$ away from the interface. This is in agreement with the behavior of a charged 2D metal nanoribbon which was discussed in Chapter 7. The corresponding effective potential is shown on Figure 8.12b and reflects the behavior seen in the density. It has been averaged over the y-direction and over the z-direction from 1 Bohr radii below the lowest positioned atom to 1 Bohr radii above the highest positioned atom using eq. (8.1).

It is worth noticing that the jumps in the barrier height isn't reflected in the density or potential which both varies smoothly with the increasing doping as shown in the insets of Figure 8.12a and 8.12b. This illustrates the difference between considering a Schottky barrier from a classical point of view and from a quantum mechanical point of view. In the classical view, the barrier is exclusively determined by the charge density and corresponding potential. In the quantum mechanical view, the barrier height is determined from the density of states available for charge transport.

On Figure 8.12c, the depletion width of the d-type interface is shown together with the corresponding widths calculated from the expressions derived by Ilatikhameneh et $al.$[109] and Nipane et $al.$[111] using classical electrostatics,

$$x_D^{Ilatikhameneh} = \frac{\pi \varepsilon_{eff} \Delta V}{ln(4) q N_{2D}},$$

$$x_D^{Nipane} = \frac{\pi^2 \varepsilon_{eff} \Delta V}{8 G q N_{2D}}.$$

ΔV is the work function difference between the two materials in the junction, ε_{eff} is the effective dielectric constant which is determined by the dielectrics surrounding the 2D material which in this case is $\varepsilon_{eff} = (\varepsilon_{above} + \varepsilon_{below})/2 = 2.45$, $G \approx 0.915$ is the Catalan's constant, and q is the elementary charge. These depletion widths have been calculated using the work function of the H- and T'-phase at each doping level using a computational cell and parameters matching those used for the electrodes of the devices.

The depletion widths extracted from the calculations are the distance from the position of the barrier to where the valence band becomes flat. The calculated depletion widths are considerably lower than what the

models predict. However, it seems that the $\Delta V/N_{2D}$ dependence is more or less followed, as illustrated on Figure 8.12d. The slope found for the calculated depletion widths is around an order of magnitude lower than the slope predicted for the classical models. The analysis presented here for the d-type boundary can be carried out for the c-type device as well. However, since the depletion width vanishes after the first three doping levels, a meaningful fit cannot be made.

In conclusion, the electrostatic response of the Schottky barrier height between T'- and H-phase $MoTe_2$ is dominated by quantum mechanical effects. The barrier height follows the expected trend from classical electrostatics when no or few states are present in the semiconductor gap at the boundary between the two phases. If there is a high density of interface states present between the Fermi level and band edge, the barrier is decreased since charge transfer is possible through these states. The interface dipole, effective potential and $\Delta V/N_{2D}$ scaling of the depletion width follow the expected behavior from classical models. However, the depletion width, like the barrier height, is determined by the atomic rearrangement at the boundary and is much smaller than predicted by the models. The electrostatic response is important to understand in the context of using these Schottky contacts in field effect transistors. This will be the subject of Chapter 11.

This concludes the part of the thesis which describes 2D Schottky contacts both from a classical point of view, a simplified theoretical point of view, and by the use of ab-initio calculations. The results underline that the 2D Schottky contacts are dominated by atomic-scale phenomenons. Atomic rearrangements, interface states, and tunneling all play a large role in determining the transport properties.

Phase-engineered MoTe$_2$ as a Next-generation Transistor

Field effect transistors (FETs) are a keystone in all modern electronic devices. They form the logic elements which allows for communication across and inside the nodes in the device. The development of the FET has been the technological backbone of the tremendous development that we have seen in the capability, down-scaling and distribution of electronic devices. Laptops, smart phones, high-performance computing and autonomous driving are just a few examples of the technologies depending on this development.

This final part of the thesis describes how FETs operate and how 2D materials can be utilized in future FET designs. Specifically, the concept of a phase-engineered FET using contacts between the semiconducting and metallic phases of TMDs is explained and the progress in fabricating and modelling such devices is reviewed. Ab-initio calculations on $MoTe_2$ heterophase FETs are used to evaluate the monolayer limit of this design.

The following chapters are organized as follows,

Chapter 9 describes the basic building blocks of modern field effect transistors, how they operate, and the figures of merit used to evaluate their performance.

Chapter 10 explains how the 2D transition metal dichalcogenides can be used in FETs and reviews the progress and challenges related to using phase-engineered MoS_2 or $MoTe_2$ as the contact-channel interface.

Chapter 11 presents ab-initio calculations on $MoTe_2$ heterophase field effect transistors.

CHAPTER 9

Field Effect Transistors

In this chapter, I will introduce the working principles behind a field effect transistor (FET) and how the transistor performance is evaluated. A simple schematic of a planar metal-oxide-semiconductor FET (MOSFET) is shown on Figure 9.1a. The transistor works by controlling the electrostatic potential between 3 contacts, the source (S), the drain (D), and the gate (G). When a potential drop is induced between the source and drain (bias, V_{sd}), the device can be turned off or on by controlling the potential between the source and the gate (gate potential, V_G). If the device is turned on, current can flow from the source to the drain if it is turned off, the current is blocked. The region between the source and the drain, where the current flow, is called the channel. The channel is made of a semiconducting material, in practice almost always silicon, where the conduction (valence) band states are responsible for the transport of electrons (holes) through the n-type (p-type) transistor. Between the channel and the source or drain a region of the silicon is heavily doped using ion implantation (extension implant). This ensures a small Schottky barrier between the contacts and channel, as discussed in Chapter 7. A number of thin metal films e.g. of TaN, TiN, or both are usually present between the gate oxide and the gate electrode. These layers modulate the effective work function of the gate stack (gate oxide + gate electrode).

The electronic band alignments between the source, drain, and channel are illustrated on the top row of Figure 9.2 for a n- and p-type device. Without any bias or gate potential, two Schottky barriers will form at the source and the drain. When a bias is applied, the semiconductor bands will move to effectively create only a single barrier either at the source or the drain, depending on the sign of the bias. This is illustrated in the middle row of Figure 9.2 with a barrier at the drain. Notice, that these illustrations are drawn with respect to electronic energy levels which means that a positive bias (in units of Volt) corresponds to a positive slope. In this condition, the gate potential can be used to raise or lower the
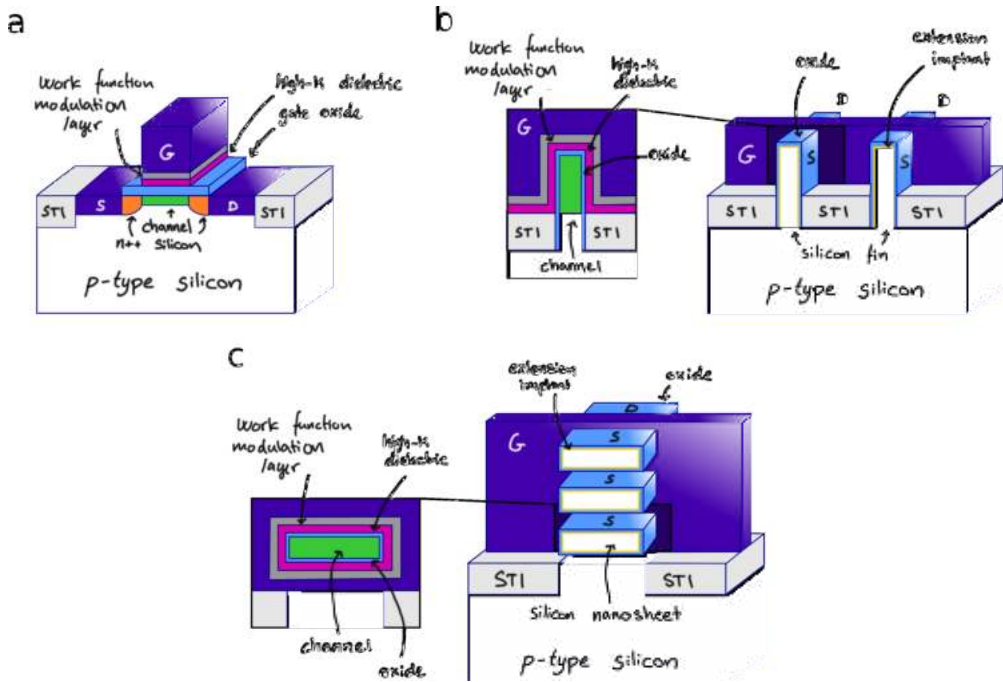
Figure 9.1: Commercial MOSFET designs. **a** shows a planar FET, **b**, a FinFET, and **c**, a Gate-All-Around FET. The source (S), drain (D), and gate (G) are marked on each design. Shallow trench isolation (STI) is used to isolate the FET from the neighbouring components.

electronic bands and thereby alter the energy barrier. This is illustrated in the bottom part of Figure 9.2. In the ON-state, the barrier is thinned to a degree where the carriers will tunnel to the other side and current flows. In the OFF-state, the electronic band are moved to form a block-like region without any available states, effectively blocking the charge transfer. The flat-band voltage is defined as the condition where both valence and conduction band becomes completely flat.

Two key measurements are used to characterize a transistor; the IV curve and the transfer characteristic. The IV curve measures the source-drain current as a function of bias and the transfer characteristic measures the source-drain current as a function of the gate potential and is typically shown on a log scale. An illustration of these curves for an n- and p-type
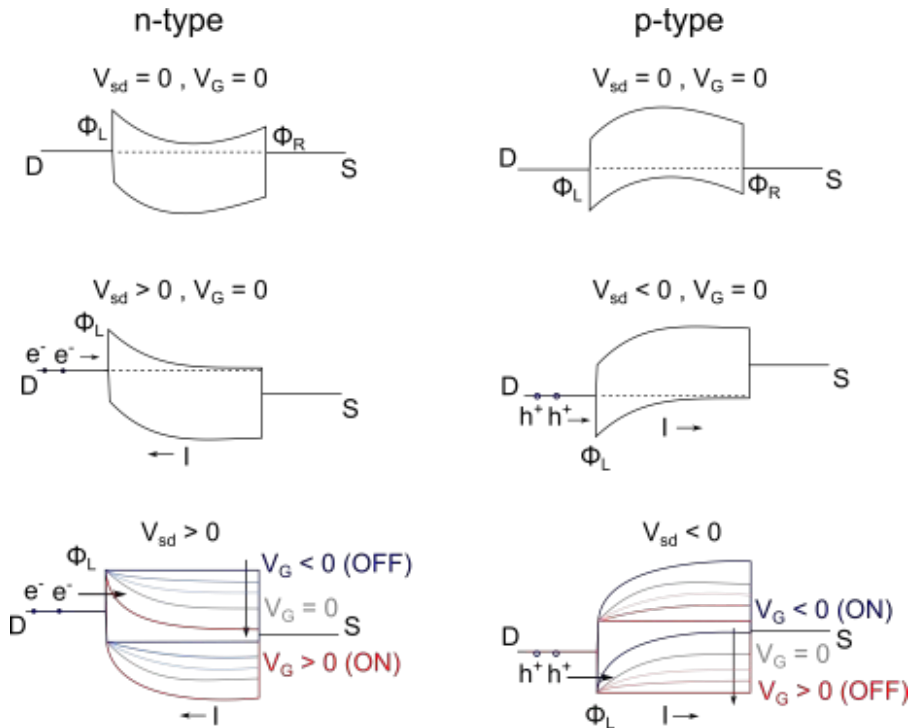
Figure 9.2: Electronic band alignment of an n- (left) or p-type (right) FET.
Top row: Zero bias, V_{sd}, and gate potential, V_G. **Middle row:** Zero
gate potential and forward (n-type) or backwards (p-type) bias creating
a single barrier at the drain. **Bottom row:** Variance with gate potential
at a fixed bias. The flat band condition is shown in dark blue (red) for
the n-type (p-type) FET.

device is shown on Figure 9.3. The IV curves show two behaviors, a linear
dependence at low biases and a saturation behavior at higher biases. The
bias which separates these two regions is called the saturation voltage and
depends on the gate potential.

The transfer characteristic can be divided into three regions. In the
OFF-state, the current is very low and the dependence on the gate po-
tential will often be too small to measure. As the device approaches
the flat-band condition, the current starts to rise exponentially (linear
on the log-plot). In this regime, the bands are inverted wrt. the device
type and thermal excitation of carriers is the only possible mechanism for
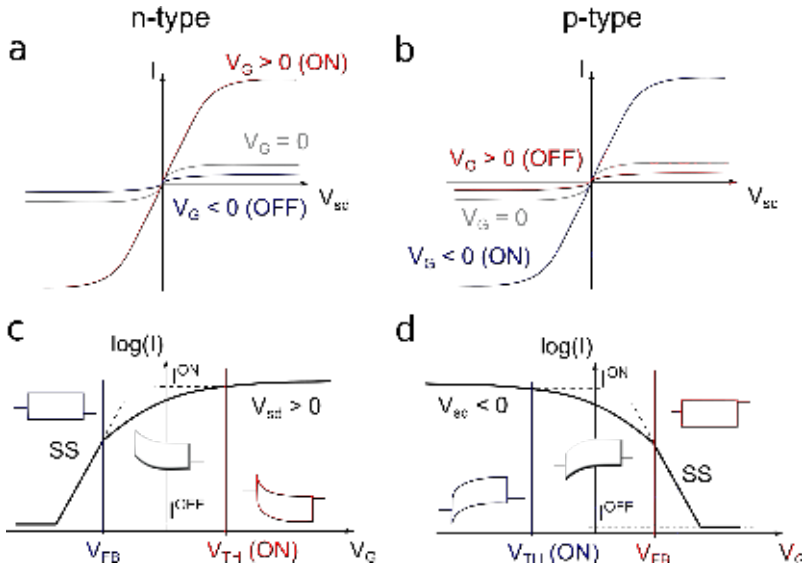
Figure 9.3: IV characteristics and transfer characteristics of a n- (left) and p-type (right) transistor. **a** and **b** show the IV characteristics at different gate potentials. **c** and **d** show the transfer characteristics and the sub-threshold slope (SS), flat band voltage (V_{FB}), threshold voltage, (V_{TH}), and OFF- and ON current (I_{ON}, I_{OFF}).

charge transport. The current therefore follows an exponential increase determined by eq. (7.3). Note that it is the gate potential which determines the alignment between the semiconductor and metal states which means that $V = V_G$ in (7.3). This exponential rise characterises the sub-threshold regime of the device and the slope on the log-plot is called the sub-threshold slope (SS). The slope is calculated as the amount of gate potential required to increase the current by one order of magnitude. A small SS is favorable since this means that only a small bias is required to move from the OFF-state to the ON-state. From eq. (7.3), the smallest possible slope will be,

$$SS = \frac{d(\log I)}{dV_G} = \frac{k_B T}{q} \ln 10 \sim 60 \, \text{mV/dec},$$

at room temperature. Since the charge transport is purely thermionic, the expression in eq. (7.6) can be used to determine the barrier rather

accurately. Measurements of the barrier as a function of the gate potential in this regime can therefore be used to extrapolate the value of the Schottky barrier back to zero gate potential.

The next regime can be denoted the Schottky barrier (SB) regime. The device approaches the ON-state and the current is conducted as a mixture of thermal excitation and tuneling. The mechanism responsible for most of the charge transfer is in many cases thermally excited tunneling i.e. thermionic-field emission (TFE) and the relative contributions from thermionic emission and tunneling are determined by both the temperature and the carrier concentration in the channel (doping level). At some point, the current response to the gate potential starts to level off. This gate potential is called the threshold voltage, V_{TH}, and above this point, scattering mechanisms in the channel starts to limit the device performance.

The current at the threshold voltage is often defined as the ON-current of the device whereas the OFF-current can be defined as the bottom of the sub-threshold region where the current response becomes too small to measure. When device performance is compared, the OFF-current is often defined at a certain level which might be higher than the lowest current in the transfer characteristics. As an example, the IEEE International Roadmap for Devices and Systems (IRDS) defines the OFF-current of a high-performance device to be 10 nA/μm.[1] The ratio between the ON- and OFF-current is often used as a device performance parameter which contains information on how well the device turns off. If the OFF-current is too high, it is a sign that 'leakage current' is running between the source and drain. This can for example be due to direct tunneling between the source and drain in a short channel device. Similarly, the gate potential difference between when the ON- and OFF-current are reached, V_{DD}, represents the required power supply voltage for the device to function and is therefore a measure of the power consumption.

FET Figures of Merit   Here follows a summary of the most common figures of merits which are used to quantify FET performance,

- Φ^{SB}, *Schottky Barrier:* The energy barrier which the charge carriers must overcome to move from the drain to the channel or from the source to the channel.

- SS, *Sub-threshold Slope*: The amount of gate potential required for the current to rise by one order of magnitude in the sub-threshold regime.

- I^{ON}, *ON-current*: The current running at the threshold voltage.

- I^{OFF}, *OFF-current*: The lowest current in the transfer characteristic or a predetermined value, e.g. 10 nA/μm.[1]

- I^{ON}/I^{OFF}, *ON-OFF Ratio*: The ratio between the ON- and OFF-current which evaluates how well the device turns off.

- V_{DD}, *Power Supply Voltage*: The gate potential difference between the ON- and OFF-state.

- FET μ, *FET Mobility*: The mobility of the carriers in the device.

9.1   Field Effect Transistor Design

Up to this point, I have described the transistor performance in the framework of a planar transistor setup as the one shown on Figure 9.1a. However, since 2011, commercial FETs have been utilizing the FinFET design illustrated on Figure 9.1b. In this design, the gate electrode is wrapped around a silicon 'fin'. The two regions of the fin which is outside the gate are utilized as the source and drain whereas the region surrounded by the gate is utilized as the channel region. The change of design was introduced since the planar transistor design had reached the limit wrt. down-scaling and effectivity. Short channel effects had begun to dominate the device performance. Such effects occur when the field between the source and the drain becomes too large such that the gate no longer controls the device properly. More power is required to turn the device ON and a leakage current will run in the OFF-state which may cause malfunction.

A new design rule rose from these challenges called the Scale Length Theory.[124–126] This defines a natural scaling length, λ, which relates the geometric properties and dielectric constants of the channel and gate oxide to the electrostatic integrity of the device. It builds on the assumption that the field between the source and drain follows an exponential law, $E_{sd}(x) \propto \mathrm{e}^{-x/\lambda}$, where the natural scaling length is

$$\lambda = \sqrt{t_{ch}t_{ox}\varepsilon_{ch}/\varepsilon_{ox}}. \tag{9.1}$$

t_{ch} is the thickness of the channel, t_{ox} is the gate oxide thickness, ε_{ch} is the dielectric constant of the channel, and ε_{ox} is the dielectric constant of the gate oxide. In order to have proper gate control, the channel length must be 5-10 times the size of λ. Within this design rule, the channel length can therefore be decreased, if the channel thickness or oxide thickness is decreased accordingly or if the oxide dielectric constant is increased.

In a planar FET design t_{ch} and t_{ox} are the height of the channel and equivalent oxide thickness (EOT) when seen from the side as on Figure 9.1a and in a finFET design t_{ch} and t_{ox} are the fin width and EOT of the gate oxide. The equivalent oxide thickness is a measure of how thick a SiO_2 film that would be needed to reproduce the same gate capacitance as a high-κ dielectric,

$$t_{EOT} = t_{high-\kappa}\frac{\varepsilon_{SiO_2}}{\varepsilon_{high-\kappa}}. \tag{9.2}$$

The gate capacitance scales as $\propto \varepsilon_{ox}/t_{ox}$ which means that a thicker layer of a high-κ dielectric will reproduce the capacitance of a thin SiO_2 film. The high-κ dielectric helped solve two problems at once, the large screening dampens the source-drain field and the increased thickness of the gate oxide layer prevents carrier tunneling between the channel and gate electrodes which was starting to become a problem as the SiO_2 film thickness was decreased.

The finFET design is a result of the design rule in eq. (9.1) and represents an improved gate control and thereby a lower power consumption. This is achieved both by decreasing the t_{ch} dimension and by placing the channel such that the gate controls the source-drain field from 3 sides. By creating the silicon fin, the channel thickness was reduced significantly. However, the down-scaling of this dimension is also limited since the charge carrier mobility of 3D semiconductors becomes severely reduced when the fin thickness decreases. The currently available lithography methods results in rough surfaces and dangling bonds when the thickness is reduced below 5-6 nm's[129] which leads to scattering of the carriers and a mobility which rapidly decreases. This is illustrated on Figure 9.4 where the thin-channel mobility of silicon- and germanium based
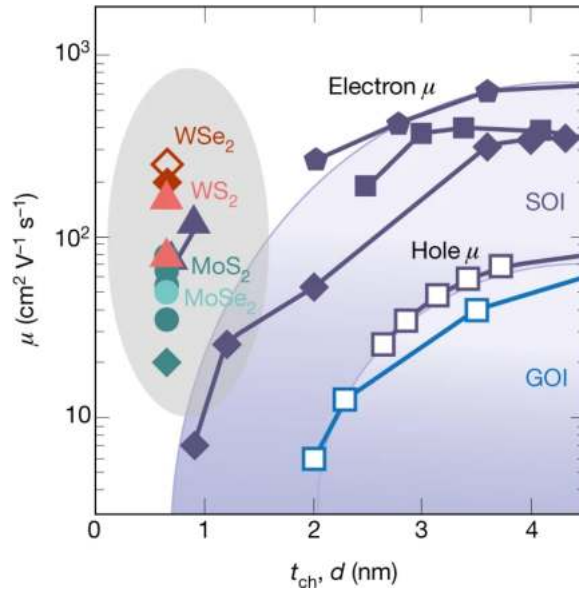
Figure 9.4: Mobility vs. channel thickness for semiconducting channels of TMDs (grey area) and for silicon-on-insulator (SOI) and germanium-on-insulator (GOI) devices (blue areas). Filled (open) symbols represent electron (hole) mobilities, respectively. Reprinted with permission from Ref. [127] and adapted with permission from Ref. [128]. Copyright 2016 American Chemical Society.

devices is compared to the mobility of 2D TMD based devices.[127] The 2D TMDs have a clear advantage on this point. Due to the layered structure, these can be exfoliated down to the monolayer limit while retaining a good mobility.

In the commercial 5 nm finFETs, the fin width is around 7 nm, the fin height is 50 nm's, and the metal pitch (distance between fins) is 28 nm's.[1] These numbers illustrate that also this design is reaching the limit with respect to improvements through down-scaling. The semiconductor industry has therefore introduced a new design which will be part of the next generation of commercial logic devices and which is illustrated on Figure 9.1c. This gate-all-around (GAA) design is a natural continuation of the finFET but where the gate is placed on all 4 sides of the channel which gains another notch on the gate control and thereby allows for a reduction in the power consumption. The IRDS 2020 GAA device requirements are

22 nm's latteral pitch, 18 nm's vertical pitch, a thickness of 7 nm's, and a width ranging from 7-30 nm's.[1] According to the roadmap, the thickness must be reduced to 5 nm's by 2031. There is general agreement that we have come to the end of Moore's era and that down-scaling will stagnate. Future device improvements must be obtained by specialising the transistors to the end application through optimization of the design and materials. This has lead to a great deal of research on utilizing alternative materials.

2D Transition Metal Dichalcogenides in Transistors

The semiconducting 2D TMDs are emerging as a possible alternative to silicon for transistor channels. The atomically thin materials offer the ultimate scaling of the channel thickness while maintaining a high mobility and the possibility of good gate control.[127,130] Furthermore, the 2D TMDs have band gaps in the region between 1-2 eV which is comparable to that of silicon. In this chapter, I will describe how the 2D TMDs can be utilized in future FET designs and review the progress in using phase-engineered MoS_2 and $MoTe_2$. Such a review is not presently available in the literature and this is therefore the first review of the combined experimental and theoretical studies of TMD heterophase devices.

A top-gated 2D FET is illustrated on Figure 10.1a. The two largest challenges of this design, is to reduce the contact resistance between the 2D channel and 3D metal electrode, and to find a method for area selective doping of the 2D channel. Solving the latter would also improve the contact resistance but local doping of the semiconductor below the contact, is not realizable using conventional ion implantation methods. The alternative doping methods and the challenges related to those where discussed in Chapter 5.

When a 2D material is contacted with a 3D metal, water or hydrocarbon layers will adsorb on the surface when the sample is exposed to air. 2D materials are more or less all surface and such surface contamination will therefore result in a large density of interface states at the interface between the 2D material and the metal. This tends to lead to Fermi level pinning and result in a large barrier for transport. Even if this
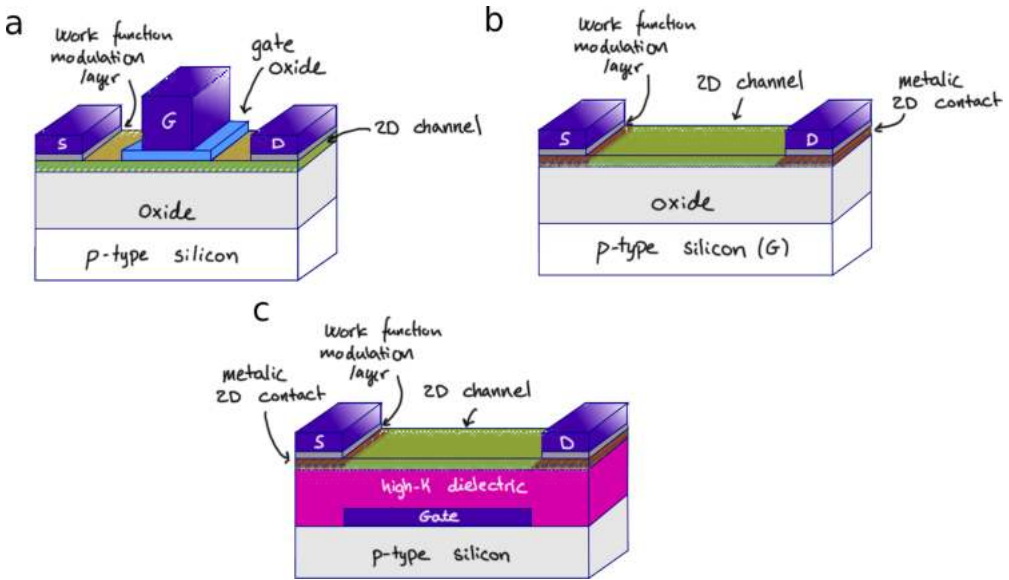
Figure 10.1: 2D TMD FET designs. **a** top-contacted 2D TMD FET, **b** phase-engineered 2D TMD FET with a back gate, and **c** state-of-the-art phase-engineered 2D TMD FET with back gate and a high-κ dielectric as the gate oxide.

effect is prevented, e.g. by fabrication in ultrahigh vacuum, a large degree of damage is induced by the following metal deposition.[19,131] Numerous experimental efforts have been conducted to reduce the amount of defects at the interface between 2D materials and their contacts. State-of-the-art devices report contact resistances down to 0.8 kΩ μm (MoS$_2$ contacted by indium capped gold).[132] However, there is still some way to go, to reach the IRDS 2022 goal for the source-drain resistance, i.e. contact and channel resistance total, of 271 Ω μm.

Edge contacts have shown some improvements over the top contacts as the distance between the atoms of the 2D material and 3D metal are closer in this setup. This results in a better orbital overlap and charge transfer.[133,134] Nevertheless, the fabrication process becomes very complicated.

A broad range of approaches have been investigated to bring down the contact resistance in the top-contacted design. Choosing the transition

metal as the contact material to enforce covalent bonding between the 2D channel and contact,[135] thin layers of e.g. Ti or In between the 2D material and contact,[132] intercalation of metal atoms between the channel and contact by annealing,[136] and inducing a phase transition to a metallic phase below the contact[11,12,70–72,79–81,89–92,137] have all proven to lower the contact resistance. In the case of phase transition, values below 100 Ω μm have been reported for both a heterophase $MoTe_2$ device[80] and a device consisting of 6 coupled MoS_2 heterophase FETs.[11]

10.1   Heterophase Transistors

A heterophase TMD FET is illustrated on Figure 10.1b. The local phase transition below the contacts ensures that the vulnerable semiconducting phase is isolated from the 3D metal contacts which is used to inject carriers into the metallic phase instead. The carrier injection between 3D metal and 2D metal has proven to be much less problematic.[91] In this section, I will review the current progress in fabricating and modelling heterophase devices based on either MoS_2 or $MoTe_2$.

The first device utilizing phase engineering was demonstrated in 2014 by Kappera *et al.*[70] In this study, the metallic 1T-phase of few layered MoS_2 was induced using a n-butyllithium treatment and then patterned with gold electrodes. The resulting contact resistance was measured to be between 0.6 and 0.7 kΩ μm. Since then, a large number of both experimental and theoretical studies have been conducted to investigate the electrical properties of these heterophase interfaces. The experimental work has mainly been focused on MoS_2 1T-2H interfaces[11,70,72,79,81] or $MoTe_2$ 1T'-2H interfaces.[12,80,89–92,137] However, heterophase devices of 1T-2H WSe_2,[71] WS_2,[149] TaS_2,[150] and NbS_2[151] have also been reported. Finally, devices where either the metal or chalcogen atom differs between the two phases have also been fabricated, examples are 2H-WS_2 with 1T'-ReS_2[152], 1T-VS_2 with 2H$-MoS_2$,[153] and H-MoS_2 with T'-$MoTe_2$.[154]

Figures of merit describing the device performance of heterophase FETs based on MoS_2 or $MoTe_2$ are summarized in Table D.1 in Appendix D. The performance of the MoS_2 based devices vary quite a bit and so does the fabrication methods and device setups. The general trend is that the devices are intrinsically n-type. The devices fabricated by Nourbakhsh
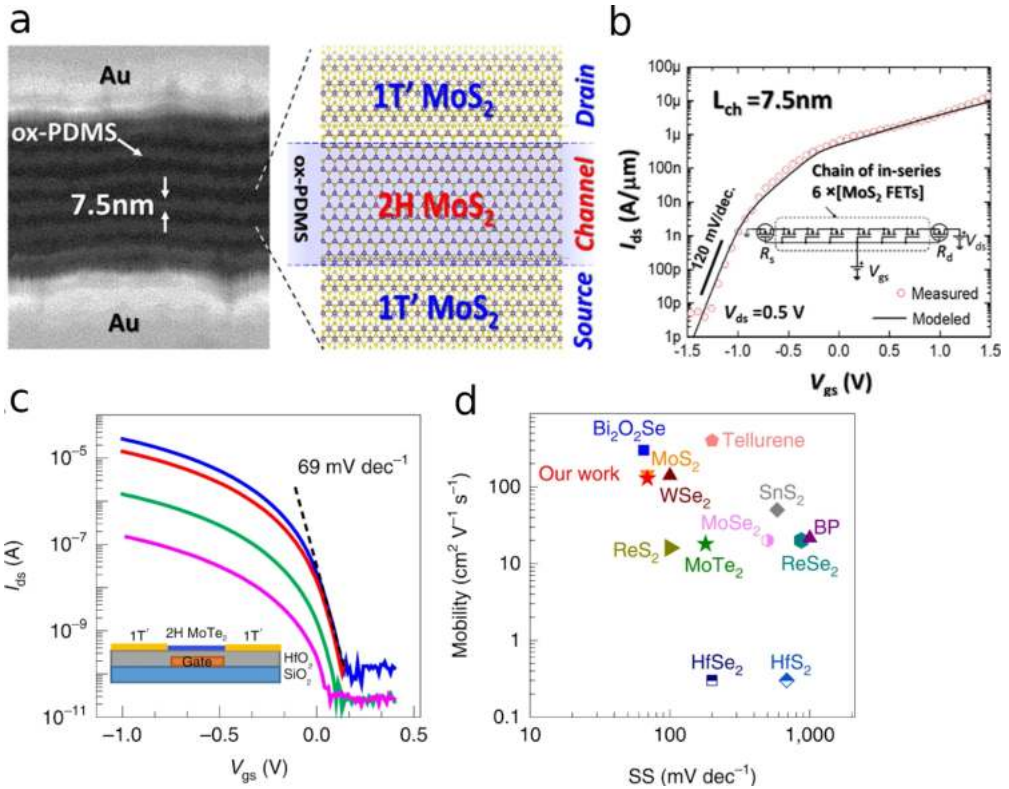
Figure 10.2: 2D TMD heterophase FET performance. **a** and **b** show a SEM image and illustration of the device and the transfer characteristics of the MoS$_2$ device fabricated by Nourbakhsh *et al.*[11] Reprinted with permission from Ref. [11]. Copyright 2016 American Chemical Society. **c** shows an illustration of the device setup and the transfer characteristics of the device fabricated by Zhang *et al.*,[12] and **d** shows a comparison between the value of the SS and mobility for 2D TMD based devices using a high-κ dielectric.[64,138–148] Reprinted with permission from Ref. [12]. Copyright 2019 Springer Nature.

et al.[11] consist of 6 vertically connected monolayer or 3-layer heterophase FETs with channel lengths of only 7.5 nm. The device is placed on 10 nm's of the high-κ dielectric HfO_2. The top part of Figure 10.2 show the device together with the transfer characteristics. The results are promising with a contact resistance of only 75 to 80 Ω μm and a sub-threshold slope of 120 mV/dec.

The performance of the $MoTe_2$ based devices show better agreement across different experiments. The contact resistance is measured to be between 0.5 and 14 kΩ μm and the FET mobility is between 7 and 50 cm^2/Vs for all devices except the one fabricated by Zhang *et al.*[12]. In this device, the back gate has been localized below the 2H-phase and the high-κ dielectric HfO_2 was used as the gate oxide as illustrated on Figure 10.2c and 10.1c. This results in an impressive FET mobility of up to 130 cm^2/Vs and a very low sub-threshold slope of only 69 mV/dec. Figure 10.2d shows a comparison of the best values of the SS and mobility of 2D TMD based homophase devices with this heterophase device. The comparison illustrates that the heterophase design results in a highly competitive performance. The Schottky barrier height has been measured using either the activation energy method and the barrier dependence on gate potential[12,80,89,91] or by Kelvin probe force microscopy[92,137]. With the exception of the device fabricated by Cho *et al.*[80], which shows n-type behavior and a barrier of 10 meV, there is agreement that the barrier is p-type with a height of 20-30 meV. The disagreement with the work by Cho *et al.* can be explained since the fabrication method of this device was laser irradiation. This method is very destructive and can easily result in a device with a large concentration of defects. As discussed in Chapter 5, the most likely defect to form is Tellurium vacancies which will correspond to an n-doping of the material.

10.1.1   Ab-initio Studies

These experimental achievements have inspired a great number of theoretical studies which have applied ab-initio calculations to gain more insight on the charge transport in these devices. Figures of merit describing the performance of simulated heterophase interfaces based on MoS_2 or $MoTe_2$ are summarized in Table D.2-D.3 in Appendix D and illustrated on Figure 10.3. The simulation methods applied in these studies can be divided into

three groups. In the order of increasing accuracy:

1. Pure DFT calculations. Either the work function of the two phases are compared from a calculation of each isolated crystal which allows for a barrier estimate from the Schottky-Mott rule or the projected band structure or density of states of a nanoribbon configuration of the interface is used to probe the electronic structure at the interface. Method 1 and 2 on Figure 10.3.

2. DFT calculations are used to create a tight-binding basis set e.g. using Wannier functions which allows for a simulation of a large scale device using a semi-classical model and this basis set. Method 3 and 4 on Figure 10.3.

3. DFT calculations are combined with the non-equilibrium Greens function method for self-consistent device simulations.(Method 5 and 6 on Figure 10.3.

As discussed in Chapter 5, the phase boundary between the 2H- and 1T- or 1T'-phase primarily form along the zigzag (ZZ) direction in MoS_2. In MoTe, the 1T'-2H phase boundary forms along the ZZ direction or at a 60 degrees angle from the ZZ direction. The theoretical studies have been carried out for monolayer interfaces both along the armchair (AC) and ZZ direction for both materials. The 60 degree rotation between the H and T'-phase is not accessible using these methods since the T'-phase isn't periodic perpendicular to this interface. The type of phase boundary is indicated on Figure 10.3 by the color. T-H interfaces along the ZZ direction form 4 distinct boundaries which correspond to the 8 boundaries of the 1T'-1H interfaces defined in Chapter 8 but where the a- and d- types and the b- and c-types become equivalent. The 4 types are illustrated on Figure E.1 in Appendix E. Two types of phase boundaries along the AC direction of the T'-H interface (AC and AC*) have been investigated and one type of the T-H interface (AC). These three phase boundaries are illustrated on Figure E.2 and E.1, respectively.

Most attention has been given to devices based on monolayer MoS_2 where at least 15 studies have been carried out.[11,79,118,155–159,161,163–168] Among these studies, both doping level and interface geometry have been varied. The 1H-1T interface without doping forms an n-type contact and the NEGF-based calculations agree on a relatively high Schottky barrier
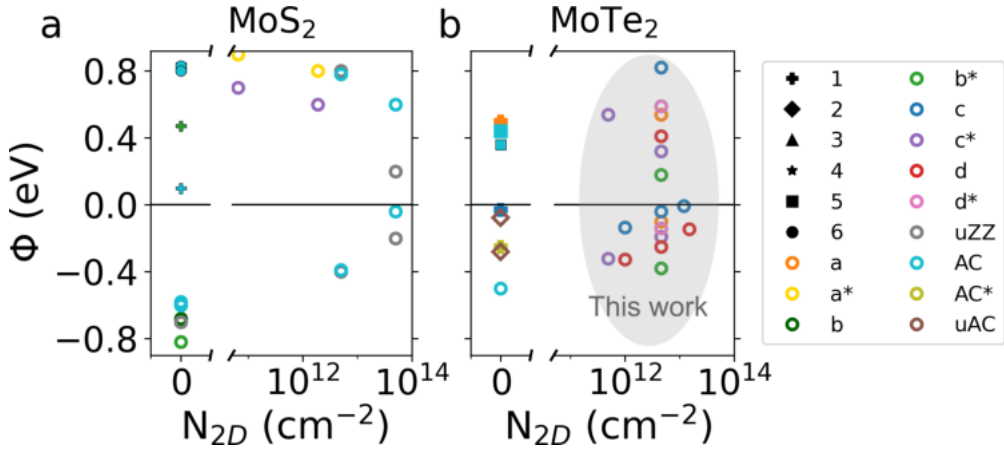
Figure 10.3: Calculated barrier heights of MoS_2 and $MoTe_2$ heterophase interfaces.[11,22,79,89,90,117,118,155–162] Filled markers show barriers of T-H interfaces and open markers show barriers of T'-H interfaces. The symbol denotes the method, 1: DFT@PBE, 2: DFT@PBE + SOC, 3:DFT@PBE+NTV, 4: DFT@PBE + TB-NEGF, 5: DFT@LDA + NEGF, 6: DFT@PBE + NEGF. The color denotes the atomic arrangements at the interface. a-d* are the configurations defined in Chapter 8, AC and AC* are the armchair interfaces defined on Figure E.2 and E.1, and uZZ and uAC denote unidentified ZZ or AC type phase boundaries.

height around 0.8 eV. The T'-H interface without doping, on the other hand, tend to form a p-type contact with a slightly lower but still rather large Schottky barrier around 0.7 eV.

The variance of the Schottky barrier height between T' and H $MoTe_2$ with the type of phase boundary and the doping level was described in Chapter 8. The results from this Chapter are marked by the grey region on Figure 10.3b. Similar investigations have been made for MoS_2 interfaces by Urquiza et $al.$[118] (cyan and grey open circles on Figure 10.3a) illustrating how the barrier decreases with increasing doping. Similar investigations have been performed by Fan et $al.$[161] and Liu et $al.$[159] who demonstrated that the barrier height can be electrostatically tuned by varying a back gate potential. The study by Urquiza et $al.$[118] concluded that changing the interface geometry between an interface along the zigzag direction to one which is along the armchair direction has limited effect

on the barriers of interfaces with a doping level of 5×10^{12} cm^{-2}. However, the barrier height of the interfaces with a doping level of 5×10^{13} cm^{-2} changed by up to a factor of 4. Saha et $al.$[157] (yellow and purple open circles on Figure 10.3a) have investigated the effect of geometry and doping on two kinds of phase boundaries along the zigzag direction. The results generally agree with the findings of Urquiza et $al.$[118]

A number of theoretical studies have also been conducted on heterophace interfaces of MoTe$_2$. Without any doping, the T-phase creates an n-type contact with the H-phase with a barrier height around 0.4 eV. The results on the H-T' interface are less consistent. Both n- and p-type contacts are reported depending on the method and phase boundary type. This is in agreement with the conclusion of Chapter 8 that the barrier heights of MoTe$_2$ heterophase interfaces are very dependent on the atomic positions at the interface.

To conclude this review, I will include a discussion on the channel lengths of the simulated devices and how this is related to comparing the simulations with the experimental results. An important thing to notice, is that many of the simulated devices have relatively short channel lengths. This is partly due to the large computational power required for simulating larger devices and partly because some of the studies wish to investigate the devices in the context of short-channel effects. As discussed in Chapter 7, the depletion width of a 2D metal semiconductor interface is very long. Most of the simulated devices on Figure 10.3 have channel lengths between 5 and 9 nm's. However, as demonstrated in Chapter 8, the depletion widths of free-standing MoTe$_2$ interfaces increases rapidly for low doping and can be more than 10 nm's already at doping levels around 5×10^{11} cm^{-2}. Correspondingly, Urquiza et $al.$[118] found that a semiconductor length of 8.5 nm wasn't enough to capture the entire depletion region of free standing MoS$_2$ interfaces without any doping. The relatively small computational cells contrast the experimentally investigated devices which all, except the ones fabricated by Nourbakhsh et $al.$[11], have channel lengths in the μm scale. If the computational cell is too small to include the entire depletion region, the interface dipole isn't completely screened which result in a charge build-up at the semiconductor boundary of the cell. The charge build-up creates a linear band bending and potentially affects the barrier height. It is therefore necessary to include either a high doping, a very large computational cell, or both, to reproduce the behavior seen in the experiments.

Simulated interfaces in which the entire depletion width is sure to have been captured have been presented by Urquiza *et al.*[118] for MoS_2 and in this thesis for $MoTe_2$. In the case of MoS_2, the highly n-doped device with an interface geometry along the zigzag direction has a calculated barrier of 0.2 eV which agrees reasonably well with the device fabricated by Katagiri *et al.*[79] who reported a n-type barrier height between 0.13 and 0.18 eV. In the case of $MoTe_2$, the p-doped c-type $MoTe_2$ interfaces have barriers below 40 meV when the doping exceeds 5×10^{12} cm^{-2} which is in agreement with the experimentally reported values of 20-30 meV. As we have seen, the barrier height varies enormously with the type of phase boundary. However, if the activation energy method is used to extract the barrier height, the result will reflect the lowest barrier at the interface. This means that if just some part of the interface has formed the favorable c-type boundary, this might result in the very low measured barrier height.

Even though some agreement can been achieved, a comparison between the experimental and theoretical results is all-in-all difficult to perform. The fabricated devices differ from the simulated devices in many ways. First of all, only a few of the simulated devices include a substrate[159–161,165] and most consider only a single interface, whereas the experiments are performed on a symmetric device with an interface at both the source and drain. Multi-layer and substrate effects, the presence of defects, and finite temperatures leading to electron-phonon interactions in the experiments may all affect the size of the barrier. The presence of defects could very well increase the probability of localized states in the interface and electron-phonon interactions could lead to phonon assisted tunneling. The next chapter will present ab-initio calculations on heterophase $MoTe_2$ FETs where both doping, substrate and a back-gate are included in order to make better comparisons with the experimental results.

In conclusion, heterophase interfaces of both MoS_2 and $MoTe_2$ have been given a great deal of attention the last decade and enormous progress has been made both in the experimental and theoretical studies. The early results were inconsistent both between different experiments and between experiment and simulation but during the last couple of years, the picture has begun to take shape and some general conclusions have been drawn. $MoTe_2$ seems be the most promising material since the phase transitions are easier to induce in this material due to the small energy difference between the H- and T'-phase and since these devices consistently show high FET mobility and small barrier heights.

Ab-initio Modelling of MoTe$_2$ Heterophase FETs

This chapter will demonstrate the performance of monolayer heterophase MoTe$_2$ FETs using ab-initio calculations. The figures of merit describing the device performance will be compared to the performance of the fabricated devices which were summarized in Table D.1 and the 2025 high-performance device requirements of the IRDS roadmap. The goal of this comparison is two-fold. The first objective is to validate that modelling
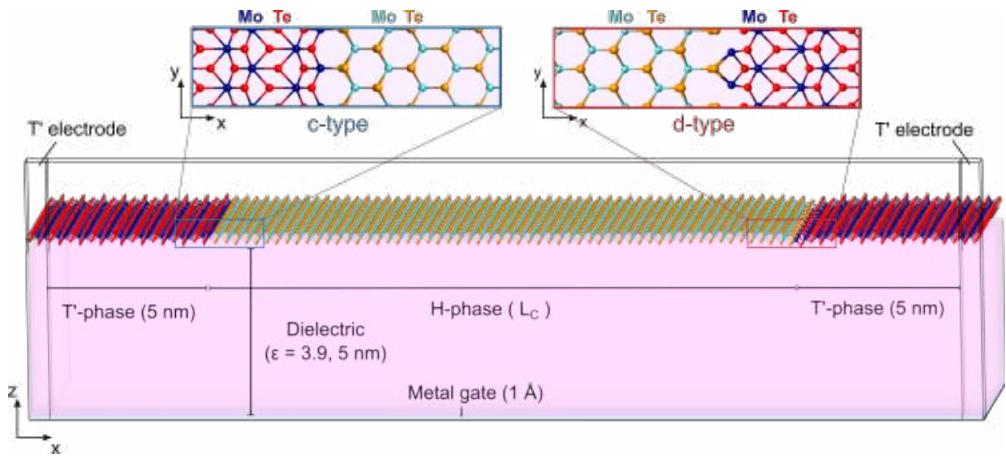

Figure 11.1: MoTe$_2$ heterophase FET on a back-gate and substrate. The top part shows the atomic configurations of the two contacts seen from the top. The bottom part shows the device consisting of a H-phase channel and two T'-phase contacts. The total cell size is $(10+L_C, 0.718, 15.0)$ nm with L_C being 18 or 20 nm's.

devices with channel lengths around 20 nm's can reproduce the behavior of the long-channel devices which the experiments are based upon. The second objective is to use the results of both the calculations and measurements to understand the trends in heterophase device behaviors and evaluate the prospects of using this technology in future transistor designs.

The device setup used for these calculations is shown on Figure 11.1 and corresponds to the setup used to investigate the effects of doping in Chapter 8 but where T'-phase contacts are placed on both sides of the H-phase channel to complete the transistor setup. Two channel lengths are investigated, 18 and 20 nm's. The phase boundaries have been chosen to be of c-type to the left and d-type to the right. All the atoms have been p-doped by $N_A = 5 \times 10^{12}$ cm^{-2} to better compare with the experimental measurements which have shown p-type behavior. The distance between the substrate and the atoms is 2.4 Å as discussed in Chapter 8. At this doping level, the depletion widths of the c- and d-type phase boundaries are zero and 3.2 nm's, respectively, which means that the entire depletion region of each contact is included at zero gate potential. The Schottky barrier heights in this condition are therefore not subject to electrostatic interactions between the two contacts in agreement with the situation in a long-channel device.

The setup corresponds to a natural scaling length of 1.48 nm's using eq. (9.1). The dielectric constant of the channel is estimated as the effective dielectric constant of the media above and below the monolayer, $\varepsilon_{ch} \sim \varepsilon_{eff} = (1 + 3.9)/2$. The thickness of the channel is defined as half the height of a 2H-phase unit cell, $t_{ch} = 0.70$ nm. Channel lengths above 15 nm's should therefore, according to the simple design rule, be free of short channel effects. Tunneling between the source and drain is avoided and since the gate and gate oxide are described classically, no tunneling can occur between the channel and gate either.

These calculations differ from previous DFT+NEGF calculations on the MoTe$_2$ heterophase device in two ways. The current in a symmetric FET setup with both a source and drain contact has not been modelled using the T'-phase as contacts before and channel length's above 9 nm's have not been modelled before.

11.1   Transfer Characteristics

To investigate the device performance, the transfer characteristics are calculated by applying a potential shift between the gate and the source (right electrode) and a small bias of $V_{sd} = -0.01$ V. The negative bias drives a current running to the left and a single barrier forms at the source (d-type phase boundary). This barrier is varied by changing the gate potential. Note, that it is a very small bias which is chosen due to convergence issues at larger biases. The convergence issue arise due to charge build-up in the 1T'-phase region at large biases. This can be avoided by including a longer 1T' phase region which hasn't been possible due to the computational cost of including more atoms. The corresponding transfer characteristics of the devices are shown on Figure 11.2. All currents are calculated at electrode temperatures of 300 K and compared to experiments conducted at this temperature.

In the range between 1.8 V and 2.4 V, the sub-threshold regime is seen. At gate potentials above 2.4 V, the devices start to show n-type behavior since the bands have been inverted. Note, that the potential at which the device switches from p- to n-type is underestimated due
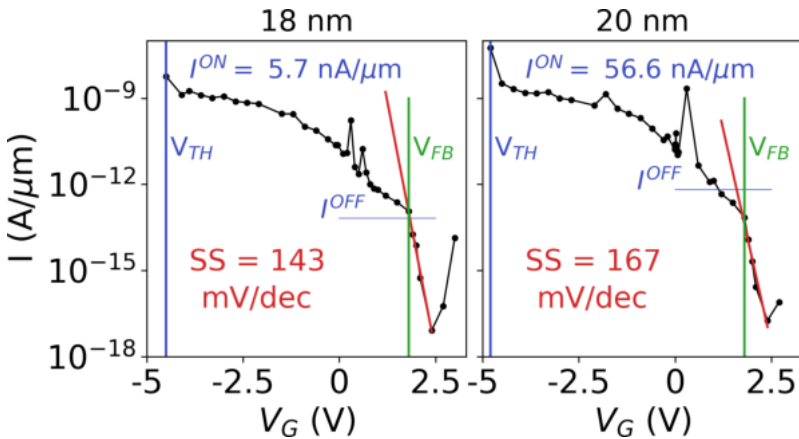

Figure 11.2: Transfer characteristics of the heterophase FETs at $V_{sd} = -0.01$ V. The ON-current, OFF-current, and sub-threshold slope (SS) are indicated. The flat-band condition is identified at $V_{FB} = 1.8$ V and the threshold voltage at $V_{TH} = -4.5$ V for the 18 nm device and $V_{TH} = -4.8$ V for the 20 nm device.

to the underestimated band gap in these PBE calculations. The region from 1.8 V and below is identified as the Schottky barrier regime. In order to compare with the previous calculations and experimental results, the lowest calculated gate potential is defined as the threshold voltage, $V_{TH} = -4.5$ V in case of the 18 nm device and $V_{TH} = -4.8$ in case of the 20 nm device. Without calculations at lower gate potentials, however, it is difficult to determine if the device is completely turned on at this point. I will return to this in the next section.

Rather large spikes in the current can be seen around zero gate potential for both devices. These spikes mainly occur due to quantum confinement effects in the channel. In the Schottky barrier regime, the semiconductor states between the barrier bottom and the valence band top are trapped in a confining potential between the barrier to the left and right. This confinement creates standing waves in the projected density of states (DOS) as illustrated in the case of the 18 nm device at $V_G = 0.3$ V on Figure 11.3. Two of these standing waves represent a peak in the DOS close to the bottom of the barrier as highlighted by shaded blue boxes and arrows in the DOS plot. Since the barrier is thin in this region, the states bridge the barrier with the same consequences as discussed in rela-
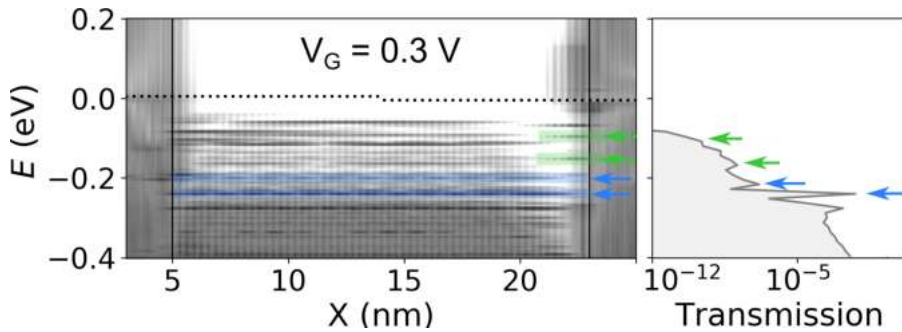
Figure 11.3: Quantum effects in the 18 nm device visualized by the projected DOS and transmission at $V_G = 0.3$ V. The chemical potentials of the left and right electrode are illustrated by the dotted lines. The green shaded areas and arrows indicate examples of interface states and blue shaded regions and arrows indicate examples of standing waves due to quantum confinement. The peaks in the transmission spectrum related to these states are indicated by the green and blue arrows.

tion to the interface states in Chapter 8. Two peaks are clearly visible in the transmission spectrum at the same energies as these standing waves and the transmission peaks result in the relatively large current seen for $V_G = 0.3$ V in the transfer characteristics. Note, that also the interface states which originate from the T'-phase are visible at this contact. These states and the corresponding rises in transmission are marked by green arrows on the figure. Both types of states are present at the other gate potentials as well and in general contribute to the total current by tunneling. At this gate potential, the effect is especially strong, as illustrated by the large peak in the transmission spectrum at the lowest of the blue arrows.

From the transfer characteristics, the sub-threshold slope, power supply voltage, ON-current, and I^{ON}/I^{OFF}-ratio can be identified and compared to the values of fabricated devices.

ON-current The ON-currents of the 18 and 20 nm devices are 5.7 and 56.6 nA/μm, respectively. These are not very large values but, keep in mind that, the bias is only -0.01 V. In Table 11.1, the ON-currents and power supply voltages of these two devices are compared to the ON-current of three fabricated devices and the IRDS 2025 goal. These three devices have been chosen for comparison since they represent the pool of fabricated

Ref.	t_{EOT}	t_{ch}	L_C	I^{ON}	$V_{sd}(I^{ON})$	V_{DD}	SS
[12]	1.87 nm	8 nm	4 μm	0.25 μA/μm	0.1 V	0.8 V	69 mV/dec
[91]	300 nm	5-6 nm	4-15 μm	15 nA/μm	50 mV	40 V	
[89]	300 nm	8 nm	20 μm	39.6 nA/μm	-0.1 V	100 V	
This Work	5 nm	ML	18 nm	5.7 nA/μm	-10 mV	6.0 V	143 mV/dec
This Work	5 nm	ML	20 nm	56.6 nA/μm	-10 mV	6.4 V	167 mV/dec
This Work*	1 nm	ML	18 nm	209 μA/μm	-0.65 V	1.2 V	29 mV/dec
This Work*	1 nm	ML	20 nm	226 μA/μm	-0.65 V	1.3 V	33 mV/dec
IRDS 2025[1]	1 nm	7 nm	14 nm	873 μA/μm	0.65 V	0.65 V	72 mV/dec

Table 11.1: EOTs, channel thicknesses, channel lengths, ON-currents, power supply voltages and sub-threshold slopes of MoTe$_2$ based heterophase devices. *Scaled using equations (11.1) and (11.2).
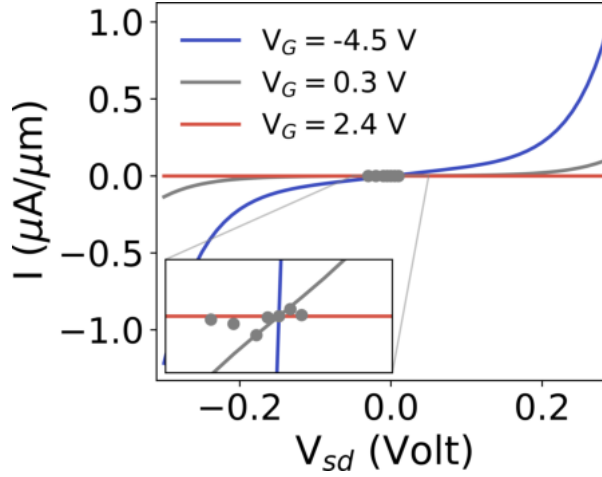
Figure 11.4: The current-bias relationship of the 18 nm device calculated using eq. (11.1) (lines) and self-consistent DFT+NEGF calculations (dots).

devices rather well and since these studies are very well documented. Not all of these values are directly reported in the papers and are therefore an estimate of the order of magnitude rather than absolute values. The two devices on 300 nm SiO_2 substrates (Ref. [91] and [71]) have ON-currents comparable to the ones calculated here. The device from Ref. [12] show a large improvement in the ON-current moving from nA to μA values. This device is placed on 12 nm's of HfO_2 which corresponds to an equivalent oxide thickness (EOT) of 1.87 nm's.[i]

In order to compare with the IRDS 2025 goal, I will estimate the currents through the modelled devices at a higher bias. The Landuar formula in eq. (8.2) is used without self-consistently updating the transmission function,

$$I \sim \frac{2q}{h} \int T(\varepsilon, V_{sd} = -0.01 \text{ V}) \left[f\left(\frac{\varepsilon - \mu_L}{k_B T} \right) - f\left(\frac{\varepsilon - \mu_R}{k_B T} \right) \right] d\varepsilon. \quad (11.1)$$

.

The resulting IV curve is shown in case of the 18 nm device on Figure 11.4 together with a few self-consistent results which where obtained at

---

[i]From eq. (9.2) using $\varepsilon_{ox} = 25$.[169]

a gate potential of $V_G = 0.3$ V. The self-consistent results are showed in the inset as round markers. Comparing to the non self-consistent approximation, the calculations performed at biases close to zero agree with the approximation. These results are not yet fully analyzed, however, the disagreement could be explained by the momentum conservation restriction which was discussed in Chapter 8. If fewer k-points contribute to the transport, the current will decrease. In a real device, impurities and electron-phonon interactions would reduce this restriction but the effects could also alter the current in less predictable ways. Assuming that the band alignment created by the gate potential is what dominates the size of the current, the approximation in eq. (11.1) gives a reasonable prediction.

Using eq. (11.1), the ON-current of the modelled devices is calculated at $V_{sd} = -0.1$ and -0.65 V in order to compare with the measurements and IRDS value. At -0.1 V, this results in a current of 59 nA/μm for the 18 nm device and 0.47 μA/μm for the 20 nm device. The difference in these two values can be attributed to the lower threshold potential of the 18 nm device. The value of the 20 nm device is in good agreement with the ON-current reported by Ref. [12]. All-in-all, the calculated ON-currents of these devices seem to agree with the fabricated devices which support that the channel lengths of these devices is sufficient to reproduce the behavior of the devices with μm scale channels.

At -0.65 V, the ON-currents are 209 and 226 μA/μm, respectively. This is a few times lower than the IRDS goal. However, this goal is based on a device with a channel thickness of 7 nm which corresponds to 10 monolayers of MoTe$_2$. Assuming that the current of each monolayer is additive, the ON-current of devices with 10 monolayers will be 2.09 and 2.26 mA/μm which reaches the ON-current goal with some room for the uncertainty in using these estimates. Since the calculations have been able to reproduce comparable ON-currents to the fabricated devices, one might speculate that those devices would be able to live up to the IRDS goals as well.

Power Supply Voltage   Table 11.1 also compares the power supply voltages of the devices. The devices on SiO$_2$ require very large power supply voltages due to the thickness of the oxide whereas the device on HfO$_2$ shows an impressively low V_{DD}. The power supply of the modelled devices is found as $V_{DD} = V_{TH} - V_{OFF}$ where the OFF-potential is defined

as the potential which corresponds to the OFF-current. The OFF-currents are indicated by the horizontal blue lines on Figure 11.2 and are defined as the ON-current divided by the I^{ON}/I^{OFF}-ratio defined by IRDS which is 8.73×10^4,

$$I^{OFF} = \frac{I^{OFF}_{IRDS}}{I^{ON}_{IRDS}} I^{ON}.$$

Note, that close to these values of the OFF-current, no large spikes occur in the current which otherwise might result in a leakage current. The power supply voltages are 6.0 and 6.4 V for the 18 and 20 nm device respectively. When the gate oxide is considered as a continuum dielectric, as it is in these calculations, a reduced oxide thickness will reduce the gate potential needed to create the same field,

$$|\vec{E}|_{ML} = \frac{V^{calc}_G}{t^{calc}_{EOT}} = \frac{V^{thin}_G}{t^{thin}_{EOT}} \Rightarrow V^{thin}_G = \frac{t^{thin}_{EOT}}{t^{calc}_{EOT}} V^{calc}_G. \qquad (11.2)$$

$|\vec{E}|_{ML}$ is the size of the electric field created by the gate at the position of the monolayer, V^{calc}_G and t^{calc}_{EOT} are the gate potential and EOT used in the self-consistent calculations, and V^{thin}_G is the gate potential creating the same field when the EOT is t^{thin}_{EOT}. Using this relation for $t^{thin}_{EOT} = 1$ nm allows for a direct comparison with the IRDS goal. This results in power supply voltages of 1.3 and 1.2 V which is about twice the size of the IRDS goal. A possible approach to improve these values further would be to use both a top and bottom gate or to make a Gate-All-Around setup to improve the gate control.

It is worth noticing that the maximum possible I^{ON}/I^{OFF}-ratios of these devices are very large, $6.9{\times}10^8$ and $3.1{\times}10^{10}$, respectively. The large I^{ON}/I^{OFF}-ratio seems to be a general feature of heterophase devices and is represented in most of the experiments and calculations. Heterophase devices may therefore be especially well-suited for applications where it is important that the current is cut off completely in the OFF-state.

Sub-threshold Slope   The sub-threshold slopes are 144 and 167 mV/dec for the 18 and 20 nm channel, respectively. The IRDS roadmap suggests a SS value of 72 mV/dec by 2025 for an EOT of 1 nm and in the study

by Zhang *et al.*[12] a value of 69 mV/dec was obtained using HfO_2 with an EOT of 1.87 nm. This study is the only experiment which have reported the SS-value. The MoS_2 based heterophase devices have SS values of 1 V/dec and 0.8 V/dec for devices placed on a thick SiO_2 substrate and 120 mV/dec for a device on 10 nm's of HfO_2 (EOT of 1.56 nm). Scaling the gate potential values in these calculations to an EOT of 1 nm using eq. (11.2) leads to very low SS values of only 29 and 33 and mV/dec. These values break the limit of 60 mV/dec defined by eq. (7.3) which suggest that either the scaling using eq. (11.2) is too simple or that eq. (7.3) does not describe the behavior very well even though thermionic emission must be the dominant transport mechanism. All-in-all these results suggests, as in the case of the power supply voltage, that good gate control is possible for the heterophase devices by using a small EOT.

11.2   Schottky Barrier

Using the projected density of states, the Schottky barrier dependence of the gate can be directly visualized. Figure 11.5 shows the evolution of the conduction and valence band and Schottky barrier height with gate potential in the device with a channel length of 18 nm. The band at the flat band potential $V_{FB} = 1.8$ V is marked in green on Figure 11.5a. Gate potentials above this value show n-type band bending whereas those below this potential show p-type behavior. At the bias of -0.01 V and zero gate potential, the bands form a p-type barrier at the d-type boundary and are flat at the c-type boundary in agreement with the behavior of the isolated interfaces described in Chapter 8. Increasing the gate potential pulls down the bands and turns the device off whereas decreasing the gate potential lifts the bands and turns the device on. The band evolution follows the simple picture which was shown on Figure 9.2 approximately even though the barrier in the left side changes quite a bit with the gate potential as well.

At the lowest gate potential, $V_G = -4.5$ V, a barrier in the right side is still present even though it is very thin. This suggests that the ON-current defined in the above could be increased by further decreasing the gate potential. Comparing to the 20 nm device, the lowest gate potential was $V_G = -4.8$ V. At this potential, the valence band is raised above
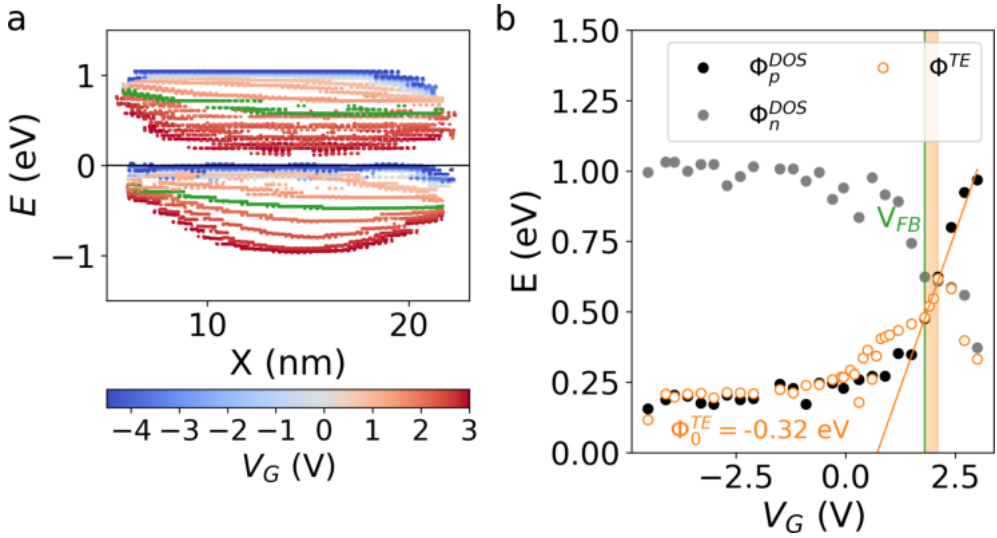
Figure 11.5: Band bending and Schottky barrier height as a function of gate potential in the 18 nm device. **a** shows the valence and conduction band at different gate potentials. The flat band potential $V_{FB} = 1.8$ V is shown in green. **b** shows both the n- and p- type barrier height at the right contact which has a d-type phase boundary. The orange open circles show the TE barrier found using the activation energy method and the orange line shows a linear fit to the values within the orange shaded region.

the Fermi level and the right side barrier has disappeared. This explains the large current at this potential seen in the transfer characteristics and suggests that the threshold voltage is indeed at this potential. The current is expected to saturate if the gate potential is decreased further since the transmission onset already occurs at the Fermi level at this potential.

The Schottky barrier height is found both using the DOS and the activation energy method and shown on Figure 11.5b. Since the device changes from being p- to n-type at high gate potentials both the n- and p-type barrier of the right contact are shown. The crossover between the n-type and p-type behavior is identified at $V_G = 2.4$ V in agreement with the behavior seen in the transfer characteristics.

The sub-threshold (ST) regime is marked by the shaded orange region on Figure 11.5b. In this region, the bands are inverted and charge is

transported via thermionic emission alone which results in a one-to-one correspondence between the TE and DOS barriers. The activation energy method for barrier extraction assumes that this linear dependence of the Schottky barrier represents the general electrostatic response of the Schottky barrier and that a linear fit to the TE barriers in this region therefore enables a determination of the Schottky barrier at zero gate potential. However, as the calculations in Chapter 8 demonstrated by varying the doping level, the electrostatic response of the Schottky barriers at these interfaces is not smooth. The behavior is dominated by barrier jumping between energies where the interface DOS is low. Such a jump can also be identified on Figure 11.5b at a p-type barrier of 0.35 eV where the linear behavior of the DOS barriers breaks. Since the gate dependence of the Schottky barrier isn't linear, the linear fit of the TE barriers in the ST regime fails to predict the zero gate barrier. The fit instead results in a barrier height of -0.32 eV which does not carry any physical meaning. The negative barrier height suggests that the thermionic emission model and eq. (7.3) does not represent the ST behavior very well and might also explain why the SS values could be scaled below 60 mV/dec.

For gate potentials below the flat-band condition, the TE barriers are generally overestimated or in agreement with the DOS barriers. Due to tunneling contributions in this regime, an underestimation would actually be expected. This underestimation does not occur due to the momentum conservation restriction which significantly limits the current, as discussed in Chapter 8.

The barrier heights of both devices are compared to the measured barriers of heterophase MoTe$_2$ devices in Table 11.2. In this table, all experiments which have estimated a barrier are included. The experimental barriers have been extracted either using the activation energy method or using Kelvin probe force microscopy (KPFM). The activation energy barriers can be compared to the calculated TE barriers and the KPFM barriers can be compared to the Schottky-Mott limit of the barrier (SM barrier).

The measured TE barriers agree very well between the experiments and there is agreement that the TE barrier is around 30 meV. However, as the calculations have demonstrated, this does not necessarily mean that the Schottky barrier defined by the electronic bands is small as well. The effects of having more than one monolayer and of electron-phonon interactions may reduce the quantum effects and result in a better agreement

Ref.	t_{EOT} / t_{ch} / L_C	Φ^{TE}	$T(\Phi^{TE})$	Φ^{SM}	Φ^{DOS}
[92]	- / ML / 20 μm			25 meV	
[137]	298 nm* / 7 ML / 10-60 μm			27.5 meV	
[89]	300 nm / 8 nm / 20 μm	30 ± 10 meV	240-300 K		
[12]	- / 8 nm / 4 μm	20 meV	300-400 K		
[12]	1.87 nm / 8 nm / 4 μm				
[91]	300 nm / 5-6 nm / 4-15 μm	22 meV	150-300 K		
This Work	5 nm / ML / 18 nm	-0.32 eV	300-450 K	0.20 eV	0.25 eV
This Work	5 nm / ML / 20 nm	-0.40 eV	300-450 K	0.20 eV	0.23 eV

Table 11.2: EOTs, channel thicknesses, channel lengths, and Schottky barriers of MoTe$_2$ based heterophase devices. *The substrate consists of 285 nm SiO$_2$ and 30 nm Al$_2$O$_3$ and the EOT is calculated using $\varepsilon_{Al_2O_3} = 9$.[169]

between the DOS and TE barrier. Since the doping level generally isn't well-known in the fabricated devices, the measured TE barriers may actually correspond to a very small band bending achieved by high doping levels. Lastly, the low measured TE barriers may be due to the favorable atomic arrangement at the c-type phase boundaries. Nonetheless, usage of eq. (7.3) for nano-scale devices based on 2D materials seems to be too simplistic, especially in the monolayer limit.

The barriers measured by KPFM are also very small in contrast to the SM barriers of these devices. The doping level of the H-phase will have a large impact on the work function difference between the two phases. As mentioned in Chapter 8, the work function of the T'-phase lies within the gap of the H-phase and a very light p-doping level may cause the favorable alignment.

The original motivation behind the heterophase devices was to find a solution to the large contact resistance between 3D metal contacts and H-phase TMDs. This contact resistance is primarily due to impurities between the contact and channel, the weak vdW bond between them, and damage from the metal deposition process. With regard to impurities, there is no reason to believe that these are more easily avoided in the heterophase devices in general. However, the weak bonds are definitely improved in the heterophase devices which form covalent bonds between

the two phases and the damage from metal deposition is not as problematic when depositing on the T'-phase. Metal contacts on the 1T'-phase create ohmic contacts.[89,91]

The contact resistance has been measured by Ref. [91] and [137] as 14 kΩ μm and 1.1 kΩ μm. These are quite high values compared to the IRDS 2025 goal for the total source-drain resistance which is 257 Ω μm. However, these resistances have been measured in devices placed on SiO_2 substrates which generally show a rather low current. The MoS_2-based devices on HfO_2 substrates fabricated by Nourbakhsh *et al.*[11] have contact resistances of 75 and 85 Ω μm. The resistance can not be obtained in a reliable fashion from the calculations presented here due to the convergence issues related to varying the bias.

To evaluate on the overall performance of the heterophase devices compared to the metal contacted 2D TMD devices, my personal guess is that they will perform comparably when using state-of-the-art fabrication methods. However, it may turn out that it is easier or cheaper to scale up the fabrication of the heterophase devices. Both Ref. [137] and [12] have presented wafers-scale arrays of heterophase devices fabricated using temperature controlled or selective precursor CVD processes.

I would like to raise the question if the zero gate Schottky barrier height is a good figure of merit for these nano-scale devices. The results presented here suggest that this is not the case. Even though the DOS barrier at zero gate potential is relatively large, the devices are capable of performing in accordance with the IRDS 2025 goals with respect to the ON-current and power supply voltage. The concept of a well-defined Schottky barrier seems to break down in the case of these devices since the barrier is punctured by quantum states from both sides, as demonstrated on Figure 11.3. As long as the device can be turned on and off without using too much power and a reasonable amount of current is produced, it doesn't really matter how high the Schottky barrier is. Using the Schottky barrier as a descriptor of the contact resistance and the contact resistance as a descriptor for the general device performance stems from the rather simplistic picture of the Schottky barrier which was presented in Chapter 7. This picture has worked relatively well in describing Schottky contacts between 3D materials but breaks down in the case of the atomic-scale device. The 2D devices are more complicated to describe, and there is no single parameter which contains enough information to evaluate the device. To evaluate 2D devices, it is necessary to measure the ON-current, power

supply voltage, and I^{ON}/I^{OFF}-ratios and evaluate the devices directly based on these quantities.

In conclusion, the DFT+NEGF method is capable of reproducing the behavior of the fabricated devices in terms of the resulting ON-current. The calculations showed that quantum mechanical effects at the atomically thin interfaces create tunneling channels which enhances the current and makes the Schottky barrier a poor descriptor of the device performance. In general, the results of these calculations and previous measurements suggests that the heterophase devices show potential of delivering a performance in accordance with the IRDS 2025 goals if a high-κ dielectric is used as the gate oxide. Adapting a finFET or Gate-All-Around (GAA) design would most likely improve the gate control further. The heterophase TMD design will probably not outcompete silicon any day soon. However, it has the potential to perform just as well and perhaps even better in the limit of very thin channels. It is a natural design for nanoribbon shaped channels which is used in the GAA design and very high I^{ON}/I^{OFF}-ratios can be achieved. So far, the experiments on the heterophase design have all presented proof-of-concepts. To truly justify this technology as a viable solution, also experimental efforts need to go to next level and demonstrate the competitiveness through comparisons to silicon based devices.

CHAPTER 12

Conclusions and Outlook

The objective of this thesis has been to demonstrate how ab-initio calculations can be used to model and understand the physics in nano-scale electronics. More specifically, the charge transfer mechanisms in 2D field effects transistors have been discussed through the conventional models and modelled using density functional theory and the non-equilibrium Green's function method. The thesis has focused on the phase-engineered 2D transition metal dichalcogenide transistor design and sought to understand and evaluate this technology.

The starting point of the thesis was to present the tools which are necessary for doing ab-initio calculations of nano-scale interfaces. A general method for evaluating the possible interfaces between two periodic crystals has been developed. There is in principle infinitely many ways to combine two crystals to an interface but using some simple parameters the possibilities can be narrowed down to the most probable interfaces. The systematic procedure evaluates which surfaces of the two crystals that are most likely to combine if the stability of an interface is assumed to correlate with the strain between the unit cells of the two surfaces and the interface cell area.

The method is based on the crystal unit cells and does not take the atomic positions into account. An improvement of the method might attempt to model the atoms by classical force fields to better estimate the stability of the resulting interface. However, as the results in this thesis have demonstrated, the chemistry at a nano-scale interface is extremely complicated and these classical potentials might not be able to reliably predict the stability. Machine learning methods are a rapidly growing field also within atom-scale physics.[170] It is perhaps a better approach to attempt to use such method for evaluating the interface stability. Minimization of inter-atomic forces has already been investigated using machine learning and interface formation energy predictions could be a continuation of these efforts.

The second part of the thesis introduced the transition metal dichalcogenides (TMDs) with focus on the electronic properties of the group-VI TMDs. The material properties which are important for understanding transport between two different phases such as the doping, defect formation and phase transformation was reviewed. Furthermore, a section was devoted to introducing the topological properties of the T'-phase TMDs which are classified as topological insulators. Interestingly, it was found that some edges of T'-phase MoS_2, $MoTe_2$, and WTe_2 host magnetic states. The magnetic states break the time-reversal symmetry which means that the properties of the edge states no longer are determined by the topological classification; the states are not protected from back-scattering and changing the topology of the bulk does not remove them. The magnetic states are not expected to influence the conductivity across the edge which is what is important in the heterophase device design.

The edges of the T'-phase which host magnetic states represent a discontinuity in the polarization. The polarization of a crystal is also a topological property which is well-defined both in the case of time-reversal symmetry and without. Gibertini *et al.*[104] have shown that the discontinuity in polarization on edges of H-phase TMDs guaranties metallic edge states. It could be interesting to investigate if the T'-phase edges are guarantied to host metallic states which are protected either by the time-reversal symmetry or the polarization. Perfectly conducting edge states have a range of interesting applications, an example is a topological transistor where the conductance is switched off or on by changing the topological state of the material.

The third part investigates how the dimensionality of a Schottky contact affects the current transport across the barrier. The classical theory of Schottky barriers is reviewed and transferred to 2D contacts. The electrostatics of a 2D Schottky contacts differs a lot from the 3D case. A 2D contact will always be a contact both between two materials and between each material and the air or vacuum. This fact, means that a field is formed in the vacuum outside a 2D interface. Furthermore, charge can not accumulate as line charge at a 2D metal edge and the interface dipole becomes long-ranging and with a spatial extend both at the metal and semiconductor side. The comparisons of charge transfer mechanisms in 2D and 3D contacts conclude that, in the 2D limit, both the thermionic emission and tunneling behaves differently and that the tunneling becomes more dominant than in 3D.

The Schottky barrier of a metal-semiconductor interface can be defined in different ways depending on which property of the contact one focuses on. In this thesis, I have classified four types of Schottky barriers in order to make fair comparisons between different calculations and experiments; the Schottky-Mott barrier, the density of states barrier, the transmission spectrum barrier, and the thermionic emission barrier. One of the main conclusions of this thesis is that the Schottky barrier isn't well-defined at atomic-scale interfaces. The need for a classification underlines this and illustrates that the concept of the Schottky barrier, in general, is rather complicated.

Ab-initio calculations are used to investigate the properties of T'-H contacts of $MoTe_2$. This investigation illustrates that the atomic configuration at the phase boundary dominates the size of the Schottky barrier seen in the density of states (DOS). Comparisons between different phase boundaries show that the atomic rearrangement at the interface generally modifies the effective potential more than the interface dipole. Tunneling currents are dominating the charge transfer and lead to relatively low TE barriers in the heterophase contacts. The tunneling is mediated by interface states which create a large density of states at the interface and in some cases results in a conducting bridge between the semiconductor conduction or valence band and the metal states. The interface states are investigated and it is found that they originate from the metallic T'-phase edge and therefore don't result in Fermi level pinning.

The doping dependence of the charge transfer properties was also investigated. It was found that the depletion width is much smaller than what the classical models predict but seems to scale as the build-in potential divided by the doping density as classically predicted. By varying the doping gradually, the effects of the interface states become very clear. The Schottky barrier seen in the DOS jumps across regions with a high interface DOS and the barrier height does not vary smoothly with the doping level.

Most of the conclusions found in this part will be valid for 2D Schottky contacts in general,

1. Tunneling is a more dominant charge transfer mechanism in 2D contacts.

2. The atomic rearrangements at the interface dominate the behavior

of the electrostatic potential.

3. Interface states affect the charge transfer.

4. The Schottky barrier is less well-defined in 2D due to the 'punctuation' of the barrier in the DOS created by interface states.

The prediction of an increased probability of tunneling is only based on the dimensionality and the dominance of the atomic rearrangement and quantum confinement is also expected to primarily be due to the 2D nature of the contacts. It would be interesting to investigate interfaces between two different 2D materials and see if interface states are present and if they dominate the behavior as much as in the case of heterophase contacts. This would enable drawing some more general conclusion on how 2D Schottky contacts behave.

The final part of the thesis was devoted to understanding and evaluating the properties of $MoTe_2$ heterophase FETs. The progress within fabricating and modelling TMD heterophase transistors was reviewed which concluded that the $MoTe_2$ based device has shown most potential so far. However, previous calculations of $MoTe_2$ devices have been based on too short channels to compare the results with the fabricated devices. Two $MoTe_2$ heterophase devices were therefore modelled with channel lengths of 18 and 20 nm's and compared to experimental measurements. The comparison concludes that the DFT+NEGF method is capable of reproducing the behavior of the fabricated devices and that the heterophase transistors have the potential to perform in accordance with the high-performance devices in the IRDS roadmap.[1] Comparing the experiments, it is clear that using a high-κ dielectric as the gate oxide is necessary in order to gain the necessary gate control.

It is easy to understand why the Schottky barrier has been used as a device metric when evaluating this very novel technology. It is highly difficult to compare different experiments because the doping is unknown and the device setup and fabrication method differ. In the simple picture, the Schottky barrier is an intrinsic property of an interface which shouldn't depend much on the experimental setup. However, the calculations presented in this thesis highlight that the Schottky barrier isn't a good indicator of the device performance in atomic-scale devices since a range of quantum effects dominate the charge transfer. Interface state mediated tunneling and enhanced charge transfer due to the standing waves

from quantum confinement have both been illustrated. When evaluating a 2D device, no single intrinsic parameter is enough to predict the performance. The metrics have to be based on the future applications of the device with focus on the energy efficiency.

The TMD heterophase FET is still at a stage of a rather simple design but using some of the same design strategies as seen in commercial devices have shown to improve the performance significantly. To fully evaluate the potential of this design, experimental efforts most go to the next level and benchmark the performance of the devices against silicon technology. Furthermore, if the heterophase devices are to become competitive with silicon based devices, a scalable method to fabricate the devices and to systematically dope the 2D channel must be developed. With such a method available, the prospects of using the 2D TMDs in transistors seems to be very promising.

Computational Details

A.1 Setting up the T'-edges

The setup and relaxation of the surface configurations follow four steps and the final configuration is shown on Figure A.1.

1. T'-phase is set up in the conventional unit cell and relaxed using periodic boundary conditions. This gives the 2D lattice parameters $a_{T'} = 5.73$ Å and $b_{T'} = 3.19$ Å.

2. The surface configuration is created from repeated units cells. The length of the central region monolayer is 50 Å which insures that the Hartree potential matches the periodic potential of the electrode at the left hand side where the electrode is attached.

3. The 3 atomic layers closest to the edge are allowed to relax and the remaining atoms are fixed.

4. A metallic region is placed in the bottom of the cell in order to apply an electric field perpendicular to the monolayer.

The structure relaxations are done without SOC and to a force tolerance of 0.02 eV/Å.

An unconventional set of boundary conditions is chosen for solving the Poisson equation. This is done to accommodate the gate construction and to avoid interactions between images. Dirichlet boundary condition (DBC) is used at the top and bottom of the cell so that the potential is fixed in the gate and grounded at the top of the cell. This is analogous to placing the surface between the two plates of a parallel-plate capacitor. For the electrode calculation, standard PBCs is used in all other directions. For the central region, on the other hand, the potential at the left side of the cell is fixed to the value of the potential of the electrode using a DBC
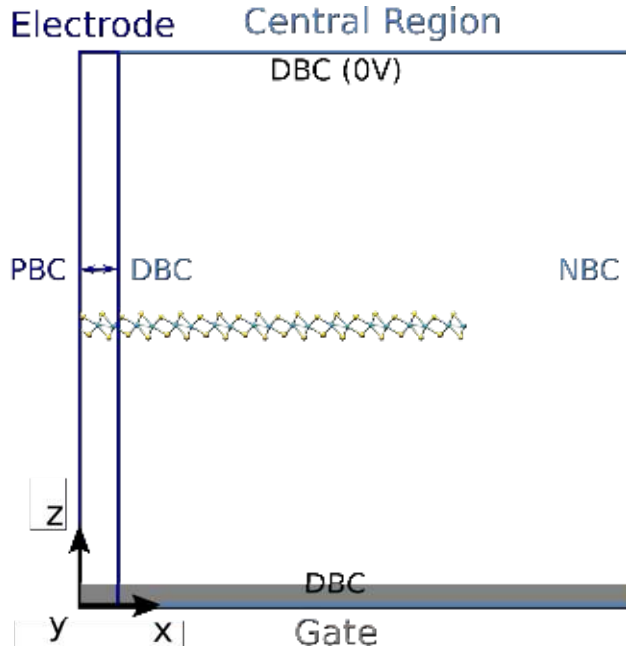
Figure A.1: The *SurfaceConfiguration* of T'-MoS$_2$ on top of a gate along with the applied boundary conditions. PBC, DBC, and NBC refers to different boundary conditions as explained in the text.

and the potential at right side is allowed to converge to the potential in the vacuum region by applying a Neumann BC (NBC).

Applying DBCs both at the top and bottom of the cell, forces the potential to be zero at those boundaries. The equipotential lines are correspondingly pushed away from these borders and the potential shift is present along the right border of the cell. Our investigations show that, if the cell is as high in the z-direction as it is long in the x-direction and has enough vacuum to the right, s.t. the potential has converged to a constant value when going from left to right, then the electronic levels of the system are equivalent to those of the ungated system. This corresponds to a cell height of 80 Å.

The k-point sampling of the (m) and (c) edge calculations are: 11 x 1 for the surface configurations, which are non-periodic in the x-direction, and 401 x 11 x 1 for the periodic 2D crystals. The k-point sampling of the (X) edge is 6 x 1 for the surface configuration, which is non-periodic

in the y-direction, and 6 x 401 x 1 for the periodic 2D crystal.

A.2   Setting up the MoTe$_2$ Interfaces

Reprinted with permission from the Supplemental material of [22]. The setup and relaxation of the device follows four steps which are illustrated in Figure A.2.

1. The 1H and 1T' phases are set up in the conventional unit cell and relaxed using periodic boundary conditions. This gives the 2D lattice parameters $a = 3.59$ Å for the 1H phase and $a = 3.52$ Å, $b = 6.37$ Å for the 1T' phase which compares well with the experimental values.[85,171]

2. The interface is created using the interface builder in QuantumATK.[30,172] The 1T' phase is strained by 2.12 % along the y-direction to make a match between the (200)-edge of 1T' and the (02-20)-edge of 1H. We choose to strain the 1T' phase in order to maintain the semiconductor properties.

3. A nanoribbon of this interface is created with 18 atomic layers of each phase and 20 Å of vacuum between periodic images in the x-direction. The 6 atomic layers closest to the interface are allowed to relax and the remaining 1T' phase is fixed while the remaining 1H phase is kept rigid to allow for a compression or elongation of the interface region.

4. The relaxed interface is converted to a device configuration in order to perform the NEGF calculations. The central region is composed of about 6 nm's of 1T' phase and 19 nm's of 1H phase. For these calculation we use Dirichlet boundary conditions between the central region and electrodes, periodic boundary conditions in the y-direction and Neumann boundary conditions in the z-direction to avoid electrostatic interactions between neighbouring interface dipoles. The cell height is 15 nm's which ensures that the out-of-plane fields due to the 2D interface are properly accounted for and that their effect on the size of the barrier is minimized.[173–175]

1 Relaxation of 1H and 1T' unit cells   **2** Creating the interface

1T' electrode:
(6.38, 7.18, 25) Å

1H electrode:
(6.22, 7.18, 25) Å

$\varepsilon_{yy}{}^{1T'} = 2.12\ \%$

(3.59, 3.59, 25) Å   (6.37, 3.52, 25) Å   (200)   (02-20)

3 Relaxation of the nanoribbon

Fixed   Free   Rigid

(135, 7.18, 25) Å

4 Creating the device

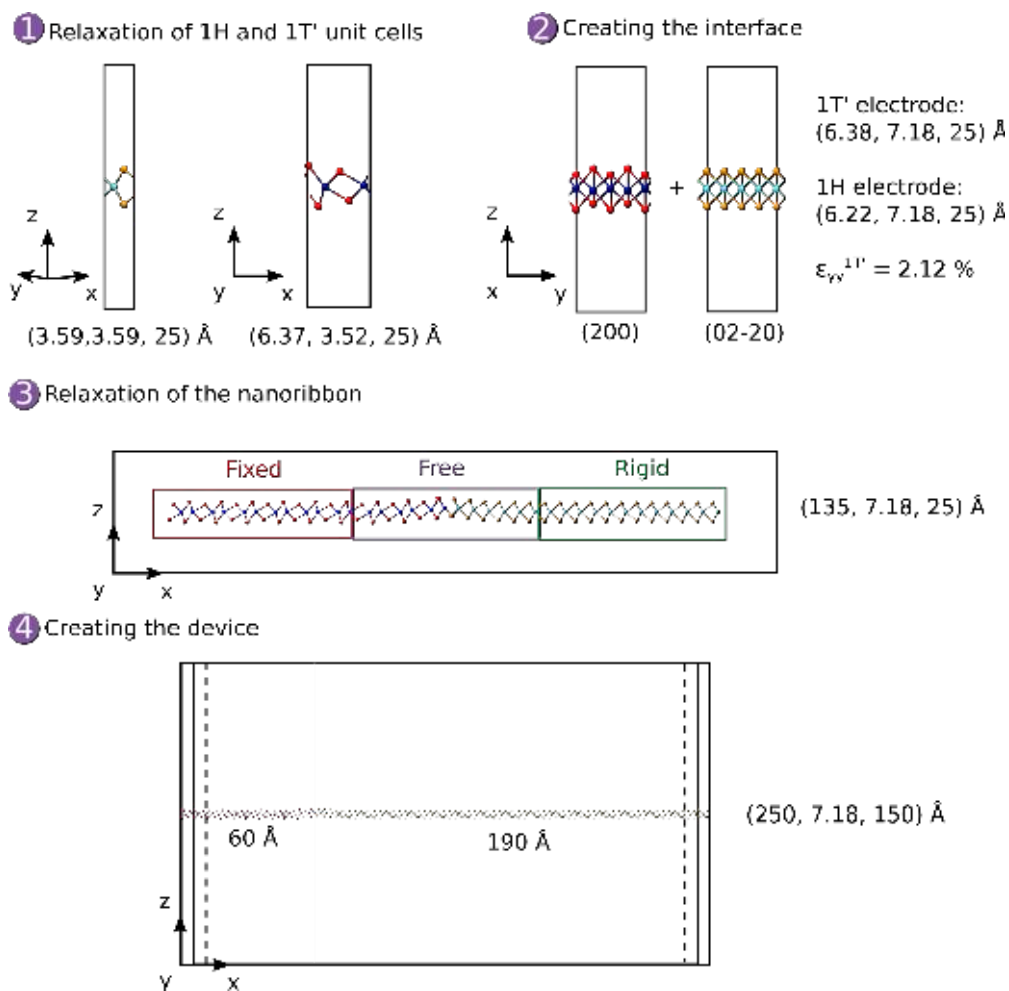60 Å   190 Å   (250, 7.18, 150) Å

Figure A.2: The relaxation scheme for setting up the device along with the unit cells of each calculation.

All the structure relaxations use a force tolerance of 0.02 eV/Å and the k-point grid for the isolated 1H phase is (7, 7, 1) while it is (6, 11, 1) for the isolated 1T' phase and $(k_x, 6, 1)$ for the remaining calculations. $k_x = 1$ for the nanoribbon calculation and $k_x = 401$ for the NEGF calculation. The occupations are described by using a Fermi-Dirac occupation function with an electronic temperature of 300 K.

Formation Energies of Edges and Interfaces

B.1 Stability of the MoS$_2$ T'-edges

Reprinted with permission from the Supplemental material of [95].

The y-cut of the 1T' phase can be made 6 different ways; 2 ways terminated by the metal atom, (m), 2 ways by a single chalcogenide atom, (c), and 2 ways by a pair of calcogenide atoms (2c). The 6 cuts can be seen on Fig B.1. We have compared the heat of formation of the (m) and (c) type edges of MoS$_2$ using the formula,

$$E_F = E_{MoS_2}^{nanoribbon} - nE_{MoS2}^{ML} - \mu_S(E_{H_2S} - E_{H_2})$$ (B.1)

$E_{MoS_2}^{nanoribbon}$ is the total energy of the nanoribbon, n is the no. of ML unit cells in the nanoribbon, and E_{MoS2}^{ML} is the total energy of the infinite monolayer. μ_S is a parameter which can be varied to represent different chemical potentials for sulfur. A value of $\mu_S = 1$ corresponds to taking one sulfur atom from a H$_2$S gas. It is zero for the (c) type edge where the nanoribbon corresponds to an integer no of ML unit cells but can be varied for the (m) type edges which is missing a sulfur atom. E_{H_2S} and E_{H_2} is the total energy of the two molecules which are calculated with the same method as the nanoribbon and ML but in a (10x10x10) Å cell and with a single k-point. The PBE functional without SOC was used for these calculations and the (m') and (c') nanoribbons are 50 Å long. The stability of the two types of edges can be seen on Fig B.2.

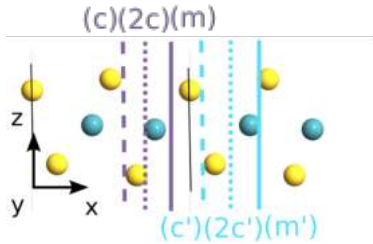Figure B.1: The six kinds of edge terminations for a cut along the y-direction.
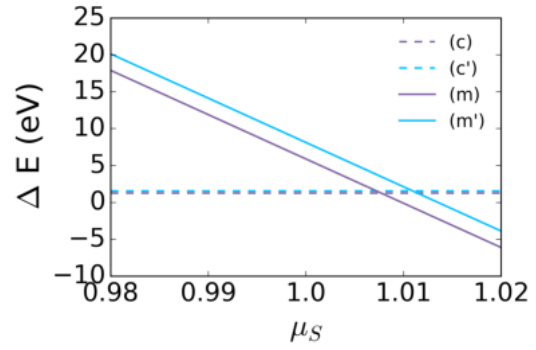

Figure B.2: The stability of (m) and (c) type edges of monolayer 1T' MoS$_2$ at varying μ_S.
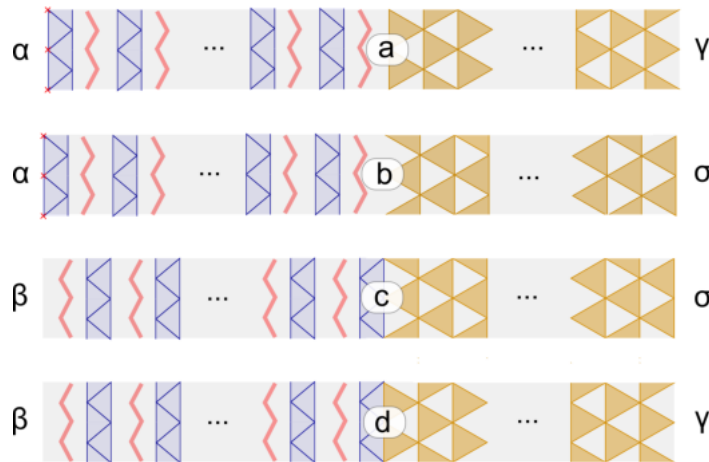

Figure B.3: The 4 nanoribbon types used to calculate the stability of the heterophase interfaces. The meaning of the geometrical shapes follow Figure 8.1 and the for types of edges are labelled α, β, σ, and γ.

B.2   Stability of MoTe$_2$ T'-H Phase Boundaries

The stability of the 8 types of phase boundaries which are illustrated on Figure 8.1 in Chapter 8 can be found by comparing nanoribbon configurations of the phase boundaries with structures of the isolated phases. The starting point is to consider 4 nanoribbons with the 4 phase boundaries illustrated on Figure B.3. Each ribbon consists of $m = 18$ unit cells of the H-phase and $n = 9$ unit cells of the T'-phase. The ribbon is doubled in the x-direction to allow for stabilizing atomic rearrangements at the interface. The set-up and calculational parameters of the nanoribbons follow the description in Appendix A.2. The heat of formation of these 4 phase boundaries can be written,

$$WE_F^a = E_{ribbon}^a - 2nE^{T'} - 2mE^H - WE_F^\alpha - WE_F^\gamma,$$
$$WE_F^b = E_{ribbon}^b - 2nE^{T'} - 2mE^H - WE_F^\alpha - WE_F^\sigma,$$
$$WE_F^c = E_{ribbon}^c - 2nE^{T'} - 2mE^H - WE_F^\beta - WE_F^\sigma,$$
$$WE_F^d = E_{ribbon}^d - 2nE^{T'} - 2mE^H - WE_F^\beta - WE_F^\gamma.$$

W is the width of the ribbon in the x-direction, E_{ribbon} is the total energy of the ribbon, $E^{T'}$ and E^H are the energies of one unit cell of the T'- and H-phase, respectively, and E_F^α, E_F^β, E_F^σ, and E_F^γ are the heat of formation of the 4 types of edges terminating the nanoribbons. Note, that using this definition, the interface is sharply defined between the atoms which originally came from the two different phases and that the edges are fixed during the calculation. E_F^α, E_F^β, E_F^σ, and E_F^γ are therefore related to edges which are fixed in the bulk crystal structure.

E_F^α and E_F^β can be found from two fixed nanoribbon configurations with an equivalent edge termination of the T'-phase on each edge as illustrated on Figure B.4. The heat of formation is,
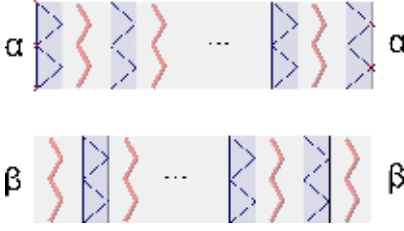
Figure B.4: The T' nanorib-
bons used to find the forma-
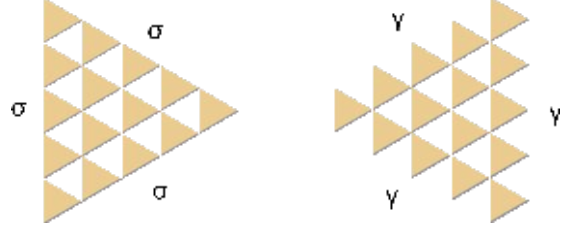tion energy of the T' edges.

Figure B.5: The H-phase triangles used
to find the formation energy of the H
edges. The triangle with σ edges is il-
lustrated for $s = 6$ and the triangle with
γ edges for $s = 5$.

$$2WE_F^\alpha = E_{ribbon}^\alpha - 2nE^{T'} - \frac{4}{3}\mu_{Te}^{T'}E_{Te_3},$$

$$2WE_F^\beta = E_{ribbon}^\beta - 2nE^{T'} - \frac{4}{3}\mu_{Te}^{T'}E_{Te_3}.$$

$\mu_{Te}^{T'}$ is a parameter which can be varied to represent different chemical
potentials of tellurium during the growth of the T'-phase. A value of
$\mu_{Te}^{T'} = 1$ corresponds to taking the Te atoms from a relaxed tellurium
alpha crystal which has 3 atoms in the unit cell.[i] The difference between
the these two formation energies becomes independent on the chemical
potential,

$$E_F^\alpha - E_F^\beta = \frac{1}{2W}\left(E_{ribbon}^\alpha - E_{ribbon}^\beta\right) = -93 \text{ meV/Å}.$$

The two types of H-phase edges can not be isolated on a nanoribbon.
Due to the symmetry of this phase, a σ edge will always be paired with a
γ edge. In order to investigate the heat of formation of these two edges,
nanoparticles in the shape of triangles are investigated instead. The total
energies of these nanoparticles are,

[i]A k-point grid of (11,11,7) was used to describe the Te alpha crystal and the
remaining parameters follow those of the nanoribbon calculations.

$$E_{tri}^{\sigma} = \frac{s(s+1)}{2}E^H - 2sE_{Te}^H + \frac{s-1}{2}WE_F^{\sigma} + 3E_F^{\sigma,corner},$$

$$E_{tri}^{\gamma} = \frac{s(s+5)}{2}E^H - 4sE_{Te}^H + \frac{s}{2}WE_F^{\gamma} + 3E_F^{\gamma,corner}.$$

s is no of Mo-atoms on each of the triangle edges, $E_F^{\sigma,corner}$ and $E_F^{\gamma,corner}$ are the energies of the two types of corners on the triangles. E_{Te}^H is the energy of a Te atom in the H-phase and can be defined as in the expression above to include the chemical potential of tellurium during the growth of the H-phase, $E_{Te}^H = 1/3\mu_{Te}^H E_{Te_3}$. These expressions can be rearranged such that the expression for the σ triangles is a linear function, f, of $s-1$ and the expression for the γ triangles is a linear function, g, of s,

$$f(s-1) = E_{tri}^{\sigma} - \frac{s(s+1)}{2}E^H$$

$$= (s-1)\left(\frac{W}{2}E_F^{\sigma} - 2E_{Te}^H\right) - 2E_{Te}^H + 3E_F^{\sigma,corner},$$

$$g(s) = E_{tri}^{\gamma} - \frac{s(s+5)}{2}E^H = s\left(\frac{W}{2}E_F^{\gamma} - 4E_{Te}^H\right) + 3E_F^{\gamma,corner}.$$

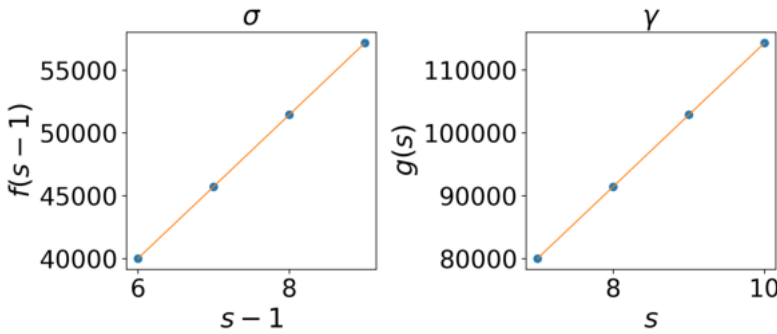Using four different sizes of the triangles, the slope of these functions can be found from a linear fit,

Figure B.6: Linear fit to the two functions $f(s-1)$ and $g(s)$.

$$\frac{\mathrm{d}f}{\mathrm{d}(s-1)} = \frac{W}{2}E_F^\sigma - 2E_{Te}^H \Rightarrow E_F^\sigma = \frac{2}{W}\frac{\mathrm{d}f}{\mathrm{d}(s-1)} + \frac{4}{3W}\mu_{Te}^H E_{Te_3},$$

$$\frac{\mathrm{d}g}{\mathrm{d}s} = \frac{W}{2}E_F^\gamma - 4E_{Te}^H \Rightarrow E_F^\gamma = \frac{2}{W}\frac{\mathrm{d}g}{\mathrm{d}s} + \frac{8}{3W}\mu_{Te}^H E_{Te_3}.$$

The fit is shown on Figure B.6 and results in the following formation energies,

$$E_F^\sigma = 1591.29 - 1588.66\mu_{Te}^H \text{ eV/Å},$$

$$E_F^\gamma = 3181.80 - 3177.33\mu_{Te}^H \text{ eV/Å},$$

$$E_F^\gamma - E_F^\sigma = 1590.51 - 1588.66\mu_{Te}^H \text{ eV/Å}.$$

The relations obtained for the edges can be used to find expressions for the formation energies of the phase boundaries,

$$E_F^a - E_F^d = \frac{1}{W}(E_{ribbon}^a - E_{ribbon}^d) - E_F^\alpha + E_F^\beta = -0.027 \text{ eV/Å},$$

$$E_F^b - E_F^c = \frac{1}{W}(E_{ribbon}^b - E_{ribbon}^c) - E_F^\alpha - E_F^\sigma = 0.28 \text{ eV/Å},$$

$$E_F^a - E_F^c = \frac{1}{W}(E_{ribbon}^a - E_{ribbon}^c) - E_F^\alpha + E_F^\beta - E_F^\gamma + E_F^\sigma$$
$$= -1589.715 + 1588.66\mu_{Te}^H \text{ eV/Å},$$

$$E_F^b - E_F^d = \frac{1}{W}(E_{ribbon}^d - E_{ribbon}^d) - E_F^\alpha + E_F^\beta - E_F^\gamma + E_F^\sigma$$
$$= -1591.05 + 1588.66\mu_{Te}^H \text{ eV/Å}.$$

These equations are transcendental which means that only the difference between the formation energies can be found. The most stable interface at $\mu_{Te}^H = 1$ is chosen as the reference level, $\Delta E_F^a = 0$ eV/Å.

$$\Delta E_F^a = 0 \text{ eV/Å},$$

$$\Delta E_F^b = 1590.0 - 1588.66\mu_{Te}^H \text{ eV/Å},$$

$$\Delta E_F^c = 1589.71 - 1588.66\mu_{Te}^H \text{ eV/Å},$$

$$\Delta E_F^d = 0.027\text{eV/Å}.$$

The formation energies of the 4 other possible phase boundaries are found in the same way from 4 nanoribbons with these phase boundaries. Since these 4 ribbons will have the same edges a the ones on Figure B.3, the energy can be found directly from,

$$\Delta E_F^{a^*} = \frac{1}{W}(E_{ribbon}^{a^*} - E_{ribbon}^a) + E_F^a.$$

All eight formation energies is plotted against the chemical potential of tellurium on Figure B.7 and summarized for $\mu_{Te}^H = 1$ in Table 8.1 in Chapter 8.
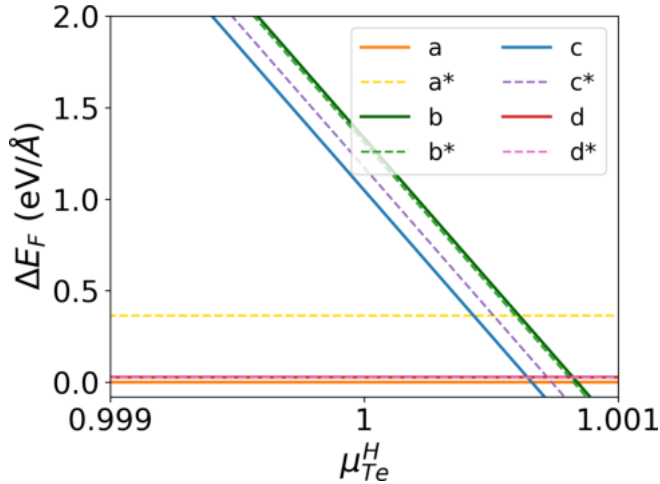
Figure B.7: The relative stability of the eight different phase boundaries between H- and T'-phase MoTe$_2$ as a function of the chemical potential of tellurium in the H-phase.

APPENDIX C

Derivations

C.1 Derivations using Elliptical Coordinates

The elliptical coordinate system is defined as,

$$x = a \, \cosh \mu \, \cos \nu,$$
$$y = a \, \sinh \mu \, \sin \nu.$$

a and $-a$ is the two foci of the ellipsis, where μ is a nonnegative real number which adjusts the distance from the plane of the foci and $\nu \in [0, 2\pi]$ is the angle. The nabla operator and Laplacian becomes,

$$\nabla \Phi = \frac{1}{a^2 \left(\sinh^2 \mu + \sin^2 \nu \right)} \left(\frac{\partial \Phi}{\partial \mu} \mathbf{h}_\mu + \frac{\partial \Phi}{\partial \nu} \mathbf{h}_\nu \right).$$

$$\mathbf{h}_\mu = a(\sinh \mu \cos \nu, \cosh \mu \sin \nu).$$
$$\mathbf{h}_\nu = a(-\cosh \mu \sin \nu, \sinh \mu \cos \nu).$$

$$\nabla^2 \Phi = \frac{1}{a^2 \left(\sinh^2 \mu + \sin^2 \nu \right)} \left(\frac{\partial^2 \Phi}{\partial \mu^2} + \frac{\partial^2 \Phi}{\partial \nu^2} \right).$$

C.1.1 Metallic Nanoribbon

Let us place a 2D metal nanoribbon at $y = 0$ and between $x = -a$ and $x = a$ and with some finite charge density. The potential inside the nanoribbon is, $-\phi_0$, corresponding to the workfunction $q\phi_0$. In elliptical coordinates,

$$\phi(y = 0, x) = -\phi_0 \Rightarrow \phi(\mu, \nu) = -\phi_0 a\mu - \phi_0.$$

The electric field at the nanoribbon is ($\mu = 0$),

$$\mathbf{E} = -\nabla\phi = -\frac{1}{a^2 \sin^2 \nu} \frac{\partial\phi}{\partial\mu}(0, a \sin \nu) = \left(0, \frac{\phi_0}{\sin \nu}\right)$$

This corresponds to a surface charge density of,

$$\sigma(x) = \frac{2\varepsilon_{eff}\phi_0}{\sin \nu}$$
$$= \frac{2\varepsilon_{eff}\phi_0}{\sqrt{1 - \left(\frac{x}{a}\right)^2}}\text{sign}(y).$$

ε_{eff} is the dielectric constant of the surroundings.

C.1.2   2D metal-semiconductor junction

In this coordinate system, the metal semiconductor interface can be represented by the following equations,

$$\frac{\partial^2\phi}{\partial x^2} + \frac{\partial^2\phi}{\partial y^2} = 0$$
$$\frac{\partial\phi}{\partial y} = -\frac{qN_{2D}}{\varepsilon_{eff}} \qquad\qquad \text{for } -a < x < a, y = 0$$
$$\phi(x) = 0 \qquad\qquad\qquad \text{for } x < -a.y = 0$$
$$\phi(x) = \Delta V \qquad\qquad\qquad \text{for } x > a, y = 0$$

which in elliptical coordinates becomes,

$$\frac{\partial^2\phi}{\partial\mu^2} + \frac{\partial^2\phi}{\partial\nu^2} = 0$$
$$\frac{\partial\phi}{\partial\mu} = -\frac{qN_{2D}}{\varepsilon_{eff}}a \, \sin\nu \qquad\qquad \text{for } \nu \in [0; \pi], \mu = 0$$
$$\phi(\nu) = \Delta V \qquad\qquad\qquad \text{for } \nu = 0$$
$$\phi(\nu) = 0 \qquad\qquad\qquad\quad \text{for } \nu = \pi$$

The solution is,

$$\phi(\mu, \nu) = \Delta V - \frac{\Delta V}{\pi}\nu + \frac{qN_{2D}}{\varepsilon_{eff}}ae^{-\mu}\sin\nu,$$

which at $y = 0$ and $x \in [-a; a]$ corresponds to,

$$\phi(x) = \Delta V - \frac{\Delta V}{\pi}\cos^{-1}\left(\frac{2x - x_D}{x_D}\right) + \frac{qN_{2D}x_D}{2\varepsilon_{eff}}\sqrt{1 - (2x - x_D/x_D)^2}$$

where a has been identified as half of the depletion width and $x = 0$ is moved to the position of the interface. The surface charge density in quasi-neutral region ($\nu = 0$) is,

$$\sigma(\mu) = -\varepsilon_{eff}\frac{\partial\phi}{\partial y}\Big|_{\nu=0} = -\frac{\varepsilon_{eff}}{a^2\sinh^2\mu}\frac{\partial\phi}{\partial\nu}\Big|_{\nu=0} a\sinh\mu$$

$$= \frac{\varepsilon_{eff}}{a\sinh\mu}\left(\frac{\Delta V}{\pi} - \frac{qN_{2D}}{\varepsilon_{eff}}ae^{-\mu}\right)$$

At the position of the interface ($\mu = 0$), converted back to Cartesian coordinates and shifting $x = 0$ to the position of the interface,

$$\sigma(x > x_D) = \left(\left(\frac{2x - x_D}{x_D}\right)^2 - 1\right)^{-1/2}$$

$$\times \left[\frac{2\varepsilon_{eff}\Delta V}{\pi x_D} - qN_{2D}\left(\frac{2x - x_D}{x_D} - \sqrt{\left(\frac{2x - x_D}{x_D}\right)^2 - 1}\right)\right].$$

The potential and surface charge density is plotted on Figure C.1 showing the divergence at the boundaries between the metal and the depletion region and the depletion region and the quasi-neutral region.

C.2   Tuneling Current using the Method of Steepest Descend

The starting point is the integral in eq. (7.5),
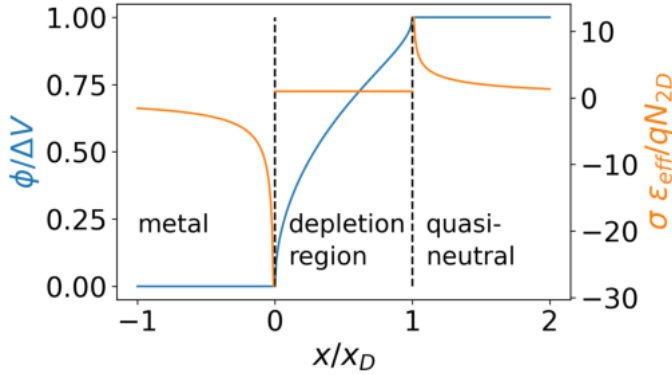
Figure C.1: Potential and surface charge density of a model where three spatial regions have been defined; (1) the metal with $\phi = 0$, (2) the depletion region with $\sigma = qN_{2D}/\varepsilon_{eff}$, and (3) the quasi-neutral region where $\phi = \Delta V$.

$$I^{TUN} \approx \frac{2q^2V}{hk_BT} \int_0^{\Phi_n - qV} \exp\left(-\frac{2}{3}\frac{(\Phi_n - qV - E)^{3/2}}{E_{00}\sqrt{\Delta V}} - \frac{E}{k_BT}\right) dE.$$

The method of steepest descend is a method for approximating an integral of the form,

$$\int_C G(x)\exp(-f(x)) \; dx.$$

The function $g(x)$ most be smooth, and the function $f(x)$ differential at lest two times and have a minima on C. The exponential function will have largest weight at the minimum of f. We therefore approximate f at the minimum,

$$f(x) \approx f(x_{min}) + \frac{1}{2}f''(x_{min})(x - x_{min})^2.$$

This leads to,

$$\int_C G(x) \exp -f(x) \approx G(x_{min}) \exp(-f(x_{min}))$$

$$\times \int_C \exp\left(-\frac{1}{2}f''(x_{min})(x - x_{min})^2\right)$$

$$\approx G(x_{min}) \exp(-f(x_{min}))\sqrt{\frac{2\pi}{f''(x_{min})}}.$$

The second integral is evaluated using the area below a Gaussian curve since we know that x_{min} lies on C. In our case $G(x) = 1$ and

$$f(E) = \frac{2}{3}\frac{(\Phi_n - qV - E)^{3/2}}{E_{00}\sqrt{\Delta V}} + \frac{E}{k_B T}$$

$$f'(E) = -\frac{(\Phi_n - qV - E)^{1/2}}{E_{00}\sqrt{\Delta V}} + \frac{1}{k_B T}$$

$$f''(E) = \frac{1}{2}\frac{(\Phi_n - qV - E)^{-1/2}}{E_{00}\sqrt{\Delta V}}.$$

The minima of $f(E)$ is the energy where the tunnel current has the most weight,

$$-\frac{(\Phi_n - qV - E_{max})^{1/2}}{E_{00}\sqrt{\Delta V}} + \frac{1}{k_B T} = 0 \Rightarrow E_{max} = \Phi_n - qV - \left(\frac{E_{00}}{k_B T}\right)^2 \Delta V$$

$$E_{max} = (\Phi_n - qV)\left(1 - \left(\frac{E_{00}}{k_B T}\right)^2\right) + q\phi_n\left(\frac{E_{00}}{k_B T}\right)^2.$$

This point lie between $q\phi_n$ and $(\Phi_n - qV)$ when $E_{00} \leq k_B T$. If $N_{3D} = 10^{18}$ cm^{-3}, $\varepsilon_s = 10\varepsilon_0$ and $m_e^* = m_0$, then $E_{00} = 2.9$ meV and it seems reasonable to assume that $E_{00} \leq k_B T$ holds unless the semiconductor is very heavily doped. The tunneling current becomes,

$$I_{3D}^{TUN} \approx \frac{2q^2V}{hk_B T}\sqrt{\frac{2\pi}{f''(E_{max})}}\exp(-f(E_{max}))$$

$$= \frac{2q^2V}{hk_B T}E_{00}\sqrt{\frac{4\pi\Delta V}{k_B T}}\exp\left(\frac{1}{3}\frac{E_{00}^2}{(k_B T)^3}\Delta V - \frac{\Phi_n}{k_B T} + \frac{qV}{k_B T}\right)$$

$$= A_{3D}^{TUN}\frac{qV\sqrt{\Delta V}}{T^{3/2}}\exp\left(\frac{E_{00}^2}{3(k_B T)^3}\Delta V\right)\exp\left(-\frac{\Phi_n}{k_B T}\right)\exp\left(\frac{qV}{k_B T}\right),$$

which defines an effective tunneling constant,

$$A_{3D}^{TUN} = \frac{2q}{h}\frac{E_{00}}{k_B^{3/2}}\sqrt{4\pi} = \frac{q^2}{k_B^{3/2}}\sqrt{\frac{N_{3D}}{4\pi m_e^* \varepsilon_s}}.$$

A comparison between this expression and the exact numerically evaluated integral with the exact difference between Fermi functions and tunneling probability from the WKB approximation using the potential in Table 7.1 is shown on Figure C.2. It can be seen that the model performs reasonably well as long as $qV < \frac{1}{2}\Phi_n$. Above this limit, the model overestimates the current since the energy of maximum transmission is pushed close to the top of the barrier and the approximation using the entire area below the Gaussian fails. The temperature dependence of the current is seen on Figure C.2b and shows that the temperature dependence is well described as well.

The corresponding 2D expression follows the same derivation with the only difference that $E_{00}^{3D}\sqrt{\Delta V} \to E_{00}^{2D}$ where,
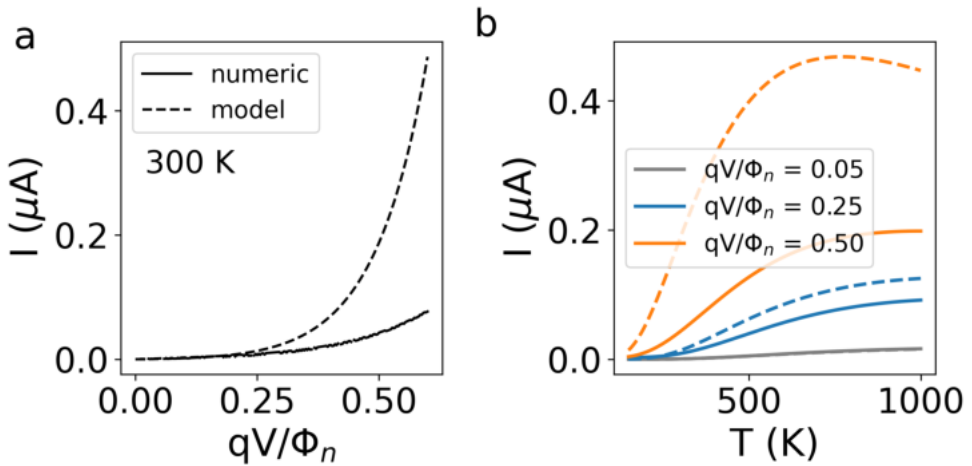
Figure C.2: Comparison between the derived expression for the 3D tunneling current and the numerically evaluated integral. **a** shows the IV curve and **b** shows the temperature dependence of the current.
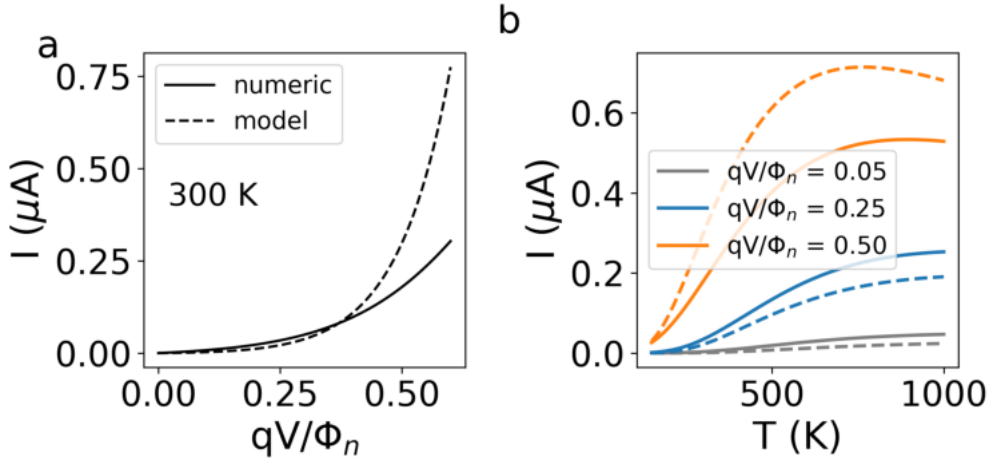
Figure C.3: Comparison between the derived expression for the 2D tunneling current and the numerically evaluated integral. **a** shows the IV curve and **b** shows the temperature dependence of the current.

$$E_{00}^{2D} = \frac{q^2 N_{2D} \ln 4}{2\pi \varepsilon_{eff}} \sqrt{\frac{\hbar^2}{2m_e^*}}.$$

The comparison between the numerically evaluated integral and the model expression is seen on Figure C.3 and generally shows a slightly better agreement than the 3D model.

Collected Studies on Heterophase Devices

Ref. (Year)	Setup	n/p	Contact	Method	t	L_C	R_C	I^{ON}/I^{OFF}	FET μ	SS	Φ^{SB}
[70] (2014)	1T-2H MoS$_2$	n	Au	1	1-3 ML	1.2 μm	0.6-0.7 kΩ μm	10^8		0.8 V/dec	
[79] (2016)	1T-2H MoS$_2$	n	Ti/Au	2	~7 ML	1.5 μm		10^4		1 V/dec	0.13-0.18 eV
[11] (2016)	1T'-2H MoS$_2$ (x6)	n	Au	1	3 ML	6 x 7.5 nm	75 Ω μm	10^7	25 cm^2/Vs	120 mV/dec	
[11] (2016)	T'-H MoS$_2$ (x8)	n	Au	1	ML	8 x 7.5 nm	80 Ω μm		12 cm^2/Vs		
[81] (2017)	T-H MoS$_2$	n	Ti/Au	3	ML	100 μm		10^5			
[72] (2018)	T'(6 ML)-H MoS$_2$	n	Cr/Au	1	ML	20 μm			40 cm^2/Vs		
[80] (2015)	1T'-2H MoTe$_2$	n	Au	4	~30 ML	2.91 μm	< 0.1 kΩ μm	10^6	~50 cm^2/Vs		~10 meV
[91] (2017)	1T'-2H MoTe$_2$	p	Au	5	5-6 nm	4-15 μm	14 kΩ μm	10^5	16.2 cm^2/Vs		22 meV
[92] (2019)	1T'-2H MoTe$_2$	p	Pd/Au	5	~6 ML	20 μm		10^4	30 cm^2/Vs		25 meV
[137] (2019)	1T'-2H MoTe$_2$	p	Pd/Au	5	7 ML	10-60 μm	~1.1 kΩ μm	10^4	23 cm^2/Vs		27.5 meV
[89] (2019)	1T'-2H MoTe$_2$	p	Ti/Au	5	8 nm	20 μm		3.5×10^3	7-8 cm^2/Vs		30 $\pm$ 10 meV
[90] (2019)	1T'-2H MoTe$_2$	p	Ti/Au	5	~10 nm	~60 μm					
[12] (2019)	1T'-2H MoTe$_2$	p	1T'	6	8 nm	~4 μm		10^3	50 cm^2/Vs		20 meV
[12] (2019)	1T'-2H MoTe$_2$^{a}	p	1T'	6	8 nm	~4μm		10^5	130 cm^2/Vs	69 mV/dec	
IDRS 2022[1]					6 nm^b	16 nm	271 Ω μm^c	9.12×10^4	125 cm^2/Vs	82 mV/dec	
IDRS 2025[1]					7 nm^d	14 nm	257 Ω μm^c	8.73×10^4	100 cm^2/Vs	72 mV/dec	

Table D.1: Figures of merit of fabricated 2D TMD heterophase FETs. Key to fabrication methods; 1: Li-intercalation, 2: E-beam exposure, 3: Ar-plasma treatment, 4: Laser irradiation, 5: Growth control, 6: Selective precursor growth.

^{a}HfO$_2$ dielectric
^{b}Fin width
^{c}R$_{sd}$
^{d}Nanosheet thickness

Ref.	Setup	n/p	Doping	Method	E_g (eV)	L_C (nm)	R_C (Ω μm)	I^{ON}/I^{OFF}	SS (mV/dec)	Φ^{SB} (eV)	x_D (nm)
							MoS$_2$ ZZ				
[79]	H-T-H (b*+a*)	n	0	1	1.66	7.5				0.47	
[163]	T-H (b)	p	0	6			~200				
[155]	T-H (b)	n	0	6	1.7	1.6	2.9×10^4			~0.8	
[156]	T'-H (b*)	p	0	6	1.7	4.4				0.82	
[156]	T'-H (b)	p	0	6	1.7	4.4				0.68	
[11]	T'-H-T' (a+c)	n	0	6		7.5	75 (MVS)	10^7	73		
[157]	T'-H (a*)	n	6.5×10^{10}	6	1.67	~8				0.9	
[157]	T'-H (a*)	n	1.9×10^{12}	6	1.67	~8				0.8	
[157]	T'-H (c*)	n	6.5×10^{10}	6	1.67	~8				0.7	
[157]	T'-H (c*)	n	1.9×10^{12}	6	1.67	~8				0.6	
[118]	T'-H	p	0	6		8.6				0.7	>8.6
[118]	T'-H	n	5×10^{12}	6		8.6				0.8	4.1
[118]	T'-H	n	5×10^{13}	6		8.6				0.2	1.1
[118]	T'-H	p	5×10^{12}	6		8.6				0.4	3.2
[118]	T'-H	p	5×10^{13}	6		8.6				0.2	1.0
							MoS$_2$ AC				
[161]	T-H-T (AC)	n	0	5	1.795	8.8		2×10^3	~60	0.82	
[163]	T-H (AC)	p	0	6			~400				
[158]	T-H (AC)	n	0	1		~2				0.10	
[159]	T-H-T (AC)	n	0	6	1.7	5				0.83	
[155]	T-H (AC)	n	0	6	1.7	1.6	3.8×10^4			~0.8	
[166]	T-H (AC)	n	0.5×10^{14}	6	1.78		~300				
[159]	T'-H-T' (AC)	p	0	6	1.7	5				0.6	
[118]	T'-H (AC)	p	0	6		8.6				0.58	>8.6
[118]	T'-H (AC)	n	5×10^{12}	6		8.6	10^7			0.78	4.5
[118]	T'-H (AC)	n	5×10^{13}	6		5.6	2000			0.60	1.3
[118]	T'-H (AC)	p	5×10^{12}	6		8.6	10^7			0.39	2.9
[118]	T'-H (AC)	p	5×10^{13}	6		8.6	750			0.04	0.9

Table D.2: Figures of merit of simulated 2D TMD heterophase interfaces along the zigzag (ZZ) or armchair (AC) direction and based on MoS$_2$. Key for simulation methods; 1: DFT@PBE, 2: DFT@PBE + SOC, 3:DFT@PBE+NTV, 4: DFT@PBE + TB-NEGF, 5: DFT@LDA + NEGF, 6: DFT@PBE + NEGF.

Ref.	Setup	n/p	Doping	Method	E_g (eV)	L_C (nm)	R_C (Ω μm)	I^{ON}/I^{OFF}	SS (mV/dec)	Φ^{SB} (eV)	x_D (nm)
						MoS$_2$ evaluated from separate cells					
[165]	T-H-T	n	0	3	1.7	5.5		4.38×10^6	72		
[165]	T-H-T	n	0	3	1.7	6.6		4.43×10^6	70		
[165]	T-H-T	n	0	3	1.7	8.3		4.65×10^6	68		
[165]	T-H-T	n	0	3	1.7	9.9		4.41×10^6	69		
						MoTe$_2$ ZZ					
[160]	T'-H (d)	n	0	4	1.06	150	167			$\sim$0.5	
[117]	T'-H (c)	p	0	1	1.07	11				0.03	
[117]	T'-H (a)	n	0	1	1.07	11				0.5	
[22]	T'-H (c*)	n	4.9×10^{11}	6	1.03	19				0.54	5.7
[22]	T'-H (c*)	n	4.6×10^{12}	6	1.03	9				0.32	1.6
[22]	T'-H (c*)	p	4.9×10^{11}	6	1.03	19				0.32	4.1
[22]	T'-H (c*)	p	4.6×10^{12}	6	1.03	19				0.19	0.76
						MoTe$_2$ AC					
[161]	T-H-T (AC)	n	0	5	1.195	8.8		1.2×10^4	$\sim$60	0.44	
[162]	T-H-T (AC)	n	0	5	1.195	8.8		10^4	$\sim$60	0.36	
[162]	T'-H-T' (AC)	n	0	5	1.195	8.8				0.44	
[159]	T'-H-T' (AC)	p	0	6	1.1	5				0.5	
[90]	H-T' (AC*)	p	0	1						0.25	
						MoTe$_2$ Evaluated from separate cells					
[89]	2H-1T' (5L)	p	0	2	0.75					0.077	
[89]	H-T' (ML)	p	0	2	1					0.28	

Table D.3: Figures of merit of simulated 2D TMD heterophase interfaces along the zigzag (ZZ) or armchair (AC) direction and based on MoS$_2$ or MoTe$_2$. Key for simulation methods; 1: DFT@PBE, 2: DFT@PBE + SOC, 3:DFT@PBE+NTV, 4: DFT@PBE + TB-NEGF, 5: DFT@LDA + NEGF, 6: DFT@PBE + NEGF.
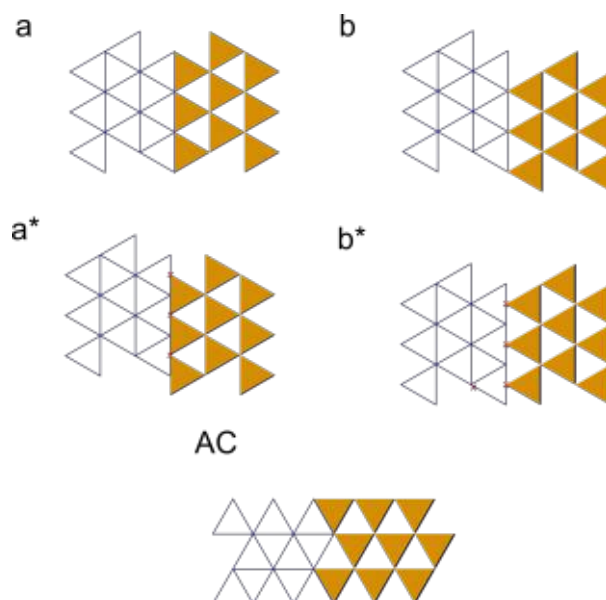
Phase Boundaries

Figure E.1: The 4 types of phase boundaries between a 1T-phase and a 1H-phase TMD along the zigzag edge (a-b*) and one along the armchair edge (AC). The yellow triangles represent the 1H-phase geometry and the blue triangles represent the 1T geometry. The metal atoms are placed at the corners of the blue and yellow triangles. Chalcogen atoms are placed in the center of all the blue triangles and of the shaded yellow triangles. Red crosses mark a triangle corner without a metal atom.
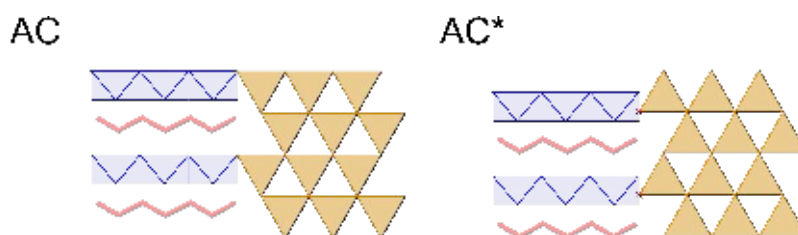

Figure E.2: The two types of phase boundaries between a 1T'-phase and a 1H-phase TMD along the armchair direction which have been investigated using ab-inito calculations. The yellow triangles represent the 1H-phase geometry and the red and blue zigzag chains represent the 1T' geometry. The metal atoms are placed at the corners of the blue and yellow triangles. Red crosses mark a triangle corner without a metal atom.

APPENDIX F

Publications

Here follows the four publications in peer review journals which have resulted from the PhD project.

"Method for determining optimal supercell representation of interfaces"
Daniele Stradi, Line Jelver, Søren Smidstrup and Kurt Stokbro.
Journal of Physics: Condensed Matter, 29, 185901 (2017)

"Determination of low-strain interfaces via geometric matching"
Line Jelver, Peter Mahler Larsen, Daniele Stradi, Kurt Stokbro, and Karsten Wedel Jacobsen.
Physical Review B, 96, 085306 (2017)

"Spontanous breaking of time-reversal symmetry at the edges of 1T' monolayer transition metal dichalcogenides"
Line Jelver, Daniele Stradi, Kurt Stokbro, Thomas Olsen, and Karsten Wedel Jacobsen.
Physical Review B, 99, 155420 (2019)

"Schottky barrier lowering due to interface states in 2D heterophase devices"
Line Jelver, Daniele Stradi, Kurt Stokbro, and Karsten Wedel Jacobsen,
Nanoscale Adv., 573, 507 (2021).

Method for determining optimal supercell representation of interfaces

Daniele Stradi, Line Jelver, Søren Smidstrup and Kurt Stokbro

QuantumWise A/S, Fruebjergvej 3, PO Box 4, DK-2100 Copenahgen, Denmark

E-mail: daniele.stradi@quantumwise.com

Abstract

The geometry and structure of an interface ultimately determines the behavior of devices at the nanoscale. We present a generic method to determine the possible lattice matches between two arbitrary surfaces and to calculate the strain of the corresponding matched interface. We apply this method to explore two relevant classes of interfaces for which accurate structural measurements of the interface are available: (i) the interface between pentacene crystals and the (1 1 1) surface of gold, and (ii) the interface between the semiconductor indium-arsenide and aluminum. For both systems, we demonstrate that the presented method predicts interface geometries in good agreement with those measured experimentally, which present nontrivial matching characteristics and would be difficult to guess without relying on automated structure-searching methods.

Keywords: interfaces, structure searching methods, metal-organic interfaces, semiconductor–superconductor interfaces, density functional theory

(Some figures may appear in colour only in the online journal)

1. Introduction

As electronic devices shrink in size to reach nanoscale dimensions, interfaces between different materials become increasingly important in defining the device characteristics [1]. In many cases, it has been shown that the effect of the interface even dominates the device properties [2], leading to the concept that 'the interface is the device' [3]. In order to optimize the performance of a device it is therefore important to understand the properties of its interfaces.

First principles modeling based on atomistic methods such as density functional theory (DFT) [4] have become an important tool for simulating the properties of interfaces [5]. To be truly predictive, atomistic methods require an accurate model for the atomic-scale geometry of the interface. As these simulations typically use periodic boundary conditions in the direction parallel to the interface, a common supercell for the surfaces of the two crystals forming the interface must be

determined. However, typically the two crystals are not commensurate and finding a common supercell requires straining one of or both the surfaces. To accommodate the resulting strain, the two surfaces can also be rotated with respect to each other. However, for rotation angles preserving a high symmetry in the supercell, this has often the side-effect of increasing considerably its dimensions. Finding a supercell with low built-in strain and without an excessive number of atoms is therefore highly nontrivial.

In this paper we present an algorithm which allows for an efficient and systematic search for common supercells between two crystalline surfaces. Given the optimized geometries of two surfaces forming the interface, the algorithm returns a list of all possible interface supercells by varying the interface strain and the rotation between the two surfaces. A related, but more simplistic method has been proposed in [6]. Compared to [6] our method automatically tests all possible rotations of the two lattices and has been implemented into a graphical user interface, the Virtual NanoLab [7].

In the paper we show that this is not only a practical procedure for generating low strain supercells for atomic-scale simulations, but it can also be used as a predictive tool for

determining interface geometries in accordance with exper-
imental data. As a first example, we consider the interface
between a pentacene crystal (PC) and the Au(1 1 1) surface,
which has been widely studied both theoretically [8–13] and
experimentally [14–24]. We show that the predicted geom-
etries of a pentacene monolayer on Au(1 1 1) recover those
observed experimentally. Using DFT, we calculate the ground
state structure and energetics of these interfaces and find that
they are thermodynamically more stable than those previously
used in the literature.

As a second example, we consider the interface between
Al and InAs. This interface is relevant for studies on semicon-
ductor nanowires (NWs) in which superconducting properties
are introduced by proximity effect with a superconductor [25–
28] and its structure has been recently resolved using high-
resolution transmission electron microscopy (HR-TEM) [29].

The organisation of the paper is the following. In section 2
we introduce the algorithm for matching the two crystal ori-
entations with minimal strain. In section 3.1 we first apply the
method to determine the geometry of a pentacene overlayer on
Au(1 1 1). In section 3.2 we determine the structure of Al on
InAs. Finally in section 4 we conclude.

2. Methods

2.1. Algorithm details

The algorithm has been implemented into the Virtual
NanoLab [7, 30] and can be summarized in four main steps.
A schematic flowchart is shown in figure 1. The algorithm
takes as input the structures of two arbitrary surfaces A and B,
described by surface unit cells with primitive vectors $(\vec{a}_1, \vec{a}_2)$
and $(\vec{b}_1, \vec{b}_2)$. In the first step, supercells are constructed for the
two non-interacting surfaces starting from the corresponding
surface unit cells. In the second and third step, the supercells
are aligned and matched to create a supercell representation
of the interface. The interface supercell is then accepted and
added to the pool of interface structures if the strain and the
rotation between the two surfaces are below given thresholds
predefined by the user. The procedure is reiterated for all the
possible supercells that can be constructed starting from the
two surface unit cells. In the following, we detail the details of
each individual step.

(1) Construction of the surface supercells:

Starting from the unit cells of the two individual surfaces
with primitive vectors $(\vec{a}_1, \vec{a}_2)$ and $(\vec{b}_1, \vec{b}_2)$, trial non-
strained surface supercells A^* and B^* are generated. These
supercells have Bravais lattice vectors $(\vec{v}_1, \vec{v}_2)$ and $(\vec{u}_1, \vec{u}_2)$,
which are described in terms of the corresponding surface
unit cells by the relations:

$$(\vec{v}_1, \vec{v}_2) = \mathbf{N}(\vec{a}_1, \vec{a}_2), \tag{1}$$

$$(\vec{u}_1, \vec{u}_2) = \mathbf{M}(\vec{b}_1, \vec{b}_2). \tag{2}$$
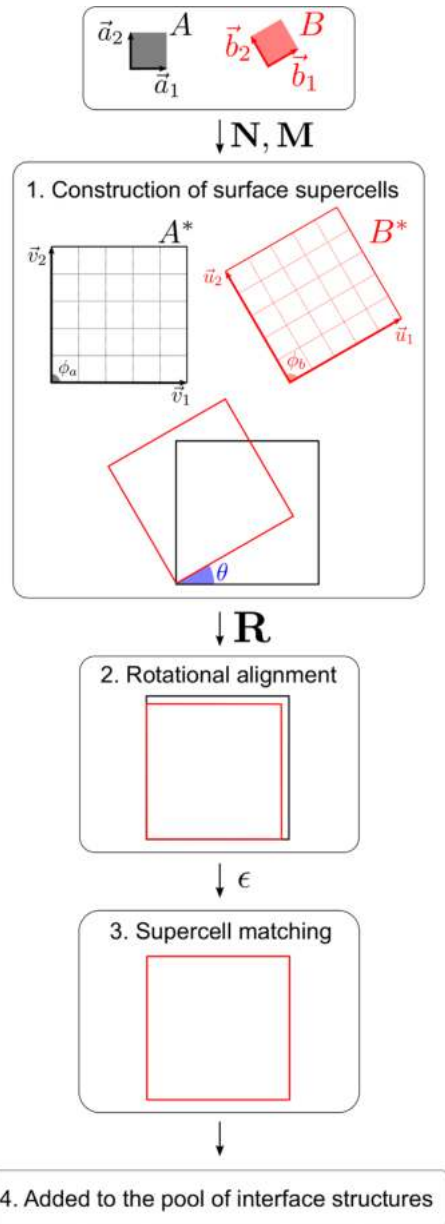

Figure 1. Flowchart diagram of the algorithm for matching two
surfaces forming an interface with minimal strain. In step 1,
two surface supercells with lattice vectors $(\vec{v}_1, \vec{v}_2)$ and $(\vec{u}_1, \vec{u}_2)$ are
constructed from the surface unit cells with lattice vectors $(\vec{a}_1, \vec{a}_2)$
and $(\vec{b}_1, \vec{b}_2)$, respectively. The two supercells are rotationally aligned
(step 2) by applying the rotation matrix $\mathbf{R}$ and then matched (step
3) using the the strain tensor ϵ. In step 4, the interface supercell is
accepted based on pre-defined threshold values (see equation (8)
and associated description).

In equations (1)–(2), **N** and **M** are 2×2 repetition matrices. **N** takes the form:

$$\mathbf{N} = \begin{pmatrix} n_{11} & n_{12} \\ n_{21} & n_{22} \end{pmatrix}, \tag{3}$$

where $n_{ij} \in Z$. An equivalent formulation to equation (3) can be given for **M**. During the generation of the supercells, we exclude equivalent lattices.

(2) Rotational alignment:

For each pair of supercells A^* and B^*, we next determine a rotation matrix **R** which rotates B^* and aligns $\vec{u}_1$ with $\vec{v}_1$:

$$\mathbf{R} = \begin{bmatrix} \cos\theta & -\sin\theta \\ \sin\theta & \cos\theta \end{bmatrix}, \tag{4}$$

where $\theta = |\phi_a - \phi_b|/2$, with $\phi_a = \angle(u_1, u_2)$ and $\phi_b = \angle(v_1, v_2)$, respectively.

(3) Supercell matching:

Once the individual supercell of the two surfaces have been aligned, the supercell vectors are matched to create the interface supercell. This matching procedure can be described by defining a strain tensor ϵ, which is applied to the Bravais lattice of B^* in order to match it to the Bravais lattice of A^*. The individual components of the strain tensor ε are:

$$\varepsilon_{xx} = \left| \frac{v_{1,x}}{u_{1,x}} \right| - 1, \tag{5}$$

$$\varepsilon_{yy} = \left| \frac{v_{2,y}}{u_{2,y}} \right| - 1, \tag{6}$$

$$\varepsilon_{xy} = \frac{1}{2} \frac{v_{2,x} - \frac{v_{1,x}}{u_{1,x}} u_{2,x}}{u_{2,y}}. \tag{7}$$

(4) Acceptance of the interface supercell:

The full equation to match the two surfaces A and B defined in terms of equations (1)–(7) reads:

$$\mathbf{N}(\vec{a}_1, \vec{a}_2) = (1 + \varepsilon)\mathbf{R}\mathbf{M}(\vec{b}_1, \vec{b}_2). \tag{8}$$

By examining equation (8), it can be seen that the search for possible interface supercells can be narrowed by (i) defining a threshold value N_{max} for the elements n_{ij} in **N** and an equivalent threshold value M_{max} for **M**, (ii) defining threshold values for the individual components of the strain tensor ϵ, and (iii) specifying a range for the angle ϕ associated with the rotation matrix **R**. We note that a procedure similar to that outlined, in which the surface B is strained, can also be applied to strain A and match it to B, or to strain equally both surfaces. For the systems considered in this study, the search for possible interface supercells has been constrained by choosing a threshold for condition (i) of $N_{max}, M_{max} = 6$ or $N_{max}, M_{max} = 12$, and by considering all possible rotations and strains. With these parameters, a scan typically takes 1s and the simulation time scales as $N_{max}^2 N_\phi$, where N_ϕ is the total number of angles. In the next section we will apply the method to determine the

structure of a Pentacene monolayer on Au(1 1 1) and the interface geometry of Al on top of InAs.

2.2. Elastic contribution to the interface energy

Straining one or both sides of the interface introduces and additional elastic contribution to the interface energetics. This contribution and its influence on the surface geometry varies considerably depending on the strength of the interaction between the overlayer and the substrate. For a substrate and a strained overlayer with cubic symmetry, we can write down the total energy per unit of area as [31]:

$$E = E^{int} + E^{surf} + (\varepsilon_{xx}^2 C_{11} + \varepsilon_{xx}\varepsilon_{yy}C_{12} + \frac{1}{2}\varepsilon_{xy}^2 C_{44})t, \tag{9}$$

where E^{int} is the interface energy between the substrate and the overlayer, E^{surf} is the energy of the free surface of the overlayer, $\varepsilon_{xx}, \varepsilon_{yy}, \varepsilon_{xy}$ have been defined in equations (5)–(7), C_{11}, C_{12}, C_{44} are the elastic constants of the overlayer material and t is its thickness. The equation can be further simplified as

$$E = E^{int} + E^{surf} + \frac{1}{2}\bar{\mathcal{E}}^2 C_{11}t, \tag{10}$$

where

$$\bar{\mathcal{E}} = \sqrt{2\varepsilon_{xx}^2 + 2\frac{C_{12}}{C_{11}}\varepsilon_{xx}^2 + \frac{C_{44}}{C_{11}}\varepsilon_{xy}^2}. \tag{11}$$

Neglecting interactions between the interface and the overlayer free surface and strain effects, E^{surf} will be independent of the interface geometry. For metals and weakly interacting interfaces, we also expect the interface energy E^{int} to be rather similar for different geometries, so that the contribution of the elastic energy will be dominant and will determine the stability trend of the different geometries. On the other hand, for interfaces between semiconductors there may be a varying number of bonds at the interface, depending on the precise overlay structure. Since binding energies for covalent bonds are typically in the range 1–2 eV, the overlayer may need to have a thickness above $\sim$2 nm before the elastic energy will dominate.

3. Results

3.1. PC/Au(1 1 1)

3.1.1. Computational details. The DFT calculations for PC/Au(1 1 1) have been performed using the ATOMISTIX TOOLKIT [32]. The Kohn–Sham orbitals have been expanded in a linear combination of pseudo-atomic orbitals (PAOs) [33]. The electronic exchange-correlation (xc) energy has been described by using the generalized gradient approximation (GGA) and the Perdew-Burke 91 (PW91) xc-functional [34]. We use this functional to compare with previous calculations [9], however, note that the GGA-PW91 xc-functional does not include van-der-Waals forces and it will therefore underestimate adsorption energies. We have used a slab geometry with periodic boundary conditions parallel to the surface and mixed (Dirichlet + Neumann) boundary conditions in the
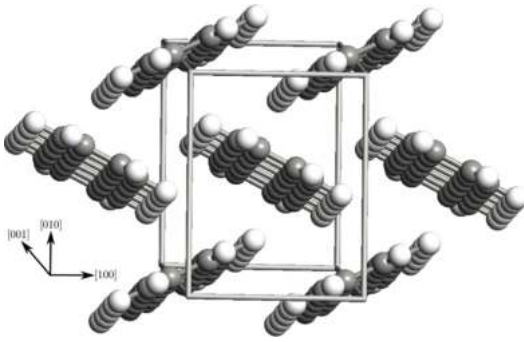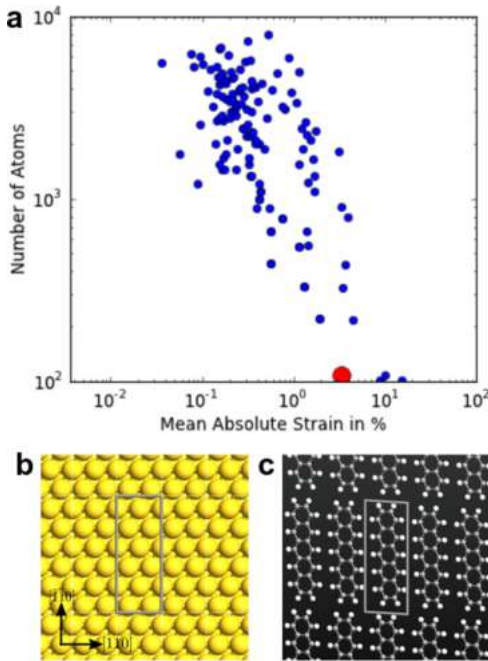
Figure 2. Structure of the pentacene crystal.

Figure 3. (a) Graph of the possible supercells generated for PC/Au(1 1 1) as a function of the mean absolute strain $\bar{\varepsilon}$ in the pentacene crystal and the number of atoms in the supercell. (b) and (c) Au(1 1 1) and pentacene surface lattices associated with supercell II. The latter is highlighted by the red dot in (a).

Table 1. Strain in the ⟨0 1 0⟩-oriented PC crystal to match Au(1 1 1). The first and second columns label each geometry by a roman number and list the supercell in the basis of the Au(1 1 1) Bravais lattice. The four indexes $(n_{11}, n_{12}; n_{21}, n_{22})$ refer to the rotation matrix as defined in equation (3). The third column lists the number of PC(0 1 0) surface cells in the structure. $\varepsilon_{11}, \varepsilon_{22}, \varepsilon_{12}$ are the components of the strain tensor applied to the PC(0 1 0) surface cell in order to match the gold supercell. $\bar{\varepsilon} = (|\varepsilon_{11}| + |\varepsilon_{22}| + |\varepsilon_{12}|)/3$ is the average strain.

Structure	Au(1 1 1)	#PC	ε_{11}	ε_{22}	ε_{12}	$\bar{\varepsilon}$
I	(2,1;0,6)	1	−16.0	10.9	3.3	10.1
II	(2,0;3,6)	1	−3.0	−4.0	2.9	3.3
III	(2,0;−3,6)	1	−6.4	−0.54	0.0	2.3
IV	(2,0;−2,13)	2	0.2	0.7	3.7	1.5
V	(6,1;5,3)	4	−0.8	−0.3	−0.5	0.5
VI	(16, −1;9, −2)	12	0.0	0.1	0.1	0.1

optimizations, while the atoms in the lowermost layers were kept frozen at their bulk position.

For carbon we have used 21 orbitals per atom with s, p and d characters and ranges up to 3.9 Å, while for hydrogen we have used 5 orbitals per atom with s and p characters and ranges up to 4.2 Å. This basis set has been optimized to reproduce hydrogen and carbon dimer total energies [37]. Using this basis set, we obtain an adiabatic ionization energy for the individual pentacene molecule (P1) $E_I = 6.34$ eV, in good agreement with the experimentally reported value $E_I^{exp} = 6.59$ eV [38]. For gold, we have used an s, p, d basis set of ranges 2.7–3.6 Å, with a total of 9 orbitals per atom. The calculated lattice constant for bulk Au using this basis is $a_{Au} = 4.17$ Å. Using a layer of gold ghost orbitals to get a better description of the isolated Au(1 1 1) surface [39], we also obtain that the surface work function is $W_{Au(1 1 1)} = 5.19$ eV. Both values are in good agreement with those obtained using similar computational parameters and a plane wave basis set [9].

Results To construct the interface between the PC (see figure 2) and Au(1 1 1), we have considered the PC unit cell according to the crystallographic parameters of [40] (P-1: a = 5.985 Å, b = 7.596 Å, c = 15.6096 Å, α = 81.25°, β = 86.56°, γ = 89.8°). The internal stress calculated in this unit cell is lower than 3 meV Å^{-3}.

We have then aligned the ⟨0 1 0⟩ direction of the PC unit cell along the normal to the Au(1 1 1) surface, and generated all possible interface supercells with $N_{max}, M_{max} \leqslant 12$ by straining the PC lattice in the plane perpendicular to the ⟨0 1 0⟩ direction[1]. Figure 3(a) shows a graph with the resulting possible supercells, sorted according to the mean absolute strain $\bar{\varepsilon}$ and the number of atoms in the supercell. The plot shows the number of atoms in the supercell as function of the average strain $\bar{\varepsilon}$. For the average strain we for simplicity use, $\bar{\varepsilon} = (|\varepsilon_{11}| + |\varepsilon_{22}| + |\varepsilon_{12}|)/3$. The measure

direction normal to the surface, the latter allows for describing slabs with different workfunctions on the upper and lower surfaces. The Brillouin zone has been sampled using an $8 \times 3 \times 1$ Monkhorst-Pack [35] grid and a Fermi-Dirac occupation scheme with a broadening of $k_B T = 25$ meV. Structural relaxations have been performed using a convergence threshold for the forces of 0.01 eV Å^{-1}. During both the structural optimization and the evaluation of binding energies, the basis set superimposition error (BSSE) has been corrected using the counterpoise (CP) correction scheme [36]. For the Au(1 1 1) surface, we have used a 6-layers slab. Only the two uppermost Au layers were allowed to relax during the structural

---

[1] To have a more consistent matching with the PC unit cell, for which experimental crystallographic parameters have been used, we have used the experimental lattice parameter of the Au(1 1 1) surface during the surface matching. However, in the calculations, the calculated lattice parameter for Au(1 1 1) has been used. We have checked that this procedure does not alter our conclusions.

Table 2. Calculated properties of the optimized geometries of PC/Au(1 1 1), for supercell I, II, III. The repetition of the Au(1 1 1) surface Bravais vectors is given in parenthesis for each supercell. E_b is the binding energy. Φ is the work function. Reference calculation values for supercell I obtained by Li *et al* [9][2] are given in the third column.

	I-(2,1;0,6)	Li *et al* [9]	II-(2,0;3,6)	III-(2,0;−3,6)	Exp.
a (Å)	5.11	5.11	5.90	5.90	5.64 [16] 5.76 [18] 5.7 [19, 21]
b (Å)	17.71	17.71	15.44	15.33	14.8 [16] 15.0 [18] 15.5 [19, 21]
z (Å)	3.35	3.1–3.5	3.18	3.17	
θ (°)	40	38	36	34	43 [17] 31 [19]
ϕ (°)	87	81	81	80	
Φ (eV)	4.25	4.29	4.48	4.50	4.52 [16] 4.4 [20] 4.6 [23]
E_b (eV)	−0.29	−0.16	−0.42	−0.42	−1.14 [18]

in equation (11) gives slightly different orderings, but we found that orderings are basically similar and therefore selected the most simple option. The lattices with lowest strain are listed in table 1. It can be seen that supercell I, which has been used in earlier reports to model the PC/Au(1 1 1) surface [9], possesses a rather large internal strain. On the other hand, our method reveals the existence of other non-trivial supercell arrangements which are associated with a much less strained PC lattice. In particular, among all the interfaces formed by a single PC(0 1 0) surface unit cell, the value of $\bar{\varepsilon}$ is 67% and 77% lower for supercell II and III, respectively.

To analyze the relationship between strain and adsorption properties in PC/Au(1 1 1), we have compared the optimized geometries of supercells I, II, and III (see table 2). For each optimized geometry we calculate the lattice vectors a, b of the PC/Au(1 1 1) supercell, and the geometrical parameters of the PC crystal: the adsorption height z and the polar and azimuthal adsorption angles θ and ϕ, see figures 4((b) and (c)). Since supercell II and III have very similar properties, in the following we will only compare supercell I and II, see figures 4((a) and (b)). The structural parameters obtained for supercell I are very similar to those obtained using a plane wave basis set [9]. However, supercell II and III provides an overall better agreement with the available experimental data. In particular, the supercell lattice vectors a, b, and the azimuthal angle ϕ are closer to those measured experimentally.

In addition to the geometrical properties, we find that the calculated work function for supercell II is also in closer agreement with that measured experimentally, compared to that calculated for supercell I. Finally, the binding energy E_b calculated for supercell II is also larger compared to that calculated for supercell I. This indicates that the supercell II and III, in addition to providing structural parameters in better agreement with those measured experimentally, lead to a structure which is thermodynamically more favorable. We note that the discrepancy relative to the experimental value, is due to the neglect of van der Waals forces.
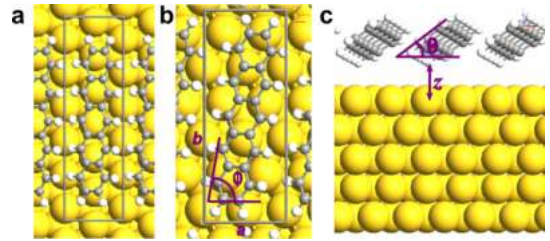

Figure 4. (a) Top view of supercell I. (b) and (c) Top and side views of supercell II. The structural parameters a, b, ϕ, θ and z are also shown (see the main text for a description of the parameters).

3.2. Al/InAs

Following recent experimental work on InAs NWs in which superconducting properties have been induced by the proximity effect with Al [25–28], we have considered two surfaces of InAs: the $(1\,\bar{1}\,0\,0)$ surface of the wurtzite phase (hereafter, $(1\,\bar{1}\,0\,0)_{WZ}$, and the $(1\,1\,1)$B surface of the zinc-blend phase (hereafter, $(1\,1\,1)$B$_{ZB}$). NWs with both these surfaces orientations have been grown experimentally, and it has been demonstrated that the precise orientation of the epitaxial Al overlayer depends on the exposed InAs surface [29].

For each of the two InAs surfaces, we have performed a scan over all Al(mkl) surfaces with $m, k, l \leqslant 3$. Subsequently, for each set of Miller indexes, we have generated all possible supercells with $N_{max}, M_{max} \leqslant 6$ and with a maximum of four InAs surface cells, by straining the Al lattice in the plane perpendicular to the interface.

For both the InAs surfaces considered, we have found that the Al surface which is predicted to have the lowest strain in the Al overlayer matches with that identified experimentally for thick ($t > 30$ nm) Al overlayers, see table 3. In the case of InAs$(1\,\bar{1}\,0\,0)_{WZ}$, this corresponds to Al$(1\,1\,\bar{2})$, whereas in the case of InAs$(1\,1\,1)$B$_{ZB}$, this corresponds to Al$(1\,1\,1)$.

Another check on the accuracy of the method can be done by comparing the structures of the predicted InAs/Al interfaces with those measured experimentally. Figure 5 shows the predicted InAs/Al interfaces, superimposed to the measured HR-TEM images for each interface. It can be seen that, for both interfaces, the agreement between the structural model and the HR-TEM pattern is excellent. On the InAs side of the interfaces, regions of dark and bright contrast can be associated with In and As atoms, respectively, whereas on the Al

---

[2] Figure 2 of Li *et al* [9] shows that the total energy as function of distance is lowest at $z \sim 3.3$ Å while the authors report $z = 3.13$ Å. To address this discrepancy, the authors put the following comment: 'We note that the extreme flatness of the potential energy surface in the range $z \sim 3.1 - 3.5$ Å does not allow for a very accurate determination of the optimal z distance'.

Table 3. Predicted InAs/Al interfaces with the three lowermost strain for the two InAs surfaces considered. The second (fifth) and third (sixth) columns show the surface orientation of the InAs (Al) supercell and its structure in the basis of the primitive cell of the corresponding InAs (Al) surface. The fourth column shows the number of InAs surface cells in the structure. ε_{11}, ε_{22}, ε_{12} are the components of the strain tensor applied to the Al surface cell in order to match the gold supercell. $\bar{\varepsilon} = (|\varepsilon_{11}| + |\varepsilon_{22}| + |\varepsilon_{12}|)/3$, is the average strain.

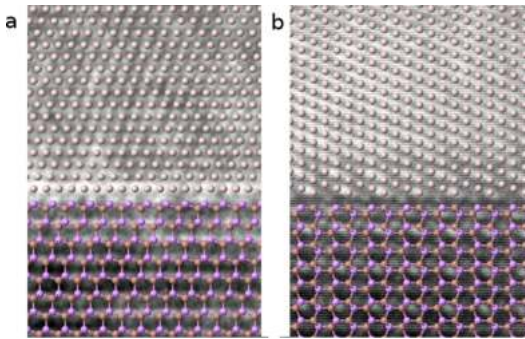| Structure	InAs surface	InAs	#InAs	Al surface	Al	ε_{11}	ε_{22}	ε_{12}	$\bar{\varepsilon}$
I	$(1\,\bar{1}\,0\,0)_{WZ}$	(2,0;0,1)	2	$(1\,1\,\bar{2})$	(3,0;0,1)	−0.26	−0.27	0	0.18
II	$(1\,\bar{1}\,0\,0)_{WZ}$	(2,0;−1,2)	4	$(1\,1\,3)$	(3,0;0,3)	−0.26	−1.79	0	0.68
III	$(1\,\bar{1}\,0\,0)_{WZ}$	(0,−1;−3,0)	3	$(1\,2\,3)$	(−1,1;2,1)	−0.27	−2.06	0	0.78
IV	$(1\,1\,1)_{BZB}$	(2,2;0,2)	4	$(1\,1\,1)$	(3,3;0,3)	−0.26	−0.26	0	0.18
V	$(1\,1\,1)_{BZB}$	(2,1;1,2)	3	$(1\,1\,1)$	(3,2;1,3)	−2.06	−2.06	0	1.37
VI	$(1\,1\,1)_{BZB}$	(2,0;1,2)	4	$(1\,1\,\bar{2})$	(3,0;0,1)	−0.26	5.79	0	2.02

Figure 5. (a) Structure of the predicted $(1\,1\,1)_{BZB}$/Al$(1\,1\,1)$ interface superimposed to the corresponding HR-TEM image measured experimentally (see [29]). The In, As and Al atoms are shown as brown, violet and grey spheres. (b) Same as (a), but for the InAs$(1\,\bar{1}\,0\,0)_{WZ}$/Al$(1\,1\,\bar{2})$ interface.

side of the interfaces, the regions with bright contrast can be associated with Al atoms.

4. Conclusions

In conclusion, we have presented a systematic and efficient method for determining a supercell geometry of the interface between two crystals. The method has been implemented into the Virtual NanoLab software [7]. The method was applied to two metal-semiconductor systems, namely the Au-pentacene and the InAs-Al interfaces. In both cases the method suggests interface geometries in good agreement with experimental data [16–19, 21, 29]. For Au-Pentacene we illustrated that previous studies [9], which does not use a systematic approach for finding a supercell geometry of the interface have lower binding energies and are not in accordance with experimental data.

Acknowledgments

References

[1] Blom A and Stokbro K 2013 *J. Comput. Electron.* **12** 623
[2] Dusastre V, Heber J, Pulizzi F, Stoddart A, Pamies P and Martin C 2012 *Nat. Mater.* **11** 91
[3] Kroemer H 2001 *Rev. Mod. Phys.* **73** 783
[4] Martin R M 2004 *Electronic Structure* (Cambridge: Cambridge University Press)
[5] Stradi D, Martinez U, Blom A, Brandbyge M and Stokbro K 2016 *Phys. Rev.* B **93** 155302
[6] Lazić P 2015 *Comput. Phys. Commun.* **197** 324
[7] Virtual NanoLab, version 2016.3 QuantumWise A/S 2016 The virtual NanoLab is freely available for academic researchers www.quantumwise.com
[8] Pieczyrak B, Abad E, Flores F and Ortega J 2011 *J. Chem. Phys.* **135** 084702
[9] Li H, Duan Y, Coropceanu V and Bredas J L 2009 *Org. Electron.* **10** 1571
[10] Lee K, Yu J and Morikawa Y 2007 *Phys. Rev.* B **75** 045402
[11] Lee K and Yu J 2005 *Surf. Sci.* **589** 8
[12] Toyoda K, Hamada I, Lee K, Yanagisawa S and Morikawa Y 2010 *J. Chem. Phys.* **132** 134703
[13] Saranyaa G, Natarajanb S N V, Kolandaivela P and Senthilkumara K 2012 *J. Mol. Graph. Mod.* **38** 334
[14] Koch N, Kahn A, Ghijsen J, Pireaus J, Schwartz J, Johnson R L and Elschner A 2007 *Appl. Phys. Lett.* **82** 70
[15] McDonald O, Cafolla A A, Carty D, Sheerin G and Hughes G 2006 *Surf. Sci.* **600** 3217
[16] Schroeder P, France C B, Park J B and Parkinson B A 2002 *J. Appl. Phys.* **91** 3010
[17] Ihm K, Kim B, Kang T H, Kim K, Joo M H, Kim T H, Yoon S S and Chung S 2006 *Appl. Phys. Lett* **89** 033504
[18] France C B, Schroeder P, Forsythe J B and Parkinson B A 2003 *Langmuir* **19** 1274
[19] Käfer D, Ruppel L and Witte G 2007 *Phys. Rev.* B **75** 085309
[20] Watkins N J, Yan L and Gao Y 2002 *Appl. Phys. Lett.* **80** 4384
[21] Kang J H and Zhu X Y 2003 *Appl. Phys. Lett* **82** 3248
[22] Soe W H, Manzano C, Sarkar A D, Chandrasekhar N and Joachim C 2009 *Phys. Rev. Lett.* **102** 176102
[23] Diao L, Frisbie C D, Schroepfer D D and Ruden P P 2007 *J. Appl. Phys.* **101** 014510
[24] Liu Z, Kobayashi M, Paul B C, Bao Z and Nishi Y 2010 *Phys. Rev.* B **82** 035311
[25] Deng M T, Vaitiekėnas S, Hansen E B, Danon J, Leijnse M, Flensberg K, Nygård J, Krogstrup P and Marcus C M 2016 *Science* **354** 1557

[26] Albrecht S M, Higginbotham A P, Madsen M, Kuemmeth F, Jespersen T S, Nygård J, Krogstrup P and Marcus C M 2016 *Nature* **531** 206

[27] Higginbotham A P, Albrecht S M, Kirŝanskas G, Chang W, Kuemmeth F, Krogstrup P, Jespersen T S, Nygård J, Flensberg K and Marcus C M 2015 *Nat. Phys.* **11** 1017

[28] Chang W, Albrecht S M, Jespersen T S, Kuemmeth F, Krogstrup P, Nygård J and Marcus C M 2015 *Nat. Nanotechnol.* **10** 232

[29] Krogstrup P, Ziino N L B, Chang W, Albrecht S M, Madsen M H, Johnson E, Nygård J, Marcus C M and Jespersen T S 2015 *Nat. Mater.* **14** 400

[30] The interface builder in VNL http://docs.quantumwise.com/technicalnotes/interface_builder/interface_builder.html

[31] Carel R, Thompson C and Frost H 1996 *Acta Mater.* **44** 2479

[32] Atomistix ToolKit, version 2016.3 QuantumWise A/S 2016 www.quantumwise.com

[33] Junquera J, Paz O, Sánchez-Portal D and Artacho E 2001 *Phys. Rev.* B **64** 235111

[34] Wang Y and Perdew J 1991 *Phys. Rev.* B **43** 8911

[35] Monkhorst H J and Pack J D 1976 *Phys. Rev.* B **13** 5188

[36] Boys S F and Bernardi F 1970 *Mol. Phys.* **19** 553

[37] Blum V, Gehrke R, Hanke F, Havu P, Ren X, Reuter K and Scheffler M 2009 *Comput. Phys. Commun.* **180** 2175

[38] Gruhn N E, da Silva Filho D A, Bill T G, Malagoli M, Coropceanu V, Kahn A and Bredas J L 2002 *J. Am Chem. Soc.* **124** 7918

[39] García-Gil S, García A, Lorente N and Ordejón P 2009 *Phys. Rev.* B **79** 075441

[40] Schiefer S, Huth M, Dobrinevski A and Nickel B 2007 *J. A. Chem. Soc.* **129** 10316

Determination of low-strain interfaces via geometric matching

Line Jelver,[1,2] Peter Mahler Larsen,[2] Daniele Stradi,[1] Kurt Stokbro,[1] and Karsten Wedel Jacobsen[2,*]

[1]*QuantumWise A/S, Fruebjergvej 3, DK-2100 Copenhagen, Denmark*
[2]*Department of Physics, Technical University of Denmark, DK-2800 Kongens Lyngby, Denmark*
(Received 10 May 2017; published 22 August 2017)

We present a general method for combining two crystals into an interface. The method finds all possible interfaces between the crystals with small coincidence cells and identifies the strain and area of the corresponding two-dimensional cells of the two crystal surfaces. We apply the method to the two semiconductor alloys $InAs_{1-x}Sb_x$ and $Ga_xIn_{1-x}As$ combined with a selection of pure metals or with NbTiN to create semiconductor/superconductor interfaces. The lattice constant of the alloy can be tuned by composition and we can extract the alloy lattice parameters corresponding to zero strain in both the metal and the alloy. The results can be used to suggest new epitaxially matched interfaces between two materials.

I. INTRODUCTION

The development of modern technology has become increasingly dependent on knowledge of interfaces at the atomic scale. As the size of electronic devices decreases, interfaces become an increasingly dominant part of the system and thus become the limiting factor for device performance [1–3]. Many difficulties are thus related to obtaining a stable and defect-free interface. When the materials are not commensurate, a large strain can build up at the interface, and result in defects and unstable interface geometries. To this end, it can be beneficial to use an alloy as one of the interface materials. By changing the alloy composition, the lattice constant for one of the interface materials can be tuned, thereby obtaining commensurate lattices across the interface. Many future devices can therefore be expected to be designed from alloys. A growing field, where alloys are commonly used, is the fabrication of core-shell nanowires. These nanowires have numerous applications, e.g., for photodetectors [4], photoelectrodes [5], and thermoelectric devices [6].

The prediction of the stability of an interface is difficult [7] and the commonly used approach is trial and error where many samples must be grown before it can be concluded whether a stable interface can be formed or not. In this paper, we present a crystal matching method which permits the combination of any two crystals and provides information on the crystal surfaces, if any, that allow for a low-strain epitaxial interface. The method is solely based on geometrical considerations of the possible surface cells of the two crystals and it leads to an identification of interfaces where both the strain and the size of the coincidence interface cell are small. Having low stress and a small interface cell does not by itself guarantee a stable interface, as the atomic structure of the interface may also play an important role. However, the simple geometrical criteria provide a good starting point for further experimental or theoretical investigations.

In a previous article [8], some of the authors have shown how to find good matches between specific surfaces of two crystals and a related, but more simplistic, method for such a two-dimensional (2D) match has also previously been

proposed [9]. With the present method, all possible crystal orientations and surfaces are investigated at the same time. Furthermore, we introduce a scaling parameter between the two crystals which can be tuned to gradually change the size of one of the crystal structures while keeping the other fixed. The scaling parameter mimics the situation where the lattice constant of one of the materials can be tuned by modifying the alloy composition, and it provides a convenient parameter for analyzing and understanding the interface-matching problem. We derive an analytical relation between the scaling parameter and the minimal strain, and demonstrate its usefulness in Sec. IV, where we investigate the matches between an arbitrary fcc crystal and an arbitrary bcc crystal.

The introduction of the scaling parameter makes the method an ideal tool for investigating interfaces containing alloys. In Sec. V, we apply the method to the two semiconductor alloys $InAs_{1-x}Sb_x$ and $Ga_xIn_{1-x}As$ combined with a range of metals (Al, Ni, Cu, Ag, Au, Pb, V, Fe, Nb, and Co) and for each metal we predict the alloy lattice constants which lead to strain free interfaces. InAs and InSb are, for example, used in semiconductor-superconductor core-shell nanowires for the realization of zero-energy localized Majorana modes [10–15]. The results obtained here therefore provide some guidelines for promising new combinations of semiconductor alloy compositions and metals for core-shell nanowires. Promising results for the generation of Majorana modes have also been shown for an $InSb-Nb_{1-x}Ti_xN$ interface [16]. The final part of this work is to investigate how the two semiconductor alloys match with this superconducting alloy.

II. INTERFACE ENERGETICS

The method we are going to describe below makes it possible to identify interfaces with small coincidence cells where only a small strain is required. The model thus takes only the material lattices into account, but not the atomic details. To what extent such interfaces will be stable is highly dependent on the particular materials and the character of the bonding. To discuss this we consider the situation where two materials A and B are homogeneously strained and put together to form an interface. The energy difference ΔE associated with straining the materials and forming the interface can be divided into

*kwj@fysik.dtu.dk

three contributions,

$$\Delta E = \Delta E^{\text{int}} + \Delta E^{\text{surf. strain}} + \Delta E^{\text{bulk strain}}, \qquad (1)$$

where the interface term is the energy gained by forming the interface from the surfaces at fixed strain,

$$\Delta E^{\text{int}} = E_{\text{AB}}^{\text{int}}(\epsilon_A, \epsilon_B) - E_A^{\text{surf}}(\epsilon_A) - E_B^{\text{surf}}(\epsilon_B). \qquad (2)$$

The second term is the energy change in the surface energy because of the strain,

$$\Delta E^{\text{surf. strain}} = E_A^{\text{surf}}(\epsilon_A) - E_A^{\text{surf}}(\epsilon_A = 0)$$
$$+ E_B^{\text{surf}}(\epsilon_B) - E_B^{\text{surf}}(\epsilon_B = 0). \qquad (3)$$

This contribution can be both positive or negative and we shall in the following assume that this term can be considered small. The third term is the energy cost associated with straining the bulk of the materials,

$$\Delta E^{\text{bulk strain}} = E_A^{\text{bulk}}(\epsilon_A) - E_A^{\text{bulk}}(\epsilon_A = 0)$$
$$+ E_B^{\text{bulk}}(\epsilon_B) - E_B^{\text{bulk}}(\epsilon_B = 0). \qquad (4)$$

If we assume that the dependency of the surface energy with strain can be neglected, we expect to get a stable interface if the energy gain from the interface ΔE^{int} dominates the cost from straining the bulk of the materials $\Delta E^{\text{bulk strain}}$. The model suggested here identifies interface matches with low-strain and small interface coincidence cells. The small strain will clearly tend to minimize the bulk strain energy as this scales quadratically with the strain. A more questionable assumption is that a small interface cell will lead to strong bonding at the interface. The bonding will often depend quite sensitively on the atomic structure at the interface, which is not considered at all by the model. However, in many cases where the interface cell is small, a translation of one of the surfaces relative to the other makes it possible to obtain favorable bonding configurations which are then repeated over the entire interface, leading to general high stability. However, if the interface cell is large, the atomic bonding configurations will often vary considerably over the cell, so that in some parts of the cell favorable bonding configurations are obtained but in other parts not. Overall this leads to weaker bonding [17].

Another advantage of a small coincidence cell is that it may be more stable with respect to shear in the interface. For a small cell, a large corrugation in the energy landscape as a function of displacement of one of the materials relative to the other one along the interface can be expected. The bonds across the interface will respond to the shear "in synchrony" leading to large variation. For a larger cell where some bonds are strong and others are weak, the bonds will respond differently to the shear presumably leading to a smaller energy corrugation.

If the materials are thick, the strain has to be very small since the bulk strain energy grows in proportion to the thickness. In this limit, only interface matches at very low strain will be acceptable. However, in practice this limit may also lead to incommensurate interfaces or defects at or close to the interface, situations clearly beyond what a simple lattice model can account for. Similarly, if the interface bonding energy is very small and has a small corrugation, as is, for example, the case with van der Waals bonding, stable interfaces with large moiré-pattern coincidence cells or even incommensurate

cells may occur. This situation can arise even for very thin films as, for example, in the case of graphene on some metal surfaces, where the interaction is weak. Despite the fact that a graphene layer is atomically thin, the strong interatomic bonding within the graphene layer results, for some metals, in little accommodation of the surface and large coincidence cells as a result [18,19].

III. CRYSTAL MATCHING METHOD

Our method for creating an interface between two crystals is general and based on 2D cells of the two crystal surfaces. The 3D vectors of the crystal, defining these surface cells, are projected from $\mathbb{R}^3$ to $\mathbb{R}^2$ as illustrated in Fig. 1(a). We begin by explaining the method behind matching two such cells and extracting the related strain.

Let the surface cell of the first crystal be defined by two vectors $\mathbf{u}_1$ and $\mathbf{u}_2$, where $\mathbf{u}_1 = [u_{1x}, u_{1y}]^T$, as shown in Fig. 1(a). Similarly, let $\mathbf{v}_1$ and $\mathbf{v}_2$ denote the two vectors which define the surface cell of the second crystal. Then, the affine transformation $\mathbf{A}$ which maps $[\mathbf{u}_1, \mathbf{u}_2]$ onto $[\mathbf{v}_1, \mathbf{v}_2]$ is given by
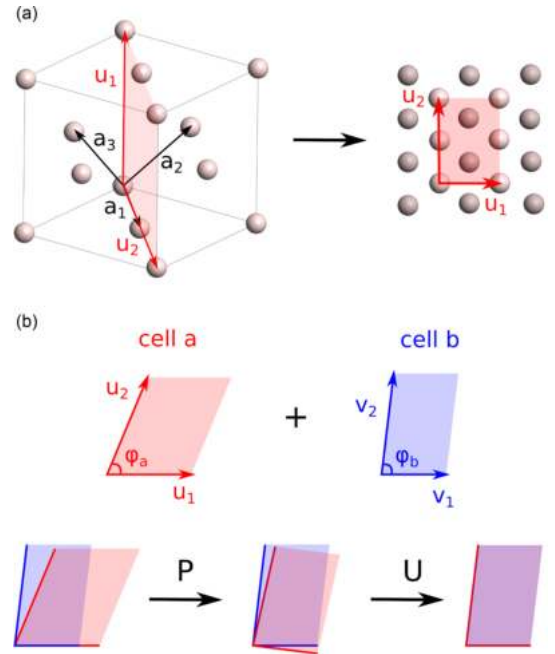

FIG. 1. The method for finding and matching the 2D surface cells of two crystals. (a) The lattice vectors of the first crystal $(\mathbf{u}_1, \mathbf{u}_2)$ are created from a linear combination of the Bravais vectors $(\mathbf{a}_1, \mathbf{a}_2, \mathbf{a}_3)$. Here $\mathbf{u}_1 = -\mathbf{a}_1 + \mathbf{a}_2 + \mathbf{a}_3$ and $\mathbf{u}_2 = 2\mathbf{a}_1$. The two vectors are then projected from the three-dimensional (3D) representation to a 2D representation on a crystal surface. (b) Two cells of two different crystals are matched by applying the affine transformation $\mathbf{A}[\mathbf{u}_1, \mathbf{u}_2] = [\mathbf{v}_1, \mathbf{v}_2]$, where $\mathbf{A} = \mathbf{UP}$ consists of a rotation $\mathbf{U}$, and a strain matrix $\mathbf{P}$.

the following system of linear equations,

$$\begin{bmatrix} A_{11} & A_{12} \\ A_{21} & A_{22} \end{bmatrix} \begin{bmatrix} u_{1x} & u_{2x} \\ u_{1y} & u_{2y} \end{bmatrix} = \begin{bmatrix} v_{1x} & v_{2x} \\ v_{1y} & v_{2y} \end{bmatrix}. \tag{5}$$

Any square matrix can be decomposed into the product of an orthonormal matrix $\mathbf{U}$, and a positive definite symmetric matrix $\mathbf{P}$. This is known as a polar decomposition [20]. The symmetric matrix defines the 2D strain tensor $\boldsymbol{\epsilon}$ for deforming one cell into the other,

$$\mathbf{P} = \mathbf{I} + \boldsymbol{\epsilon} = \begin{bmatrix} 1 + \epsilon_{xx} & \epsilon_{xy} \\ \epsilon_{xy} & 1 + \epsilon_{yy} \end{bmatrix}. \tag{6}$$

The first vectors are rotated along the x axis s.t. $u_{1y} = v_{1y} = 0$. This can be done without loss of generality and leads to

$$A_{11} = \frac{v_{1x}}{u_{1x}}, \tag{7}$$

$$A_{12} = \frac{v_{2x}}{u_{2y}} - \frac{v_{1x}u_{2x}}{u_{1x}u_{2y}}, \tag{8}$$

$$A_{21} = 0, \tag{9}$$

$$A_{22} = \frac{v_{2y}}{u_{2y}}. \tag{10}$$

We now make the polar decomposition of $\mathbf{A}$ s.t. $\mathbf{A} = \mathbf{UP}$, where $\mathbf{U}$ is a rotation matrix because of the chosen projection to $\mathbb{R}^2$,

$$\mathbf{U} = s \begin{bmatrix} A_{11} + A_{22} & A_{12} \\ -A_{12} & A_{11} + A_{22} \end{bmatrix}$$
$$= \begin{bmatrix} \cos(\phi) & -\sin(\phi) \\ \sin(\phi) & \cos(\phi) \end{bmatrix}, \tag{11}$$

$$\mathbf{P} = \mathbf{U}^T \mathbf{A}, \tag{12}$$

where s is a factor which makes the columns of $\mathbf{U}$ unit vectors. The $\mathbf{U}$ matrix defines the counterclockwise rotation of the $[\mathbf{u}_1, \mathbf{u}_2]$ cell onto the $[\mathbf{v}_1, \mathbf{v}_2]$ cell by the angle $\phi = |\phi_a - \phi_b|/2$ as shown in Fig. 1(b). Using this method, Eqs. (7)–(12) thus yield the strain matrix of any given cell combination.

A. Algorithm

We now explain the algorithm behind extracting the strain matrix of all the possible matches between two crystals. The procedure is illustrated in the flow chart in Fig. 2.

1. Create (i,j,k) list from ℓ_{max}

The first step is to create all the possible lattice vectors of each crystal up to a specified maximum length ℓ_{max}. The vectors are created as integer combinations of the Bravais vectors of the crystal, as illustrated in Fig. 1(a),

$$\mathbf{u} = i\mathbf{a}_1 + j\mathbf{a}_2 + k\mathbf{a}_3, \quad |\mathbf{u}| < \ell_{max}. \tag{13}$$

This will create a list of (i,j,k) values for each crystal.

2. Create vector pair list

The next step is to combine the created vectors such that a list of unique surface cells is created for each crystal. This
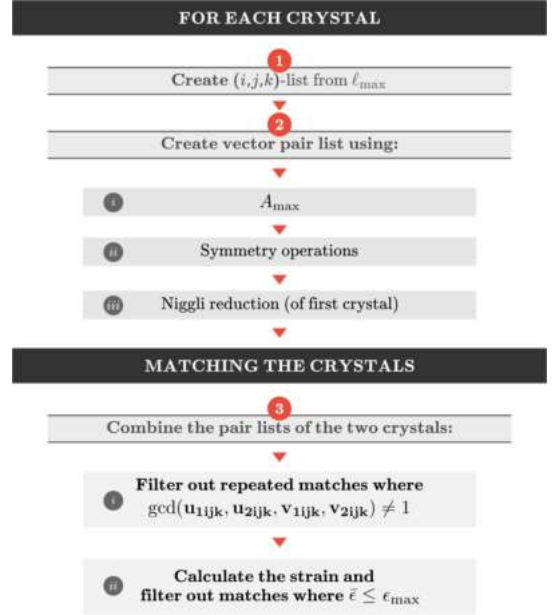

FIG. 2. Flow chart behind the algorithm for matching two crystals.

procedure uses two kinds of filters to remove equivalent surface cells from the list; the symmetry operations of the atom-free crystal [21] and Niggli reductions of the cells [22].

As a starting point, we create a list of symmetrically unique vectors of the crystal by applying the symmetry operations $\{\mathbf{S}\}$ to each vector in the generated (i,j,k) list. Let $\mathbf{u}$ be the vector we apply the operations to and let $\{\mathbf{Su}\}$ be the set of all the vectors created when applying the symmetry operations. We define the canonical representation of this set as its *least element* with respect to the lexicographic ordering. When iterating through the (i,j,k) list, noncanonical vectors are discarded.

To create the unique surface cells, we combine each vector from the original (i,j,k) list with the vectors in the symmetry reduced (i,j,k) list. The combination is discarded if the two vectors are parallel or if the area that they span exceeds A_{max}. The symmetry operations of the crystal are then reapplied, this time on both vectors: $\{\mathbf{S}[\mathbf{u}_1,\mathbf{u}_2]\}$. Again, any noncanonical pairs are discarded.

The final test is to investigate whether the cell is a Niggli reduced cell. A Niggli reduced 2D cell fulfils

$$\mathbf{u}_1 \cdot \mathbf{u}_1 \leqslant \mathbf{u}_2 \cdot \mathbf{u}_2, \quad \mathbf{u}_1 \cdot \mathbf{u}_2 \leqslant \tfrac{1}{2}\mathbf{u}_1 \cdot \mathbf{u}_1. \tag{14}$$

The cells that are not Niggli reduced are discarded. This is only done for the first crystal, since a Niggli reduced cell may be strained into a non-Niggli reduced cell when the two crystals are combined. After these calculations, we have created a list of surface cells for each crystal and the next step is to combine these two lists.

3. Combine the pair lists of the two crystals

When the cells of the two crystals are matched, the first step is to filter out repeated matches. As an example, let a $[\mathbf{u}_1,\mathbf{u}_2]$ cell of the first crystal be combined with a $[\mathbf{v}_1,\mathbf{v}_2]$ cell where $\mathbf{u}_{1ijk} = (1,0,0)$, $\mathbf{u}_{2ijk} = (2,0,1)$, $\mathbf{v}_{1ijk} = (0,0,2)$, and $\mathbf{u}_{2ijk} = (4,4,2)$. This combination is equivalent to the $((2,0,0),(4,0,2),(0,0,4),(8,8,4))$ combination. We avoid investigating both combinations by discarding any combinations whose greatest common divisor, $\gcd(\mathbf{u}_{1ijk},\mathbf{u}_{2ijk},\mathbf{v}_{1ijk},\mathbf{v}_{2ijk})$, is not 1. After this preliminary test, the strain matrix of the match is calculated using the method explained in the beginning of this section.

We now define a measure for the average strain of a match,

$$\bar{\epsilon} = \sqrt{\frac{\epsilon_{xx}^2 + \epsilon_{yy}^2 + \epsilon_{xx}\epsilon_{yy} + \epsilon_{xy}^2}{4}}, \quad (15)$$

where $\epsilon_{xx},\epsilon_{xy}$, and ϵ_{yy} are the components of the 2D strain tensor shown in Eq. (6). This average strain is an invariant of the strain tensor, since $4\bar{\epsilon}^2 = \text{Tr}(\boldsymbol{\epsilon})^2 - \det(\boldsymbol{\epsilon})$. Matches with an average strain below a given strain threshold $\varepsilon_{\max}$ are kept.

This concludes the algorithm for finding all the matches between two crystals. The parameters determining which matches to include in the search are $\ell_{\max}$, $A_{\max}$, and $\varepsilon_{\max}$. These parameters help to filter out the cells that wouldn't create a physically meaningful interface. The area and length threshold ensures that we don't investigate unreasonably large or narrow cells and the strain threshold filters out the most strained matches.

The algorithm is implemented using C++ with a Python interface and has good performance; finding all matches between a InAs fcc crystal and a Cobalt hcp crystal with the parameters, $\ell_{\max} = 50\,\text{Å}$, $A_{\max} = 200\,\text{Å}^2$, and $\epsilon_{\max} = 2\%$, takes approximately 20 min on a normal laptop. The algorithm is available in VIRTUAL NANOLAB version ATK-VNL-2017 [23].

IV. MATCHING OF A FCC CRYSTAL WITH A BCC CRYSTAL

In the previous section, we have explained how to match two specific crystals with fixed lattice parameters. Here, we discuss the matching of any fcc crystal with any bcc crystal. To this end, we introduce an isotropic scaling parameter k, which is applied to the Bravais vectors of the bcc crystal. This scaling parameter can then be defined as the ratio between the lattice constants of the two crystals, $k = a_{\text{fcc}}/a_{\text{bcc}}$. The effect of k on the strain matrix is linear,

$$\mathbf{A} = k\mathbf{U}\mathbf{P} = \mathbf{U}\begin{bmatrix} k(1+\epsilon_{xx}) & k\epsilon_{xy} \\ k\epsilon_{xy} & k(1+\epsilon_{yy}) \end{bmatrix}. \quad (16)$$

This means that the effect of the scaling parameter on the average strain can be described by the simple analytical relation,

$$4\bar{\epsilon}^2(k) = k^2\left(\epsilon_{xx}^2 + \epsilon_{yy}^2 + \epsilon_{xx}\epsilon_{yy} + \epsilon_{xy}^2\right) + k^2(3\epsilon_{xx} + 3\epsilon_{yy} + 3)$$
$$- k(3\epsilon_{xx} + 3\epsilon_{yy} + 6) + 3, \quad (17)$$

where the strain tensor components are referring to the case of $k = 1$. This relation allows us to calculate the average strain of a match at any k value once the strain matrix has been
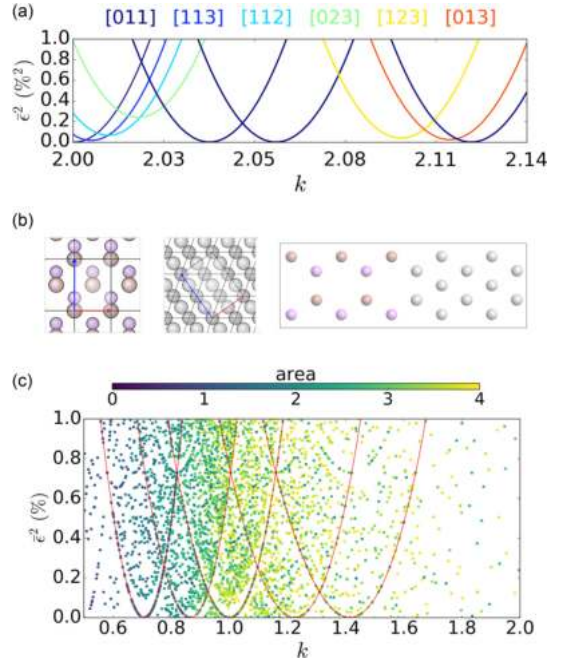

FIG. 3. The matches between a fcc and a bcc crystal. k represents the scaling between the two lattice constants, $k = a_{\text{fcc}}/a_{\text{bcc}}$. (a) The $\bar{\epsilon}^2(k)$ relation of (17) for optimal matches involving the [110] surface of the fcc crystal. The color of the curves represents different surfaces of the bcc crystal. (b) The surface cells and corresponding interface of the perfect $k = 2$ match shown on (a). Illustrated here for InAs with vanadium. (c) Scatter plot of matches where the minima of the strain parabola gets below 10%. The dots represent the minimal strain of the match and the k value where this strain occurs. We have chosen $\ell_{\max}$ and $A_{\max}$ as four times the lattice constant of the unstrained crystal. The color represents the area of the fcc surface cell of the match.

calculated for any one specific value of k. Equation (17) defines a strain parabola; the minimal strain of a match, along with the corresponding k value, can be found from the minimum of this parabola.

The strain parabolas for the optimal matches [24] between an fcc[110] surface and a bcc crystal with k values between 2.0 and 2.14 are illustrated in Fig. 3(a). This range is of relevance for the matching of a InAsSb alloy with vanadium. It can be seen that the two [110] surfaces have perfect matches at $k = 2.0$, 2.04, 2.06, and 2.12. The surface cells and corresponding interface of the perfect $k = 2.0$ match are illustrated in Fig. 3(b) for InAs and vanadium. This k value can be obtained, when matching, e.g., $InAs_{0.996}Sb_{0.004}$ to vanadium or $Ga_{0.786}In_{0.214}As$ to iron. As such, this specific match reappears in the results of the next section where these two alloys are matched to a range of metals.

To obtain the full picture of the matches between a fcc and a bcc crystal, we use the algorithm described in Sec. III and apply the strain threshold to the minimal strain of a given match. It corresponds to the following flow chart in Fig. 2 but where step 3.ii. is altered such that after calculating the strain

matrix, we use Eq. (17) to find the minimal strain of the match and only keep the matches where this is lower than the strain threshold. In this manner, we can retrieve the strain parabolas of all the relevant matches by doing a single calculation at $k = 1$. We have chosen $\ell_{\max}$ and $A_{\max}$ as four times the lattice constant of the unstrained crystal and $\epsilon_{\max} = 10\%$.

Figure 3(c) shows the results of this general investigation. For each match, we plot the minimal strain and the corresponding k value. Note, that the y axis shows the squared strain, since this illustrates the general shape of the matches better. The structure shows curves where zero strain minimas appear, e.g., at the points $k = 1/\sqrt{2} \approx 0.71$, $k = \sqrt{3}/2 \approx 0.87$, $k = 1$, $k = \sqrt{3/2} \approx 1.22$, and $k = \sqrt{2} \approx 1.41$. The matches lying on these curves are related to a uniaxial strain between the two surface cells. The perfect matches at $k = 1$ appear since this value corresponds to the [100] facets of the two cubic crystals fitting perfectly together. All other matches on this $k = 1$ curve correspond to a match where one of the cells is rotated and then stretched in one direction only. The other zero strain points also represent some symmetry of the two crystals. The zero strain match at $k = 1/\sqrt{2}$, e.g., corresponds to matching the rotated bcc[100] surface with cell vectors $\mathbf{v}_1 = [\sqrt{2}a_{\mathrm{bcc}},0]$ and $\mathbf{v}_2 = [0,\sqrt{2}a_{\mathrm{bcc}}]$ to a [100] facet of the fcc crystal. The other matches lying on this curve represents a uniaxial strain on top of this perfect match where one of the cells is rotated, stretched in both directions by $\sqrt{2}$, and then stretched in one direction afterwards. The matches lying on a specific curve are thus related by having a fixed eigenvalue of the $\mathbf{P}$ matrix of $1/k_{\mathrm{zsm}}$, where k_{zsm} is the k value at the zero strain minimum of the curve. For example, all matches on the $k = 1/\sqrt{2}$ curve have $\mathbf{P}$ matrices with the eigenvalue $\sqrt{2}$.

Two things are important to note about this plot. First, the length and area limits of the vectors and cells determine the density of the found matches. Without these limits the entire $(\bar{\epsilon},k)$ space would be filled with points. Secondly, the constraining to cubic structures lead to points with nonzero strain; if the crystal structures were allowed to vary arbitrarily, all points would have zero strain.

These results demonstrate that the method represents a general tool for crystal matching. The strength of the method is that it only relies on the geometry of the crystals. This makes it possible to calculate results for two arbitrary crystals and apply these results to all interfaces between materials of these crystal structures. Furthermore, it is an ideal tool for investigating alloy crystals where the lattice parameter can be varied as the composition of the alloy is changed. This will be the subject of the next section.

V. INTERFACES BETWEEN SEMICONDUCTOR ALLOYS AND METALS

We apply the method to two different semiconductor alloys, $\mathrm{InAs}_{1-x}\mathrm{Sb}_x$ and $\mathrm{Ga}_x\mathrm{In}_{1-x}\mathrm{As}$, and match their surfaces with those of 10 different metals (Al, Ni, Cu, Ag, Au, Pb, V, Fe, Nb, and Co). In particular, we study how the orientation and strain of the metallic surface depends on the lattice parameter of the semiconductor surface, which can be tuned by changing the mole fraction. The two alloys form a zincblende crystal
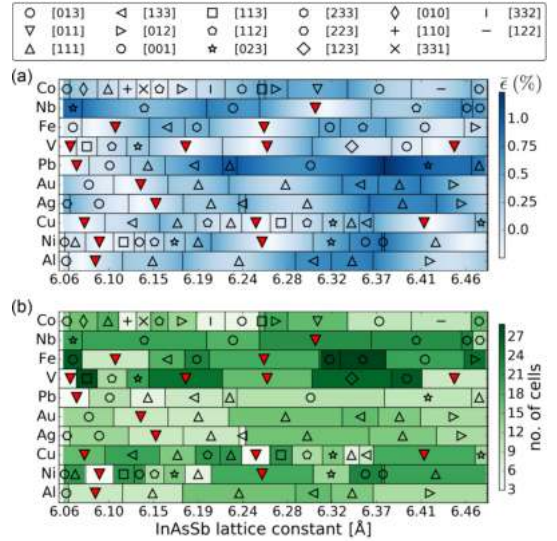

FIG. 4. (a) The InAsSb[1$\bar{1}$0] surface matched with 10 different metals. Each block represents the match which results in the lowest average strain between the two materials. The background color shows the strain in percent and the markers show the involved metal surface. Filled markers denote a match where zero strain can be obtained. (b) Same as (a) but where the background color shows the area given by the number of alloy surface unit cells of the match.

and the relation between the lattice constant and mole fraction x can be approximated by the linear relations [25]:

$$a_{\mathrm{InAsSb}}(x) = 6.0583 + 0.4207x, \qquad (18)$$

$$a_{\mathrm{GaInAs}}(x) = 6.0583 - 0.405x. \qquad (19)$$

We use the experimentally determined lattice constants [26] of the metals and strain the metal surfaces to match the alloy surfaces. The chosen parameters [27] are $\ell_{\max} = 50$ Å, $A_{\max} = 200$ Å^2, and $\epsilon_{\max} = 2\%$. In addition, we set a limit on the Miller index of the crystal surfaces. If the highest value in the Miller index is above the threshold, $m_{\max} = 3$, the match is discarded. The matches are calculated for a single value of the mole fraction and the scaling relation (17) of Sec. IV is then used to get the results for the rest of the x values. This is possible, since each x value directly corresponds to a k value, $k = a_{\mathrm{alloy}}(x)/a_{\mathrm{metal}}$.

In Fig. 4, we show the matches involving the [1$\bar{1}$0] surface of InAsSb. Each block in the plot corresponds to a certain match and a certain strain parabola in a plot like Fig. 3(a). The background of Fig. 4(a) therefore represents the strain value of the lowest lying strain parabola. Figure 3(a) shows InAsSb[1$\bar{1}$0] matched to vanadium and it is seen how the variation of the lattice parameter results in different optimal matches. For instance, from a perfect [110] match to a low-strain [113] match as the lattice constant is increased from 6.06 to 6.08.
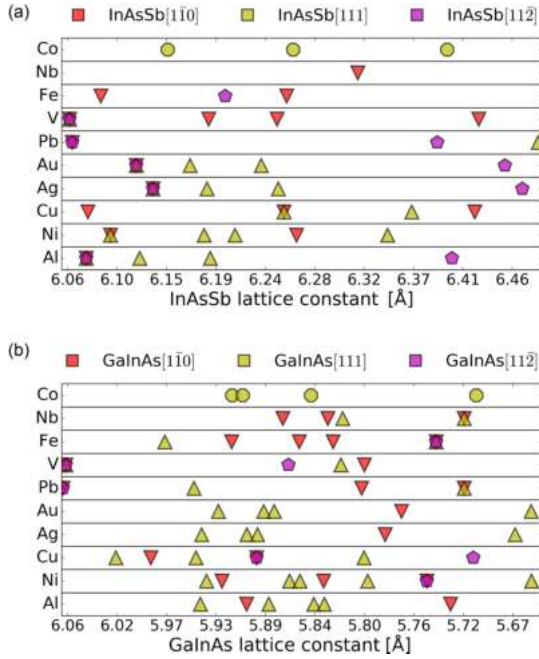
FIG. 5. The perfect matches of the [1$\bar{1}$0], [111], and [11$\bar{2}$] surfaces of (a) InAsSb and (b) GaInAs. The markers denote the metal surface (see Fig 4 for labels) and the color denotes the alloy surface. Each marker is placed at the alloy lattice constant which results in a zero strain match.

TABLE I. The perfect matches between NbTiN and the [1$\bar{1}$0], [111], and [11$\bar{2}$] surfaces of InAsSb and GaInAs. The NbTiN surface is the same as the given alloy surface.

InAsSb	k value	No. of cells	GaInAs	k value	No. of cells
[1$\bar{1}$0]	1.414	2	[1$\bar{1}$0]	1.354	11
[1$\bar{1}$0]	1.5	9	[111]	1.271	21
[111]	1.363	13	[111]	1.309	12
[111]	1.453	19	[111]	1.323	14
[111]	1.5	9	[111]	1.333	16
			[111]	1.363	13
			[11$\bar{2}$]	1.265	8
			[11$\bar{2}$]	1.291	5
			[11$\bar{2}$]	1.323	7

that can be found in the literature [28–31],

$$a_{\text{NbTiN}}(y) = 4.30 + 0.17y \quad y \in [0; 1]. \quad (20)$$

With this definition, the k value is given by $k = a_{\text{alloy}}(x)/a_{\text{NbTiN}}(y)$. The used matching parameters are the same as for the investigation of the pure metals and the perfect match results can be seen in Table I. For InAsSb, we find two zero strain matches for the [1$\bar{1}$0] surface and the first of these matches also has a very small unit cell of only two alloy surface unit cells. For the [111] surface, we find three zero strain matches and the $k = 1.5$ match has a reasonably small unit cell of nine surface cells. Plots like Figs. 4 and 5 showing all the matches between the semiconductors and NbTiN can be found in Supplemental Material [32].

VI. CONCLUSION

We have presented a general method for matching two crystals at an interface. A scaling parameter between the lattice constants of two crystals was introduced. Using this scaling parameter, we can consider a general match between an fcc and a bcc crystal. Matches for any value of the lattice constant ratio can be found by performing a single calculation. The method was applied to the two semiconductor alloys InAs$_{1-x}$Sb$_x$ and Ga$_x$In$_{1-x}$As matched with a range of metals (Al, Ni, Cu, Ag, Au, Pb, V, Fe, Nb, and Co). The scaling parameter was used to tune the lattice constant of the alloys with their composition. Results for the [1$\bar{1}$0], [111], and [11$\bar{2}$] alloy surfaces showed many perfect match solutions over a broad spectrum of the alloy lattice constant which is promising for realizing some of these matches experimentally. Finally, we have matched the two semiconductors to the superconducting alloy NbTiN. The results showed perfect matches with low surface cell areas for several of the investigated semiconductor surfaces.

The area of the match, given as the number of alloy surface unit cells, is illustrated in Fig. 4(b). It is seen that several zero strain matches are possible between the InAsSb[1$\bar{1}$0] surface and those of the metals. Nickel, copper, lead, and vanadium even have perfect matches with very small unit cells, indicating that these interfaces will potentially be stable. The geometry of this small area match between InAsSb and vanadium can be seen in Fig. 3(b).

Figure 5 shows all the perfect matches of the [1$\bar{1}$0], [111], and [11$\bar{2}$] surfaces of both InAsSb and GaInAs. The red triangles in Fig. 5(a) therefore represents the same matches as those highlighted in Fig. 4. The surfaces have been chosen since they typically terminate nanowires of the two investigated alloys. Many zero strain solutions are possible, especially for the [111] surfaces. Furthermore, it is seen that the perfect matches are distributed well across the range of lattice constants which should make it easier to realize some of these interfaces experimentally. Details of all the matches of the remaining two surfaces of InAsSb and the three surfaces of GaInAs is in the Supplemental Material [32].

The method has also been used to find matches between the two semiconductors and the superconductor Nb$_{1-x}$Ti$_x$N. Since this material is an alloy in the NaCl structure, this is yet another case of varying the scaling parameter. We use a linear scaling of the NbTiN lattice constant in between the values

[1] A. Blom and K. Stokbro, J. Comput. Electron. **12**, 623 (2013).

[2] V. Dusastre, J. Heber, F. Pulizzi, A. Stoddart, P. Pamies, and C. Martin, Nat. Mater. **11**, 91 (2012).

[3] H. Kroemer, Rev. Mod. Phys. **73**, 783 (2001).

[4] Y. Yang, K. Wang, H.-W. Liang, G.-Q. Liu, M. Feng, L. Xu, J.-W. Liu, J.-L. Wang, and S.-H. Yu, Sci. Adv. **1**, e1500714 (2015).

[5] Y. Myung, D. M. Jang, T. K. Sung, Y. J. Sohn, G. B. Jung, Y. J. Cho, H. S. Kim, and J. Park, ACS Nano **4**, 3789 (2010).

[6] P. K. Kasanaboina, S. K. Ojha, S. U. Sami, C. L. Reynolds, Jr., Y. Liu, and S. Iyer, Semicond. Sci. Technol. **30**, 105036 (2015).

[7] A. L.-S. Chua, N. A. Benedek, L. Chen, M. W. Finnis, and A. P. Sutton, Nat. Mater. **9**, 418 (2010).

[8] D. Stradi, L. Jelver, S. Smidstrup, and K. Stokbro, J. Phys.: Condens. Matter **29**, 185901 (2017).

[9] P. Lazi, Comput. Phys. Commun. **197**, 324 (2015).

[10] P. Krogstrup, N. L. B. Ziino, W. Chang, S. M. Albrecht, M. H. Madsen, E. Johnson, J. Nygård, C. M. Marcus, and T. S. Jespersen, Nat. Mater. **14**, 400 (2015).

[11] W. Chang, S. M. Albrecht, T. S. Jespersen, F. Kuemmeth, P. Krogstrup, J. Nygård, and C. M. Marcus, Nat. Nanotechnol. **10**, 232 (2015).

[12] M. T. Deng, S. Vaitieknas, E. B. Hansen, J. Danon, M. Leijnse, K. Flensberg, J. Nygård, P. Krogstrup, and C. M. Marcus, Science **354**, 1557 (3016).

[13] A. P. Higginbotham, S. M. Albrecht, G. Kiranskas, W. Chang, F. Kuemmeth, P. Krogstrup, T. S. Jespersen, J. Nygård, K. Flensberg, and C. M. Marcus, Nat. Phys. **11**, 1017 (2015).

[14] S. M. Albrecht, A. P. Higginbotham, M. Madsen, F. Kuemmeth, T. S. Jespersen, J. Nygård, P. Krogstrup, and C. M. Marcus, Nature (London) **531**, 206 (2016).

[15] V. Mourik, K. Zuo, S. M. Frolov, S. R. Plissard, E. P. A. M. Bakkers, and L. P. Kouwenhoven, Science **336**, 1003 (2012).

[16] H. Zhang, Ö Gül, S. Conesa-Boj, K. Zuo, V. Mourik, F. K. de Vries, J. van Veen, D. J. van Woerkom, M. P. Nowak, M. Wimmer, D. Car, S. Plissard, E. P. A. M. Bakkers, M. Quintero-Pérez, S. Goswami, K. Watanabe, T. Taniguchi, and L. P. Kouwenhoven, arXiv:1603.04069.

[17] D. Stradi, S. Barja, C. Díaz, M. Garnica, B. Borca, J. J. Hinarejos, D. Sánchez-Portal, M. Alcamí, A. Arnau, A. L. Vázquez de Parga, R. Miranda, and F. Martín, Phys. Rev. B **88**, 245401 (2013).

[18] M. Batzill, Surf. Sci. Rep. **67**, 83 (2012).

[19] D. Stradi, S. Barja, C. Díaz, M. Garnica, B. Borca, J. J. Hinarejos, D. Sánchez-Portal, M. Alcamí, A. Arnau, A. L. Vázquez de Parga, R. Miranda, and F. Martín, Phys. Rev. Lett. **106**, 186102 (2011).

[20] K. Shoemake and T. Duff, *Proceedings of the Conference on Graphics Interface '92* (Morgan Kaufmann Publishers Inc., San Francisco, CA, 1992), pp. 258–264.

[21] We use the symmetry operations of the empty cell, since the algorithm does not take atomic positions into account.

[22] P. Niggli, *Krystallographische und Strukturtheoretische Grundbegriffe* (Akademische Verlagsgesellschaft, Leipzig, 1928).

[23] http://www.quantumwise.com; the VIRTUAL NANOLAB is freely available for academic researchers.

[24] The matching parameters ℓ_{max}, A_{max}, ε_{max}, and m_{max} are chosen as for the alloy investigations in Sec. V.

[25] I. P.-T. Institute, Electronic archive New semiconductor materials Characteristics and properties, http://www.ioffe.ru/SVA/NSM/Semicond/.

[26] C. Kittel, *Introduction to Solid State Physics*, 8th ed. (Wiley, New York, 2004).

[27] The area constraint is set for the cell size when using the lowest lattice constant of each alloy.

[28] K. Makise, H. Terai, M. Takeda, Y. Uzawa, and Z. Wang, IEEE Trans. Appl. Supercond. **21**, 139 (2011).

[29] P. Bosland, F. Guemas, M. Juillard, M. Couach, and A. Khoder, in *Proceedings of the Fifth Workshop on RF Superconductivity* (DESY, Hamburg, 1991), p. 497.

[30] T. Shiino, S. Shiba, N. Sakai, T. Yamakura, L. Jiang, Y. Uzawa, H. Maezawa, and S. Yamamoto, Supercond. Sci. Technol. **23**, 045004 (2010).

[31] H. Myoren, T. Shimizu, T. Iizuka, and S. Takada, IEEE Trans. Appl. Supercond. **11**, 3828 (2001).

[32] See Supplemental Material at http://link.aps.org/supplemental/10.1103/PhysRevB.96.085306 for further results for interfaces between the semiconductor alloys InAsSb or GaInAs and metals or NbTiN.

Spontaneous breaking of time-reversal symmetry at the edges of 1T′ monolayer transition metal dichalcogenides

Line Jelver,[*] Daniele Stradi, and Kurt Stokbro

Synopsys Denmark, Fruebjergvej 3, PostBox 4, DK-2100 Copenhagen, Denmark

Thomas Olsen and Karsten Wedel Jacobsen[†]

CAMD, Department of Physics, Technical University of Denmark, Bldg. 307, DK-2800 Kongens Lyngby, Denmark

Using density functional theory (DFT) calculations and the Greens's function formalism, we report the existence of magnetic edge states with a noncollinear spin texture present on different edges of the 1T′ phase of the three monolayer transition metal dichalcogenides (TMDs): MoS_2, MoTe_2, and WTe_2. The magnetic states are gapless and accompanied by a spontaneous breaking of the time-reversal symmetry. This may have an impact on the prospects of utilizing WTe_2 as a quantum spin Hall insulator. It has previously been suggested that the topologically protected edge states of the 1T′ TMDs could be switched off by applying a perpendicular electric field [X. Qian, J. Liu, L. Fu, and J. Li, Science **346**, 1344 (2014)]. We confirm with fully self-consistent DFT calculations that the topological edge states can be switched off. The investigated magnetic edge states are seen to be robust and remain gapless when applying a field.

I. INTRODUCTION

In 2005, graphene was predicted to be a quantum spin Hall insulator (QSHI) [1] with a band gap emerging at the Dirac point as a consequence of spin-orbit coupling (SOC). However, due to the tiny SOC in graphene, it has not yet been possible to verify the prediction experimentally. The quantum spin Hall effect was, however, predicted and observed in HgTe quantum wells in 2007 [2,3] and the three-dimensional (3D) analog of the effect was realized in Bi and Sb chalcogenides in 2009 [4,5]. Meanwhile, several predictions for two-dimensional (2D) materials exhibiting the quantum spin Hall effect had appeared. For example, the graphenelike materials silicene [6,7], germanene [8,9], and stanene [10] as well as certain monolayers (MLs) of transition metal dichalcogenides (TMDs) in either the 1T′ phase [11] or the Haeckelite crystal structure [12]. In contrast to other commonly occurring TMDs, WTe_2 is of particular interest, since the 1T′ structure is the naturally occurring phase, and MLs can thus be obtained by direct exfoliation. Indeed, the quantum spin Hall effect in WTe_2 has recently been verified experimentally at temperatures up to 100 K [13–15] and the band gap was reported to be about 50 meV.

2D insulators with an electronic structure which is invariant under time-reversal symmetry can be characterized as being either trivial insulators or QSHIs [16]. This distinction constitutes a topological $\mathbb{Z}_2$ classification, $\mathbb{Z}_2 = 0$, denoting the topologically trivial state, and $\mathbb{Z}_2 = 1$ denoting the QSHI state. It is only possible for a material to change from one of

these topological states to the other if either the gap closes or time-reversal symmetry is broken. For bulk materials, the topological state does not have any direct observational consequences. However, assuming that time-reversal symmetry is conserved, any interface between a trivial insulator and a QSHI, i.e., between the two different topological states, is guaranteed to host gapless boundary states. Since vacuum can be regarded as a trivial insulator, it follows that any edge of a QSHI also hosts gapless states.

The gapless boundary or edge states in QSHIs are protected from backscattering by time-reversal symmetry. The nontrivial topology simply implies that there is no available scattering channel and the edge conductance is predicted to be exactly e^2/h. If time-reversal symmetry is broken, it is no longer guaranteed that gapless edge states persist at the edge. Even if they do, the conductance may deviate from the quantized value due to impurity scattering. This has been observed in WTe_2 where the presence of an external magnetic field significantly reduces the edge conductance [15]. Likewise, the presence of magnetic impurities at edges which may lead to broken time-reversal symmetry [17–19] and destroy the topological edge states. Finally, time-reversal symmetry may be broken *spontaneously* by the presence of magnetism without introducing any impurities. This possibility seems to be largely overlooked in the literature although it by no means is an unlikely scenario. For example, first-principles calculations have shown that edges of a ML MoS_2 in the 2H phase acquires magnetic edge states although the bulk 2D material is nonmagnetic [20]. If time-reversal symmetry is spontaneously broken at an edge of a QSHI, the presence of gapless edge states is no longer guaranteed. Even if they persist, the observable consequences of the quantum Hall state could in principle be removed by a suitable edge modification. In the present paper, we have used first-principles calculations

---

[*]Also at CAMD, Dept. of Physics, Technical University of Denmark, Bldg. 307, DK-2800 Kongens Lyngby, Denmark.
[†]kwj@fysik.dtu.dk

to demonstrate that certain edges of TMDs may acquire magnetic moments, leading to spontaneously broken time-reversal symmetry. The spontaneously symmetry breaking at edges is therefore not a mere academic possibility but could destroy the gapless edge states that are typically assumed to be protected by topology.

It is highly desirable to be able to change the topological index of insulators by external means. This would imply that gapless surface states can be removed or introduced at a given edge which may form the basis of 1D transistors. In the case of TMDs, it has been demonstrated that an external electric field can induce a transition from the quantum spin Hall state to a trivial state [11]. External electric fields may thus comprise a means to switch between conductive and insulating edges. However, the calculations were based on a tight-binding model and constitute a proof of concept rather than an actual quantitative prediction. In the present paper, we have performed full first-principles calculations of TMDs in electric fields. We verify that electric fields can be used to switch the topological state in these materials but find that the magnetic states remain gapless.

The paper is organized as follows. In the second section, we introduce the calculational method and in the third section, we introduce the materials and types of edges that are investigated. The fourth section contains the results on the MoS_2 edges and the fifth section contains the results on three other TMDs. In the final section, we investigate the effect of gating on the three MoS_2 edges.

II. METHOD

The calculations are carried out using DFT [21,22] and the surface Green's function method as implemented in QuantumATK [23]. We consider three different configurations in this study: Fig. 2(a), a nanoribbon configuration with two edges and periodic boundary conditions (PBCs); Fig. 2(b), a surface configuration (*SurfaceConfiguration* [23]) with a single edge and a semi-infinite electrode; and Fig. 2(c), the surface configuration with a gate below. The nanoribbon configuration is used to compare the results of a surface configuration to pinpoint the effect of having a single edge instead of two edges. The gated configuration is used to investigate the response of the edge to an electric field.

To describe the single edge of the ML, we use a surface configuration as shown in Fig. 1. This type of configuration consists of two regions: the electrode and the central region. The electrode is used to describe the bulk properties of the system and the central region contains all the information on the physics of the edge. The calculation is done in two steps. First, a DFT calculation is performed on the isolated and periodic electrode and then a DFT calculation using the Green's function method is performed for the central region. The second calculation uses Green's functions to couple the central region to the electron reservoir of a ML which is periodic in the x and y directions (2D crystal). The electron reservoir is included through the self-energy matrix of the semi-infinite electrode. This self-energy matrix is created from the Hamiltonian of the 2D crystal by a recursive method. More details on the surface Green's function method can
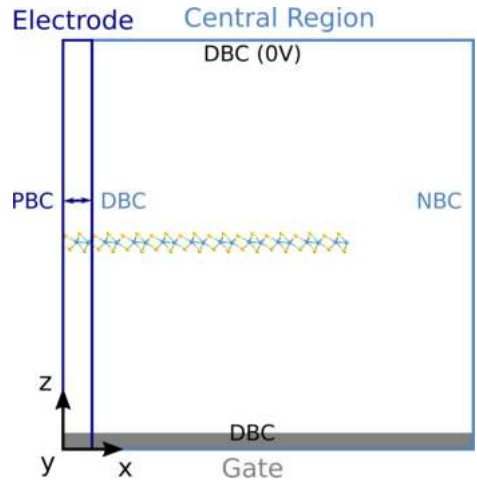

FIG. 1. The *SurfaceConfiguration* of a ML $1T'$ MoS_2 on top of a gate along with the applied boundary conditions. PBC, DBC, and NBC refer to different boundary conditions as explained in the text.

be found in Ref. [23]. The length of the ML in the central region is determined by converging the Hartree potential with respect to length and making sure that it matches the periodic potential of the electrode. A ML length of 50 Å is adequate for all the systems investigated here.

Special care needs to be taken when describing the electrostatics of 2D interfaces or surfaces. The equipotential and corresponding field lines of the effective potential of the three configurations are shown in Fig. 2. This illustrates the field which is created by the 1D dipole (monopole) line along the nanoribbon (single edge). Such a field decreases logarithmically and therefore reaches far out into the vacuum region of the system.

Different treatments are needed for the three types of configurations. In the nanoribbon calculation, we have PBCs for all directions. This means that a sufficient amount of vacuum must be applied both above and below the ML and to the left and right of the ribbon to avoid the spurious interaction between the periodic images of the ribbon. In the case of the surface configuration without a gate, where we only include a single edge, there is also the issue that there is a slope in the potential above and below the ML. This can be seen on Fig. 2(b), where the equipotential lines are perpendicular to the top and bottom of the cell. The slope represents the two distinct electronic levels to the right and to the left of the cell. To the left, the work required for an electron to leave the 2D crystal will be determined by the work function of the crystal. To the right, the work required for an electron to leave the edge will be influenced by the created monopole at the edge and therefore not be equal to the work function of the 2D crystal. The effect is that a macroscopic field is set up which persists even infinitely far away. This is an inherent issue of 2D systems [24], whereas a 3D system with a 2D mono- or dipole only experiences a local potential shift at the surface or interface. To correctly describe
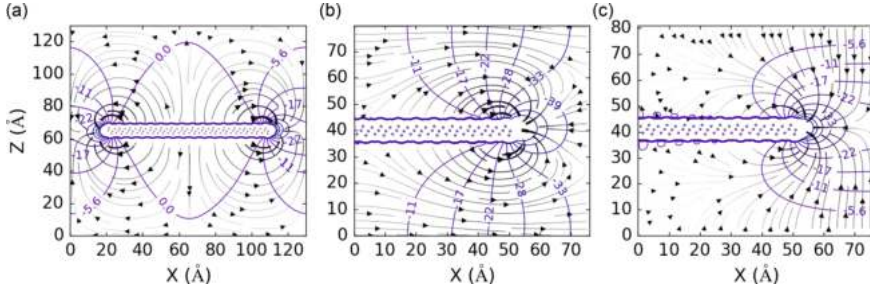
FIG. 2. The equipotential and field lines of the effective potential of (a) a nanoribbon calculation, (b) a surface configuration without a metallic gate, and (c) the surface configuration shown in Fig. 1 with a grounded metallic gate. The equipotential lines are given in meV.

the potential slope and to avoid that it affects the electronic levels, we require that the cell is as high in the z direction as it is long in the x direction. This ensures that the potential has an approximately linear slope at the top and bottom at the cell.

In the case of the gated system, an unconventional set of boundary conditions is chosen for solving the Poisson equation. This is done to accommodate the gate construction and to avoid interactions between images. We apply a Dirichlet boundary condition (DBC) at the top and bottom of the cell so that the potential is fixed in the gate and grounded at the top of the cell. This is analogous to placing the surface between the two plates of a parallel-plate capacitor. For the electrode calculation, we use standard PBCs in all other directions. For the central region, on the other hand, the potential at the left side of the cell is fixed to the value of the potential of the electrode using a DBC and the potential at right side is allowed to converge to the potential in the vacuum region by applying a Neumann BC (NBC). All these boundary conditions are summarized in Table I.

Applying DBCs both at the top and bottom of the cell forces the potential to be zero at those boundaries. The equipotential lines are correspondingly pushed away from these borders and the potential shift is present along the right border of the cell as can be seen in Fig. 2(c). Our investigations show that if the cell keeps the same height as the ungated system and has enough vacuum to the right such that the potential has converged to a constant value when going from left to right, then the electronic levels of the system are equivalent to those of the ungated system.

TABLE I. Boundary conditions used to solve the Poisson equation for the gated surface configuration.

	Electrode	Central region
$-x$	PBC	DBC
$+x$	PBC	NBC
$-y$	PBC	PBC
$+y$	PBC	PBC
$-z$	DBC	DBC
$+z$	DBC	DBC

We apply the Perdew-Burke-Ernzerhof [25] exchange correlation (xc) functional including SOC and noncollinear spin. The wave functions are expanded as a linear combination of atomic orbitals using SG15 pseudopotentials [26] together with the SG15 medium basis set [23]. The occupations are described using a Fermi-Dirac occupation function with an electronic temperature of 300 K. All structure relaxations are done without SOC and to a force tolerance of 0.02 eV/Å.

III. MATERIALS

Of all the 2D TMDs, MoS_2 is by far the most studied material. This is largely due to the fact that it is easily available in the form of the mineral molybdenite. We will therefore begin by investigating the edges of a MoS_2 ML in the $1T'$ phase. The $1T'$ phase possesses a small band gap of 80 meV [27] due to spin-orbit splitting of the bands occurring between the Γ and Y point in the Brillouin zone (BZ). In Fig. 3(a), the band structure is shown with and without SOC to illustrate this. Note that we obtain a gap of 48 meV which is only slightly lower than the experimental value obtained using scanning tunneling spectroscopy (STS) [27]. We will consider three different edges, as indicated in Fig. 3(c). The X edge is a cut along the x direction and the m and c edges are cuts along the y direction. The y cut can be made in several different ways, but these two edges represent the most stable ones for the Mo and single-S terminated kinds, respectively,
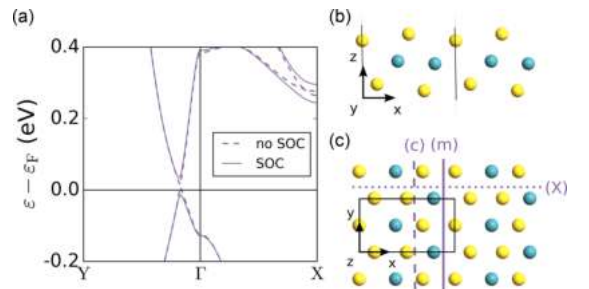

FIG. 3. (a) The band structure of ML MoS_2 in the $1T'$ phase with and without spin-orbit coupling. (b) Side view of the $1T'$ phase. (c) Top view of the $1T'$ phase showing the three investigated edges.
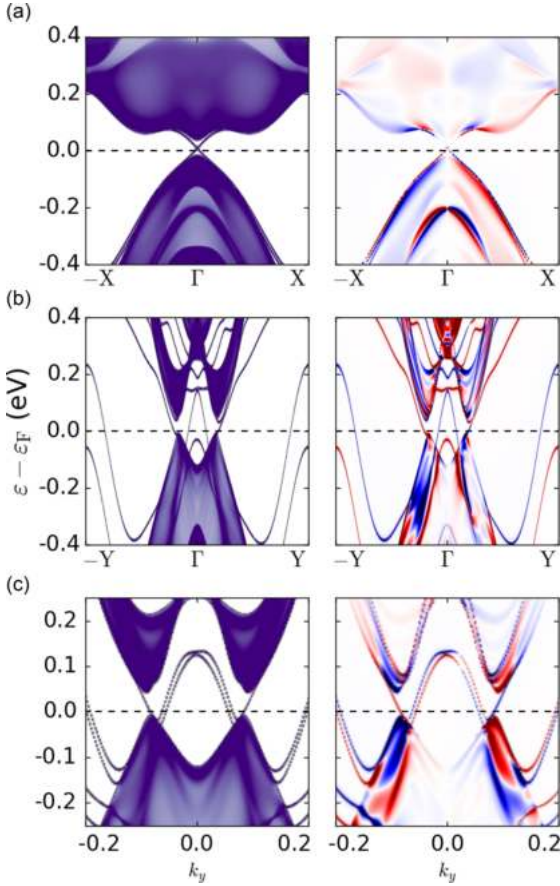
FIG. 4. The electronic bands for (a) the X edge, (b) the m edge, and (c) the c edge of monolayer $1T'$ MoS_2. Left side shows the sum of all spin components and right side shows the spin-polarized density of states with respect to the y direction (a) and the x direction (b), (c).

FIG. 5. The magnetization density with respect to the x and z axis of (a) the m edge and (b) the c edge of MoS_2.

see the Supplemental Material [28] for a stability analysis. The k-point sampling of the m and c edge calculations are 1 x 11 x 1 k-points for the nanoribbons, 11 x 1 for the surface configurations, which are nonperiodic in the x direction, and 401 x 11 x 1 for the periodic 2D crystals. The k-point sampling of the X edge is 6 x 1 x 1 k-points for the nanoribbon, 6 x 1 for the surface configuration, which is nonperiodic in the y direction, and 6 x 401 x 1 for the periodic 2D crystal.

Even though MoS_2 is the most studied TMD, it is not the most studied in the $1T'$ phase since this is unstable with respect to the conventional 1H phase of the ML. Studies of the $1T'$ ML TMD phase have primarily been based on WSe_2 [29,30] and WTe_2 [13–15], where the $1T'$ phase is more stable. We have therefore included these two materials in our investigations. Finally, we include $MoTe_2$ which has been studied as a material for field-effect transistors where few layered $1T'$ and 2H phase materials are used as the contact and channel material, respectively [31].
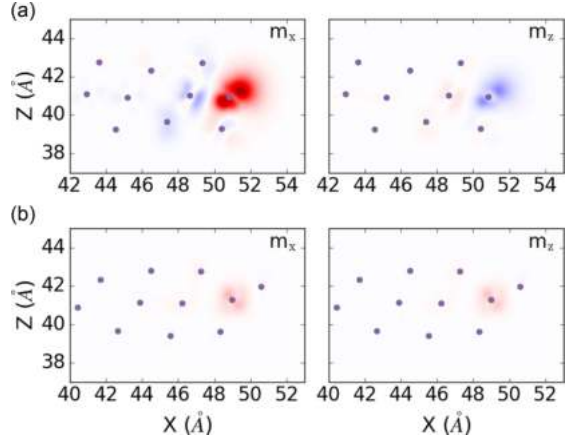
IV. THE EDGES OF $1T'$ MoS_2

We begin by studying the electronic bands of the three different edges of MoS_2. This is done by calculating the density of states for the k-points along the $Y \rightarrow \Gamma \rightarrow Y$ path of the Brillouin zone. The band structures can be seen in Fig. 4 both for the total number of states and for the spin-polarized states weighted by the spin component in the x and y directions, respectively. The solid areas represent the bulk states and the edge states can be identified as the isolated and spin-polarized bands. All three edges host gapless edge states. The X edge has two edge states which are degenerate two-by-two in the high symmetry points of the Brillouin zone. This is exactly what we would expect for the topologically protected edge states of a topological insulator. However, the behavior is different for the other two edges, for which time-reversal symmetry is broken. The effect is most pronounced for the m edge and can be seen in Fig. 4(b), where the spin polarization is equal instead of opposite for any k and $-k$ pair of the edge state. Furthermore, it can be seen that the degeneracy at the high symmetry points is lifted and the bands are separated by approximately 0.25 eV at the Y and $-Y$ points. For the c edge, the effect is more subtle and can only be seen for the edge states close to the gamma point between the two dips of the conduction band. Here, the spin polarization changes, not at the Γ point, but at a small positive value of k going in the Y direction.

The origin of this effect is that the time-reversal symmetry is spontaneously broken as a magnetic state is formed at the edge. This can be illustrated by a plot of the magnetization density as shown in Fig. 5. Note that the spin configuration is noncollinear and we therefore have a magnetization density with respect to each spatial direction. The figure only shows the x and z components, since the y component is zero. The magnetic moments point to the right and downward (upward) for the m (c) edge and have most weight on the last Mo atom of the surface. By investigating the projected density of states near the Γ point, we find that the edge states primarily stem

TABLE II. Calculated band gaps, total magnetization in $\mu_B \times 10^{-2}$, and magnetization vector in μ_B per transition metal atom on the edge for the four different $1T'$ monolayer TMDs.

	E_g[a]	m edge		c edge	
		m	**m**	m	**m**
MoS_2	48 meV	6.7	$(0.26,0,-0.069)$	0.82	$(0.035, 0, 0.028)$
$MoTe_2$	0 meV	17	$(0.75, 0, 0.26)$	-	
WSe_2	10 meV	-		-	
WTe_2	0 meV	5.7	$(0.23, 0, 0.10)$	1.0	$(0.035, 0, -0.030)$

[a]Difference between valance band maxima and conduction band minima.

from the Mo d-orbitals and S p-orbitals with the approximate relative weight of 3:1 for the m edge and 5:2 for the c edge.

From the nanoribbon calculation with two m-type edges [as illustrated in Fig. 2(a)], it can be seen that the magnetic state points in the same spatial direction on both edges. This is also in contrast to the QSHI where two spin channels going in opposite directions reside on each edge. The electronic bands of the nanoribbon are symmetric with respect to k since the two edges are symmetric so that the edge state at each $-k$ point from the left edge has an identical state at the k point on the right edge. A spin-resolved density of states (DOS) will of course still reveal the breaking of the time-reversal symmetry. Nevertheless, this underlines the strength of the surface configuration for investigating single edges one at a time. More results from the nanoribbon calculation can be found in the Supplemental Material [28].

In conclusion, we find that the time-reversal symmetry can be broken on the edges of $1T'$ ML MoS_2 and that it leads to magnetic states which behave very differently from the expected topological states. This means that the gapless states on these edges are not topologically protected and one could imagine that they could be removed by reconstructions of the edge.

V. MAGNETIC EDGES ON $1T'$ TMDS

We now turn our attention to the other three TMDs of the study: WSe_2, WTe_2, and $MoTe_2$. In the investigations of these materials, we use the configuration shown in Fig. 2(b), since we do not wish to apply a field to these edges. The resulting electronic bands can be seen in the Supplemental Material [28]. All investigated edges exhibit edge states. To quantify the magnetism, we calculate the magnetization vector,

$$\mathbf{m} = \frac{1}{N_M} \int \mathbf{m}(\mathbf{r}) \, dV, \qquad (1)$$

and the total magnetization,

$$m = \frac{1}{N_M} \int \sqrt{\mathbf{m}^2(\mathbf{r})} \, dV, \qquad (2)$$

per transition metal atom on the edge, N_M. Note that for all three investigated edges, $N_M = 1$. The results for the m and c edges of all the four investigated materials are seen in Table II along with the distance between the valance and conduction bands. We note that $MoTe_2$ and WTe_2 are metallic since the valence and conduction bands overlap in energy. However,

the bands are separated in k-space, which means that the character of the electronic structure is similar to the other materials and that a topological index can be defined. The magnetic edge state is present for MoS_2, $MoTe_2$, and WTe_2 but missing for WSe_2. As seen in the table, the magnetic m edges show a higher magnetism than the magnetic c edges for the same material. This can be understood through the different stoichiometry of the two termination. At the m-type edge, the outermost metal atoms are completely exposed and missing three of the nearest chalcogenide atoms. This means that the metal atoms are hindered in transferring electrons and end up with a small excess of electrons compared to a metal atom in the 2D crystal. These excess electrons will be filled into the d-band, resulting in a higher DOS at the Fermi level. This higher DOS results in magnetism in accordance with the Stoner criterion. At the c-type edges, the outermost metal atoms only lacks a single chalcogenide neighbor. The bonds are therefore more saturated, the d-band less filled, and the magnetism smaller. From the projected density of states, we find that the edges which become magnetic have edge states where the d-orbitals have a weight which is larger than twice the weight on the p-orbitals. This agrees with the explanation above and shows that the magnetism arise when d-type states dominate the Fermi level.

VI. THE EFFECT OF GATING

It has previously been shown, based on electronic structure calculations [11], that the metallic edge states of the $1T'$ TMD QSHIs can be switched off by applying an electric field perpendicular to the ML. This field closes the band gap and thereby changes the topological state of the material. At a higher field strength, the gap opens again, the system has become topologically trivial, and the gapless edge states are removed. We do similar investigations for the three edges of MoS_2 using full self-consistent DFT to describe the response to the electric field. To find the critical field at which the gap closes, calculations are performed for a range of field strengths perpendicular to the electrode cell of the configuration. For these calculations, we use a k-point grid of 6 x 11 x 1. This describes the response of the 2D crystal and can be seen in Fig. 6(a). The field is applied by adding an external potential as a shift between the gate and the top of the cell and then running a self-consistent DFT calculation. The corresponding field strength in the vacuum region and in the ML can be found as the slope of the effective potential in these regions. The zero field potential is subtracted to extract the slope in the ML region. The effective potentials for zero bias and the critical potential of 130 V is shown in Fig. 6(b) along with the difference between the two. The resulting critical fields are $E_c^{vac} = 1.7$ V/Å in the vacuum and $E_c^{ML} = 6.4 \times 10^{-2}$ V/Å in the ML. The critical field in the ML is about half the size of the reported value from the previous study [11] where the field is added as a correction to the diagonal elements of the Hamiltonian. The large difference between the vacuum field and and field inside the material shows that the ML strongly screens the field. In particular, the longitudindal part of the dielectric constant in the z direction can be estimated as the ratio between the vacuum field and the ML field, $\varepsilon_{ML} = E^{vac}/E^{ML} = 27$.
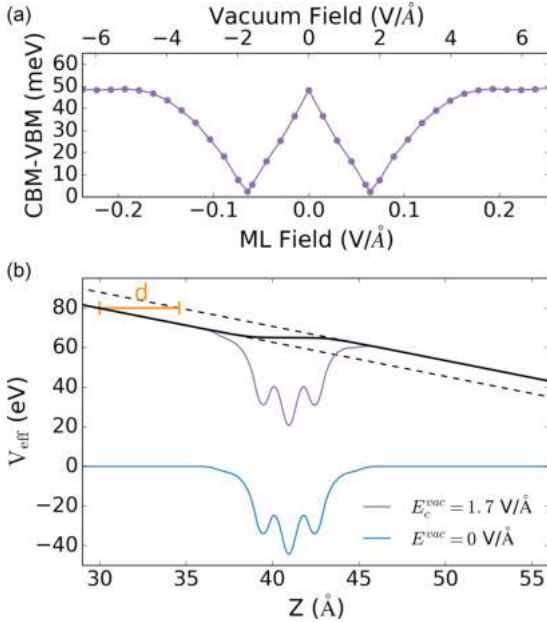
FIG. 6. (a) Gap between valence and conduction band of ML $1T'$ MoS$_2$ as function of the effective potential in the vacuum region and the ML, and (b) effective potential of the zero bias and critical field configurations.

As indicated by the dashed lines in Fig. 6(b), a characteristic distance over which the potential on either side of the ML is shifted can be found. Since the induced field must vanish in the vacuum region, it is straightforward to verify that this shift can be written as

$$d = -\frac{1}{E^{\text{vac}}} \int dz [E^{\text{ML}}(z) - E^{\text{vac}}] = \frac{4\pi}{E^{\text{vac}}} \int dz P_\perp(z)$$
$$= \frac{4\pi P_\perp^{\text{2D}}}{E^{\text{vac}}} = 4\pi \alpha_\perp^{\text{2D}} \tag{3}$$

for any applied field. $P_\perp^{\text{2D}}$ is the 2D polarization perpendicular to the ML, i.e., the dipole per unit area. Except for a factor of 4π, we can thus identify d with the perpendicular component of the 2D polarizability $\alpha_\perp^{\text{2D}} \equiv P_\perp^{\text{2D}}/E_\perp$. For the case of M$oS_2$ in the $1T'$ phase shown in Fig. 6 we get $d = 4.6$ Å. This compares reasonably well with the value of $\alpha_\perp^{\text{2D}}$, calculated using random-phase approximation (RPA) for the Computational 2D Materials Database [32], which yields $d = 5.40$ Å.

Having determined the critical field, we perform calculations on the three edges with the critical field and twice the critical field applied. The electronic bands can be seen in Fig. 7. The edge which has been investigated previously in Ref. [11] is the nonmagnetic X edge. For this edge, we see the expected behavior. Above the critical field, the gapless states have disappeared and no conducting channels are available. For the two magnetic edges, on the other hand, the metallic edge states persist relatively unaltered above the critical field. For the case of the magnetic edges, it is therefore not possible to remove the conducting states by applying a field. Due to the
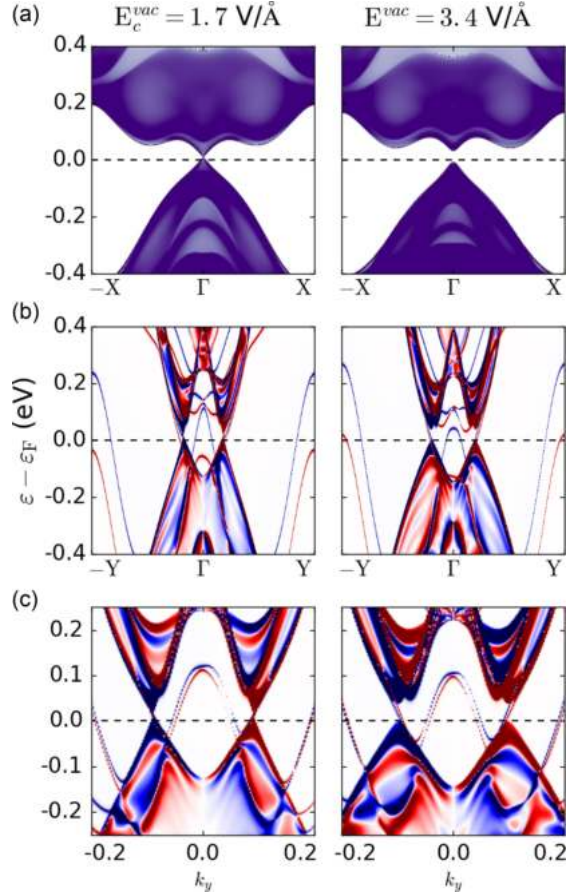

FIG. 7. Response from of the electronic bands of $1T'$ MoS$_2$ when applying a perpendicular field. (a) The X edge, (b) the m edge, and (c) the c edge.

weak coupling between the magnetic and electronic degrees of freedom, the total magnetization also remains relatively unaltered with respect to the field strength.

VII. CONCLUSION

Using DFT and the Greens's function method, we have studied the single isolated edges of four different ML TMDs in the $1T'$ phase. We find that several of the edges show breaking of the time-reversal symmetry and exhibit magnetic edge states. This means that the gapless edge states of these edges are no longer protected against impurity scattering and that they, in principle, could be removed by edge modifications. The total magnetization varies over the four materials and is strongest for one of the MoTe$_2$ edges with a value of 0.17 μ_B per unit cell. We have also studied the response of the edge states of MoS$_2$ when applying a perpendicular field. Self-consistent DFT calculations show that only the topologically protected gapless edge states are removed above a critical field while the gapless magnetic edge states remain relatively unaltered.

ACKNOWLEDGMENTS

[1] C. L. Kane and E. J. Mele, Phys. Rev. Lett. **95**, 226801 (2005).

[2] B. A. Bernevig, T. L. Hughes, and S.-C. Zhang, Science **314**, 1757 (2006).

[3] M. König, S. Wiedmann, C. Brüne, A. Roth, H. Buhmann, L. W. Molenkamp, X.-L. Qi, and S.-C. Zhang, Science **318**, 766 (2007).

[4] D. Hsieh, Y. Xia, D. Qian, L. Wray, F. Meier, J. H. Dil, J. Osterwalder, L. Patthey, A. V. Fedorov, H. Lin, A. Bansil, D. Grauer, Y. S. Hor, R. J. Cava, and M. Z. Hasan, Phys. Rev. Lett. **103**, 146401 (2009).

[5] H. Zhang, C.-X. Liu, X.-L. Qi, X. Dai, Z. Fang, and S.-C. Zhang, Nat. Phys. **5**, 438 (2009).

[6] M. Ezawa, Phys. Rev. Lett. **109**, 055502 (2012).

[7] M. Ezawa, Phys. Rev. B **87**, 155415 (2013).

[8] L. Zhang, P. Bampoulis, A. N. Rudenko, Q. Yao, A. van Houselt, B. Poelsema, M. I. Katsnelson, and H. J. W. Zandvliet, Phys. Rev. Lett. **116**, 256804 (2016).

[9] T. Amlaki, M. Bokdam, and P. J. Kelly, Phys. Rev. Lett. **116**, 256805 (2016).

[10] P. Tang, P. Chen, W. Cao, H. Huang, S. Cahangirov, L. Xian, Y. Xu, S.-C. Zhang, W. Duan, and A. Rubio, Phys. Rev. B **90**, 121408(R) (2014).

[11] X. Qian, J. Liu, L. Fu, and J. Li, Science **346**, 1344 (2014).

[12] S. M. Nie, Z. Song, H. Weng, and Z. Fang, Phys. Rev. B **91**, 235434 (2015).

[13] Z. Fei, T. Palomaki, S. Wu, W. Zhao, X. Cai, B. Sun, P. Nguyen, J. Finney, X. Xu, and D. H. Cobden, Nat. Phys. **13**, 677 (2017).

[14] S. Tang, C. Zhang, D. Wong, Z. Pedramrazi, H.-Z. Tsai, C. Jia, B. Moritz, M. Claassen, H. Ryu, S. Kahn, J. Jiang, H. Yan, M. Hashimoto, D. Lu, R. G. Moore, C.-C. Hwang, C. Hwang, Z. Hussain, Y. Chen, M. M. Ugeda, Z. Liu, X. Xie, T. P. Devereaux, M. F. Crommie, S.-K. Mo, and Z.-X. Shen, Nat. Phys. **13**, 683 (2017).

[15] S. Wu, V. Fatemi, Q. D. Gibson, K. Watanabe, T. Taniguchi, R. J. Cava, and P. Jarillo-Herrero, Science **359**, 76 (2018).

[16] C. L. Kane and E. J. Mele, Phys. Rev. Lett. **95**, 146802 (2005).

[17] Q. Liu, C.-X. Liu, C. Xu, X.-L. Qi, and S.-C. Zhang, Phys. Rev. Lett. **102**, 156603 (2009).

[18] V. D. Kurilovich, P. D. Kurilovich, and I. S. Burmistrov, Phys. Rev. B **95**, 115430 (2017).

[19] J.-H. Zheng and M. A. Cazalilla, Phys. Rev. B **97**, 235402 (2018).

[20] A. Vojvodic, B. Hinnemann, and J. K. Nørskov, Phys. Rev. B **80**, 125416 (2009).

[21] P. Hohenberg and W. Kohn, Phy. Rev. **136**, B864 (1964).

[22] W. Kohn and L. J. Sham, Phys. Rev. **140**, A1133 (1965).

[23] S. Smidstrup, D. Stradi, J. Wellendorff, P. A. Khomyakov, U. G. Vej-Hansen, M.-E. Lee, T. Ghosh, E. Jónsson, H. Jónsson, and K. Stokbro, Phys. Rev. B **96**, 195309 (2017).

[24] J. Zhang, W. Xie, J. Zhao, and S. Zhang, 2D Mater. **4**, 015038 (2017).

[25] J. P. Perdew, K. Burke, and M. Ernzerhof, Phys. Rev. Lett. **77**, 3865 (1996).

[26] M. Schlipf and F. Gyg, Comp. Phys. Comm **196**, 36 (2015).

[27] H. Xu, D. Han, Y. Bao, F. Cheng, Z. Ding, S. J. R. Tan, and K. P. Loh, Nano Lett. **18**, 5085 (2018).

[28] See Supplemental Material at http://link.aps.org/supplemental/10.1103/PhysRevB.99.155420 for the stability of different edge terminations, electronic structure calculation on a nanoribbon and electronic band structures of MoTe_2, WTe_2, and WSe_2.

[29] M. M. Ugeda, A. Pulkin, S. Tang, H. Ryu, Q. Wu, Y. Zhang, D. Wong, Z. Pedramrazi, A. Martín-Recio, Y. Chen, F. Wang, Z.-X. Shen, S.-K. Mo, O. V. Yazyev, and M. F. Crommie, Nat. Commun. **9**, 3401 (2018).

[30] P. Chen, W. W. Pai, Y.-H. Chan, W.-L. Sun, C.-Z. Xu, D.-S. Lin, M. Y. Chou, A.-V. Fedorov, and T.-C. Chiang, Nat. Commun. **9**, 2003 (2018).

[31] J. H. Sung, H. Heo, S. Si, Y. H. Kim, H. R. Noh, K. Song, J. Kim, C.-S. Lee, S.-Y. Seo, D.-H. Kim, H. K. Kim, H. W. Yeom, T.-H. Kim, S.-Y. Choi, J. S. Kim, and M.-H. Jo, Nat. Nanotechnol. **12**, 1064 (2017).

[32] S. Haastrup, M. Strange, M. Pandey, T. Deilmann, P. S. Schmidt, N. F. Hinsche, M. N. Gjerding, D. Torelli, P. M. Larsen, A. C. Riis-Jensen, J. Gath, K. W. Jacobsen, J. J. Mortensen, T. Olsen, and K. S. Thygesen, 2D Mater. **5**, 042002 (2018).

Check for updates

Schottky barrier lowering due to interface states in 2D heterophase devices†

Line Jelver, [ab] Daniele Stradi,[b] Kurt Stokbro[b] and Karsten Wedel Jacobsen [*a]

The Schottky barrier of a metal–semiconductor junction is one of the key quantities affecting the charge transport in a transistor. The Schottky barrier height depends on several factors, such as work function difference, local atomic configuration in the interface, and impurity doping. We show that also the presence of interface states at 2D metal–semiconductor junctions can give rise to a large renormalization of the effective Schottky barrier determined from the temperature dependence of the current. We investigate the charge transport in n- and p-doped monolayer $MoTe_2$ 1T′–1H junctions using *ab initio* quantum transport calculations. The Schottky barriers are extracted both from the projected density of states and the transmission spectrum, and by simulating the IT-characteristic and applying the thermionic emission model. We find interface states originating from the metallic 1T′ phase rather than the semiconducting 1H phase in contrast to the phenomenon of Fermi level pinning. Furthermore, we find that these interface states mediate large tunneling currents which dominates the charge transport and can lower the effective barrier to a value of only 55 meV.

1 Introduction

The contact–channel interface is a crucial performance bottleneck in the development of new transistor technologies. The energy barrier which charge carriers must overcome to move from the metal contact to the semiconductor channel, the Schottky barrier, is one of the main parameters in evaluating the performance of the device. The atomically-thin transition metal dichalcogenides (TMDs) are emerging as a possible alternative to silicon for transistor channels in the next generations of technology nodes.[1,2] However, the technology suffers from large contact resistance between the TMD and the metallic electrode. The resistance can be reduced by locally inducing the metallic 1T[3,4] or the semi-metallic 1T′ phase[5–8] of the TMD and thereafter pattern the 3D electrodes directly on the 1T/1T′ regions. Understanding and quantifying the energy barrier of TMD 1T′–1H interfaces is therefore of great importance for the development of this technology.

Several techniques exist for extracting the Schottky barrier of 2D metal–semiconductor junctions both theoretically and experimentally. Electronic structure calculations most often extract the barrier height from the projected density of states (DOS) along the transport direction[9–12] but the barrier can also

be extracted from the transmission spectrum (TS).[11,13] Experimental methods include Kelvin probe force microscopy,[7] scanning photocurrent microscopy correlated with photoluminescence imaging[14] and application of the thermionic emission (TE) model.[4–6,8,15–17] The TE model has been utilized to extract barriers of fabricated TMD heterophase devices typically in the order of a few tens of meV whereas *ab initio* calculations estimate orders-of-magnitude larger barriers.[9–13]

In this work, we analyze the Schottky barrier height of pristine monolayer 1T′–1H $MoTe_2$ heterophase devices using density functional theory (DFT) and non-equilibrium's Green's function (NEGF) transport calculations. Compared to previous investigations,[9–13] we include both the effect of doping and semiconductor lengths up to 19 nm, which allows for the entire depletion region to be accounted for. Furthermore, we compare the barriers extracted both from the projected DOS, the TS, and using the IT-characteristic and TE model. We study both n- and p-type devices which, due to tunneling effects, show significant reductions in the effective barriers extracted from the IT-characteristic (TE barrier) compared to the barriers obtained from the projected DOS or the TS. Tunneling between the metal and semiconductor states reduces the TE barriers by up to a factor 1.5 whereas tunneling between interface states and semiconductor states can reduce the barrier by a factor of 6. When the tunneling is mediated by interface states, we find the TE barrier of a n-type device to be 55 meV which is comparable to the experimentally measured barriers. An analysis of the interface states reveals that they originate from the metallic phase which renders them relatively insensitive to the doping

[a]CAMD, Dept. of Physics, Technical University of Denmark, Bldg. 309, DK-2800 Kongens Lyngby, Denmark. E-mail: kwj@fysik.dtu.dk

[b]Synopsys QuantumATK, Fruebjergvej 3, PostBox 4, DK-2100 Copenhagen, Denmark
† Electronic supplementary information (ESI) available: Computational details, WKB approximation to model the addition of a substrate or removal of the interface states, and transmission eigenstates of the highly p-doped device. See DOI: 10.1039/d0na00795a

level. This discovery illustrates that these interface states do not result in Fermi level pinning which is an otherwise well-known issue of metal-contacted 1H TMDs.[18–20]

2 Methodology

We choose a free-standing monolayer interface between the MoTe₂ 1T′ and 1H phase as our model system. Even though a transistor will have two Schottky barriers, one at the source and one at the drain, a forward bias will effectively create a single barrier at the source which will dominate the device behavior.[21] We do not include any substrate or gate but investigate the behavior of the isolated heterophase interface. A substrate below the 2D TMDs may have several effects: a small change of the band gap,[22] longer depletion widths,[23] and a modulation of the work function or doping level.[24] A longer depletion width would result in a lower tunneling current but wouldn't change our conclusions. An estimate of this effect can be found in the ESI.† We use doping levels of $N_{D/A} = 4.9 \times 10^{11}$ cm⁻² and $N_{D/A} = 4.6 \times 10^{12}$ cm⁻². The first value corresponds to the estimated p-doping level reported by Sung et al.[6] and the second value is comparable with more recent estimated doping levels in 1H phase TMDs.[25,26] The doping of a 2D material is extremely difficult to control and even to measure. Since almost the entire material is a surface, it is very sensitive to both the environment and local impurities. This means that the doping level can vary significantly across a sample, which makes it important to consider, how different doping levels affect the barriers.

We apply three methods for the Schottky barrier extraction. The DOS barrier, Φ^{DOS}, is extracted from the projected DOS as the distance between the Fermi level and the maximum (minimum) of the conduction (valence) band for the n-type (p-type) devices. Φ^{DOS} therefore includes the band bending due to the electric field created by the interface dipole. This is a macroscopic electrostatic effect ranging over many atomic layers.

The TS barrier, Φ^{TS}, is defined as the distance between the Fermi level and the energy at which the device experience full transmission, defined in this work as 1% of maximum transmission. This definition is discussed further in the results section. Φ^{TS} represents a microscopic quantity that depends directly on the electronic states available for transport.

The TE barrier, Φ^{TE}, is found by applying the TE model to find the barrier from the temperature dependence of the current. We have chosen to evaluate the barriers using this model since it is the most commonly applied experimental method for measuring the Schottky barrier in 2D devices.[4–6,8,15–17] As the name implies, this model assumes that the current is dominated by coherent transport of thermally excited electrons above the Schottky barrier. From this assumption, a relationship between the current, temperature, and barrier height can be derived, which can be used to experimentally determine the Schottky barrier. The most commonly used expression is,[6,17,27]

$$I_{n/p}^{TE} \approx \pm A_{2D}^* T^{3/2} e^{-\frac{\Phi^{TE}}{k_B T}} e^{\pm \frac{eV_{sd}}{k_B T}}. \tag{1}$$

V_{sd} is the voltage drop between the source (semiconductor) and drain (metal), e is the electron charge, k_B is the Boltzmann constant, T is the temperature, A_{2D}^* is the Richardson constant and Φ^{TE} is the barrier height. The different signs in front of the current and bias originate from the fact that holes are the main charge carriers in a p-type device. This means that the current runs from drain to source and that the hole barrier is lowered by decreasing the source–drain bias rather than increasing it. The barrier is extracted by measuring the current in a range of different temperatures and extracting the slope in an Arrhenius plot of $\ln(|I|/T^{2/3})$ vs. $1/T$. The barrier height becomes $\Phi_{n/p}^{TE} = \pm eV_{sd} - \alpha k_B T$ for n- or p-type devices respectively where α is the slope.

As mentioned previously, this model assumes a purely thermionic current. However, many metal–semiconductor junctions form tunneling barriers where the current will have contributions from both the thermal excitation of the electrons and the tunneling. The contribution from the tunneling current has a different temperature dependence which will result in a smaller slope in the Arrhenius plot. Some of the tunneling contributions to the current can be included in eqn (1) using an ideality factor. The ideality factor is unity if no tunneling current is running and increases as the tunneling current becomes more dominant. The factor, η, is included in the exponential term as $\exp(\pm eV_{sd}/\eta k_B T)$. In this work, we explicitly calculate and analyze the tunneling contributions to the current and therefore do not include this factor.

In many experiments the issue of a tunneling current can be avoided by measuring in a regime where tunneling contributions are negligible. This regime is attempted to be reached either by fitting the current response at high temperatures or by applying a gate voltage to reach the flat band condition. In this condition, the semiconductor bands are completely flat and no tunneling can occur. In our calculations, we do not attempt to avoid tunneling contributions but rather seek to investigate the effect these contributions have on the extracted TE barriers. We have therefore not included a back-gate in our simulations and will likewise compare our results to experimentally extracted barriers measured at zero gate voltage.

We extract the TE barriers in accordance with the experimental method. A small bias of $V_{sd} = \pm 0.01$ V is applied for the n- and p-type device, respectively, and we extract the barrier from the temperature dependence of the total current using eqn (1).‡ We use a temperature range between 300 and 450 K to extract the Arrhenius slopes which is similar to the range used in experiments.

The calculations are carried out using DFT[28,29] and the non-equilibrium Green's function method as implemented in QuantumATK.[30] We apply the Perdew–Burke–Ernzerhof (PBE)[31]

---

‡ Eqn (1) assumes the limit where $eV_{sd} \gg k_B T$ whereas the opposite limit would result in a $T^{1/2}$ dependence in the current and an Arrhenius slope which is independent of the bias. We have investigated the effect of varying the temperature exponent in the prefactor and found that the results depends only weakly on this. We wish to investigate a broad temperature range and therefore choose the dependence from eqn (1) and a very small bias such that the slope is dominated by the size of the barrier.
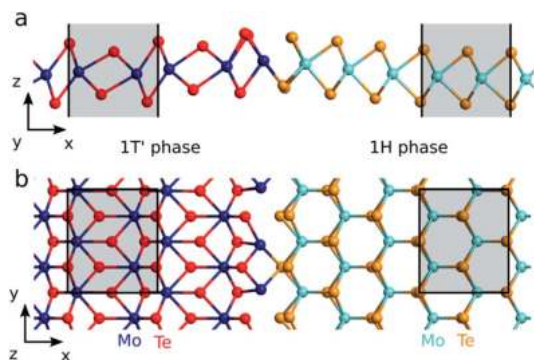
Fig. 1 The 1T′–1H interface of ML MoTe$_2$ observed by Sung et al.[6] seen from (a) the side and (b) the top. Note, that only the region around the interface is shown. The total cell size is (25.0, 0.718, 15.0) nm. The shaded area show the unit cells of the two phases. The largest distance between the final Mo atoms of the 1T′ phase and the first Te atoms in the 1H phase is no more than 3.05 Å.

exchange–correlation functional and a linear combination of atomic orbitals using PseudoDojo pseudopotentials[32] to expand the wave functions. We use a continuous doping model where the electrons per atom is modified and a neutralizing compensation charge is added to the atomic charge.[33] The doping is added to those atoms which belong to the 1H phase before relaxation. These are colored cyan and orange in Fig. 1.

The generalized gradient approximation (GGA) functionals are known to produce bandgaps and work functions which are too small for the free standing TMD monolayers.[34–36] Our calculations show a 1H phase bandgap of 1.03 eV in agreement with previous PBE calculations.[10–12] This should be compared to the value of 1.56 eV obtained by GW calculations.[37] Previous investigations[18–20] have shown that the Schottky barrier between metals and semiconducting 2D TMDs deviate significantly from the Schottky–Mott rule. Therefore, we do not expect the barriers to be dominated by the difference between the metal work function and semiconductor electron affinity or ionization potential but rather by the local charge transfer at the interface. We expect this to be well described within PBE, since the band structure of both conduction and valence band is very similar between PBE and GW calculations.[37] We do not include the spin–orbit coupling which would open a small gap in the 1T′ phase. This is justified by previous calculations[38] showing that the barrier in TMD monolayer heterojunctions changes very little when including this effect.

We set up the interface in the geometry found by Sung et al.[6] using tunneling electron microscopy. The interface is between the (100)-edge of 1T′ and the (01$\bar{1}$0)-edge of 1H and is shown in Fig. 1. We double the cell in the y-direction since this allows for a small distortion that stabilises the interface compared to the single cell geometry. The applied unit cells of the two phases are shown as the shaded areas in Fig. 1. The size of our computational cell for the NEGF calculations is (25.0, 0.718, 15.0) nm and the k-point grid is (401, 6, 1). Further computational details can be found in the ESI.†

3 Results and discussion

We will begin by studying the devices with a doping level of $N_{D/A}$ = 4.9×10^{11} cm^{-2}. For these devices, the depletion width is too long for the interface states to play a part in the quantum transport. These devices will therefore serve as a reference for studying the effect of the interface states in the high-doping devices. For each device, we calculate the projected DOS and the transmission spectrum in equilibrium. The projected DOS of the devices can be seen on Fig. 2a and c. The n-doped device shows a tunneling barrier and significant band bending. The barrier height is 0.54 eV and the depletion width, x_D, is found to be 5.7 nm, assuming a band bending following $CB(x) \propto e^{-x/x_D}$. The corresponding transmission spectrum can be seen on Fig. 2b showing significant contributions from tunneling. The transmission spectrum has several sharp features which stems from the large variance of the DOS with energy in both of the 2D electrodes. This makes the energy of full transmission difficult to define. In order to find a barrier from the transmission, we therefore consider the energy interval where the transmission reaches between 1 and 10% of it's maximum value. This corresponds to a TS barrier between 0.61 and 0.70 eV. The barrier corresponding to 1% of maximum transmission is illustrated on Fig. 2b.

Fig. 2c and d show the corresponding projected DOS and transmission of the p-doped device. In this case, the DOS barrier height is 0.32 eV and the depletion width is 4.1 nm. The transmission once again shows a significant tunneling contribution and the TS barrier is between 0.32 and 0.59 eV corresponding to 1–10% of maximum transmission. We will refer to
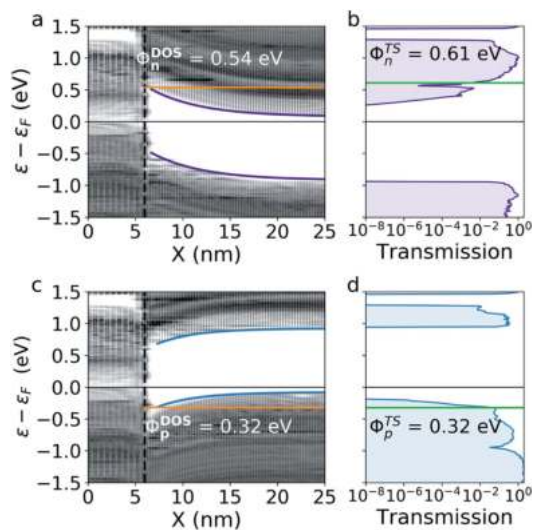

Fig. 2 Projected DOS and transmission spectrum of the devices with n- and p-doping of $N_{D/A} = 4.9 \times 10^{11}$ cm^{-2}. (a) and (c) show the band bending and DOS barrier (orange) for electrons and holes respectively. (b) and (d) show the transmission spectrum and the TS barrier (green) determined using 1% of maximum transmission.

the TS barrier heights corresponding to 1% of full transmission in the remaining of the paper. These agree reasonably well with the barriers extracted from the DOS.

For the TE barrier extraction, we perform self-consistent calculations of the current and use the Landauer–Büttiker expression to calculate the temperature dependence,

$$I^{TUN} = \frac{2e}{h} \int_{\mu_R}^{\Phi^{DOS}} T(E, \mu_L, \mu_R) \times \left[f\left(\frac{E - \mu_L}{k_B T}\right) - f\left(\frac{E - \mu_R}{k_B T}\right) \right] dE. \tag{2}$$

$$I_{n/p}^{TE} = \frac{2e}{h} \int_{\Phi^{DOS}}^{\pm\infty} T(E, \mu_L, \mu_R) \times \left[f\left(\frac{E - \mu_L}{k_B T}\right) - f\left(\frac{E - \mu_R}{k_B T}\right) \right] dE. \tag{3}$$

$$I = I^{TUN} + I^{TE} \tag{4}$$

T is the transmission from the NEGF calculation,[30] h is Planck's constant, and μ_L and μ_R are the chemical potentials of the 1T′ and 1H electrode respectively. The current is separated into a tunneling and thermionic contribution by dividing the energy integral into a tunneling part running from the chemical potential of the 1H electrode to the barrier height observed in the DOS and a thermionic part running from the barrier to infinity. The resulting Arrhenius plot is seen on Fig. 3a showing the total, tunneling and thermionic current of each device. The n-doped device shows a dominating tunneling behavior below 600 K and thermionic behavior above, which can be identified by the two distinct slopes above and below this temperature. These two regimes indicate the existence of a tunneling barrier and the behavior agrees qualitatively with the ones reported by Sung et al.[6] and Ma et al.[8] We extract an TE barrier of 0.37 eV in the temperature range 300–450 K, which is a factor 1.5 lower than the DOS barrier extracted from the equilibrium

calculation. The temperature dependence of the TE barriers is illustrated on Fig. 3b. The barrier of the n-doped device is seen to be lower than the two barriers extracted from the DOS and TS up to 750 K. This illustrates that the tunneling current is non-negligible up to very large temperatures.

The p-doped device shows a tunneling dominated current at least up to 1000 K and the TE barrier is found to be 0.27 eV between 300 and 450 K. The temperature dependence of the barrier is seen in Fig. 3b and shows a negligible variation with temperature with a value below both the DOS and TS barrier. The small variation with temperature reflects the linear behavior seen in the Arrhenius plot and might therefore easily be mistaken to reflect a purely thermionic current. This highlights the difficulty in interpreting these types of Arrhenius plots. From these investigations, we can conclude that both n- and p-type MoTe₂ heterophase junctions are dominated by tunneling currents in the 300–450 K regime which lower the effective barriers.

We now consider, how a higher doping level affects the devices. The projected DOS of these devices are seen on Fig. 4a and d and show DOS barriers of 0.32 eV and 0.19 eV with a depletion width of 1.6 nm and 0.76 nm for the n- and p-doped devices respectively. The computational cells match those of the lower doping level devices except that the highly n-doped device is shortened to 15 nm's in the x-direction to help convergence. The lowering of the DOS barriers as a result of the higher doping level is in agreement with existing theory and with previous studies of heterophase junctions between 1T′- and 1H-phase MoS₂.[13,39] It can be seen from the projected DOS of both devices, that one or more interface states are present in the band bending region between the Fermi level and the barrier height. The positions of the interface states are indicated with arrows. In the n-doped device, interface states or resonances are seen around 0.12 eV and 0.28 eV above the Fermi level. The states are predominantly localized in the interface region with a high DOS which decays both towards the metal and the semiconductor. In the p-doped device, interface states are seen 0.15 eV and 0.24 eV below the Fermi level. It is important to highlight that these states are present in the devices with a lower doping level as well. We will return to this point in the discussion on the origin of the interface states.

The TS barriers are illustrated on Fig. 4b and e. The TS barrier of the n-doped device is 0.30 eV and the p-doped device has a TS barrier of 0.19 eV. A peak is seen in both transmission spectra around the energy of the interface states closest to the Fermi level which illustrates that these states contribute significantly to the charge transport. The peak is most visible in the n-doped device where the position of the interface state is well below the barrier height whereas it is more difficult to see in the p-doped device, where the interface state is positioned very close to the barrier. Another difference in the two spectra is that in the n-doped device, the transmission increases very rapidly above the conduction band edge whereas for the p-doped device, there is no transmission at the valence band edge. The transmission onset occurs around 40 meV below the valence band edge and rises much slower than the transmission of the n-doped device. This is due to the conservation of
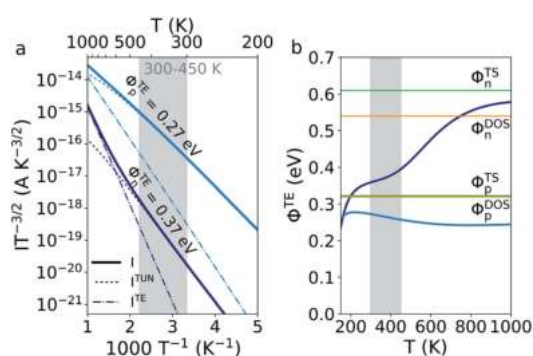
Fig. 3 (a) Arrhenius plot showing the temperature dependence of the total, tunneling and thermionic current with a bias of ±0.01 V for the two devices with $N_{D/A} = 4.9 \times 10^{11}$ cm⁻². Currents of the n- and p-doped devices are shown in deep and light blue respectively. The TE barriers are extracted from the slope in a temperature range of 300–450 K. (b) Temperature dependence of the IT barrier of the two devices. The orange and green lines show the barriers extracted from the DOS and TS respectively.

Fig. 4 Projected DOS, transmission spectrum, and Arrhenius plot of the devices with a doping of $N_{D/A} = 4.6 \times 10^{12}$ cm^{-2}. (a) and (d) show the band bending, interface states (indicated by the arrows), and DOS barrier (orange) of the n- and p-doped device respectively. (b) and (e) show the transmission spectrum and the TS barrier (green) of the two devices. (c) and (f) show the k_y-dependence of the transmission spectra of the devices. The white sta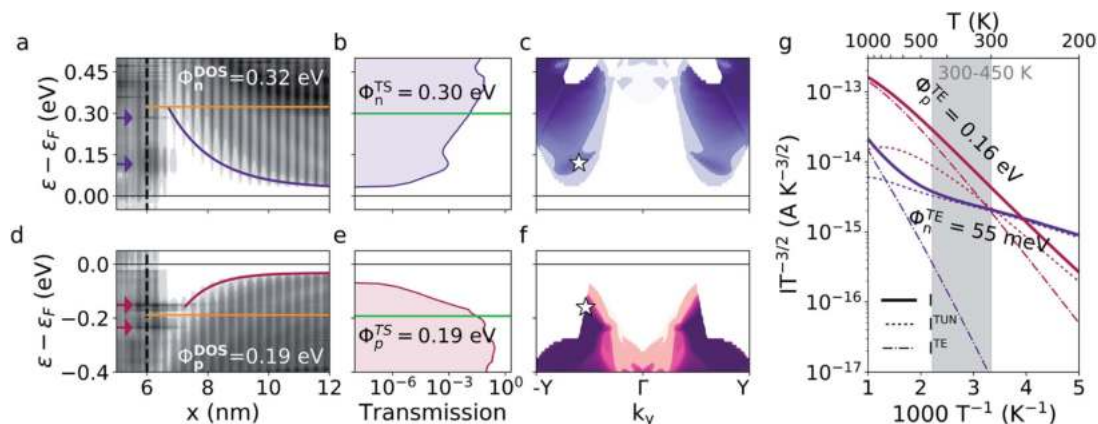r on (c) marks the position at which the transmission eigenstates on Fig. 5 have been calculated. (g) shows the Arrhenius plot and TE barriers at ±0.01 V bias. 201 k_y-points have been used for the non-selfconsistent calculations of the transmission spectra and current.

momentum perpendicular to the transport direction as we shall now see.

The k_y-resolved transmission spectrum for both devices are shown on Fig. 4c and f. For the n-doped device, a reasonably range of k_y points contribute to the transmission already at the conduction band edge. For the p-doped device, the transmission is much more narrow in k-space. This is reflected in the rapid decay of the transmission from the energy of the interface states towards the transmission onset on Fig. 4e where the transmission is summed over all k_y-points. The k-dependence of the transmission arises due to the different dispersion relations of the 1T′ and 1H phase. In order to have momentum conservation perpendicular to the transport direction, a state must be available at the same k_y-value in both phases. This is possible for a larger range of k_y-points for the n-doped device than for the p-doped device. This is also the reason why the transmission onset of the p-doped device occurs below the valence band edge. There are no states available in the 1T′ phase for transport at the valence band edge of the 1H phase.

The temperature dependence of the currents is seen on Fig. 4g and shows an TE barrier of 55 meV for the n-doped device and 0.16 eV for the p-doped device between 300 and 450 K. The n-doped device shows tunneling dominated current up to around 740 K whereas the p-doped device becomes dominated by thermal excitations already around 320 K. The very low TE barrier in the n-doped device reflects the steep increase in the transmission spectrum. The temperature dependence of the current is evaluated through eqn (2)–(4) where the transmission is integrated with the two Fermi distributions of the electrodes. A steep transmission onset therefore results in a significant amount of current running already at low temperatures and the current will only have a weak dependence on the temperature. In the p-doped device, the interface states only has a small effect. This is partly because

these interface states are positioned close to the DOS barrier and partly because only few states are available for transport. We have summarized the three calculated barrier heights of all four devices in Table 1.

The lowering of an TE barrier due to tunneling through a barrier, which dominate the low-doping devices, is a well-known phenomenon[11,21] which also occurs in 3D systems.[40] The behavior seen in the highly n-doped device illustrates how the presence of interface states can increase the tunneling dramatically and lower the TE barrier by more than a factor of 6. Using the Wentzel–Kramers–Brillouin method,[41] we have estimated the TE barrier of this device without the presence of the interface states. The calculations can be found in the ESI† and result in an TE barrier of 0.18 eV. This supports, that it is the presence of the interface states, and not the well-known barrier tunneling, which is responsible for the very low TE barrier.

To illustrate the hybridization between the interface states and the conduction band states, the transmission eigenstates of the n-doped device at 0.12 eV above the Fermi level and at the k_y-value of -0.3 (as indicated by the white star on Fig. 4c) are plotted on Fig. 5a and b. The green and yellow isosurface illustrates the eigenstate originating from the 1T′ electrode, Ψ^L,

Table 1   Calculated barriers of all four devices extracted from the projected DOS, the TS and using the TE model. The TS barriers assume full transmission at 1% of the maximum transmission and the TE barriers are extracted in a temperature range of 300–450 K

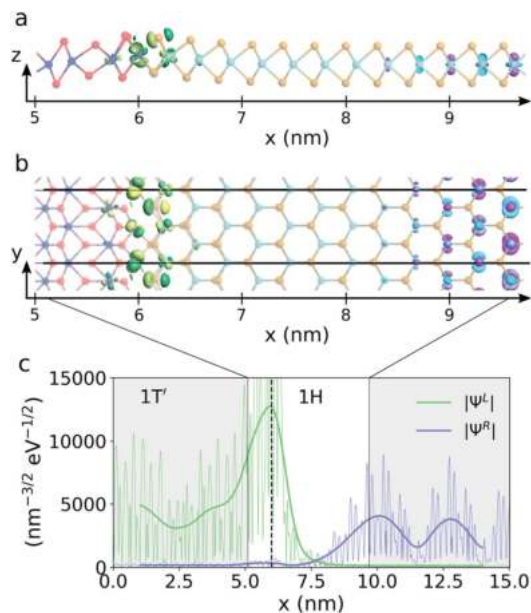| Type	Doping (cm^{-2})	Φ^{DOS}	Φ^{TS}	Φ^{TE}
n-Type	4.9×10^{11}	0.54 eV	0.61 eV	0.37 eV
p-Type	4.9×10^{11}	0.32 eV	0.32 eV	0.26 eV
n-Type	4.6×10^{12}	0.32 eV	0.30 eV	55 meV
p-Type	4.6×10^{12}	0.19 eV	0.19 eV	0.16 eV

Fig. 5 Transmission eigenstates of the device with n-doping $N_D = 4.6 \times 10^{12}$ cm^{-2} at $\varepsilon = 0.12$ eV and $k_y = -0.3$. (a) and (b) show the iso-surfaces of the eigenstate from the 1T′ electrode, Ψ^L, (green and yellow isosurface) and the eigenstate from the 1H electrode, Ψ^R, (cyan and pink isosurface) seen from the side and top of the ML respectively. (c) shows the norm of the two eigenstates summed over the yz-plane and projected along the x-axis. The fat trend lines have been created using Gaussian smoothing.

Fig. 6 Density of states around the Fermi level projected on the last atom of the 1T′ phase at $x = 6.0$ nm. The arrows indicate the energy of maximum DOS of the interface states placed closest to the Fermi level.

and the pink and cyan isosurface illustrate the eigenstate orig-inating in the 1H electrode, Ψ^R. It is seen that the transport primarily occurs between d_{yz} like orbitals on the molybdenum atoms in the interface and d_{z^2} like orbitals in the 1H phase. On Fig. 5c, we plot the norm of the two transmission eigenstates. The state coming from the 1H electrode decays at the interface but the exponential tail of the conduction band states reaches into the 1T′ phase and the transmission eigenstate rises again at the position of the interface state. This illustrates that a coupling between the interface state and 1H conduction band states is possible due to the short depletion width. A similar analysis for the transmission eigenstates in the p-doped device at the point indicated by the white star on Fig. 4f can be found in the ESI† and show the same behavior.

We will now discuss the origin of the interface states. The effect of the interface states described in this work is very different from Fermi level pinning (FLP). FLP tends to pin the Fermi level at the charge neutrality level of the semiconductor surface (edge in 2D). Many previous investigations have shown barrier heights of interfaces between 3D metals and 1H phase TMDs which have a very small dependence on the metal work function, suggesting that FLP dominates.[18–20] However, in our calculations, we find that interface states are present, not at the Fermi level, but above and below. Furthermore, if FLP
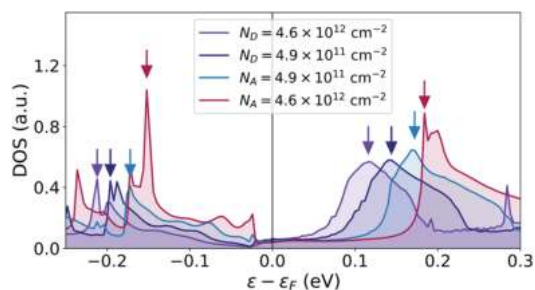
dominated, we would expect that the charge neutrality level would be shifted corresponding to the shift in the barrier height when going from a low to a high doping level. Not only the charge neutrality level, but all the interface states would be shifted by this amount. In our cases, it corresponds to a shift of 0.2 eV for the n-type devices and 0.14 eV for the p-type devices. To quantify this energy shift, we plot the DOS close to the interface at the position of the last Mo-atom belonging to the 1T′ phase. This corresponds to $x = 6.0$ nm at the peak of the transmission eigenstate norm on Fig. 5c. The DOS can be seen on Fig. 6 and shows that the peak of the interface state above the Fermi level only moves about 20 meV (from 0.12 eV to 0.14 eV) going from high to low n-doping. This is only a tenth of the expected shift. An isosurface plot of the left transmission eigenstate of the low n-doped device at 0.14 eV above the Fermi level results in the same isosurface as seen on Fig. 5, identifying it as the same state. The interface state is placed close to this energy even for the p-type devices with a peak at 0.17 eV for the low p-doping and 0.18 eV for the high p-doping. However, since there is no transmission at this energy for the p-type devices, we are unable to confirm this by plotting the transmission eigen-state isosurfaces. The interface state peak below the Fermi level shows a similar behavior shifting about 20 meV going from high to low p-doping.

Based on these observations, we conclude that the interface states are mainly determined by the 1T′ phase rather than 1H phase. These heterophase junctions are therefore free of FLP which agrees with a recent study by Urquiza et al.[39] who have investigated doped 1T′–1H MoS$_2$ junctions. The FLP of inter-faces between 3D metals and 1H phase TMDs has in previous studies been attributed to defects[42] or negative ionization of the outmost S atom complex.[19] The reason why we do not observe such behavior might therefore be that our systems represent perfect crystalline interfaces without any defects with dangling bonds. We suggest, that what we observe are resonances which originate from a hybridization between a localized metal edge state and the 1H conduction band. This conclusion agrees with the decaying DOS both towards the metal and semiconductor. Note, that this is somewhat different from the phenomenon of metal induced gap states which are the result of the exponential

tail of extended bulk metal states protruding into the semi-conductor gap region.

To summarize, our investigations show that the effective barrier extracted from the IT-characteristic can be decreased dramatically due to interface states. In contrast to the effect of Fermi level pinning where the charge neutrality level of the semiconductor edge dominates the band bending and DOS barrier, we see that interface resonances originating from edge states of the metallic phase can dominate the size of the effective barrier by enhancing the tunneling current. We can state three conditions for this effect to be present. Firstly, the bond types in the interface must host interface states originating from the 1T′ phase which are placed relatively close to the Fermi level. Secondly, the depletion width must be short enough to allow for an overlap between the interface states and conduction or valence band states in the 1H phase. Finally, there must be a reasonable amount of available states for momentum conserving transport at the energy of the interface states. TMDs with group six metals have very similar dispersion relations and chemical bonds. We therefore find it very likely that the effect will be present in other heterophase devices as well.

One reason to investigate the TE barriers of the devices is to get a better understanding of why experimentally extracted barriers are much smaller than the barriers extracted from *ab initio* calculations. We will therefore compare our results to the previously measured barrier heights for $MoTe_2$ heterophase devices which are summarized in Table 2. Note, that these results are extracted at zero gate voltage which allows us to make the comparison with our calculations. Our TE barrier of the highly doped n-type device is the only one which is the same order of magnitude as the measured barriers. To our knowledge, we are the first to report barriers of these systems using the DFT + NEGF method which reach values down to this order. The fact, that it is the TE barrier which reaches a comparable value, demonstrates that charge transport mediated by interface states is capable of reducing a measured barrier dramatically. That being said, the fabricated devices differ from our devices in many ways. Multi-layer and substrate effects, the presence of defects, and finite temperatures may all affect the size of the barrier. The presence of defects could very well increase the probability of localized states in the interface and electron–phonon interactions could lead to phonon assisted tunneling. Inelastic transport has previously been shown to have a large effect on the transmission, for instance, it strongly dominates in a reverse biased silicon p–n junction.[43] The presence of defects or inelastic properties would reduce the effect of momentum conservation, which in our calculations suppress the tunneling in the highly p-doped device. The suppressed

tunneling results in the TE barriers of the highly doped devices showing the opposite trend compared to the barriers in the DOS. This leads us to suspect that an inclusion of the contributions from inelastic transport in the p-type device would result in a much better agreement with the experimental results.

4 Conclusions

In conclusion, we have extracted the Schottky barriers of monolayer $MoTe_2$ 1T′–1H heterophase junctions of n- and p-type using the most commonly applied methods for barrier extraction in 2D systems. We found that the barrier heights differ significantly between the extraction methods which highlights that care must be taken if barriers from different methods are to be compared. Furthermore, we found that interface states originating from the 1T′ edge are present in these devices and that they can play a large role in the transport properties. For sufficiently short widths of the depletion region, the edge states hybridize with the states in the 1H phase and significantly enhance the tunneling current. In the highly n-doped device, this decreases the barrier determined using the TE model to 55 meV, which is comparable to experimentally determined barrier heights and which is a factor of 6 lower than the barrier seen in the projected DOS. In the low-doping devices, we found that the depletion width is too long for the interface states to affect the transmission through the device. Regular tunneling effects reduce the TE barriers by a factor 1.5 for the n-doped device and 1.2 for the p-doped device. However, the size of these barriers remains an order-of-magnitude larger than the experimentally measured barriers. Our results, combined with the results of previous *ab initio* studies,[9–13] suggest that the low Schottky barriers measured in these systems are caused by large tunneling currents mediated by interface states.

Conflicts of interest

There are no conflicts to declare.

Acknowledgements

References

1 D. Akinwande, C. Huyghebaert, C.-H. Wang, M. I. Serna, S. Goossens, L.-J. Li, H.-S. P. Wong and F. H. L. Koppens, *Nature*, 2019, **573**, 507–518.

2 *International Roadmap for Devices and Systems*, https://irds.ieee.org, 2018.

3 R. Kappera, D. Voiry, S. E. Yalcin, B. Branch, G. Gupta, A. D. Mohite and M. Chhowalla, *Nat. Mater.*, 2014, **13**, 1128–1134.

4 Y. Katagiri, T. Nakamura, A. Ishii, C. Ohata, M. Hasegawa, S. Katsumoto, T. Cusati, A. Fortunelli, G. Iannaccone,

Table 2 Experimentally measured TE barriers of $MoTe_2$ heterophase devices at zero gate voltage

Type	Doping (cm^{-2})	Φ^{TE}	Fit range
n-Type	—	10 meV (ref. 5)	300–450 K
p-Type	4.9×10^{11}	24 meV (ref. 6)	150–300 K
p-Type	—	25 meV (ref. 8)	240–300 K

G. Fiori, S. Roche and J. Haruyama, *Nano Lett.*, 2016, **16**, 3788–3794.

5 S. Cho, S. Kim, J. H. Kim, J. Zhao, J. Seok, D. H. Keum, J. Baik, D.-H. Choe, K. J. Chang, K. Suenaga, S. W. Kim, Y. H. Lee and H. Yang, *Science*, 2015, **349**, 625–628.

6 J. H. Sung, H. Heo, S. Si, Y. H. Kim, H. R. Noh, K. Song, J. Kim, C.-S. Lee, S.-Y. Seo, D.-H. Kim, H. K. Kim, H. W. Yeom, T.-H. Kim, S.-Y. Choi, J. S. Kim and M.-H. Jo, *Nat. Nanotechnol.*, 2017, **12**, 1064.

7 X. Xu, S. Chen, S. Liu, X. Cheng, W. Xu, P. Li, Y. Wan, S. Yang, W. Gong, K. Yuan, P. Gao, Y. Ye and L. Dai, *J. Am. Chem. Soc.*, 2019, **141**, 2128–2134.

8 R. Ma, H. Zhang, Y. Yoo, Z. P. Degregorio, L. Jin, P. Golani, J. Ghasemi Azadani, T. Low, J. E. Johns, L. A. Bendersky, A. V. Davydov and S. J. Koester, *ACS Nano*, 2019, **13**, 8035–8046.

9 D. Saha and S. Mahapatra, *Appl. Phys. Lett.*, 2016, **108**, 253106.

10 X.-W. Jiang, L.-W. Wang, Z.-Q. Fan, J.-W. Luo, S.-S. Li, L.-Y. Jiao and R. Huang, *Phys. Rev. B*, 2017, **96**, 165402.

11 Z. Q. Fan, X. W. Jiang, J. Chen and J. W. Luo, *ACS Appl. Mater. Interfaces*, 2018, **10**, 19271–19277.

12 S. Liu, J. Li, B. Shi, X. Zhang, Y. Pan, M. Ye, R. Quhe, Y. Wang, H. Zhang, J. Yan, L. Xu, Y. Guo, F. Pan and J. Lu, *J. Mater. Chem. C*, 2018, **6**, 5651–5661.

13 D. Saha and S. Mahapatra, *IEEE Trans. Electron Devices*, 2017, **64**, 2457–2460.

14 M. Chhowalla, S. Lei, G. Gupta, H. Yamaguchi, J. J. Crochet, S. Najmaei, A. D. Mohite, J.-C. Blancon, J. Lou, B. D. Mangum, R. Kappera and P. M. Ajayan, *ACS Nano*, 2014, **9**, 840–849.

15 X. Cui, G. H. Lee, Y. D. Kim, G. Arefe, P. Y. Huang, C. H. Lee, D. A. Chenet, X. Zhang, L. Wang, F. Ye, F. Pizzocchero, B. S. Jessen, K. Watanabe, T. Taniguchi, D. A. Muller, T. Low, P. Kim and J. Hone, *Nat. Nanotechnol.*, 2015, **10**, 534–540.

16 M. H. Guimarães, H. Gao, Y. Han, K. Kang, S. Xie, C. J. Kim, D. A. Muller, D. C. Ralph and J. Park, *ACS Nano*, 2016, **10**, 6392–6399.

17 X. Zheng, A. Calò, E. Albisetti, X. Liu, A. S. M. Alharbi, G. Arefe, X. Liu, M. Spieser, W. J. Yoo, T. Taniguchi, K. Watanabe, C. Aruta, A. Ciarrocchi, A. Kis, B. S. Lee, M. Lipson, J. Hone, D. Shahrjerdi and E. Riedo, *Nat. Electron.*, 2019, **2**, 17–25.

18 C. Kim, I. Moon, D. Lee, M. S. Choi, F. Ahmed, S. Nam, Y. Cho, H. J. Shin, S. Park and W. J. Yoo, *ACS Nano*, 2017, **11**, 1588–1596.

19 P. Bampoulis, R. Van Bremen, Q. Yao, B. Poelsema, H. J. Zandvliet and K. Sotthewes, *ACS Appl. Mater. Interfaces*, 2017, **9**, 19278–19286.

20 Q. Wang, Y. Shao, P. Gong and X. Shi, *J. Mater. Chem. C*, 2020, **8**, 3113–3119.

21 M. Houssa, D. Athanasios and A. Molle, *2D materials for nanoelectronics*, CRC Press, 2016.

22 S. Borghardt, J. S. Tu, F. Winkler, J. Schubert, W. Zander, K. Leosson and B. E. Kardynał, *Phys. Rev. Mater.*, 2017, **1**, 054001.

23 H. Yu, A. Kutana and B. I. Yakobson, *Nano Lett.*, 2016, **16**, 5032–5036.

24 H. Ilatikhameneh, H. Sahasrabudhe, J. Hellerstedt, R. Rahman, Q. Zhang, C. Zheng, S. Li, M. S. Fuhrer, W. H. Duan, Z. Chen, B. Weber, Q. Bao, Y. Zhang and F. Chen, *ACS Nano*, 2017, **11**, 2785–2793.

25 Z. Cheng, Y. Yu, S. Singh, K. Price, S. G. Noyce, Y. C. Lin, L. Cao and A. D. Franklin, *Nano Lett.*, 2019, **19**, 5077–5085.

26 J. R. Nasr, D. S. Schulman, A. Sebastian, M. W. Horn and S. Das, *Adv. Mater.*, 2019, **31**, 1806020.

27 Y. S. Ang, H. Y. Yang and L. K. Ang, *Phys. Rev. Lett.*, 2018, **121**, 56802.

28 P. Hohenberg and W. Kohn, *Phys. Rev.*, 1964, **136**, B864.

29 W. Kohn and L. J. Sham, *Phys. Rev.*, 1965, **140**, A1133.

30 S. Smidstrup, T. Markussen, P. Vancraeyveld, J. Wellendorff, J. Schneider, T. Gunst, B. Verstichel, D. Stradi, P. A. Khomyakov, U. G. Vej-Hansen, M.-E. Lee, S. T. Chill, F. Rasmussen, G. Penazzi, F. Corsetti, A. Ojanperä, K. Jensen, M. L. N. Palsgaard, U. Martinez, A. Blom, M. Brandbyge and K. Stokbro, *J. Phys.: Condens. Matter*, 2019, **32**, 015901.

31 J. P. Perdew, K. Burke and M. Ernzerhof, *Phys. Rev. Lett.*, 1996, **77**, 3865.

32 M. van Setten, M. Giantomassi, E. Bousquet, M. Verstraete, D. Hamann, X. Gonze and G.-M. Rignanese, *Comput. Phys. Commun.*, 2018, **226**, 39–54.

33 The details on the doping methods implemented in the ATK code can be found in the QuantumATK technical notes at http://docs.quantumatk.com/manual/technicalnotes/.

34 F. A. Rasmussen and K. S. Thygesen, *J. Phys. Chem. C*, 2015, **119**, 13169–13183.

35 Y. Cai, G. Zhang and Y.-W. Zhang, *Sci. Rep.*, 2014, **4**, 6677.

36 D. Y. Qiu, F. H. da Jornada and S. G. Louie, *Phys. Rev. Lett.*, 2013, **111**, 216805.

37 S. Haastrup, M. Strange, M. Pandey, T. Deilmann, P. S. Schmidt, N. F. Hinsche, M. N. Gjerding, D. Torelli, P. M. Larsen, A. C. Riis-Jensen, J. Gath, K. W. Jacobsen, J. J. Mortensen, T. Olsen and K. S. Thygesen, *2D Mater.*, 2018, **5**, 042002.

38 Y. Liu, P. Stradins and S.-H. Wei, *Sci. Adv.*, 2016, **2**, e1600069.

39 M. L. Urquiza and X. Cartoixà, *2D Mater.*, 2020, **7**, 045030.

40 D. Stradi, U. Martinez, A. Blom, M. Brandbyge and K. Stokbro, *Phys. Rev. B*, 2016, **93**, 155302.

41 H. Jeffreys, *Proc. London Math. Soc.*, 1925, **2–23**, 428–436.

42 Y. Liu, J. Guo, E. Zhu, L. Liao, S. J. Lee, M. Ding, I. Shakir, V. Gambin, Y. Huang and X. Duan, *Nature*, 2018, **557**, 696–700.

43 T. Gunst, T. Markussen, M. L. Palsgaard, K. Stokbro and M. Brandbyge, *Phys. Rev. B*, 2017, **96**, 161404(R).

Bibliography

[1] *IEEE International Roadmap for Devices and Systems.* 2020. URL: https://irds.ieee.org/editions/2020.

[2] *Global digital population as of October 2020.* 2020. URL: https://www.statista.com/statistics/617136/digital-population-worldwide.

[3] N. Jones. "How to stop data centres from gobbling up the world's electricity." In: *Nature* 561 (2018), pp. 163–166.

[4] *Air pollution.* 2021. URL: https://www.who.int/health-topics/air-pollution#tab=tab_1.

[5] V. Masson-Delmotte et al. *Global Warming of 1.5°C. An IPCC Special Report on the impacts of global warming of 1.5°C above pre-industrial levels and related global greenhouse gas emission pathways, in the context of strengthening the global response to the threat of climate change, sustainable development, and efforts to eradicate poverty.* 2018. URL: https://www.ipcc.ch/sr15.

[6] *microprocessor trend data.* 2019. URL: https://github.com/karlrupp/microprocessor-trend-data.

[7] M. Roser and H. Ritchie. "Technological Progress." In: *Our World in Data* (2013). https://ourworldindata.org/technological-progress.

[8] R. Zafar. *Apple A13 For iPhone 11 has 8.5 Billion Transistors,Quad-Core GPU.* 2019. URL: https://wccftech.com/apple-a13-iphone-11-transistors-gpu.

[9] *13 Sextillion & Counting: The Long & Winding Road to the Most Frequently Manufactured Human Artifact in History.* 2018. URL: https://computerhistory.org/blog/13-sextillion-counting-the-long-winding-road-to-the-most-frequently-manufactured-human-artifact-in-history/.

[10] G. E. Moore. "Cramming more components onto integrated circuits." In: *Electronics* 38.8 (1965), p. 114.

[11] A. Nourbakhsh et al. "MoS_2 Field-Effect Transistor with Sub-10 nm Channel Length." In: *Nano Letters* 16.12 (2016), pp. 7798–7806.

[12] Q. Zhang et al. "Simultaneous synthesis and integration of two-dimensional electronic components." In: *Nature Electronics* 2.4 (2019), pp. 164–170.

[13] P. Hohenberg and W. Kohn. "Inhomogeneous Electron Gas." In: *Phy. Rev.* 136 (1964), B864.

[14] W. Kohn and L. J. Sham. "Self-Consistent Equations Including Exchange and Correlation Effects." In: *Phys. Rev.* 140 (1965), A1133.

[15] S. Smidstrup et al. "QuantumATK: an integrated platform of electronic and atomic-scale modelling tools." In: *Journal of Physics: Condensed Matter* 32.1 (2019), p. 015901.

[16] J. Kohanoff. *Electronic Structure Calculations for Solids and Molecules: Theory and Computational Methods.* Cambridge: Cambridge University Press, 2006.

[17] J. P. Perdew, K. Burke, and M. Ernzerhof. In: *Phys. Rev. Lett.* 77 (1996), p. 3865.

[18] L. Hedin. "New Method for Calculating the One-Particle Green's Function with Application to the Electron-Gas Problem." In: *Phys. Rev.* 139 (3A 1965), A796–A823.

[19] C. Kim et al. "Fermi Level Pinning at Electrical Metal Contacts of Monolayer Molybdenum Dichalcogenides." In: *ACS Nano* 11.2 (2017), pp. 1588–1596.

[20] P. Bampoulis et al. "Defect Dominated Charge Transport and Fermi Level Pinning in MoS_2/Metal Contacts." In: *ACS Applied Materials and Interfaces* 9.22 (2017), pp. 19278–19286.

[21] Q. Wang et al. "Metal-2D multilayered semiconductor junctions: layer-number dependent Fermi-level pinning." In: *Journal of Materials Chemistry C* 8.9 (2020), pp. 3113–3119.

[22]   L. Jelver et al. "Schottky barrier lowering due to interface states in 2D heterophase devices." In: *Nanoscale Advances* 3.2 (2021), pp. 567–574. arXiv: `1911.09521`.

[23]   S. Haastrup et al. "The Computational 2D Materials Database: high-throughput modeling and discovery of atomically thin crystals." In: *2D Materials* 5.4 (2018), p. 042002.

[24]   D. R. Hamann. "Optimized norm-conserving Vanderbilt pseudopotentials." In: *Phys. Rev. B* 88 (8 2013), p. 085117.

[25]   M. Schlipf and F. Gyg. "Optimization algorithm for the generation of ONCV pseudopotentials." In: *Comp. Phys. Comm* 196 (2015), p. 36.

[26]   M. van Setten et al. "The PseudoDojo: Training and grading a 85 element optimized norm-conserving pseudopotential table." In: *Computer Physics Communications* 226 (2018), pp. 39–54.

[27]   *The details on the doping methods implemented in the ATK code can be found in the QuantumATK technical notes.* 2021. URL: `http://docs.quantumatk.com/manual/technicalnotes/`.

[28]   S. Smidstrup et al. "First-principles Green's-function method for surface calculations: A pseudopotential localized basis set approach." In: *Physical Review B* 96.19 (2017), p. 195309.

[29]   M. P. L. Sancho et al. "Highly convergent schemes for the calculation of bulk and surface Green functions." In: *Journal of Physics F: Metal Physics* 15.4 (1985), pp. 851–858.

[30]   L. Jelver et al. "Determination of low-strain interfaces via geometric matching." In: *Physical Review B* 96.8 (2017), p. 085306.

[31]   A. Blom and K. Stokbro. "Atomistic modeling of semiconductor interfaces." In: *J. Comput. Electron.* 12.4 (2013), pp. 623–637.

[32]   V. Dusastre et al. "The interface is still the device." In: *Nature Materials* 11 (2012), p. 91.

[33]   H. Kroemer. "Nobel Lecture: Quasielectric fields and band offsets: teaching electrons new tricks." In: *Rev. Mod. Phys.* 73 (2001), p. 783.

[34] K. Shoemake and T. Duff. "Matrix animation and polar decomposition." In: *Proceedings of the conference on Graphics interface 92* (1992), pp. 258–264.

[35] Y. Yang et al. "A new generation of alloyed/multimetal chalcogenide nanowires by chemical transformation." In: *Science Advances* 1.10 (2015).

[36] Y. Myung et al. "Composition-Tuned ZnO−CdSSe Core−Shell Nanowire Arrays." In: *ACS Nano* 4.7 (2010), pp. 3789–3800.

[37] P. K. Kasanaboina et al. "Bandgap tuning of GaAs/GaAsSb core-shell nanowires grown by molecular beam epitaxy." In: *Semiconductor Science and Technology* 30.10 (2015).

[38] I. P.-T. Institute. *Electronic archive. New Semiconductor Materials. Characteristics and Properties.* NIST. URL: http://www.ioffe.ru/SVA/NSM/Semicond/.

[39] C. Kittel. *Introduction to Solid State Physics.* 8th. Wiley, 2004.

[40] P. Krogstrup et al. "Epitaxy of semiconductor –superconductor nanowires." In: *Nature Materials* 14.4 (2015), pp. 400–406.

[41] S. Manzeli et al. "2D transition metal dichalcogenides." In: *Nature Reviews Materials* 2 (2017).

[42] P. Joensen, R. F. Frindt, and S. Morrison. "Single-layer MoS_2." In: *Materials Research Bulletin* 21.4 (1986), pp. 457–461.

[43] J. A. Wilson and A. D. Yoffe. "The transition metal dichalcogenides discussion and interpretation of the observed optical, electrical and structural properties." In: *Advances in Physics* 18.73 (1969), pp. 193–335.

[44] D. Pasquier and O. V. Yazyev. "Crystal field, ligand field, and interorbital effects in two-dimensional transition metal dichalcogenides across the periodic table." In: *2D Materials* 6.2 (2019), p. 25015.

[45] F. A. Rasmussen and K. S. Thygesen. "Computational 2D Materials Database: Electronic Structure of Transition-Metal Dichalcogenides and Oxides." In: *The Journal of Physical Chemistry C* 119.23 (2015), pp. 13169–13183.

[46]   K. A. N. Duerloo, Y. Li, and E. J. Reed. "Structural phase transitions in two-dimensional Mo- and W-dichalcogenide monolayers." In: *Nature Communications* 5.May (2014).

[47]   Z. Fei et al. "Edge conduction in monolayer WTe_2." In: *Nat. Phys.* 13.7 (2017), pp. 677–682.

[48]   S. Tang et al. "Quantum spin Hall state in monolayer 1T'-WTe_2." In: *Nat. Phys.* 13.7 (2017), pp. 683–687.

[49]   S. Wu et al. "Observation of the quantum spin Hall effect up to 100 kelvin in a monolayer crystal." In: *Science* 359.6371 (2018), pp. 76–79.

[50]   Y. Wang, Y. Li, and Z. Chen. "Not your familiar two dimensional transition metal disulfide: structural and electronic properties of the PdS_2 monolayer." In: *Journal of Materials Chemistry C* 3.37 (2015), pp. 9603–9608.

[51]   X. Qian et al. "Quantum spin Hall effect in two-dimensional transition metal dichalcogenides." In: *Science* 346.6215 (2014), pp. 1344–1347.

[52]   M. Chhowalla et al. "The chemistry of two-dimensional layered transition metal dichalcogenide nanosheets." In: *Nature Chemistry* 5.4 (2013), pp. 263–275.

[53]   K. S. Thygesen. "Calculating excitons, plasmons, and quasiparticles in 2D materials and van der Waals heterostructures." In: *2D Materials* 4.2 (2017), p. 022004.

[54]   R. F. Frindt, A. D. Yoffe, and F. P. Bowden. "Physical properties of layer structures : optical properties and photoconductivity of thin crystals of molybdenum disulphide." In: *Proceedings of the Royal Society of London. Series A. Mathematical and Physical Sciences* 273.1352 (1963), pp. 69–83.

[55]   S. Najmaei et al. "Vapour phase growth and grain boundary structure of molybdenum disulphide atomic layers." In: *Nature Materials* 12.8 (2013), pp. 754–759.

[56]   A. M. van der Zande et al. "Grains and grain boundaries in highly crystalline monolayer molybdenum disulphide." In: *Nature Materials* 12.6 (2013), pp. 554–561.

[57] K. Kang et al. "High-mobility three-atom-thick semiconducting films with wafer-scale homogeneity." In: *Nature* 520.7549 (2015), pp. 656–660.

[58] J. Park et al. "Layer-modulated synthesis of uniform tungsten disulfide nanosheet using gas-phase precursors." In: *Nanoscale* 7.4 (2015), pp. 1308–1313.

[59] D. Dumcenco et al. "Large-Area Epitaxial Monolayer MoS_2." In: *ACS Nano* 9.4 (2015), pp. 4611–4620.

[60] S. Balasubramanyam et al. "Area-Selective Atomic Layer Deposition of Two-Dimensional WS2 Nanolayers." In: *ACS Materials Letters* 2.5 (2020), pp. 511–518.

[61] S. Haldar et al. "Systematic study of structural, electronic, and optical properties of atomic-scale defects in the two-dimensional transition metal dichalcogenides MX_2 (M = Mo, W; X = S, Se, Te)." In: *Physical Review B - Condensed Matter and Materials Physics* 92.23 (2015), pp. 1–12. arXiv: 1509.01445.

[62] S. Barja et al. "Identifying substitutional oxygen as a prolific point defect in monolayer transition metal dichalcogenides." In: *Nature Communications* 10.1 (2019), pp. 1–8.

[63] T. Y. Jeong et al. "Spectroscopic studies of atomic defects and bandgap renormalization in semiconducting monolayer transition metal dichalcogenides." In: *Nature Communications* 10.1 (2019).

[64] J. Liu et al. "Conversion of Multi-layered $MoTe_2$ Transistor Between P-Type and N-Type and Their Use in Inverter." In: *Nanoscale Research Letters* 13 (2018).

[65] P. Luo et al. "Doping engineering and functionalization of two-dimensional metal chalcogenides." In: *Nanoscale Horizons* 4.1 (2019), pp. 26–51.

[66] B. Balasubramaniam et al. "Engineering of transition metal dichalcogenide based 2D nanomaterials through doping for environmental applications." In: *Molecular Systems Design and Engineering* 4.4 (2019), pp. 804–827.

[67] J. Suh et al. "Reconfiguring crystal and electronic structures of MoS_2 by substitutional doping." In: *Nature Communications* 9.1 (2018), p. 199.

[68]   G. Eda et al. "Coherent Atomic and Electronic Heterostructures of Single-Layer MoS_2." In: *ACS Nano* 6.8 (2012), pp. 7311–7317.

[69]   Y.-C. Lin et al. "Atomic mechanism of the semiconducting-to-metallic phase transition in single-layered MoS_2." In: *Nature Nanotechnology* 9.5 (2014), pp. 391–396.

[70]   R. Kappera et al. "Phase-engineered low-resistance contacts for ultrathin MoS_2 transistors." In: *Nature Materials* 13.12 (2014), pp. 1128–1134.

[71]   Y. Ma et al. "Reversible Semiconducting-to-Metallic Phase Transition in Chemical Vapor Deposition Grown Monolayer WSe_2 and Applications for Devices." In: *ACS Nano* 9.7 (2015), pp. 7383–7391.

[72]   L. Sun et al. "Layer-Dependent Chemically Induced Phase Transition of Two-Dimensional MoS_2." In: *Nano Letters* 18.6 (2018), pp. 3435–3440.

[73]   B. Chamlagain et al. "Scalable lateral heterojunction by chemical doping of 2D TMD thin films." In: *Scientific Reports* 10.1 (2020), pp. 1–9.

[74]   S. Bertolazzi, D. Krasnozhon, and A. Kis. "Nonvolatile Memory Cells Based on MoS_2/Graphene Heterostructures." In: *ACS Nano* 7.4 (2013), pp. 3246–3252.

[75]   J. Wang et al. "Floating Gate Memory-based Monolayer MoS_2 Transistor with Metal Nanocrystals Embedded in the Gate Dielectrics." In: *Small* 11.2 (2015), pp. 208–213.

[76]   A. Allain and A. Kis. "Electron and Hole Mobilities in Single-Layer WSe_2." In: *ACS Nano* 8.7 (2014), pp. 7180–7185.

[77]   Y. Wang et al. "Field Effect Modulation of Heterogeneous Charge Transfer Kinetics at Back-Gated Two-Dimensional MoS_2 Electrodes." In: *Nano Letters* 17.12 (2017), pp. 7586–7592.

[78]   Z. Melnikova-Kominkova et al. "Strong and efficient doping of monolayer MoS_2 by a graphene electrode." In: *Physical Chemistry Chemical Physics* 21.46 (2019), pp. 25700–25706.

[79]   Y. Katagiri et al. "Gate-tunable atomically thin lateral MoS_2 Schottky junction patterned by electron beam." In: *Nano Letters* 16.6 (2016), pp. 3788–3794.

[80] S. Cho et al. "Phase patterning for ohmic homojunction contact in MoTe$_2$." In: *Science* 349.6248 (2015), pp. 625–628.

[81] J. Zhu et al. "Argon Plasma Induced Phase Transition in Monolayer MoS2." In: *Journal of the American Chemical Society* 139.30 (2017), pp. 10216–10219.

[82] Y. Kang et al. "Plasmonic Hot Electron Induced Structural Phase Transition in a MoS$_2$ Monolayer." In: *Advanced Materials* 26.37 (2014), pp. 6467–6471.

[83] S. Song et al. "Room Temperature Semiconductor-Metal Transition of MoTe$_2$ Thin Films Engineered by Strain." In: *Nano Letters* 16.1 (2016), pp. 188–193.

[84] A. Apte et al. "Structural Phase Transformation in Strained Monolayer MoWSe$_2$ Alloy." In: *ACS Nano* 12.4 (2018), pp. 3468–3476.

[85] Y. Wang et al. "Structural phase transition in monolayer MoTe$_2$ driven by electrostatic doping." In: *Nature* 550 (2017), p. 487.

[86] P. Byrley, M. Liu, and R. Yan. "Photochemically induced phase change in monolayer molybdenum disulfide." In: *Frontiers in Chemistry* 7.JUN (2019), pp. 1–9.

[87] A. L. Friedman et al. "Evidence for Chemical Vapor Induced 2H to 1T Phase Transition in MoX$_2$ (X = Se, S) Transition Metal Dichalcogenide Films." In: *Scientific Reports* 7.1 (2017), p. 3836.

[88] Y. Yoo et al. "In-Plane 2H-1T' MoTe$_2$ Homojunctions Synthesized by Flux-Controlled Phase Engineering." In: *Advanced Materials* 29.16 (2017), pp. 1–5.

[89] R. Ma et al. "MoTe$_2$ Lateral Homojunction Field-Effect Transistors Fabricated using Flux-Controlled Phase Engineering." In: *ACS Nano* 13.7 (2019), pp. 8035–8046.

[90] X. Zhang et al. "Low Contact Barrier in 2H/1T' MoTe$_2$ In-Plane Heterostructure Synthesized by Chemical Vapor Deposition." In: *ACS Applied Materials and Interfaces* 11.13 (2019), pp. 12777–12785.

[91] J. H. Sung et al. "Coplanar semiconductor–metal circuitry defined on few-layer MoTe$_2$ via polymorphic heteroepitaxy." In: *Nature Nanotechnology* 12 (2017), p. 1064.

[92]   X. Xu et al. "Millimeter-Scale Single-Crystalline Semiconducting MoTe$_2$ via Solid-to-Solid Phase Transformation." In: *Journal of the American Chemical Society* 141.5 (2019), pp. 2128–2134.

[93]   X. Xu et al. "Atomic-Precision Repair of a Few-Layer 2H-MoTe$_2$ Thin Film by Phase Transition and Recrystallization Induced by a Heterophase Interface." In: *Advanced Materials* 32.23 (2020), p. 2000236.

[94]   B. Han et al. "Correlating the electronic structures of metallic/semi-conducting MoTe$_2$ interface to its atomic structures." In: *National Science Review* February (2020), pp. 1–7. arXiv: 1911.09885.

[95]   L. Jelver et al. "Spontaneous breaking of time-reversal symmetry at the edges of 1T' monolayer transition metal dichalcogenides." In: *Physical Review B* 99.15 (2019), p. 155420. arXiv: 1812.09082.

[96]   C. L. Kane and E. J. Mele. "Z2 Topological Order and the Quantum Spin Hall Effect." In: *Physical Review Letters* 95.14 (2005), p. 146802.

[97]   Q. Liu et al. "Magnetic Impurities on the Surface of a Topological Insulator." In: *Phys. Rev. Lett.* 102 (15 2009), p. 156603.

[98]   V. D. Kurilovich, P. D. Kurilovich, and I. S. Burmistrov. "Indirect exchange interaction between magnetic impurities near the helical edge." In: *Phys. Rev. B* 95 (11 2017), p. 115430.

[99]   J.-H. Zheng and M. A. Cazalilla. "Nontrivial interplay of strong disorder and interactions in quantum spin-Hall insulators doped with dilute magnetic impurities." In: *Phys. Rev. B* 97 (23 2018), p. 235402.

[100] A. Vojvodic, B. Hinnemann, and J. K. Nørskov. "Magnetic edge states in MoS$_2$ characterized using density-functional theory." In: *Phys. Rev. B* 80 (12 2009), p. 125416.

[101] H. Xu et al. "Observation of Gap Opening in 1T' Phase MoS$_2$ Nanocrystals." In: *Nano Letters* 18.8 (2018), pp. 5085–5090.

[102] M. M. Ugeda et al. "Observation of topologically protected states at crystalline phase boundaries in single-layer WSe$_2$." In: *Nature Communications* 9.1 (2018), pp. 1–7. arXiv: 1802.01339.

[103] P. Chen et al. "Large quantum-spin-Hall gap in single-layer 1T WSe2." In: *Nature Comm.* 9.2003 (2018).

[104]   M. Gibertini and N. Marzari. "Emergence of One-Dimensional Wires of Free Carriers in Transition-Metal-Dichalcogenide Nanostructures." In: *Nano Letters* 15.9 (2015), pp. 6229–6238.

[105]   Y. Liu, P. Stradins, and S.-H. Wei. "Van der Waals metal-semiconductor junction: Weak Fermi level pinning enables effective tuning of Schottky barrier." In: *Science Advances* 2.4 (2016), e1600069.

[106]   W. Schottky. "Halbleitertheorie der Sperrschicht." In: *Naturwissenschaften* 26.52 (1938), p. 843.

[107]   H. Bethe and M. I. of Technology. Radiation Laboratory. *Theory of the Boundary Layer of Crystal Rectifiers*. Report (Massachusetts Institute of Technology. Radiation Laboratory). Radiation Laboratory, Massachusetts Institute of Technology, 1942.

[108]   S. Sze and K. Ng. *Physics of Semiconductor Devices*. Wiley, 2006.

[109]   H. Ilatikhameneh et al. " Direct Observation of 2D Electrostatics and Ohmic Contacts in Template-Grown Graphene/WS$_2$ Heterostructures." In: *ACS Nano* 11.3 (2017), pp. 2785–2793.

[110]   L. D. Landau and E. M. Lifshitz. *Electrodynamics of Continuous Media (Second Edition)*. Vol. 8. Amsterdam: Pergamon, 1984.

[111]   A. Nipane et al. "Electrostatics of lateral p-n junctions in atomically thin materials." In: *Journal of Applied Physics* 122.19 (2017), p. 194501.

[112]   Y. S. Ang, H. Y. Yang, and L. K. Ang. "Universal Scaling Laws in Schottky Heterostructures Based on Two-Dimensional Materials." In: *Physical Review Letters* 121.5 (2018), p. 56802.

[113]   H. Jeffreys. "On certain approximate solutions of lineae differential equations of the second order." In: *Proceedings of the London Mathematical Society* 2-23.1 (1925), pp. 428–436.

[114]   X. Cui et al. "Multi-terminal transport measurements of MoS$_2$ using a van der Waals heterostructure device platform." In: *Nature Nanotechnology* 10.6 (2015), pp. 534–540.

[115]   M. H. Guimarães et al. "Atomically Thin Ohmic Edge Contacts between Two-Dimensional Materials." In: *ACS Nano* 10.6 (2016), pp. 6392–6399.

[116] X. Zheng et al. "Patterning metal contacts on monolayer MoS_2 with vanishing Schottky barriers using thermal nanolithography." In: *Nature Electronics* 2.1 (2019), pp. 17–25.

[117] A. Li et al. "Electrical contacts of coplanar 2H/1T' $MoTe_2$ monolayer." In: *Journal of Applied Physics* 125.7 (2019).

[118] M. L. Urquiza and X. Cartoixà. "Schottky barriers, emission regimes and contact resistances in 2H-1T' MoS_2 lateral metal-semiconductor junctions from first-principles." In: *2D Materials* 7.4 (2020), p. 045030.

[119] Y. Liu et al. "Approaching the Schottky-Mott limit in van der Waals metal-semiconductor junctions." In: *Nature* 557.7707 (2018), pp. 696–700.

[120] Y. Sun et al. "First-principle high-throughput calculations of carrier effective masses of two-dimensional transition metal dichalcogenides." In: *Journal of Semiconductors* 39.7 (2018).

[121] J. A. Woollam and R. B. Somoano. "Superconducting critical fields of alkali and alkaline-earth intercalates of MoS_2." In: *Phys. Rev. B* 13 (9 1976), pp. 3843–3853.

[122] S. Borghardt et al. "Engineering of optical and electronic band gaps in transition metal dichalcogenide monolayers through external dielectric screening." In: *Physical Review Materials* 1.5 (2017), p. 054001.

[123] H. Yu, A. Kutana, and B. I. Yakobson. "Carrier Delocalization in Two-Dimensional Coplanar p-n Junctions of Graphene and Metal Dichalcogenides." In: *Nano Letters* 16.8 (2016), pp. 5032–5036.

[124] R.-H. Yan, A. Ourmazd, and K. Lee. "Scaling the Si MOSFET: from bulk to SOI to bulk." In: *IEEE Transactions on Electron Devices* 39.7 (1992), pp. 1704–1710.

[125] K. Suzuki et al. "Scaling theory for double-gate SOI MOSFET's." In: *IEEE Transactions on Electron Devices* 40.12 (1993), pp. 2326–2329.

[126] D. Frank, Y. Taur, and H.-S. Wong. "Generalized scale length for two-dimensional effects in MOSFETs." In: *IEEE Electron Device Letters* 19.10 (1998), pp. 385–387.

[127] D. Akinwande et al. "Graphene and two-dimensional materials for silicon technology." In: *Nature* 573.7775 (2019), pp. 507–518.

[128] C. D. English et al. "Improved Contacts to MoS$_2$ Transistors by Ultra-High Vacuum Metal Deposition." In: *Nano Letters* 16.6 (2016), pp. 3824–3830.

[129] Y.-K. Choi, T.-J. King, and C. Hu. "Spacer FinFET: nanoscale double-gate CMOS technology for the terabit era." In: *Solid-State Electronics* 46.10 (2002), pp. 1595–1601.

[130] D. Akinwande et al. "Graphene and two-dimensional materials for silicon technology." In: *Nature* 573.7775 (2019), pp. 507–518.

[131] A. Allain et al. "Electrical contacts to two-dimensional semiconductors." In: *Nature Materials* 14.12 (2015), pp. 1195–1205.

[132] Y. Wang et al. "Van der Waals contacts between three-dimensional metals and two-dimensional semiconductors." In: *Nature* 568.7750 (2019), pp. 70–74.

[133] J. Kang et al. "Computational study of metal contacts to monolayer transition-metal dichalcogenide semiconductors." In: *Physical Review X* 4.3 (2014), pp. 1–14.

[134] L. Wang et al. "One-Dimensional Electrical Contact to a Two-Dimensional Material." In: *Science* 342.6158 (2013), pp. 614–617.

[135] J. Kang, W. Liu, and K. Banerjee. "High-performance MoS$_2$ transistors with low-resistance molybdenum contacts." In: *Applied Physics Letters* 104.9 (2014), p. 093106.

[136] M. Abraham and S. E. Mohney. "Annealed Ag contacts to MoS$_2$ field-effect transistors." In: *Journal of Applied Physics* 122.11 (2017), p. 115306.

[137] X. Xu et al. "Scaling-up Atomically Thin Coplanar Semiconductor–Metal Circuitry via Phase Engineered Chemical Assembly." In: *Nano Letters* 19.10 (2019), pp. 6845–6852.

[138] J. Wu et al. "High electron mobility and quantum oscillations in non-encapsulated ultrathin semiconducting Bi$_2$O$_2$Se." In: *Nature Nanotechnology* 12.6 (2017), pp. 530–534.

[139] H. C. P. Movva et al. "High-Mobility Holes in Dual-Gated WSe$_2$ Field-Effect Transistors." In: *ACS Nano* 9.10 (2015), pp. 10402–10410.

[140] P. Bolshakov et al. "Improvement in top-gate MoS_2 transistor performance due to high quality backside Al_2O_3 layer." In: *Applied Physics Letters* 111.3 (2017), p. 32110.

[141] D. Chu, S. W. Pak, and E. K. Kim. "Locally Gated SnS_2/hBN Thin Film Transistors with a Broadband Photoresponse." In: *Scientific Reports* 8.1 (2018), p. 10585.

[142] E. Liu et al. "Integrated digital inverters based on two-dimensional anisotropic ReS_2 field-effect transistors." In: *Nature Communications* 6.1 (2015), p. 6991.

[143] S. Larentis et al. "Reconfigurable Complementary Monolayer $MoTe_2$ Field-Effect Transistors for Integrated Circuits." In: *ACS Nano* 11.5 (2017), pp. 4832–4839.

[144] E. Zhang et al. "Tunable Ambipolar Polarization-Sensitive Photodetectors Based on High-Anisotropy $ReSe_2$ Nanosheets." In: *ACS Nano* 10.8 (2016), pp. 8067–8077.

[145] N. Youngblood et al. "Waveguide-integrated black phosphorus photodetector with high responsivity and low dark current." In: *Nature Photonics* 9.4 (2015), pp. 247–252.

[146] C. D. Young et al. "(Invited) Evaluation of Few-Layer MoS2 Transistors with a Top Gate and HfO2 Dielectric." In: *ECS Transactions* 75.5 (2016), pp. 153–162.

[147] M. J. Mleczko et al. "$HfSe_2$ and $ZrSe_2$: Two-dimensional semiconductors with native high-κ oxides." In: *Science advances* 3.8 (2017), e1700481–e1700481.

[148] X.-R. Nie et al. "Impact of Metal Contacts on the Performance of Multilayer HfS_2 Field-Effect Transistors." In: *ACS Applied Materials & Interfaces* 9.32 (2017), pp. 26996–27003.

[149] P. Kumar et al. "Polymorphic In-Plane Heterostructures of Monolayer WS2 for Light-Triggered Field-Effect Transistors." In: *ACS Applied Nano Materials* 3.4 (2020), pp. 3750–3759.

[150] J. Wu et al. "Solution Processing for Lateral Transition-Metal Dichalcogenides Homojunction from Polymorphic Crystal." In: *Journal of the American Chemical Society* 141.1 (2019), pp. 592–598.

[151] F. Bischoff et al. "Nanoscale Phase Engineering of Niobium Diselenide." In: *Chemistry of Materials* 29.23 (2017), pp. 9907–9914.

[152]   D. Liu et al. "Synthesis of 2H-1T' WS$_2$-ReS$_2$ Heterophase Structures with Atomically Sharp Interface via Hydrogen-Triggered One-Pot Growth." In: *Advanced Functional Materials* 30.16 (2020), pp. 1–11.

[153]   W. S. Leong et al. "Synthetic Lateral Metal-Semiconductor Heterostructures of Transition Metal Disulfides." In: *Journal of the American Chemical Society* 140.39 (2018), pp. 12354–12358.

[154]   C. H. Naylor et al. "Synthesis and Physical Properties of Phase-Engineered Transition Metal Dichalcogenide Monolayer Heterostructures." In: *ACS Nano* 11.9 (2017), pp. 8619–8627.

[155]   M. Houssa et al. "First-Principles Study of the Contact Resistance at 2D Metal/2D Semiconductor Heterojunctions." In: *Applied Sciences* 10.8 (2020), p. 2731.

[156]   D. Saha and S. Mahapatra. "Atomistic modeling of the metallic-to-semiconducting phase boundaries in monolayer MoS$_2$." In: *Applied Physics Letters* 108.25 (2016), p. 253106.

[157]   D. Saha and S. Mahapatra. "Asymmetric Junctions in Metallic-Semiconducting-Metallic Heterophase MoS$_2$." In: *IEEE Transactions on Electron Devices* 64.5 (2017), pp. 2457–2460.

[158]   H. F. Bai et al. "The intrinsic interface properties of the top and edge 1T/2H MoS$_2$ contact: A first-principles study." In: *Journal of Applied Physics* 123.9 (2018).

[159]   S. Liu et al. "Gate-tunable interfacial properties of in-plane ML MX$_2$ 1T'-2H heterojunctions." In: *Journal of Materials Chemistry C* 6.21 (2018), pp. 5651–5661.

[160]   Z. Dong and J. Guo. "On Low-Resistance Contacts to 2-D MoTe$_2$ by Crystalline Phase Junctions." In: *IEEE Transactions on Electron Devices* 65.4 (2018), pp. 1583–1588.

[161]   X.-W. Jiang et al. " In-plane Schottky-barrier field-effect transistors based on 1T/2H heterojunctions of transition-metal dichalcogenides." In: *Physical Review B* 96.16 (2017), p. 165402.

[162]   Z. Q. Fan et al. "Improving Performances of In-Plane Transition-Metal Dichalcogenide Schottky Barrier Field-Effect Transistors." In: *ACS Applied Materials and Interfaces* 10.22 (2018), pp. 19271–19277.

[163]   W. S. Paz and J. J. Palacios. "A theoretical study of the electrical contact between metallic and semiconducting phases in monolayer MoS_2." In: *2D Materials* 4.1 (2016), p. 015014.

[164]   M. Houssa et al. " Contact Resistance at MoS_2 Based 2D Metal/Semiconductor Lateral Heterojunctions." In: *ACS Applied Nano Materials* 2.2 (2019), pp. 760–766.

[165]   D. Marian et al. "Transistor Concepts Based on Lateral Heterostructures of Metallic and Semiconducting Phases of MoS_2." In: *Physical Review Applied* 8.5 (2017), p. 054047.

[166]   E. Yang et al. "Intrinsic limit of contact resistance in the lateral heterostructure of metallic and semiconducting $PtSe_2$." In: *Nanoscale* 12.27 (2020), pp. 14636–14641.

[167]   X. Guo et al. "Structural, mechanical and electronic properties of in-plane 1T/2H phase interface of MoS_2 heterostructures." In: *AIP Advances* 5.9 (2015).

[168]   R. Thakur et al. "Electronic properties of in-plane phase engineered 1T'/2H/1T' MoS_2." In: *AIP Conference Proceedings* 1942.April (2018).

[169]   J. Robertson. "High dielectric constant oxides." In: *European Physical Journal Applied Physics* 28.3 (2004), pp. 265–291.

[170]   G. Csányi, M. J. Willatt, and M. Ceriotti. "Machine-Learning of Atomic-Scale Properties Based on Physical Principles." In: ed. by K. T. Schütt et al. Cham: Springer International Publishing, 2020, pp. 99–127.

[171]   C. H. Naylor et al. "Monolayer single-crystal 1T -$MoTe_2$ grown by chemical vapor deposition exhibits weak antilocalization effect." In: *Nano Letters* 16.7 (2016), pp. 4297–4304.

[172]   D. Stradi et al. "Method for determining optimal supercell representation of interfaces." In: *Journal of Physics Condensed Matter* 29.18 (2017). arXiv: 1702.00933.

[173]   J. Zhang et al. "Band alignment of two-dimensional lateral heterostructures." In: *2D Materials* 4.1 (2017), p. 15038.

[174]   F. A. Chaves and D. Jiménez. "Electrostatics of two-dimensional lateral junctions." In: *Nanotechnology* 29.27 (2018), p. 275203.

[175]   O. Leenaerts et al. "System-size dependent band alignment in lateral two-dimensional heterostructures." In: *2D Materials* 3.2 (2016), p. 025012.

"Jeg vil have dig for evigt" - Nora Jelver Mathisen